INSTRUMENTATION AND METHODS FOR THE CHARACTERIZATION OF ION STRUCTURE AND INTERNAL ENERGY IN THE GAS PHASE

Philip M. Remes

A dissertation submitted to the faculty of the University of North Carolina at Chapel Hill in partial fulfillment of the requirements for the degree of Doctor of Philosophy in the Department of Chemistry.

Chapel Hill

2007

Approved by:

Advisor: Gary L. Glish

Committee Members: Tomas Baer

R. Mark Wightman

J. Michael Ramsey

Garegin A. Papoian

ABSTRACT

Philip M. Remes

Instrumentation and Methods for the Characterization of Ion Structure and Internal Energy in the Gas Phase
(Under the direction of Dr. Gary L. Glish)

The traditional domains of mass spectrometry (MS) include simple analyte identification by measurement of mass-to-charge value and structural connectivity determinations obtained by tandem mass spectrometry (MS/MS). Tandem MS spectra also contain information about ion three dimensional (3D) conformation, based on the observation of complex reaction pathways only available to certain ion structures. These pathways can involve rearrangement reactions that would never be considered possible in the solution phase. Elucidating 3D structure from MS/MS is therefore very difficult, and information from rearrangement reactions is not currently used by any automatic MS spectral interpretation programs. One of the goals of this dissertation is to build MS based instrumentation that will probe ion 3D structure, so that the dissociation processes in MS/MS can be better understood. Two instruments will be described; a quadrupole ion trap for low temperature IR spectroscopy studies for determination of smaller ion structures, and a high field asymmetric waveform ion mobility spectrometer (FAIMS) for selecting larger ion conformers and subsequently probing these ions via a host of MS/MS methods. Despite the title of the dissertation, the reader will not find any ion structures have been elucidated yet. This is the task of the next generation of Glish lab members. Rather, most of the

experimental chapters herein are of a more preliminary nature and are focused on the study of ion internal energy, which is a significant factor in the study of 3D structure, as well as an important area of study for MS in and of itself.

ACKNOWLEDGEMENTS

I would like to thank my parents and brother and sisters for everything they have done for me, which includes being supportive and excited about whatever I was doing, and giving me the notion that it was possible to be anything I wanted if I put my mind to it.

I would like to thank Dr. Gary L. Glish for setting the bar for scientific curiosity, originality, and rigor, for entrusting tasks to me in areas where I had no experience, and giving me every advantage I could hope for to advance my scientific career.

Thanks to all the Glish Lab members, for being exemplary collegues and good friends.

Thanks Amran, for being my friend and always telling it how it is.

Thank you Maria, for making my last year in Chapel Hill the best one, and showing me the proper way to prioritize my life.

TABLE OF CONTENTS

LIST OF TABLES.....xiv

LIST OF FIGURES..... xv

LIST OF ABBREVIATIONS AND SYMBOLS.....xviii

1. MASS SPECTROMETRY AS A TOOL FOR THE THREE DIMENSIONAL STRUCTURE ANALYSIS OF IONS……1

1.1. Introduction…….. 1

1.1.1. Higher order structure……1

1.1.2. Advantages of Gas-Phase Analysis……... 3

1.2. The Quadrupole Ion Trap Mass Spectrometer……. 5

1.2.1. Theory of Operation……...5

1.2.1.1.Bath Gas…….. 5

1.2.1.2.The Equations of Motion……. 7

1.2.1.3.Pseudopotential Trapping Well……8

1.2.1.4.Manipulating Ions…… 9

1.2.1.4.1. Resonance Ejection……..10

1.2.1.4.2. Collision Induced Dissociation…… 10

1.3. IR Spectroscopy……12

1.3.1. Action Spectroscopy…….. 13

1.3.2. IRMPD Mechanism……... 14

1.3.3. Theoretical Methods for Calculating Structure……..15

1.3.3.1.*Ab Initio* Calculations…….. 16

1.3.3.2.Density Functional Theory Calculations……. 18

1.3.3.3.Calculated Vibrational Modes……. 19

1.4. Other Methods for Ion Higher Order Structure Determination in the Gas Phase… 20

1.4.1. Ion Mobility Spectrometry…….21

1.4.2. High Field Asymmetric Waveform Ion Mobility Spectrometry……22

1.5. Summary……...28

1.6. References…….31

2. EXPERIMENTAL METHODS……. 38

2.1. Ionization……. 38

2.1.1. Nano-Electrospray……...…….. 38

2.1.2. Atmospheric Pressure Matrix Assisted Laser Induced Desorption……... 41

2.1.3. Electron Impact……..42

2.2. Ion Accumulation……. 44

2.3. Ion Dissociation……46

2.3.1. Collision Induced Dissociation……..46

2.3.2. High Amplitude Short Time Excitation…….48

2.3.3. Infrared Multiphoton Dissociation…….48

2.4. Theoretical Methods……49

2.4.1. Structure Calculations……49

2.4.2. Internal Energy Distributions…….50

2.4.3. Ion Trajectory Modeling……51

2.5. References……53

3. DESIGN AND OPERATION OF A QUADRUPOLE ION TRAP FOR INFRARED ACTION SPECTROSCOPY……...55

3.1. Introduction…….. 55

3.2. Method of Low Temperature Ion Trap IR Spectroscopy……. 57

3.3. Low Temperature Considerations…….58

3.3.1. Closed Cycle Helium Refrigeration……...58

3.3.2. Temperature Controller……..59

3.3.3. Thermal Properties of Materials……..60

3.4. Vacuum Housing Design……..61

3.4.1. Trap Enclosures……. 61

3.4.2. Pressure Calibration……...62

3.4.3. Pumping Calculations…… 64

3.4.4. Main Vacuum Chamber……65

3.4.5. Nano-Electrospary Ionization Source…… 66

3.4.6. Octopole Ion Guide……67

3.4.7. RF Oscillator……68

3.4.8. Electron Ionization Source…….70

3.5. Operation of Instrument……71

3.5.1. Tuning the rf Circuit…….. 71

3.5.2. Calibrating the Mass-to-Charge Scale……... 73

3.5.3. “Finding” Ions……74

3.6. Computer Control of Instrument…….. 74

3.6.1. Summary of Control Software……... 74

3.6.2. Interface with PPLN software……76

3.6.3. Data Workup……..77

3.6.4. IR Spectra……...77

3.7. Summary……...78

3.8. References……79

4. COLLISIONAL COOLING IN A QUADRUPOLE ION TRAP AT SUB-AMBIENT TEMPERATURES…….. 83

4.1. Introduction…….. 83

4.1.1. The Quadrupole Ion Trap as a High Pressure Instrument……..83

4.1.2. Perceived Benefits and Challenges of Low Temperature Operation for IRMPD Spectroscopy…… 84

4.2. Methods…… 85

4.3. Theory……...88

4.3.1. Energy Transfer Mechanisms…… 88

4.3.2. Relationship Between Population of Excited Ions and Fragmentation Efficiency…….. 89

4.4. Results and Discussion……. 90

4.4.1. Experimental Determination of Energy Required to Reach a Constant Internal Energy by CID…….. 90

4.4.2. Theoretical Determination of Energy Required to Reach a Constant Internal Energy by Vibrational Energy Analysis……92

4.4.3. Determination of Collisional Cooling Rates……..93

4.5. Conclusions…….. 95

4.6. References…… 97

5. MAPPING THE DISTRIBUTION OF ION POSITIONS AS A FUNCTION OF QUADRUPOLE ION TRAP MASS SPECTROMETER OPERATING PARAMETERS TO OPTIMIZE INFRARED MULTIPHOTON DISSOCIATION…… 100

5.1. Introduction…….. 100

5.2. Influence of q_z, Mass, and Trapping Frequency on Pseudopotential Well Depth… 101

5.3. Experimental Methods……..103

5.3.1. Instrumental……... 103

5.3.2. SIMION Simulation Parameters…… 104

5.3.3. Theoretical Fragmentation Efficiency……... 106

5.4. Results…….. 107

5.4.1. Effect of rf Voltage on Ion Cloud Size……..107

5.4.2. Ion Trajectory Simulations…… 108

5.4.3. Effect of Drive Frequency on Ion Cloud Size……... 110

5.4.4. Effect of Mass on Ion Cloud Size……..111

5.5. Conclusions…….. 112

5.6. References…… 114

6. THEORETICAL ESTIMATION OF PEPTIDE INTERNAL TEMPERATURE FOR HIGH AMPLITUDE SHORT TIME EXCITATION COLLISION INDUCED DISSOCIATION IN A QUADRUPOLE ION TRAP…… 117

6.1. Introduction…….. 117

6.2. Unimolecular Reaction Basics……..119

6.3. Methods and Theory……120

6.3.1. Experimental Parameters……... 120

6.3.2. Simulation of Mass Spectra……... 121

6.3.2.1. Internal Energy Distributions…….122

6.3.3. Rates of Dissociation……. 123

6.3.4. RRKM Parameters……125

6.3.5. Product Ion Internal Energy……...129

6.3.6. Final Scaling of Calculated Intensities…….. 129

6.4. Results and Discussion……. 131

6.4.1. RRKM Parameters……. 131

6.4.2. Comparison of Simulation and Experiment……...132

6.5. Conclusions…….. 137

6.6. References……138

7. ON THE TIME SCALE OF INTERNAL ENERGY RELAXATION OF AP-MALDI AND NANO-ESI IONS IN A QUADRUPOLE ION TRAP……. 141

7.1. Introduction…….. 141

7.1.1. Reexamination of Reported Results…….. 143

7.1.2. Possible Factors Leading to Discrepancies……144

7.2. Methods…… 145

7.2.1. Equalizing Number of Ions for Both Ionization Techniques……148

7.2.2. Higher Time Resolution Cooling Study…… 148

7.2.3. Ion Trajectory Calculations……149

7.3. Theory……...149

7.3.1. Calculation of Space Charge Effects……. 149

7.3.2. Sphere of Constant Charge Density……...149

7.3.3. Gaussian Distribution……150

7.4. Results and Discussion……. 150

7.4.1. Comparison of AP-MALDI vs. nano-ESI …… 150

7.4.2. Effect of Ion Population on Cooling Curves……..154

7.4.3. Experimentally Measured Shifts in Secular Frequency……155

7.4.4. Ion Trajectory Simulations…… 156

7.4.5. Theoretical Shift in Secular Frequency……..159

7.5. Conclusions……...161

7.6. References……163

8. DESIGN AND CONSTRUCTION OF A FAIMS-QEB FOR HIGHER ORDER STRUCTURE DETERMINATION…… 166

8.1. Introduction…….. 166

8.2. Instrumental Layout and Rationale……...168

8.3. Pumping Calculations……...169

8.4. FAIMS Considerations……170

8.4.1. Planar versus Cylindrical Geometry…….. 171

8.4.1.1.Field Shape……...172

8.4.1.2.Simulations…….. 173

8.4.2. Buffer Gas…… 177

8.4.3. Temperature……... 178

8.5. FAIMS-Qq Design……180

8.5.1. Use of TSQ 700……. 180

8.5.2. FAIMS …….. 181

8.5.3. Source…… 183

8.5.4. Octopole……185

8.5.5. Quadrupole Mass Filter……..186

8.5.6. Storage Quadrupole……... 186

8.6. Isolation Transformers……..186

8.7. Control Software…….. 187

8.8. Results…….. 188

8.8.1. EI……188

8.8.2. Nano-ESI……188

8.8.3. Trapping……190

8.8.4. Collision Cross Section Measurements……. 191

8.8.5. FAIMS……... 194

8.9. Summary……...196

8.10. References……..197

9. CONCLUSIONS AND FUTURE DIRECTIONS……. 201

9.1. Summary……...201

9.2. Three Dimensional Mass Spectrometry……201

9.2.1. Action Spectroscopy…….. 201

9.2.2. Ion Mobility……... 202

9.3. Collisional Cooling Measurements……...204

9.4. Ion Cloud Size…….. 205

9.5. Estimation of the Internal Temperature of Ions ……...207

9.6. On the Time Scale of Internal Energy Relaxation of Ions……208

9.7. Conclusions……...209

9.8. References…….210

APPENDIX A LABVIEW PROGRAMS…… 212

APPENDIX B SIMION PROGRAM AND GEOMETRY FILES…….. 221

APPENDIX C DIAGRAMS OF ELECTRONIC CIRCUITRY…….. 229

APPENDIX D TIPS ON OPERATION OF IR-TRAP AND TSQ 700…… 234

APPENDIX E MECHANICAL DRAWINGS……. 236

LIST OF TABLES

Table

3.1 Properties of materials used in the IR-Trap. ……... 60

4.1 Parameters for exponential fit to $y = y_o + A \cdot e^{-Temp / B}$ …….. 90

6.1 Experimental CID parameters ……...121

6.2a RRKM parameters derived from fitting of breakdown curves for $[YGGFL+H]^+$. RA denotes the rearrangement ion at 323 u …… 131

6.2b RRKM parameters derived from fitting of breakdown curves for $[YGAFL+Na]^+$, $[YGGFL+Na]^+$, $[CH_3COONa]_6Na^+$…… 132

6.3 Effective Temperatures Achieved During Conventional CID and HASTE CID…….. 134

7.1 Ion Secular Frequency in kHz at Times After Parent Ion Isolation……...156

LIST OF FIGURES

Figure

1.1 A cutaway view of a QITMS……5

1.2 Supplementary voltages applied to endcaps…….. 10

1.3 Two models for the potential energy well of a bond……. 15

1.4 Geometry optimization from Gaussian……...17

1.5 Calculated structure and IR spectrum for methylvinylketone……... 19

1.6 FAIMS experiment…… 24

1.7 FAIMS Waveforms……25

2.1 Nano-Electrospray Setup……... 36

2.2 Diagram of electron ionization (EI) source……... 44

2.3 Scan functions for ion activation……... 46

3.1 Proposed positioning of CO_2 and PPLN-OPO lasers for IRMPD spectroscopy…….. 58

3.2 Closed-cycle helium cryostat…… 59

3.3 QITMS inside copper enclosure…… 62

3.4 ITMS vacuum housing used as base for IR-Trap…….. 65

3.5 Nano-ESI source for IR-Trap…….66

3.6 Octopole ion guide……67

3.7 General schematic of octopole oscillator circuit……69

3.8 IR-Trap configured for EI…….. 70

3.9 RF circuit for QITMS in open loop (no feedback) configuration……...71

3.10 Structure of instrument control program for IR-Trap…… 75

4.1 Experimental timing diagram for determination of collisional cooling rate constant…….. 86

4.2 Fragmentation efficiency curves for $[YGGFL+H]^+$ at various trap temperatures from 295 K (left side) to 25 K (right side)……... 91

4.3 Relationship between internal energy and internal temperature for n-butylbenzene molecular ion……... 93

4.4 Experimental cooling curve for n-butylbenzene at $5.8x10^{-4}$ Torr He, 295 K……. 94

4.5 Comparison of collisional cooling rate constants vs trap temperature and CID voltage required to reach a constant internal energy vs trap temperature…… 95

5.1 Pseudopotential trapping well depth…….. 102

5.2 Close up of center of SIMION electrode array used to simulate ion trajectories…… 105

5.3 Experimental fragmentation efficiency versus q_z value for tetracycline at various laser powers……... 108

5.4 Calculated probability distribution for ion position at various q_z values for protonated tetracycline ion……... 110

5.5 Fragmentation efficiency versus q_z value for n-butylbenzene molecular ion…….. 112

6.1 Thermal internal energy distributions at different effective temperatures for $[YGGFL+H]^+$……... 122

6.2 Mass spectra calculation…… 124

6.3 Experimental breakdown curves for the a_4^+ ion of YGGFL dissociating to its product ions in conventional CID…… 125

6.4 Comparison of two methods for calculating the internal temperature of ions during conventional CID……127

6.5 Procedure for calculating the product ion internal energy distribution (**p(E)**), demonstrated for $[YGGFL+H]^+$ at 500 K internal energy……130

6.6 Comparison of experimental and calculated MS/MS spectra……136

7.1 Scan function for Finnigan ITMS showing rf trapping voltage as a function of time, and the timing of supplementary waveforms for ion ejection and excitation……... 146

7.2 Fragmentation efficiency versus CID excitation voltage……...151

7.3 The effect of cooling time before CID on fragmentation efficiency……. 153

7.4 Effect of cooling time before CID on fragmentation efficiency…… 154

7.5 Fragmentation efficiency versus CID excitation frequency…….. 156

7.6 Simulation of precursor isolation……...157

7.7 Fourier transform of simulated ion axial positions over a 2 ms time period……. 160

8.1 Diagram of FAIMS-Qq-EB instrument……. 168

8.2 Electric field gradient at 3300 V in a 2 mm space……. 173

8.3 Simulation of $[Cl]^-$ for DV=-3300 V, f = 300 kV over one waveform cycle in FAIMS……..174

8.4 Simulations of $[Cl]^-$…… 175

8.5 Calculated spectra for $[Leucine-H]^-$ in a planar……. 176

8.6 Schematic of FAIMS-Qq……... 181

8.7 Drawing of FAIMS instrument…….. 182

8.8 Electrospray source with interface……. 184

8.9 Octapole ion guide……. 185

8.10 Overlay of all the proteins analyzed by nano-ESI on the Qq instrument to date……...189

8.11 Timing diagram for trapping ions in octapole……... 191

8.12 Stopping curves taken of the 10^+ charge state of bovine ubquitin……193

8.13 FAIMS Simulations with Real Waveform……195

LIST OF ABBREVIATIONS AND SYMBOLS

3D	three dimensional
$<u>$	average gas velocity
A	amphere
a	acceleration
Å	Angstrom; (10^-10 m)
ac	alternating current
AI	analog in
AO	analog out
AP	atmospheric pressure
AP-MALDI	atmospheric pressure matrix assisted laser desorption ionization
Ar	argon
a_z	axial dimensionless parameter in Matheiu stability equation
B	magnetic field strength
B	magnetic sector
B3LYP	common DFT functional
C	capacitance
C	Celcius; unit of temperature
Cd	drag coefficient
c-FAIMS	cylindrical FAIMS
CID	collision induced dissociation
cm	centimeter
CO_2	carbon dioxide
CV	compensation voltage
cw	continuous output
$c_{\mu i}$	molecular orbital expansion coefficient
Da	Dalton; unit of mass equal to 1 amu
dc	direct current
DFT	density functional theory
DHB	dihydroxybenzoic acid
DNA	deoxyribonucleic acid
DO	Digital out
DV	disperision voltage
D_z	pseudo-potential trapping well
$d_{\mu p}$	basis set constants
$d\tau$	volume element
E	electric field strength
e	fundamental charge constant; equal to 1.602e-19 coloumbs/mole
E	energy

E	electric field
E	electric sector
E/N	electric field divided by gas number density
ECD	electron capture dissociation
E_{com}	center of mass collision energy
EI	electron ionization
E_J	electron-electron repulsion
E_{lab}	laboratory frame collision energy
E_T	translational energy
eV	electron volt; unit of energy equal to 1.602e-19 J
E_V	vibrational energy
E_{XC}	electron exchange correlation energy
F	force
f	frequency
FAIMS	high field asymmetric waveform ion mobility spectrometry
FE	fragmentation efficiency
FT-ICR	Fourier transform ion cyclotron resonance mass spectrometer
GC	gas chromatography
g_p	gaussian function
GUI	graphic user interface
H_2	hydrogen gas
HASTE	high amplitude short time excitation
He	Helium
HF	Hartree-Fock
Hz	Hertz; unit of frequency equal to 1 cycle per second
IMS	ion mobility spectrometry
IR	infrared
IRMPD	infrared multiphoton dissociation
ITMS	Ion Trap Mass Spectrometer, an instrument sold by Finnigan in the 1980's and 1990's
IVR	intramolecular vibrational relaxation
J	Joule; unit of energy equal to one Newton-meter
k	force constant
K	mobility
K	Kelvin; unit of temperature
k_b	Boltzmann's constant 1.38e-23 J/K
k_{cc}	collisional cooling rate constant
KE	kinetic energy
K_h	high field ion mobility

kHz	kiloHertz; 1e3 Hz
K_I	low field ion mobility
kV	kilavolt
L	liter
L	drift tube length
l	ion path length
L	liter; unit of volume
LC	liquid chromatography
LIT	linear ion trap
LMCO	low mass cut off; lowest mass ion trapped in a QITMS at a given trapping voltage
LSIMS	liquid secondary ion mass spectrometry
m	meter
m	mass
M	molarity; unit of concentration, moles per liter of solution
m/z	mass-to-charge ratio
m_1	ion mass
m_2	neutral molecule mass
MALDI	matrix assisted laser desorption ionization
m_b	buffer gas mass
mbar	millibar; unit of pressure, equal to 0.75 Torr
mg	milligrams
MHz	MegaHertz; 1e9 Hz
mL	milliliter
mm	millimeter
M_n	mass of neutral collision gas
M_p	mass of parent ion
MS	mass spectrometry
ms	millisecond
MS/MS	tandem mass spectrometry
MS^n	*n* stages of tandem mass spectrometry
MΩ	megaOhms
N	number density
$N^{\ddagger}(E)$	summation of states
N_2	nitrogen
N_A	Avagadro's number; equal to 6.02e23 /mol
nano-ESI	nano-electrospray ionization
nL	nano-Liter; (1e-9 L)
nm	nanometer

NMR	nuclear magnetic resonance
O_2	oxygen
P	pressure
P	parent ion intensity
P	pressure
P_0	initial parent ion intensity
PEEK	polyetheretherketone
pF	pico Farad; unit of capaciance
p-FAIMS	planar FAIMS
PFTBA	perfluorotributylamine
P_{FWHM}	peak full width at half maximum
P_o	peak center position
q	charge
Q	mass resolving quadrupole
q	rf only (non-mass resolving) quadrupole
QITMS	quadrupole ion trap mass spectrometer
q_r	radial dimensionless parameter in Matheiu stability equation
q_z	axial dimensionless parameter in Matheiu stability equation
R	molar gas constant; equal to 0.08206 Latm/mol K
r	position coordinate in radial direction in a QITMS
R	resolving power
r	radius
r	multipole rod radius
R_{eq}	equilibrium ion radius in FAIMS device
rf	radio frequency
R_{in}	radius of inner FAIMS electrode
r_o	radial dimension of a QITMS
r_o	multipole field radius
R_{out}	radius of outer FAIMS electrode
RRKM	Rice-Ramsperger-Kassel-Marcus theory
s	seconds
S	entropy term
S/N	signal-to-noise ratio
SCF	self consistent field theory
SF_6	sulfer-hexafluoride
T	temperature
t	time
Td	Townsend; unit of electric field over number density, 1e-17 Vcm^2

t_d	drift time
T_{eff}	effective temperature
TIC	total ion current
TOF	time of flight (type of mass spectrometer)
Torr	unit of pressure equal to 760 mm of mercury (Hg)
TSQ	triple stage quadrupole
U	dc trapping voltage in QITMS
UNC	University of North Carolina
UV	ultraviolet
V	volt
v	velocity
V	ac trapping voltage in QITMS
V	volts
v/v	volume to volume ratio
v_d	ion drift velocity
V_{pp}	peak-to-peak ac voltage amplitude
W	Watt; unit of power; 1 Joule per second
x_i	abundance of gas i
z	collision frequency
z	position coordinate in axial direction in a QITMS
z	charge
z_o	axial dimension of a QITMS
α	radial extent of gaussian function
β_z	Matheiu stability parameter, see eq 1.10
$\Delta S^{\neq}$	transition state entropy
ε_o	permittivity of vacuum; 8.854e-12 C^2/Jm
μ	reduced mass
v	vibrational state
ξ	dimensionless parameter in Matheiu stability equation
ρ	gas number density
ρ	charge density
$\rho(E)$	density of states
σ	collision cross section
σ	standard deviation
ΣF	sum of fragment ion intensities
Φ	electrical potential (V)
Φ_i	molecular orbital i
Ω	Ohm; unit of electrical resistivity
Ω	QITMS rf voltage frequency in radians per second

$\Omega^{(1,1)}_{avg}$	orientationally averaged collision cross section
ω_z	ion secular frequency in QITMS

Chapter 1

1. Mass Spectrometry as a Tool for the Three Dimensional Structure Analysis of Ions

1.1. Introduction

1.1.1. Higher order structure

Three dimensional (3D) structure, higher order structure, and tertiary structure are all terms used to describe how the atoms of a molecule are oriented in space. This type of spatial information is vital to a full appreciation of any molecule's chemical properties. However, the concept of higher order structure can be improperly conveyed by common molecular representations. For example, molecular formulas and many molecular drawings are one or two dimensional and give mostly connectivity information. These representations sometimes give an unclear idea of the spatial proximity of atoms that are not connected to one another.

The study of organic macromolecules has determined that biological functions are closely related to conformation.[1] Biomolecules, such as proteins, must retain a certain shape to selectively act on their targets. For example, enzymes bind molecules in such specific ways that the rate of making or breaking certain substrate bonds can be accelerated by more than 1000 times.[2] Such specificity is created by a precise three dimensional conformation.

Mass spectrometry (MS) based methods are attractive platforms for solving higher order structure problems, due to the speed and sensitivity of analysis and the ability to routinely assay complex mixtures when coupled to gas and liquid chromatography (GC and

LC). For these reasons, one goal of this dissertation is to create new MS-based instrumentation and methods for probing the 3D structure of many different chemical species. A second important goal, as evidenced by the title of this dissertation, is the characterization of the internal energy of ions. Internal energy refers to the total energy of a molecule resulting from the particular rotational, vibrational and electronic states of the molecule.[3] The peaks and their intensities in a mass spectrum are dictated by internal energy, because of its large effect on the various ways an ion might react with other species or break apart (uni-molecular reaction), and the rates at which these processes will occur. In the case of higher order structure determinations, internal energy is vital to consider because the likelihood of a molecule adopting any one conformation, as well as the probability of isomerization between conformers, is determined by the available internal energy.

Unfortunately, the internal energy of an ion in a mass spectrometer is usually not known, mainly because the precise mechanisms and energetics of the ionization processes are not understood, and any number of uncontrolled collisions with background neutral gas molecules may happen before mass analysis occurs. If the factors affecting ion internal energy in mass spectrometers can be better understood, then more reproducible and potentially even predictable mass spectra will be the result.

Although the instruments constructed for this dissertation are nominally designed to study ion 3D structure, the bulk of the experimental chapters deal with more preliminary questions of how ion internal energy is affected by various instrumental parameters. The remainder of this introductory chapter will present the theoretical background for the rest of the dissertation, allowing each of the experimental chapters to consist of a more concise scientific narrative.

1.1.2. Advantages of Gas-Phase Analysis

There are many analytical techniques for determining higher order structure of molecules. Two of the most useful are nuclear magnetic resonance (NMR) spectroscopy and X-ray diffraction. These condensed phase methods, while powerful under a certain set of circumstances, have inherent drawbacks. NMR requires a relatively large amount of analyte to make a measurement, on the order of milligrams (mg), especially for low abundance C^{13} atoms.[4] To achieve suitable signal to noise ratios (S/N), averaging for several hours to several days is commonplace, and samples must be >95% pure for structural elucidation. Analysis of large molecules becomes increasingly difficult as the signals from the various atoms begin to overlap. Without special labeling techniques, the upper size limit to protein characterization by NMR is about 20 kDa.[5] X-ray diffraction theoretically has no upper mass limit, but has the rather special requirement that the analyte be a well-formed crystal of very high purity.[4] Given these limitations, neither NMR nor X-ray diffraction could be considered a high sensitivity, high-throughput technique. MS, in contrast, is a highly sensitivity technique amenable to high-throughput analyses of complex mixtures, prompting increasing interest in adapting MS based methods to the characterization of higher order structure.

MS techniques differ fundamentally from NMR and X-ray diffraction because mass spectrometers analyze ionic species in the gas phase. There is legitimate skepticism about whether the condensed phase conformation is retained during the transition to the gas phase. One important study showed that a protein complex could retain essentially the same shape in the gas phase as in the solution phase, as evidenced by measurements of the protein cross section in both environments.[6] Another experiment brought a protein into the gas-phase, deposited it onto a surface, and re-solvated it in solution. The protein retained its biological

activity and thus native conformation.[7] While the solution phase structure isn't necessarily the only structure formed in the gas phase, these studies showed that it can be one of them.

Preservation of the same three dimensional structure in the gas as the condensed phase must be proven for proteins, after all, the protein folding mechanism is thought to be largely a result of minimizing the energy of interaction between the various amino acid side residues and the surrounding water molecules.[2, 8, 9] However, the technique of X-ray diffraction analyzes proteins in the crystalline state, the conditions of which are not necessarily the same as the solution state. A high degree of correlation between structures obtained by X-ray diffraction and NMR has been demonstrated however,[10] indicating that the native-state conformations have some inherent stability, even without a mediating solvent. This same principle could apply to MS and gas phase structures.

Gas phase techniques such as MS are advantageous because they allow finer control of the information being gathered than condensed phase methods. For example, in the condensed phase, solvent effects have the tendency of "masking" interesting interactions within a system, such as hydrogen bonds[11] and salt-bridges[12]. Gas-phase experiments provide a more ideal environment in which to probe intramolecular interactions, free from intermolecular interferences[12-14]. The interactions of the ion with solvent can also be studied progressively, by adding solvent molecules in a stepwise manner. Unlike in the solution phase, a variety of very different conformers can be present in the gas phase.[6] Although more conformers could complicate the experiment, they also offer the opportunity to study the driving forces behind the adoption of any one particular structure.

1.2. The Quadrupole Ion Trap Mass Spectrometer

The type of mass analyzer used in the experiments in this dissertation is the quadrupole ion trap mass spectrometer (QITMS). This instrument was first developed in the 1960's by physicists Wolfgang Paul and Helmut Steinwedel, who were given the Nobel Prize for this work in 1989.[15] The diagram in Figure 1.1 is a cutaway view of a QITMS showing the hyperbolic shaped electrodes and the alternating current (ac) voltage generators used for mass analysis and various manipulations of the ions which are described below and in **Chapter 2**.

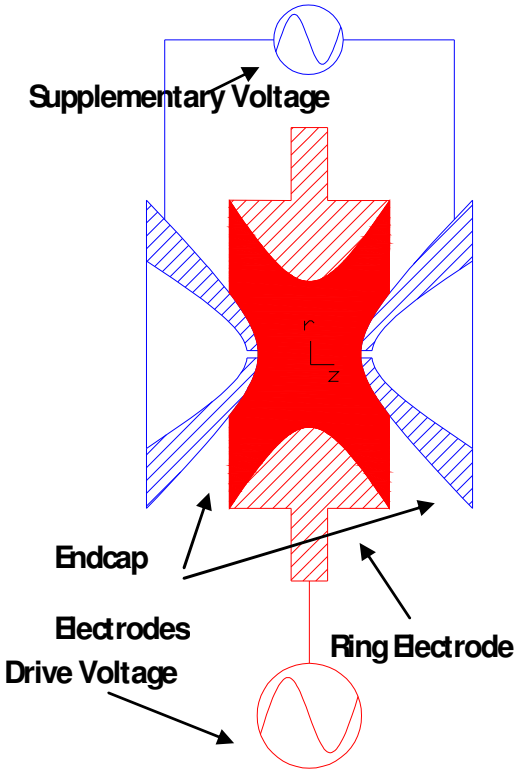

Figure 1.1. A cutaway view of a QITMS with r and z coordinates labeled. Ion are trapped with a high ac voltage on the ring electrode, and various ion manipulations are performed using the supplementary voltage.

Because numerous reviews and primers of the basic operation of a QITMS have been written[16-18], only the information necessary to understand the experiments in this dissertation will be introduced in the following sections.

1.2.1. Theory of Operation

1.2.1.1.Bath Gas

The pressure required for a particular mass spectrometer depends on the path length of the ion. The vacuum generated should be such that the mean free path between ion/molecule collisions is longer than the ion path length *l*, which is given in Equations 1.1

and 1.2. Here <*u*> is average gas velocity and *z* is collision frequency. Substituting for *z* gives the last part of Equation 1.1, where ρ is gas number density and σ is collision cross section. Equation 1.12 substitutes in the ideal gas value for ρ, which adds *R*, the molar gas constant, *T*, temperature, N_A, Avagadro's number, and *P*, pressure.

$$l = \frac{\langle u \rangle}{z} = \frac{\langle u \rangle}{2^{1/2} \rho \sigma \langle u \rangle} = \frac{1}{2^{1/2} \rho \sigma} \qquad \text{(Equation 1.1)}$$

$$l = \frac{RT}{2^{1/2} N_A \sigma P} \qquad \text{(Equation 1.2)}$$

As pressure is increased, the collision frequency increases and the ion will travel a smaller distance between each collision. As an example, in a triple quadrupole mass spectrometer, the ion path length is on the order of a meter, and the pressure is around $1x10^{-6}$ Torr. In a Fourier transform ion cyclotron resonance (FT-ICR), the ion path length may be hundreds of meters, thus, the required pressure is around $1x10^{-9}$ Torr.

In a QITMS, the ion path length is also very long, so the presence Helium (He) gas at ~$1x10^{-3}$ Torr may be surprising. The reasons for this high pressure are several-fold. To be able to trap ions formed from sources external to the QITMS, a *bath*, or *buffer* gas must be present to kinetically cool the ions to the center of the trapping volume. Ion stability in the QITMS depends on initial position and velocity conditions as well as mass-to-charge ratio, making injection of externally generated ions unfavorable without a buffer gas to slow the ions down in the correct location.

Collisional focusing by the bath gas increases performance in the mass analysis stage by three mechanisms. The distance between the ions and the electrode surfaces, which may have slight field-distorting imperfections, is maximized. The ions are less likely to collide with the endcap electrodes during mass analysis, improving transmission through the hole to

the detector. Finally, because the ions are ejected from a more precise point at the center of the trap, ions of the same mass-to-charge ratio reach the detector at a more precise time during mass analysis, improving spectral resolution.

He gas in particular is chosen as the buffer gas because it is small, safe, and non-reactive. Collisions between ions and background gas molecules can result in transfer of kinetic energy into internal energy. The maximum kinetic energy converted is given in Equation 1.3, where E_{com} is the center-of-mass kinetic energy, E_{lab} is the laboratory-frame kinetic energy, M_n is mass of the neutral collision gas, and M_p is the mass of the parent ion species.

$$E_{com} = E_{lab} \frac{M_n}{M_n + M_p} \qquad \text{(Equation 1.3)}$$

According to equation 1.3, the smaller the mass of the neutral species, the less energy will be transferred per collision. He therefore minimizes kinetic energy transfer, reducing ion losses from dissociations and from scattering, which in the end improves mass resolution. Hydrogen gas, (H_2), would be an even better choice from a mass resolution standpoint, but is not used for safety reasons.

1.2.1.2.The Equations of Motion

The elementary equations of force on an ion due to the electric field in a QITMS can be used to derive equations of motion for a single ion starting from rest at the center of the trap.[16-18] The equation for the axial, or z position, may be written in the general form of the Mathieu equation, given in Equation 1.4**.**

$$\frac{d^2 z}{d\xi^2} + (a_z - 2q_z \cos 2\xi) z = 0 \qquad \text{(Equation 1.4)}$$

A similar equation can be written for radial position, or *r***,** although generally speaking, most important processes in the QITMS happen in the *z* direction. The dimensionless parameters ξ, a_z, and q_z are given in the following equations,

$$\xi = \Omega t/2 \qquad \text{(Equation 1.5)}$$

$$a_z = -\frac{16eU}{m(r_0^2 + 2z_0^2)\Omega^2} \qquad \text{(Equation 1.6)}$$

$$q_z = \frac{8eV}{m(r_0^2 + 2z_0^2)\Omega^2} \qquad \text{(Equation 1.7)}$$

where Ω is the rf trapping voltage, t is time, U and V are the amplitudes of the dc and maximum zero to peak rf voltage applied to the ring electrode of the trap, e is the fundamental unit of charge, m is mass, and r_o and z_o are the radial and axial dimensions of the trap. To use the method of mass-selective instability[19], one sets U to zero and increases V in a linear fashion, such that ions are ejected from the trap when they reach the stability boundary at q_z = 0.908. The above equations, familiar to most mass spectrometrists, are the foundation for understanding how ions move in the QITMS.

1.2.1.3.Pseudopotential Trapping Well

The pseudopotential well model assumes that ion motion in a QITMS can be decoupled into a high frequency ripple caused by the drive frequency Ω on top of a lower frequency oscillation, called the ion *secular* or *fundamental* frequency.[15] At low rf values (q_z<0.4) the high frequency ripple can practically be ignored.[16, 20, 21] Under these conditions ion motion can be approximated as that of a harmonic oscillator, where the depth of the well in the axial direction is D_z, as in Equation 1.8.

$$D_z = \frac{mq_z^2\Omega^2 z_0^2}{16e} \qquad \text{(Equation 1.8)}$$

Equation 1.8 can be used for the radial direction as well, substituting q_r and r_o for q_z and z_o. If the axial and radial dimensions of the trap were equal, then D_z would be 4 D_r, because $q_z = -2\ q_r$. The $q_z = -2\ q_r$ relation arises from weighting coefficients from solving Laplace's equation for a quadrupolar geometry. Due to the axially stretched geometry of the ITMS™, the actual relationship between axial and radial well depths is $D_z = 2.45\ D_r$. The ion secular frequency ω_z can be estimated by Equation 1.9, where β_z is given by Equation 1.10 when $q_z < 0.4$ and the higher frequency oscillations can be ignored.

$$\omega_z = \frac{1}{2}\beta_z \Omega \qquad \text{(Equation 1.9)}$$

$$\beta_z = (a_z + \frac{1}{2}q_z^2)^{\frac{1}{2}} \qquad \text{(Equation 1.10)}$$

When $q_z > 0.4$, higher order frequencies in the ion oscillation are no longer negligible, and the equation for β_z is more complicated, but can still be calculated recursively.[16] The q_z value is of great importance because it allows calculation of the voltage amplitude necessary for ejection of an ion of particular mass-to-charge value. The q_z value also allows calculation of the ion secular frequency, which can be used to manipulate ions in several ways.

1.2.1.4.Manipulating Ions

At certain times in a QITMS experiment, small ac voltages may be applied to the endcap electrodes (Figure 1.1) to improve mass resolution, increase the range of mass-to-charges analyzed, and perform tandem MS experiments. The supplementary voltage creates an axially oriented dipolar contribution to the quadrupolar trapping field. Typically, the supplementary voltage waveform applied to one endcap is applied 180 degrees out of phase to the voltage applied to the opposite endcap, thereby doubling the electric field magnitude that would be created if one endcap was grounded, as illustrated in Figure 1.2.

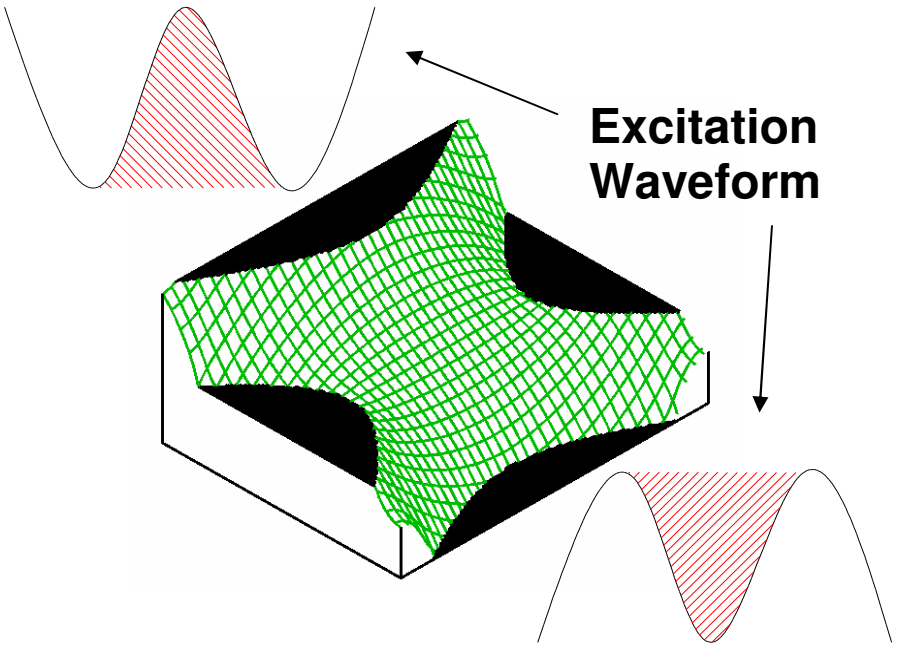

Figure 1.2. Supplementary voltages applied to endcaps at 180 degree phase difference

1.2.1.4.1. Resonance Ejection

The spectral resolution of mass-selective-instability may be improved by applying a supplementary voltage at the frequency corresponding to a particular q_z value. For example, a supplementary voltage may be applied at the frequency corresponding to just slightly less than the normal ejection point of $q_z = 0.908$, causing ions to move in phase with each other when the trapping voltage is increased and they reach that q_z value. Ion coherence leads to more precise ejection times, resulting in narrower spectral peaks on the mass-to-charge scale. Ejection of ions can take place at any q_z value by applying the appropriate frequency.

1.2.1.4.2. Collision Induced Dissociation

One may wish to extract more information about an ion than its mass-to-charge ratio. Structural connectivity information may be obtained about the analyte by dissociating it and

analyzing the resulting ionic fragments in a MS/MS experiment. Collision induced dissociation (CID) is an often used MS/MS method[22-24]. During CID, the parent ion is accelerated into a non-reactive gas species such as Ar, N_2, or He, such that the kinetic energy of motion may be converted into a gain in internal energy of the parent ion, as described by Equation 1.3. CID can be performed using a wide range of instrument configurations, target gases and gas pressures, ion kinetic energies, and ion types. This broad range of applicable instrumental conditions and relative ease of implementation make CID the most common technique used for ion activation.[22, 23] Due to high MS/MS efficiency, sometimes approaching 100%, the QITMS is one of the more popular platforms for performing CID. MS/MS efficiency is defined in Equation 1.11, where P_0 is the initial parent ion intensity, and ΣF is the sum of the fragment ion intensities.

$$MS/MS\ efficiency = \frac{\sum F}{P_o} \qquad \text{(Equation 1.11)}$$

Two other performance characteristics help to understand the meaning of MS/MS efficiency: fragmentation efficiency and collection efficiency, given in Equations 1.12 and 1.13 respectively. The term P is the final parent ion intensity after dissociation.

$$Fragmentation\ efficiency = \frac{\sum F}{P + \sum F} \qquad \text{(Equation 1.12)}$$

$$Collection\ efficiency = \frac{P + \sum F}{P_o} \qquad \text{(Equation 1.13)}$$

Fragmentation efficiency describes how well the parent ion was converted into product ions, and can be calculated from the final MS/MS spectrum. Collection efficiency describes how

many ions were lost due to processes, such as scattering, during the MS/MS event. To calculate this quantity, two spectra are needed: an initial spectrum containing just the parent ion before dissociation, and a final MS/MS spectrum. Multiplying Equations 1.12 and 1.13 gives Equation 1.11, therefore MS/MS efficiency is a term that takes into account both the conversion of parent ion to products and the ability of the instrument to retain ions during the MS/MS event.

CID may be useful for understanding the connectivity of atoms in an ion, but it is not obvious how one would obtain higher order structure information from CID data alone. There are ways, however, to use CID information to reveal ion internal energy details, requiring first that the collisions between ion and neutral are well defined.[25-27] One type of experiment is to sequentially increase the energy of collisions and record the abundance of the parent and product ions at each step. Such a graph of abundance versus collision energy, or fragmentation efficiency versus collision energy is referred to as a *breakdown curve*. Breakdown curves will be employed in **Chapters 4, 6,** and **7**. For now, though, the theme of higher order structure will be continued, and several methods for 3D structure determination will be introduced.

1.3. IR Spectroscopy

Spectroscopy studies the interaction of chemical species with light. Because of quantum theory, we know that atoms and molecules only exist in discrete energy states. When a species changes state, an amount of energy exactly equal to the difference between states must be absorbed or emitted.[28] A direct absorption experiment is one way to find out which energy states are present. In these experiments, a sample is irradiated with light of a particular energy and the decrease in photon intensity after the light passes through the

sample is measured. Repeating this at a range of different wavelengths can provide a spectral signature that is characteristic of the molecule. Infrared (IR) spectroscopic studies the interaction of chemical species with light in the IR range, roughly between 13,000 cm^{-1} and 10 cm^{-1}.[28] This energy range coincides with the energies of the vibrational motion of molecules, thus, at the most basic level, IR spectroscopy provides information about bond strength.

IR spectroscopy is useful because of the structural information contained in these spectra. The slightest changes in chemical environment will be reflected in the vibrational modes of the ion or molecule, such that deduction of 3D structure from IR spectra is possible.[11, 29-31] Here quantum chemical calculations of the type described in the following sections are indispensable. A useful procedure is to use a low-level molecular modeling program to calculate ion energies as all bonds are rotated and stretched. Tens of thousands of possible ion conformations can be reduced to a suitably small number of low energy conformations to be further optimized by higher level calculations.[32] The IR spectra of the final lowest energy candidate structures are computed and compared to the experimental IR spectra to infer what are the most likely ion structure or structures.[30, 33, 34]

1.3.1. Action Spectroscopy

To acquire an IR spectrum of a gas phase ion requires special instrumentation and methodologies. Due to the repulsion of like charges, sufficient gaseous ion densities cannot be obtained to make traditional direct absorbance measurement possible.[31, 35, 36] Therefore, techniques have been devised to measure some other chemical process whose rate can be changed by the absorption of a photon. This type of spectroscopy has been called *action spectroscopy*, and for ions, the most common process to monitor is the photodissociation of

the initial ion and concomitant formation of product ions.[35] Depending on the absorption cross section of the ion at a particular wavelength, varying amounts of internal energy can be deposited into the ion, and the photodissociation rate will vary with wavelength. Most typically, fragmentation efficiency (Equation 1.12) is plotted as a function of wavelength to give the photodissociation spectrum. The basic IR photodissociation technique described above has already been applied to numerous types of ions, ranging from oligosaccharides[32, 37], polycyclic aromatics[31, 38], metal ion clusters[33, 39], water clusters[40, 41], peptides[29, 34, 42], and even proteins[13].

1.3.2. IRMPD Mechanism

Because the energy necessary to break a bond is much greater than the energy imparted by a photon in the IR range, absorption of multiple photons, that is, infrared multiphoton dissociation (IRMPD), is necessary for IR action spectroscopy. For a molecule with a bond dissociation energy of 4 eV, it would take absorption of ~16 photons at a laser wavelength of 2000cm^{-1} (0.248 eV), to cause dissociation to occur, assuming that all the gained energy stayed in this same bond. Coherent, that is, step-wise excitation from vibrational states υ=0 → υ=1, υ=1 → υ=2…υ=15→ υ=16, would be possible in the harmonic oscillator model, where each vibrational state is separated by an equal amount of energy $h\nu$. In reality, anharmonicities cause the energy difference between vibrational states to decrease with increasing υ, as is seen in Figure 1.3. Since anharmonicity from one transition to the next is on the order of 1-10 cm^{-1}[3, 43], a vibrational mode would quickly go out of resonance with the laser before a typical dissociation threshold could be reached. Therefore, multiple photon absorption most likely is able to occur via a sequential, incoherent process, whereby absorbed photon energy is quickly (<1ns) redistributed

throughout the rest of the molecule via coupling to other vibrational modes, and the "bright" mode (one being excited with the laser) relaxes to its starting point energy. [31, 36, 44-46] This event is known as intramolecular vibrational relaxation (IVR), and is most often observed when the density of vibrational states of a molecule is more than 100 states/cm^{-1}, called the "quasi-continuum" of vibrational states[31, 44, 45]. Once in the quasi-continuum, the internal energy of the whole molecule is raised in an absorption process that looks like:

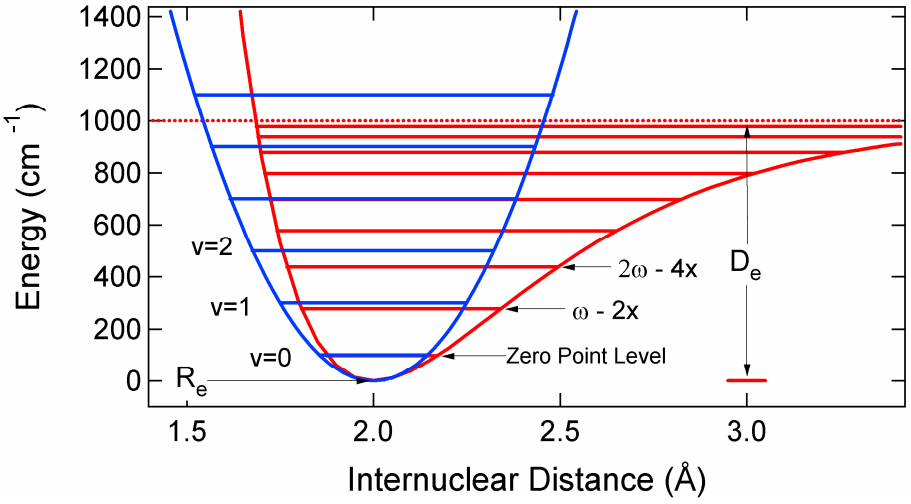

Figure 1.3: Two models for the potential energy well of a bond are shown, the harmonic oscillator in blue and anharmonic oscillator

υ=1 → υ=2, IVR, υ=1 → υ=2, IVR, etc…until enough energy is absorbed to break a bond. Because of the increased anharmonic coupling to other vibrational modes in the quasi-continuum, IRMPD spectroscopy spectra are generally red-shifted from normal IR absorbance spectra or theoretically calculated frequencies.[31, 44, 45]

1.3.3. Theoretical Methods for Calculating Structure

The most common methods used to predict theoretical structures and IR spectra may be divided into two groups. The first are those methods that are based on fundamental physical constants, or *ab initio*, and use approximations to solve the wave function of a particle or group of particles.[47] The second approach is to model the system *via* functionals,

or functions of functions, of electron density. This second method is termed density functional theory, or DFT.

1.3.3.1.Ab Initio Calculations

Ab initio calculations take advantage of molecular orbital theory to construct a wavefunction ψ from a combination of molecular orbitals Φ_i, and calculate the energy of an atom, molecule, or ion.[47] Molecular orbitals give the spatial distribution of an electron around an atom. The set of equations comprising a molecular orbital are referred to as basis functions. Programs like Gaussian[48] use gaussian-style functions for these basis functions of the form given in Equation 1.14, where α is related to the radial extent of the function, x, y, and z are spatial coordinates raised to constants n, m, and l depending on the type of orbital being modeled, c is a normalization constant, and r is composed of the x, y, and z coordinates. Equation 1.15 describes the general form of a molecular orbital, where $c_{\mu i}$ is the molecular orbital expansion coefficients, $d_{\mu p}$ are fixed constants for each basis set, and g_p is the gaussian-type functions. The subscript i refers to the specific molecular orbital, μ is for the specific basis function, and p is for each *primitive* gaussian function making up the *contracted* gaussian (term in parenthesis of 1.15) of each basis function.[47]

$$g(\alpha, r) = cx^n y^m z^l e^{-\alpha \cdot r^2} \qquad \text{(Equation 1.14)}$$

$$\Phi_i = \sum_{\mu} c_{\mu \cdot i} \left(\sum_{p} d_{\mu \cdot p} g_p \right) \qquad \text{(Equation 1.15)}$$

When configuring a Gaussian input file, one must choose a *basis set*, or group of basis functions to describe the shape of the electronic orbitals being modeled. These basis sets are given names that reflect the number of Gaussian primitives per basis function and the number of basis functions per valence orbital.[47] For example, the 3-21G basis set uses 3

gaussian primitives per basis function, and at least 2 basis functions per valence orbital. Additional functions can be added to more accurately model the atom, such as in the commonly used 6-31G(d) basis set, which adds the d electron functions.[47]

In the self-consistent-field (SCF) or Hartree-Fock (HF) theory the molecular orbital expansion coefficients of the molecular orbitals are adjusted to yield the minimum energy of the system. The minimum energy is desired because of the variation principle, which says that energies calculated from a method such as HF will always be greater than the actual energy of the system. Therefore, the lower the calculated energy, the more accurate is the calculation. HF therefore will iteratively solve for the molecular orbitals until the minimum energy is reached, and the field generated by these orbitals will in turn produce the same orbitals, accounting for the SCF name.[47]

Programs like Gaussian can optimize a particular structure to give a configuration that lies in local minimum energy well. All the bonds in a molecule are stretched and rotated systematically, and the energy gradient is followed until a minimum is found. A geometry optimization output file from

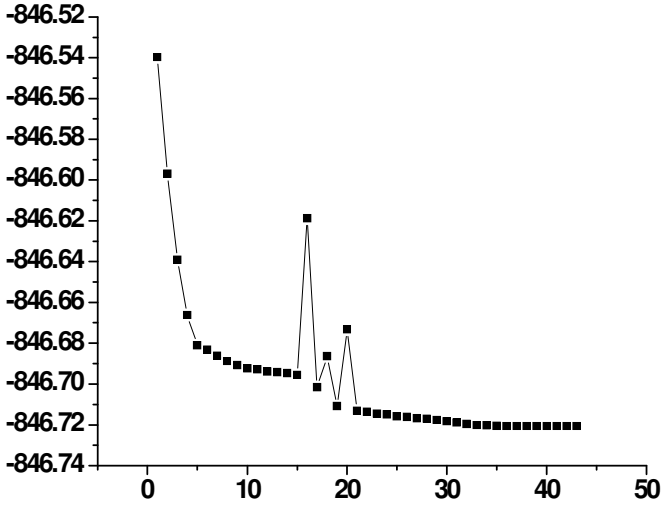

Figure 1.4. Geometry optimization from Gaussian

Gaussian is plotted in Figure 1.4. Care must be taken using this method, because the initial input geometry can play a role in the final optimized structure if the calculation gets stuck in a local minimum instead of finding the global minimum.

1.3.3.2.Density Functional Theory Calculations

DFT calculations are based on the idea that the energy of an atomic or molecular system can be calculated by knowing the electron density of the system.[49, 50] The total electronic energy is divided up into parts as in Equation 1.16, where E_T is translational energy, E_V is the potential energy of nuclear-electron attraction, E_J is electron-electron repulsion, and E_{XC} is the electron exchange-correlation energy.[49]

$$E = E_T + E_V + E_J + E_{XC} \qquad \text{(Equation 1.16)}$$

Although the terms in Equation 1.16 are also in the Hamiltonian, DFT describes them as functions of the electron density. The most complicated variable is E_{XC}**,** and within this term, the electron correlation is most important. Electron correlation explains how electrons attempt to avoid each other, and can be modeled by something called a "hole function".[49] What makes DFT calculations semi-empirical in nature is that this hole function can be approximated by measurements of real physical systems, such as the density of an electron gas.[49, 50] There has been a gradual process of refinement of DFT methods, some of the most notable being the addition of gradients to the electron density, instead of assuming homogeneity, and combining DFT with Hartree-Fock theory to make hybrid functionals.[47, 49, 50] One of the most commonly used functionals is the B3LYP, where the E_{XC} term is a mixture of contributions from HF theory, Becke's exchange functional, and the correlation functional of Lee, Yang, and Parr.[47] The advantage of DFT is that high accuracy calculations can be carried out with a much smaller computational cost than for an equal accuracy HF method.

1.3.3.3.Calculated Vibrational Modes

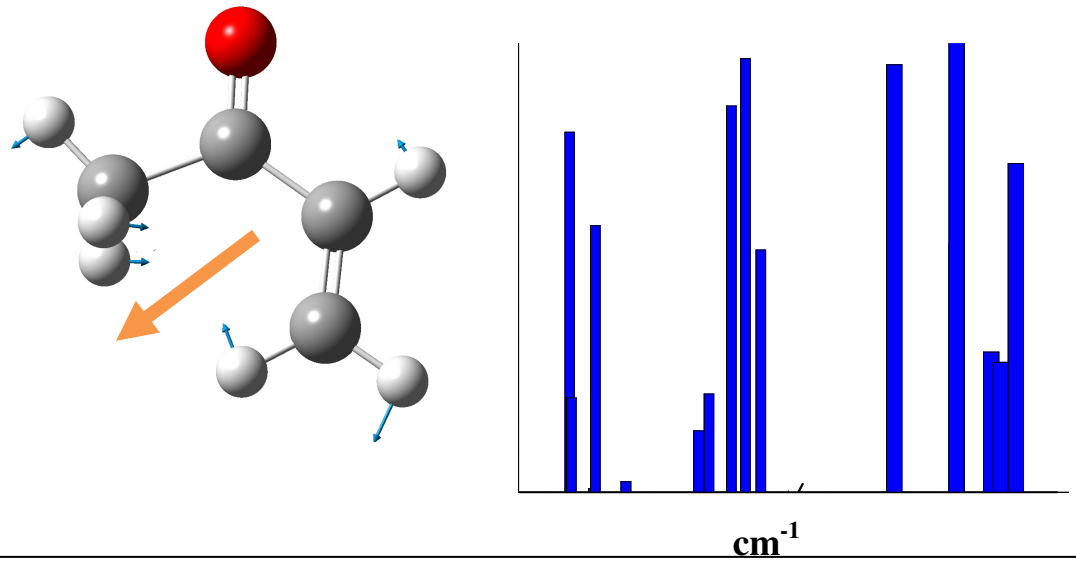

Figure 1.5. Calculated structure and IR spectrum for methylvinylketone. Blue arrows are atomic motion paths for one vibrational mode. The dipole moment for this mode is given in the gold arrow.

Vibrational bands are estimated by calculating energy as the atoms in the molecule are displaced from their equilibrium positions. The potential energy of a harmonic oscillator bond is;

$$V(x) = \frac{1}{2}kx^2 \qquad \text{(Equation 1.17)}$$

so that if energies are calculated as the bond is stretched in the *x* direction, taking the second derivative of energy will give the force constant, *k*. Energy gradients are evaluated for all atoms in the molecule and placed in a special matrix called a Hessian. This matrix takes the general form of Equation 1.18 for a function $f(x_1, x_2, \ldots x_n)$, where in this case *x* is a direction, and *n* would be nth atom in the molecule.

$$H(f) = \begin{bmatrix} \frac{\partial^2 f}{\partial x_1^2} & \frac{\partial^2 f}{\partial x_1 \partial x_2} & \cdots & \frac{\partial^2 f}{\partial x_1 \partial x_n} \\ \frac{\partial^2 f}{\partial x_2 \partial x_1} & \frac{\partial^2 f}{\partial x_2^2} & \cdots & \frac{\partial^2 f}{\partial x_2 \partial x_n} \\ \vdots & \vdots & \ddots & \vdots \\ \frac{\partial^2 f}{\partial x_n \partial x_1} & \frac{\partial^2 f}{\partial x_n \partial x_2} & \cdots & \frac{\partial^2 f}{\partial x_n^2} \end{bmatrix} \quad \text{(Equation 1.18)}$$

The y and z dimension gradients are added into this matrix to make it 3N x 3N, where N is number of atoms. This matrix is diagonalized and the resulting eigenvalues are the normal vibrational modes of the molecule.[51]

An example DFT calculated IR spectrum from Gaussian using the B3LYP/6-31G(d) basis set is given in Figure 1.5 for the molecular ion of methyl vinyl ketone, along with an illustration of the geometry optimized structure, with one vibrational mode and corresponding dipole moment overlaid.

1.4. Other Methods for Ion Higher Order Structure Determination in the Gas Phase

While IR laser spectroscopy can offer a detailed structure determination of many smaller systems, for large macromolecules its utility is lessened. The complex folding and sheer number of atoms in proteins create a situation where there are many different types of interacting structural moieties whose vibrations overlap, making spectral assignments difficult.[52] Instead of assigning all or most of the peaks in a spectrum to their corresponding vibrational modes, IR spectroscopy of proteins (typically in solution-phase) involves looking for the presence or absence of specific secondary structure elements (α-helicies, β-sheets) through interpretation of very large vibrational bands, and individual stretches are almost never resolved.[53] Thus, other methods of conformational selection and characterization are needed, which will be described in the following sections.

1.4.1. Ion Mobility Spectrometry

While the large number of intra-molecular interactions in proteins complicate their analysis somewhat, gas-phase measurements of protein cross section by a technique called ion mobility spectrometry (IMS), especially when coupled with MS, are increasingly valuable for determining higher-order structure. Ion mobility is based on the velocity with which an ion moves through a buffer gas under the influence of an electric field.[54, 55] The force on the ion from the electric field is balanced by the force of the collisions with the buffer gas, such that the ion moves at a constant drift velocity. Mobility, K**,** is given in Equation 1.19, where v_d is the ion drift velocity, and E is the electric field.[54]

$$K = \frac{v_d}{E} \qquad \text{(Equation 1.19)}$$

K is measured by pulsing a packet of ions through a drift tube at around 1-10 Torr of buffer gas, and measuring the time they take to reach a detector. The mobilities measured in this way are generally standardized to 273.3 K and 760 Torr to be able to compare results between instruments and laboratories. The standardized K_o is given in Equation 1.20, where L is drift tube length, t_d is drift time, V is voltage drop across drift tube, T is temperature in Kelvin, and P is pressure in Torr.[54]

$$K_o = \frac{L^2}{t_d V} \times \frac{273.2}{T} \times \frac{P}{760} \qquad \text{(Equation 1.20)}$$

Mobility is related to the structure of an ion through the basic fact that an ion with a larger cross section will undergo more collisions with the buffer gas and have a slower drift velocity than an ion with a smaller cross section. The theoretical mobility for an ion of mass m**,** number of charges z**,** and an average collisional cross section $\Omega^{(1,1)}_{avg}$, in a buffer gas m_b

and of number density N, is given in Equation 1.21. The other terms e and k_b are the fundamental charge unit and Boltzmann's constant.[54]

$$K = \frac{(18\pi)^{1/2}}{16}\left[\frac{1}{m}+\frac{1}{m_b}\right]^{1/2}\frac{ze}{(k_bT)^{1/2}\Omega_{avg}^{(1,1)}}\frac{1}{N} \qquad \text{(Equation 1.21)}$$

Clearly from Equation 1.21, an ion with a larger collision cross section will have a smaller mobility and thus reach the end of the drift tube later than an ion of equal mass and smaller collision cross section. As in IR spectroscopy, molecular modeling programs exist to calculate the cross sections of candidate conformers for comparison to experimental data.[54]

One important application of IMS/MS is the on-going quest to determine the influence of solvent in determining higher order structure and the correlation between gas-phase and solution-phase structures. The solution-phase cross section is one of the conformations retained by some protein complexes after ionization by ESI.[6] However, the composition of the ESI solution plays an important role in the distribution of charge states observed for proteins and peptides[56], and there is evidence that protein structure is dependent on charge state.[13, 57, 58] When the charge state is low, proteins tend to exist in compact balls that resemble the solution-state structure, while increasing the number of charges tends to elongate the protein, as coulombic repulsion unravels the protein backbone. Several studies have probed the protein unfolding process by measuring cross section as a function of temperature or excitation.[57-59]

1.4.2. High Field Asymmetric Waveform Ion Mobility Spectrometry

Up to this point in the dissertation, the IMS theory described is applicable to the "low-field limit", that is, at low values of E/N (electric field over buffer gas number density). The low-field limit is characterized by mobility being independent of the E/N ratio.[55] When

E/N is low, the average collision energy depends only on the kinetic temperature of the gas. However, at high values of E/N, the collision energy depends on the gas temperature plus the velocity of the ion, thus mobility becomes dependent on electric field.[60] The dependence of mobility on E/N is given in Equation 1.22. The terms *a*, *b*, and *c* are empirically determined constants dependent on factors that are not yet well understood.[61]

$$K_o\left(E/N\right) = K_o\left[1 + a\left(E/N\right)^2 + b\left(E/N\right)^4 + c\left(E/N\right)^6 + \cdots\right] \qquad \text{(Equation 1.22)}$$

The higher order terms in Equation 1.22 become significant at electric fields greater than about 10^4 V/cm at atmospheric pressure, which is close to the breakdown point of air.[61] The difference in high and low field mobilities, called K_h and K_l respectively, may be exploited using a fairly recently developed atmospheric pressure technique known as high field asymmetric ion mobility spectrometry (FAIMS).[62]

In FAIMS, ions are pushed down the space between two electrodes by a buffer gas. An asymmetric waveform called the *dispersion voltage* (DV) is applied to the electrodes, consisting of a short period of very high voltage, followed by a long period of lower voltage, as in Figure 1.6. Over one period of the waveform, the voltage integral would be 0, such that if K_h and K_l were the same, the ion would travel down the center of the apparatus and never touch the electrodes.[62] However, when K_h and K_l are not the same, the ion will experience a drifting towards one electrode or the other. Ions can be characterized empirically as either A ions when $K_h > K_l$, C ions when $K_h < K_l$, and B ions when K_h first increases and then decreases.[62] The drift toward one of the electrodes can be offset by the application of a small dc *compensation voltage* (CV) so that ions of different differential mobility are sequentially made to pass to the end of the device, while all other ions hit the electrodes and are filtered out. The waveform in Figure 1.6 is square, and this shape is predicted to provide the best

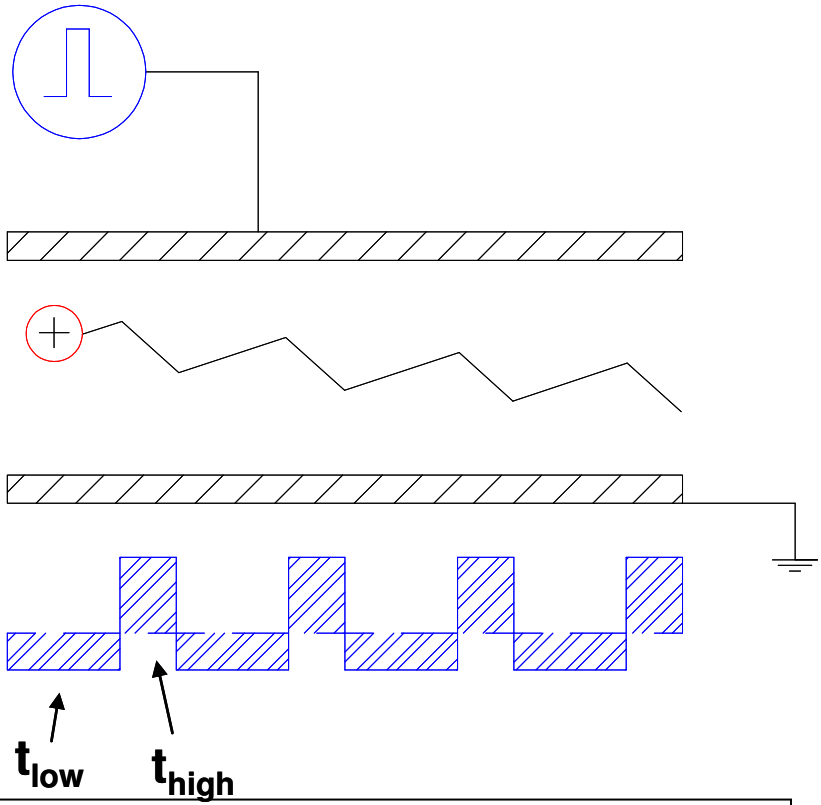

Figure 1.6. FAIMS experiment, where planar electrodes are shown in black, and ideal asymmetric waveform is in blue, t_{low} is the low field part of waveform and t_{high} is the high field part.

resolving power.[61] However, with peak dispersion voltages reaching as high as 5 kV, the power supply necessary to create this "instantaneous" voltage would have to generate several amps of current at high voltage. The current necessary to drive a capacitor to a particular voltage is given in Equation 1.23, where *dV/dt* is the derivative of voltage with respect to time, or *slew rate*, and *C* is capacitance. A typical capacitance value for a FAIMS analyzer is 12-20 pF.

$$A = \frac{\partial V}{\partial t} \cdot C \qquad \text{(Equation 1.23)}$$

Such a power supply can be commercially acquired at some cost, but the FAIMS device would not be very safe. The solution to the problem is to couple two sine waves

generated separately via LC circuitry[63]. The general waveform equation is given in Equation 1.24. The best performance is found when f=2, h=2, φ= π/2, and V_{max} = 5kV[61], which for a plate separation of 2 mm at atmosphere in air is close to the breakdown voltage of 5900 V predicted by Paschen's law.

$$V(t) = [f \sin(\omega t) + \sin(h\omega t - \phi)] \frac{V_{\max}}{(f+1)} \qquad \text{(Equation 1.24)}$$

Two sine waves and their summation are shown in Figure 1.7a, as well as their slew rates in Figure 1.7b. As shown in the insets, the current necessary to create high voltage, low current sine waves is in the tens of microamps, much lower than for a square wave.

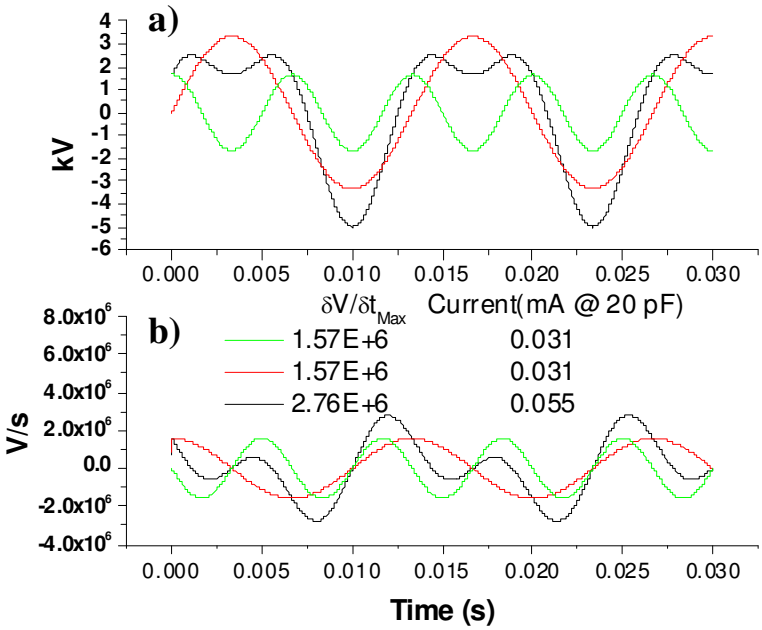

Figure 1.7. a) two sine waves and their summation (black). b) slew rates of above waveforms and maximum currents

The advance that made FAIMS a viable commercial technology was the use of curved electrodes instead of planar ones, which greatly increased sensitivity due to a focusing effect of the curved field.[61, 64] The enhancement in sensitivity comes at the price of resolution, and recent experiments with planar electrodes show that the resolving power of planar FAIMS for proteins can be more than 2x that of cylindrical FAIMS.[65] These considerations will be described in more detail in **Chapter 8**.

The resolving power of FAIMS is typically on the order of 10-30, where resolving power is defined in Equation 1.25. The term P_o is the peak center, and P_{FWHM} is the peak full width at half maximum. Different device geometries and buffer gas compositions may enhance performance, as will be discussed in **Chapter 8**.

$$R = \frac{P_o}{P_{FWHM}} \qquad \text{(Equation 1.25)}$$

IMS resolving power is around 100-200, although for proteins R is on the order of 10-30.[57, 65-67] Protein resolving power is much less than what is predicted theoretically, apparently because with so many degrees of freedom there exists a number of similar but slightly different conformations.[68] FAIMS resolving power for proteins is about the same or slightly lower than for other analytes.

The buffer gas generally used for FAIMS is N_2, or N_2 mixed with He.[60, 69] The resolution and sensitivity of FAIMS separations appear to increase as He content increases, but the amount of He is limited by electrical breakdown to 60% by volume when mixed with N_2. Generally speaking, when the terms in Equation 1.22 are known for a particular analyte, then the effect of mixing gases may be predicted, and especially interesting results have been reported for mixtures of highly disparate gases such as He/SF_6, for which a resolving power for Cs^+ of 100 was reported.[69] However, this effect is not universally applicable, and a combination of N_2/He appears to work best for most species.

FAIMS separation is fundamentally not the same as a conventional IMS separation. Neither is there any reason *a priori* to suppose that there is a correlation between a function and its derivative, ie between K_o and dK/dE.[57] FAIMS appears to be strongly correlated to IMS drift time, but almost no correlation at all is found between FAIMS and collision cross section.[57] This observation appears counterintuitive; however, ions of different cross section

can have the same drift time if they have different masses and/or charges. FAIMS CV values for ions are also largely orthogonal to mass-to-charge value, while there is a strong degree of correlation between IMS drift time and mass-to-charge.[57] This means that FAIMS/MS could theoretically contain more information than IMS/MS. However, because IMS theory is much more well developed than FAIMS theory, FAIMS analysis do not, at this time, have the power of IMS to determine cross section directly from a single spectrum.[57, 66] More specifically, the way in which the constants from Equation 1.22 depend on ion structure cannot yet be calculated theoretically.

Instead of calculating cross sections directly from CV values, a procedure to calibrate the CV scale to cross section must be used.[66, 67] The common procedure uses a gas filled quadrupole collision cell to measure the kinetic energy lost as ions pass through the gaseous interior. The loss in kinetic energy from colliding with the gas can be related to the cross section through Equation 1.26. E_o is the kinetic energy of the ions with no collision gas in the cell, E is the ion kinetic energy after passing through the gas filled cell, ρ is the gas number density, m_2 is the collision gas mass, m_1 is the ion mass, σ is the ion cross section, l is the ion path length, and C_d is the drag coefficient, a term which relates the force on an ion traveling through a gas to collision cross section.[70, 71]

$$\frac{E}{E_o} = \exp\left(-\frac{C_d \rho m_2 \sigma l}{m_1}\right) \qquad \text{(Equation 1.26)}$$

Kinetic energy is measured by successively raising the dc bias on an instrument element after the collision cell and measuring signal depletion. The standard practice is to take the voltage of 10% signal depletion as the average ion kinetic energy in electron volts (eV).[66, 70, 71] While this procedure can characterize the average collision cross section of all

ions present, it cannot separate the contributions from different conformations.[57] Care must be therefore be exercised in interpretations of these results.

FAIMS is a relatively new development in IMS, and, as was mentioned, direct structural data cannot yet be obtained from CV values. For this to happen, the precise characteristics leading to a given high field mobility need to be better understood. However, the high degree of orthogonality with MS means that there is incentive for further studies. As it is, FAIMS is still valuable for separating different gas phase conformers, and supplementary experiments such as conventional IMS, energy loss measurements, and different dissociation techniques can then be used to characterize the selected structures.

1.5. Summary

The goal of this introduction has been to set the theoretical foundation for the rest of this dissertation, which will describe specific efforts towards determinations of gas-phase ion higher order structure, with a side-emphasis on ion internal energy. Higher order structure is important in all chemical reactions, and is intimately linked to the function of biological molecules. Ion internal energy plays a role in these matters by influencing the adaptation of any one specific structure by a chemical species, as well as setting chemical reaction rates, which ultimately dictate the appearance of the data obtained by our structural determination methods.

Chapter 2 is meant to provide a procedural reference for performing all the common experiments, so that each chapter does not contain redundant information. Details on performing various ionization methods, dissociation techniques, theoretical calculations will be provided.

Chapter 3 describes the construction of a QITMS for low temperature IR spectroscopy. Pertinent mechanical, electrical, and computation particulars will be laid out, containing references to drawings and programs in the Appendices. Although no IR spectra have yet been acquired, the projected best method of doing this will be detailed. The instrument described in this chapter will also be the platform for the experiments in **Chapters 4 and 5**.

Chapter 4 builds off previous work in our lab to study the collisional cooling process in the QITMS. Because the IRMPD spectroscopy experiment in **Chapter 3** depends on ion dissociation, here we first investigate the relationship between ion temperature and the critical energy required to observe fragment ions. Then collisional cooling is shown to be the key factor influencing the shape of the temperature critical energy curve.

Chapter 5 began as an attempt to optimize the fragmentation efficiency of IRMPD in the temperature controlled QITMS, which led to the desire to better understand the nature of the "ion cloud", or volume occupied by a trapped packet of ions. The shape of the ion cloud is studied theoretically, and a contraction or expansion of the cloud is demonstrated as trapping parameters are adjusted systematically. Fragmentation efficiency is shown to improve when the ion cloud is compressed as small as possible.

Chapter 6 begins to look at the internal energy of ions in tandem MS experiments. Conventional CID is compared to a new procedure called high amplitude short time excitation (HASTE). The basis for comparison is a calculation of internal ion temperature, based on fitting experimental CID spectra to theoretically calculated CID spectra. The theoretical temperature of the matching spectrum is then taken as an estimation of the actual ion temperature. The new method, HASTE, is activated to temperatures ~100 K higher than

the conventional CID procedure, putting a semi-empirical value on HASTE's qualitatively observable energetic advantage.

Chapter 7 continues to probe of internal energy with a focus on the relative energetics of two ionization mechanisms, nano-ESI and AP-MALDI, in a QITMS. This chapter grew out of a discrepancy with a result from another lab, which made claims about the collisional cooling process that appeared inaccurate, judging from the experience gained in the chapter 4 experiments. A possible reason is proposed based on the methodology of the questionable report, and data are presented to show how their results could arise. The comparison of nano-ESI and AP-MALDI is then repeated under more ideal conditions.

Chapter 8 describes a new instrument for probing protein higher order structure. The instrument uses a FAIMS front end to separate protein conformers, a quadrupole mass analyzer to select a mass-to-charge (Q), and then various collision cells (q) and regions to probe the effects of conformation on different dissociation techniques. There will be a collision cell for characterizing cross section and trapping ions for either reactions or dissociations caused by several means. Finally, an electric/magnetic sector (EB) will be coupled to the above apparatus for specialized energy loss measurements. **Chapter 8** will describe mostly considerations for building and operating the FAIMS and Qq, with references to supplemental information in the Appendix. Finally, **Chapter 9** will summarize the results and implications of each chapter and provide some future directions for study.

1.6. References

1. Wright, P. E.; Dyson, H. J. *Intrinsically unstructured proteins: Re-assessing the protein structure-function paradigm*. *J. Mol. Biol.* **1999,** *293*, 321-331.

2. Stryer, L. *Biochemistry*, 4 ed.; W.H. Freeman and Company: New York, 1995.

3. McQuarrie, D. A.; Simon, J. D. *Physical Chemistry: A Molecular Approach*; University Science Books: Sausalito, 1997.

4. Crews, P.; Rodriguez, J.; Jaspars, M. *Organic Structure Analysis*; Oxford University Press: New York, 1998.

5. Takeuchi, K.; Ng, E.; Malia, T. J.; Wagner, G. *1-13C amino acid selective labeling in a 2H15N background for NMR studies of large proteins*. *Journal of Biomolecular NMR* **2007,** *38*, 89-98.

6. Ruotolo, B. T.; Giles, K.; Campuzano, I.; Sandercock, A. M.; Bateman, R. H.; Robinson, C. V. *Evidence for macromolecular protein rings in the absence of bulk water*. *Science* **2005,** *310*, 1658-1661.

7. Gologan, B.; Takats, Z.; Alvarez, J.; Wiseman, J. M.; Talaty, N.; Ouyang, Z.; Cooks, R. G. *Ion soft-landing into liquids: Protein identification, separation, and purification with retention of biological activity*. *J. Am. Soc. Mass Spectrom.* **2004,** *15*, 1874-1884.

8. Kuwajima, K. *The Molten Globule State as a Clue for Understanding the Folding and Cooperativity of Globular-Protein Structure*. *Proteins-Structure Function and Genetics* **1989,** *6*, 87-103.

9. Privalov, P. L.; Khechina.Nn *Thermodynamic Approach to Problem of Stabilization of Globular Protein Structure - Calorimetric Study*. *J. Mol. Biol.* **1974,** *86*, 665-684.

10. Brunner, K.; Gronwald, W.; Trenner, J. M.; Neidig, K.-P.; Kalbitzer, H. R. *A general method for the unbiased improvement of solution NMR structures by the use of related x-ray data, the AUREMOL-ISIC algorithm*. *BMC Structural Biology* **2006,** *6*, No pp. given.

11. Pivonka, N. L.; Kaposta, C.; Bruemmer, M.; von Helden, G.; Meijer, G.; Woste, L.; Neumark, D. M.; Asmis, K. R. *Probing a strong hydrogen bond with infrared spectroscopy:*

vibrational predissociation of BrHBr-.Ar. Journal of Chemical Physics **2003,** *118*, 5275-5278.

12. Schaefer, M.; Schmuck, C.; Geiger, L.; Chalmers, M. J.; Hendrickson, C. L.; Marshall, A. G. *Structurally related non-covalent complexes examined by quadrupole ion trap (QIT) MS2 and infrared multiphoton dissociation Fourier transform ion cyclotron resonance mass spectrometry IRMPDFT-ICR MS: evidence for salt-bridge structures in the gas phase*. Int. J. Mass Spectrom. **2004,** *237*, 33-45.

13. Oh, H.; Breuker, K.; Sze, S. K.; Ge, Y.; Carpenter, B. K.; McLafferty, F. W. *Secondary and tertiary structures of gaseous protein ions characterized by electron capture dissociation mass spectrometry and photofragment spectroscopy*. Proc. Natl. Acad. Sci. U. S. A. **2002,** *99*, 15863-15868.

14. Solca, N.; Dopfer, O. *Spectroscopic Identification of Oxonium and Carbenium Ions of Protonated Phenol in the Gas Phase: IR Spectra of Weakly Bound C6H7O+-L Dimers (L = Ne, Ar, N2)*. J. Am. Chem. Soc. **2004,** *126*, 1716-1725.

15. March, R. E.; Todd, J. F. J. *Practical Aspects of Ion Trap Mass Spectrometry*; CRC Press: New York, 1997.

16. March, R. E.; Todd, J. F. J. In *Chemical Analysis*; Winefordner, J. D., Ed.; John Wiley & Sons, Inc.: Hoboken, NJ, 2005; Vol. 165, pp 346.

17. March, R. E. In *Encyclopedia of Analytical Chemistry*; Meyers, R. A., Ed.; John Wiley & Sons Ltd.: Chichester, 2000, pp 11848-11872.

18. March, R. E. *An Introduction to Quadrupole Ion Trap Mass Spectrometry*. J. Mass Spectrom. **1997,** *32*, 351-369.

19. Stafford, G. C. J.; Kelley, P. E.; Syka, J. E. P.; Reynolds, W. E.; Todd, J. F. J. *Recent Improvements in and Analytical Applications of Advanced Ion Trap Technology*. Int. J. Mass Spectrom. Ion Processes **1984,** *60*, 85-98.

20. Major, F. G.; Dehmelt, H. G. *Exchange-Collision Technique for the rf Spectroscopy of Stored Ions*. Physical Review **1968,** *170*, 91-107.

21. Dehmelt, H. G. In *Advances in Atomic and Molecular Physics*; Bates, D. R., Estermann, I., Eds.; Academic Press: New York, 1967, pp 53-72.

22. McLuckey, S. A. *Principles of Collisional Activation in Analytical Mass Spectrometry*. *J. Am. Soc. Mass Spectrom.* **1992,** *3*, 599-614.

23. Louris, J. N.; Cooks, R. G.; Syka, J. E. P.; Kelley, P. E.; Stafford, G. C.; Todd, J. F. J. *Instrumentation, Applications, and Energy Deposition in Quadrupole Ion Trap Mass Spectrometry*. *Anal. Chem.* **1987,** *59*, 1677-1685.

24. Douglas, D. J. *Mechanism of the Collision-Induced Dissociation of Polyatomic Ions Studied by Triple Quadrupole Mass-Spectrometry*. *J. Phys. Chem.* **1982,** *86*, 185-191.

25. Laskin, J.; Futrell, J. *Internal Energy Distributions Resulting from Sustained Off-Resonance Excitation in Fourier Transform Ion Cyclotron Resonance Mass Spectrometry. II. Fragmentation of the 1-Bromonaphthalene Radical Cation*. *Journal of Physical Chemistry A* **2000,** *104*, 5484-5494.

26. Laskin, J.; Byrd, M.; Futrell, J. *Internal energy distributions resulting from sustained off-resonance excitation in FTMS. I. Fragmentation of the bromobenzene radical cation*. *Int. J. Mass Spectrom.* **2000,** *195/196*, 285-302.

27. Laskin, J.; Futrell, J. H. *On the Efficiency of Energy Transfer in Collisional Activation of Small Peptides*. *Journal of Chemical Physics* **2002,** *116*, 4302-4310.

28. Skoog, D. A.; Leary, J. J. *Principles of Instrumental Analysis*, 4th ed.; Saunders College Publishing: Fort Worth, 1992.

29. Bakker, J. M.; Mac Aleese, L.; Meijer, G.; von Helden, G. *Fingerprint IR Spectroscopy to Probe Amino Acid Conformations in the Gas Phase*. *Phys. Rev. Lett.* **2003,** *91*, 203003/1-203003/4.

30. Polfer, N. C.; Oomens, J.; Dunbar, R. C. *IRMPD spectroscopy of metal-ion/tryptophan complexes*. *Physical Chemistry Chemical Physics* **2006,** *8*, 2744-2751.

31. Oomens, J.; Meijer, G.; Helden, G. v. *Gas Phase Infrared Spectroscopy of Cationic Indane, Acenaphthene, Fluorene, and Fluoranthene*. *J. Phys. Chem. A* **2001,** *105*, 8302-8309.

32. Jockusch, R. A.; Kroemer, R. T.; Talbot, F. O.; Snoek, L. C.; Carcabal, P.; Simons, J. P.; Havenith, M.; Bakker, J. M.; Compagnon, I.; Meijer, G.; von Helden, G. *Probing the Glycosidic Linkage: UV and IR Ion-Dip Spectroscopy of a Lactoside*. *J. Am. Chem. Soc.* **2004,** *126*, 5709-5714.

33. Asmis, K. R.; Bruemmer, M.; Kaposta, C.; Santambrogio, G.; von Helden, G.; Meijer, G.; Rademann, K.; Woeste, L. *Mass-selected infrared photodissociation spectroscopy of V4O10+*. Physical Chemistry Chemical Physics **2002,** *4*, 1101-1104.

34. Mac Aleese, L.; Simon, A.; McMahon, T. B.; Ortega, J.-M.; Scuderi, D.; Lemaire, J.; Maitre, P. *Mid-IR spectroscopy of protonated leucine methyl ester performed with an FTICR or a Paul type ion-trap*. Int. J. Mass Spectrom. **2006,** *249/250*, 14-20.

35. Duncan, M. A. *Frontiers in the spectroscopy of mass-selected molecular ions*. Int. J. Mass Spectrom. **2000,** *200*, 545-569.

36. Oomens, J.; Moore, D. T.; Meijer, G.; Helden, G. v. *Infrared multiple photon dynamics and spectroscopy of cationic PABA and its dehydroxylated fragment ion*. Phys. Chem. Chem. Phys. **2004,** *6*, 710-718.

37. Simons, J. P.; Jockusch, R. A.; Carcabal, P.; Hung, I.; Kroemer, R. T.; Macleod, N. A.; Snoek, L. C. *Sugars in the gas phase. Spectroscopy, conformation, hydration, co-operativity and selectivity*. International Reviews in Physical Chemistry **2005,** *24*, 489-531.

38. Oomens, J.; Tielens, A. G. G. M.; Sartakov, B. G.; Helden, G. v.; Meijer, G. *Laboratory infrared spectroscopy of cationic polycyclic aromatic hydrocarbon molecules*. The Astrophysical Journal **2003,** *591*, 968-985.

39. Brummer, M.; Kaposta, C.; Santambrogio, G.; Asmis, K. R. *Formation and photodepletion of cluster ion-messenger atom complexes in a cold ion trap: Infrared spectroscopy of VO+, VO2+, and VO3+*. Journal of Chemical Physics **2003,** *119*, 12700-12703.

40. Yeh, L. I.; Okumura, M.; Myers, J. D.; Price, J. M.; Lee, Y. T. *Vibrational spectroscopy of the hydrated hydronium cluster ions H3O+.(H2O)n (n = 1, 2, 3)*. Journal of Chemical Physics **1989,** *91*, 7319-30.

41. Wang, Y. S.; Tsai, C. H.; Lee, Y. T.; Chang, H. C.; Jiang, J. C.; Asvany, O.; Schlemmer, S.; Gerlich, D. *Investigations of Protonated and Deprotonated Water Clusters Using a Low-Temperature 22-Pole Ion Trap*. Journal of Physical Chemistry A **2003,** *107*, 4217-4225.

42. Fukui, K.; Takada, Y.; Sumiyoshi, T.; Imai, T.; Takahashi, K. *Infrared Multiphoton Dissociation Spectroscopic Analysis of Peptides and Oligosaccharides by Using Fourier Transform Ion Cyclotron Resonance Mass Spectrometry with a Midinfrared Free-Electron Laser*. Journal of Physical Chemistry B **2003,** *110*, 16111-16116.

43. Oomens, J.; Remes, P. M., Ed., 2004.

44. Black, J. G.; Yablonovitch, E.; Bloembergen, N. *Collisionless Multiphoton Dissociation of SF6: A statistical thermodynamic process*. Physical Review Letters **1977,** *38*.

45. Kerstel, E. R. T.; Lehmann, K. K.; Mentel, T. F.; Pate, B. H.; Scoles, G. *Dependence of Intra molecular vibrational relaxation on central atom substitution:*. j. Phys. Chem. **1991,** *95*, 8282-8293.

46. Grant, E. R.; Schulz, P. A.; Sudbo, A. S.; Shen, Y. R.; Lee, Y. T. *Is Multiphoton Dissociation of Molecules a Statistical Thermal Process?* Physical Review Letters **1978,** *40*.

47. Foresman, J. B., Frisch Aeleen *Exploring Chemistry with Electronic Structure Methods*; Gaussian, Inc.: Pittsburgh, PA, 1993.

48. Frisch, M. J. *Gaussian 03, Revision C.02 Gaussian, Inc., Wallingford CT*. Gaussian 03, Revision C.02 Gaussian, Inc., Wallingford CT **2004**.

49. Ziegler, T. *Approximate Density Functional Theory as a Practical Tool in Molecular Energetics and Dynamics*. Chem. Rev. **1991,** *91*, 651-667.

50. Becke, A. D. *Density-Functional Thermochemistry .1. The Effect of the Exchange-Only Gradient Correction*. Journal of Chemical Physics **1992,** *96*, 2155-2160.

51. Ochterski, J. W. *Vibration Analysis in Gaussian*. Technical Support Information: Gaussian Inc. **1999**.

52. Surewicz, W. K.; Mantsch, H. H.; Chapman, D. *Determination of Protein Secondary Structure by Fourier-Transform Infrared-Spectroscopy - a Critical-Assessment*. Biochemistry **1993,** *32*, 389-394.

53. Barth, A.; Zscherp, C. *What vibrations tell us about proteins*. Q. Rev. Biophys. **2002,** *35*, 369-430.

54. Clemmer, D. E.; Jarrold, M. F. *Ion mobility measurements and their applications to clusters and biomolecules*. J. Mass Spectrom. **1997,** *32*, 577-592.

55. Eiceman, G. A. *Ion-mobility spectrometry as a fast monitor of chemical composition*. Trac-Trends in Analytical Chemistry **2002,** *21*, 259-275.

56. Gumerov, D. R.; Dobo, A.; Kaltshov, I. A. *Protein - Ion charge state distributions in electrospray ionization mass spectrometry: distinguishing conformational contributions from masking effects*. Eur. J. Mass Spectrom. **2002,** *8*, 123 - 129.

57. Shvartsburg, A. A.; Li, F. M.; Tang, K. Q.; Smith, R. D. *Characterizing the structures and folding of free proteins using 2-D gas-phase separations: Observation of multiple unfolded conformers*. Anal. Chem. **2006,** *78*, 3304-3315.

58. Breuker, K.; Oh, H.; Horn, D. M.; Cerda, B. A.; McLafferty, F. W. *Detailed Unfolding and Folding of Gaseous Ubiquitin Ions Characterized by Electron Capture Dissociation*. J. Am. Chem. Soc. **2002**, 6407-6420.

59. Shavartsburg, A. A. L., Fumin ; Tang, Keqi ; Smith, Richard D. *Distortion of Ion Structures by Field Asymmetric Waveform Ion Mobility Spectrometry*. Anal. Chem. **2007,** *79*, 1523-1528.

60. Barnett, D. A.; Ells, B.; Guevremont, R.; Purves, R. W.; Viehland, L. A. *Evaluation of Carrier Gases for Use in High-Field Asymmetric Waveform Ion Mobilty Spectrometry*. J. Am. Soc. Mass Spectrom. **2000**, 1125-1133.

61. Shvartsburg, A. A.; Tang, K. Q.; Smith, R. D. *Modeling the resolution and sensitivity of FAIMS analyses*. J. Am. Soc. Mass Spectrom. **2004,** *15*, 1487-1498.

62. Purves, R. W.; Guevremont, R.; Day, S.; Pipich, C. W.; Matyjaszczyk, M. S. *Mass Spectrometric Characterization of a High-Field Asymmetric Waveform Ion Mobility Spectrometer*. Review of Scientific Instruments **1998,** *69*, 4094-4105.

63. Krylov, E. V. *Pulses of Special Shapes Formed on a Capacitive Load*. Instruments and Experimental Techniques **1997,** *40*, 628-631.

64. Guevremont, R.; Purves, R. W. *Atmospheric pressure ion focusing in a high-field asymmetric waveform ion mobility spectrometer*. Review of Scientific Instruments **1999,** *70*, 1370-1383.

65. Shvartsburg, A. A.; Li, F. M.; Tang, K. Q.; Smith, R. D. *High-resolution field asymmetric waveform ion mobility spectrometry using new planar geometry analyzers*. Anal. Chem. **2006,** *78*, 3706-3714.

66. Purves, R. W.; Barnett, D. A.; Ells, B.; Guevremont, R. *Investigation of bovine ubiquitin conformers separated by high-field asymmetric waveform ion mobility spectrometry: Cross section measurements using energy-loss experiments with a triple quadrupole mass spectrometer*. J. Am. Soc. Mass Spectrom. **2000,** *11*, 738-745.

67. Purves, R. W.; Barnett, D. A.; Ells, B.; Guevremont, R. *Elongated Conformers of Charge States +11 to +15 of Bovine Ubiquitin Studied Using ESI-FAIMS-MS*. J. Am. Soc. Mass Spectrom. **2001,** *12*, 894-901.

68. Robinson, E. W.; Sellon, R. E.; Williams, E. R. *Peak deconvolution in high-field asymmetric waveform ion mobility spectrometry (FAIMS) to characterize macromolecular conformations*. Int. J. Mass Spectrom. **2007,** *259*, 87-95.

69. Shvartsburg, A. A.; Tang, K. Q.; Smith, R. D. *Understanding and designing field asymmetric waveform ion mobility spectrometry separations in gas mixtures*. Anal. Chem. **2004,** *76*, 7366-7374.

70. Covey, T.; Douglas, D. J. *Collision Cross Sections for Protein Ions*. J. Am. Soc. Mass Spectrom. **1993,** *4*, 616-623.

71. Chen, Y.-L.; Collings, B. A.; Douglas, D. J. *Collision Cross Sections of Myoglobin and Cytochrome c Ions with Ne, Ar, and Kr*. J. Am. Soc. Mass Spectrom. **1997**, 681-687.

Chapter 2

2. Experimental Methods

Although a number of different instruments were used in the experiments of this dissertation, there is a set of common methods. The following sections will serve as a reference for those experimental techniques, and will be cited in subsequent chapters instead of repeating the same description.

2.1. Ionization

2.1.1. Nano-Electrospray

Nano-ESI is a versatile ionization technique that can be adapted to many mass spectrometers. Two basic experimental arrangements are illustrated in Figure 2.1. Figure 2.1a shows a general scheme for nano-ESI in which ions traverse a glass transfer capillary from atmosphere into the vacuum chamber. The voltage required for nano-ESI is typically applied to a metal surface on the end of the capillary. A metal sleeve fitting over the end can be used, or the capillary can be metalized. A syringe is used to introduce the solution to be analyzed into a pulled glass needle, which in turn is inserted into a metal block attached to a platinum wire. The wire is inside the needle and acts as the nano-ESI electrode. To do positive nano-ESI, the wire must be held at a potential of about 1000 V higher than a counter electrode placed a few millimeters away from the needle. For safety reasons, the wire is held at ground potential, and the end of the glass capillary at -1000 V. Because the glass capillary is an insulator, the potential on the low pressure side of the capillary does not have to

correspond to the potential on the atmospheric side. For example, if the atmospheric side is at -1000 V, the low pressure side can be set to 200 V. At lower pressure, without the insulating capillary, ions would need at least 200 eV of kinetic energy to overcome the

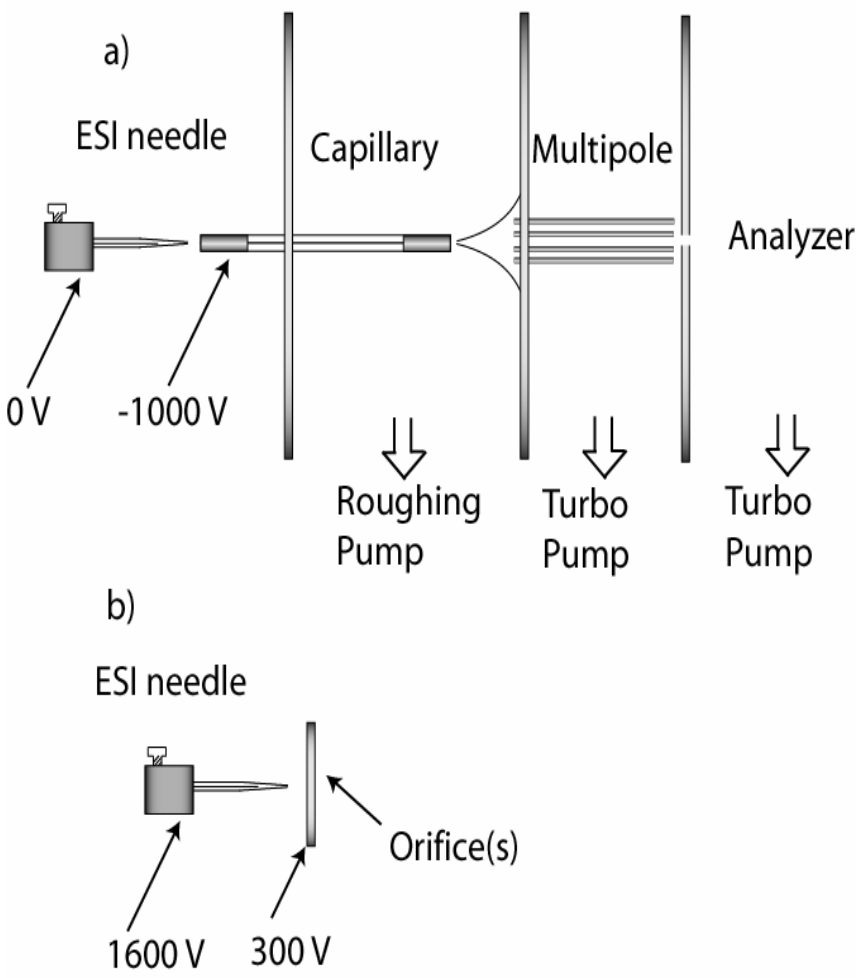

Figure 2.1. a) positive ion nano-ESI setup using glass capillary b) positive ion nano-ESI setup where interface between atmosphere and vacuum is a conductive lens element.

electric field of this lens. At the end of the glass capillary, the 200 V lens helps guide the ions into the next areas of the instrument, which are usually closer to ground potential.

Some instruments do not have glass transfer capillaries, in which case the barrier between atmosphere and the inside of the vacuum chamber is an electrically isolated piece of

metal with a suitably sized hole or holes, as in Figure 2.1b. In this configuration, positive nano-ESI is performed with a wire inside the needle at approximately 1600 V, and the metal interface at some positive voltage, around 300 V. The voltage difference between the wire and the counter electrode is still about 1000 V, but now there is some relationship between the counter electrode voltage at 300 V and voltage of the next focusing element in the instrument. The ions will be accelerated based on the difference between these two voltages, although the kinetic energy of the ions is not simply described, because of the numerous collisions with ~1 Torr of background gas.

If necessary to improve ion signal, desolvation of the electrospray droplets in the transfer capillary or metal interface can be done through heating of these elements. A countercurrent flow of gas is sometimes used for this purpose, although none of the custom-made instruments in the Glish lab utilize this option. Figure 2.1a also shows that there are two lower pressure regions after the high pressure capillary region, which is a typical arrangement. A multipole (hexapole or octopole) ion guide is commonly used to transfer ions through the intermediate pressure region.

Once the analyte solution is in the glass needle, nano-ESI is performed as follows. The glass needle is inserted into the block with the platinum wire, which is held by a micrometer stage near the mass spectrometer source interface. The voltage leads are attached, and the tip of the needle is moved slowly closer to the front of the counter electrode, off to the side of the orifice. If this is done slowly, a fine mist will appear on the counter electrode, instead of a single large droplet. Once the spray has initiated, the needle is backed up slightly and moved in front of the orifice. Generally a greater distance (5 mm) is better than a shorter one (1 mm). If the distance is too small the orifice can clog, and the

signal will be intermittent. Also, if the needle is too close, the solution can be drawn out of the needle very quickly, and alignment is more difficult. If everything is done properly, 50 μL of solution can spray for several hours. The distance between the orifice and the needle and/or the ESI voltage can be varied to give the best ion current. To a certain degree, lower voltages and greater distances give less noise and greater signal.

The analyte solution used for peptides and proteins is typically 1-100 μM in 75/20/5 v/v/v of methanol, water, and acetic acid, respectively. Other proportions of the same chemicals seem to work just as well, such as 80/20/0.1, or 50/50/1. The voltage required to start the spray depends on the viscosity of the solution. Thus, when the solution contains more water, more voltage is needed and *vice versa*.

2.1.2. Atmospheric Pressure Matrix Assisted Laser Induced Desorption

Like nano-ESI, the AP-MALDI process is performed outside the vacuum chamber, and the ions are transferred to the analyzer using differential pumping. The Glish lab only has one instrument configured for AP-MALDI, the Bruker Esquire. A good description and drawings of the aerodynamic based source can be found in Ryan Danell's dissertation.[1]

To carry out AP-MALDI on the Bruker, the same analyte solution as for nano-ESI can be used. For the experiments in this dissertation, a matrix solution of 2,5-dihydroxybenzoic acid (DHB) was made up at 100 mM or 200 mM, and mixed in a 4:1 ratio with the analyte solution to give a 4000:1 final molar ratio of matrix to analyte. The solution was spotted in the sample wells and allowed to evaporate. When prepared properly, the crystals were formed around the edge of the sample hole, but not clogging the hole. The sample plate was placed against the glass transfer capillary of the Bruker and sealed against it with a piece of rubber. The output end of the fiber optic carrying light from the N_2 laser was

placed into the sample hole, as close as possible to the crystals. The N_2 laser fires at 10 Hz, triggered during the ion accumulation time of the Bruker. Therefore, for 2 laser shots the ion accumulation time must be set to 200 ms. Generally more laser shots give greater ion signal, but deplete the sample quicker. No matter how many laser shots are used, eventually the sample in a particular region will be used up, and the laser must be moved to a fresh part of the bunch of crystals.

There are a few significant conditions for making AP-MALDI work after crystals are formed. The temperature of the capillary is very important. Ion signal is not observed below about 140 C, and is generally best at greater than 200 C. Note that this temperature depends somewhat on the position of the thermocouple in the heating device. If the heating device is ever replaced, optimum signal sometimes will occur at a different temperature. This could be due either to how well the thermocouple is wrapped in the heating wire, or due to actual power dissipation of the different heater configurations. The power of the laser is also important. Laser power can be measured with the Rm-6600 Universal Power Meter from Laser Precision Corporation. The measurement is more accurate when the power meter is triggered off of the same signal as the N_2 laser. The laser power may be maximized by translating the elements that focus the beam into the fiber optics, and by exposing a fresh end of the fiber optics on the delivery end. Cutting the fiber optic properly seems to be something of an art. In the end, a laser power of 10-20 μJ was usually obtained when AP-MALDI was successful.

2.1.3. Electron Impact

Although EI has the notable limitation that sample must be volatile, the robustness of the technique makes it invaluable in an instrument development laboratory.[2] Optimizing the

various lens voltages to give good performance in nano-ESI can be very difficult, so the analyzer of a new instrument should be tested first with a constant beam of EI ions. Besides providing a constant high flux of ions, EI also allows one to define the kinetic energy of the ions very easily. Ion kinetic energy is a key variable to the proper performance of a mass spectrometer. For EI, the kinetic energy of the ions at the analyzer is simply the potential difference between the source region and the analyzer. For nano-ESI the situation is a little more complicated because of the ion expansion through several different pressure regimes. For example, although the end of the transfer capillary in ESI is held at 200 V, when the ions reach the analyzer they will not have 200 eV of kinetic energy. The high pressure of air in the volume around the capillary dampens ion motion such that kinetic energy is no longer simply defined, as it is in the absence of collisions. Measuring the distribution of ion kinetic energies for EI or nano-ESI can be done by measuring ion signal as the voltage of a lens element is increased. The plot generated with this method is a "stopping curve", and the first derivative of ion signal with respect to voltage gives the most probable ion kinetic energy.

A diagram of the ionization source from a Finnigan TSQ 70 is given in Figure 2.2. The simplest EI experiment is to turn on the filament and ionize residual air and water in the vacuum chamber. Other gases can be metered into the ionizing volume with needle valves. Although pressure gauges are calibrated for N_2, an indicated pressure of $1x10^{-6}$ -$1x10^{-5}$ Torr is sufficient to give good signal for many analytes. Vapor from liquid samples can be ionized easily as well. Typical voltages for TSQ EI source are given in **Appendix D**.

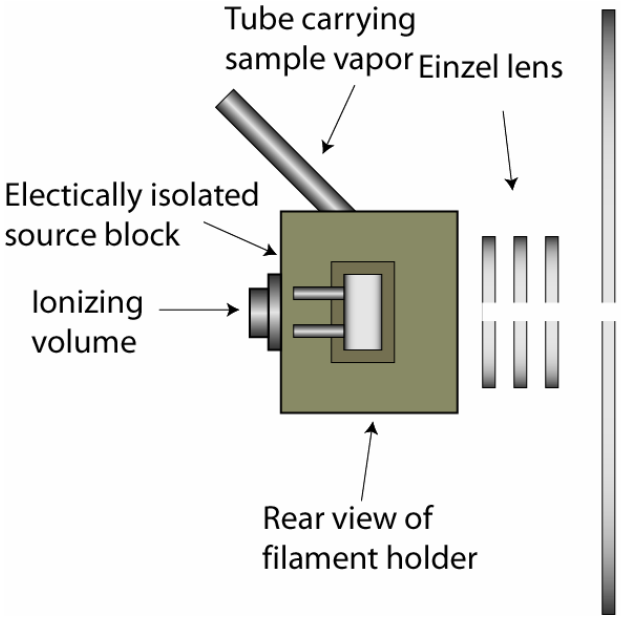

Figure 2.2. Diagram of electron ionization (EI) source

2.2. Ion Accumulation

When a continuous source of ions, such as for nano-ESI or EI, is coupled to a non-continuous analyzer, such as a QITMS, the beam of ions must be periodically interrupted so they do not disturb the analysis or detection events. This gating of the ion beam can be accomplished by pulsing the voltage on a lens element to deflect or pass ions during the appropriate times. A typical circuit for pulsing between two dc voltages is given in **Appendix C**. The Bruker Esquire pulses the voltage on the skimmer interface between the high pressure source and mid-pressure octopole region, the ion trap in **Chapter 3** (IR-Trap) pulses the voltage on the lens after the octopole, and the ITMS pulses the voltage on one half of a split circular lens. Observations show that the least leakage of any charged particles through the gate is found when the blocking voltage is >100 V.

A careful balance of parameters is required to trap ions formed in an external source. Ions must have sufficient kinetic energy to overcome the electric field barriers at the entrance holes of the trap, yet the kinetic energy must not be so great that the He buffer gas is unable to slow the ions down in the center of the trapping volume. The optimum ion kinetic energy for injection is 7-25 eV.[3] The amplitude of the trapping rf voltage during the ion accumulation period is also a key parameter. The rf voltage threshold for trapping ions scales as the square root of mass, presumably because larger ions are collisionally dampened less efficiently.[3] Larger potential wells are therefore required to trap larger ions. In terms of q_z, however, larger ions are trapped at slightly lower values and over smaller ranges of q_z. Typically on the ITMS, a rf voltage corresponding to LMCO 40 during ion injection works well, however for higher masses LMCO of 50 or more is better. The QITMS's in the lab that run at lower frequency require a higher LMCO during ion injection. The Bruker Esquire uses LMCO 50-80 Da, while the IR-Trap typically works best at LMCO 80-150. These differences in optimum LMCO for ion injection over different instruments may be due to the pseudopotential well dependence on the square of trapping frequency, as in Equation 1.8. However, the IR-Trap currently runs at around 950 kHz, the Bruker at ~800 kHz, and the ITMS at 1.10 MHz, therefore the trend in LMCO during injection versus trapping frequency is not perfectly linear. Another hypothesis is that special focusing requirements on the IR-Trap necessitate higher ion kinetic energies and therefore larger trapping wells than the other two instruments. When all three instruments are operating correctly, accumulation times need only be ~5 ms to get sufficient ion populations for experiments.

2.3. Ion Dissociation

2.3.1. Collision Induced Dissociation

Background information on CID was given in **Chapter 1.2.1.4.2**. When performing a tandem MS method, typically the parent ion must first be isolated to get rid of unwanted background ions. Ions at a mass-to-charge less than the parent ion can be ejected from the trap by ramping up the rf voltage so that the parent ion has a q_z value slightly less than 0.908.

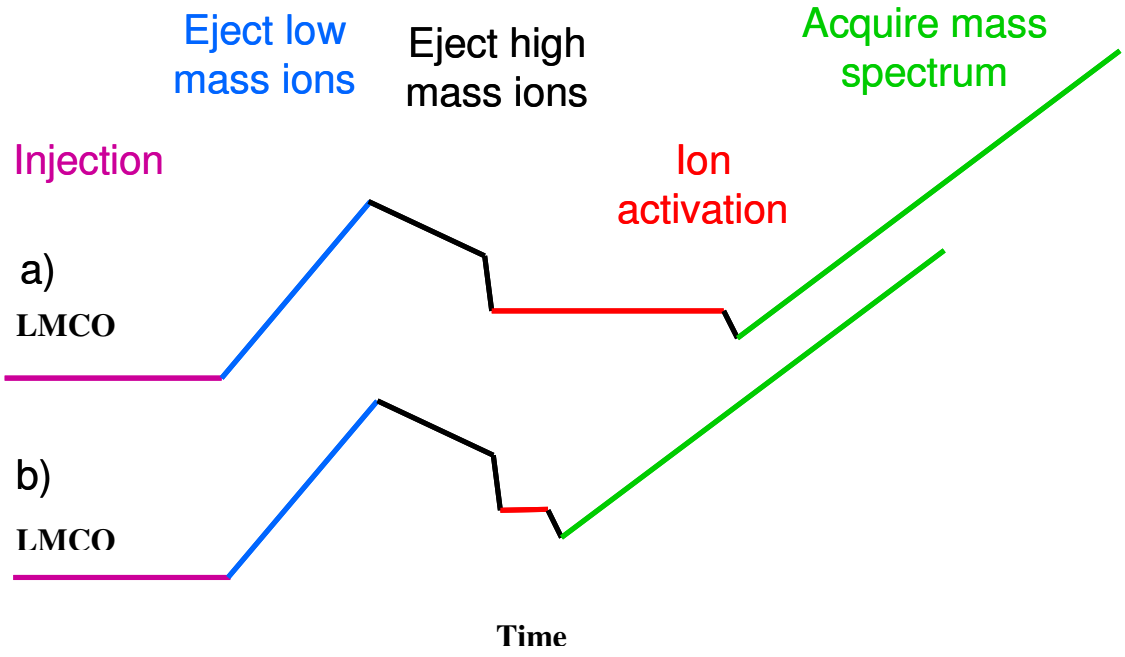

Figure 2.3. Scan functions for ion activation by conventional CID or IRMPD a) and by HASTE CID b). Y axis is rf voltage or LMCO, x axis is time.

A representation of rf voltage amplitude versus time, or scan function, is given in Figure 2.3a. If resonance ejection is being used, then the parent ions are brought to a q_z value just less than the q_z of resonance ejection, typically ~0.25. To eject ions of mass-to-charge greater than the parent ion a supplementary voltage is applied that corresponds to a higher mass and the rf voltage is ramped down. One starts by ramping down 100 Da or so and visually verifying how well the parent ion has been isolated. The endpoint of this ramp down

is adjusted until all the high mass ions are gone and the parent ion intensity has not been reduced unnecessarily. About 10-30 ms each for ramping up and ramping down is typically sufficient.

The ions are allowed to cool for about 20 ms to lose kinetic energy gained during the isolation process. The importance of cool time will be discussed in more detail in **Chapter 7**. Next, the frequency and amplitude of the supplementary voltage for ion activation are ascertained. A starting point for the ion secular frequency can be calculated with Equations 1.9 and 1.10. This frequency is only a starting point because Equations 1.9 and 1.10 assume that only one ion is in the trap. When multiple ions are in the QITMS, their motion begins to be affected by mutual charge repulsion. The cumulative effect of many ions adds a dc voltage component to the trapping voltage, creating an appreciable a_z term in Equation 1.10. Thus, multiple positive ions tend to have secular frequencies a few hundred to a few thousand Hz less than the theoretical secular frequency for one ion. To find the optimum excitation frequency, the excitation frequency is set to the theoretical ion secular frequency, and the amplitude is set to approximately 4 V. This is a large voltage for CID, therefore the ion will absorb sufficient power, even with off-resonance excitation, to dissociate extensively. The amplitude is then adjusted such that about 50% fragmentation efficiency is reached (Equation 1.12) and then the excitation frequency is varied to get 100% fragmentation efficiency. The voltage amplitude is lowered again to 50% fragmentation efficiency and the process is repeated until the maximum MS/MS efficiency is achieved (Equation 1.11). Extensive fragmentation information can be obtained at high excitation amplitudes, but the goal is to dissociate every parent ion without unintentionally ejecting any

of them out of the trap. Excitation amplitudes of 500-1200 mV and excitation times of 10-40 ms are generally used.

2.3.2. High Amplitude Short Time Excitation

A new set of parameters for doing CID, called HASTE CID, was recently developed.[4] Quite simply, the main difference is that HASTE CID uses excitation amplitudes of 2500-6000 mV and 0.5-2 ms are used instead of the values given above for conventional CID. Excitation and dissociation of an ion are distinct events, separated in time. Because excitation happens so quickly in HASTE (shown in Figure 2.3b), the rf amplitude can be dropped to a lower q_z value before some ions dissociate, and the low mass cut-off problem can be partially circumvented. The large excitation voltages used in HASTE cause MS/MS efficiency to be poorer than conventional CID, but because the trapping voltage is lowered after excitation, the poor efficiency can be offset in part by raising the q_z value (a larger pseudopotential well) during excitation. Values of q_z as high as 0.89 have been used.[5]

2.3.3. Infrared Multiphoton Dissociation

IRMPD is performed with the same general procedure as conventional CID except that instead of applying a resonant excitation voltage after parent ion isolation, an IR laser is turned on during this time with a TTL signal from the QITMS hardware. The CO_2 lasers used for IRMPD are a 10.6 μm, continuous output (cw), 0-100 W Synrad Firestar f100 on the IR-Trap, and 0-50 W Synrad Model 48-5 on the ITMS. The laser beam is delivered with silicon mirrors and focused to the center of the trap with a 38.1 cm focal length ZnSe lens. Laser power is set by a manufacturer supplied digital controller (analog for ITMS). Power was generally set at ~ 10 to 30 W, depending on pressure, temperature, and ion species.

Photons do not appreciably change the momentum of the ions they interact with, so there is no competition between excitation and ejection like with CID. Thus, before HASTE CID, the low mass cutoff problem was traditionally solved by using photodissociation. IRMPD does present its own complications, however. The collisions of the He bath gas thermalize ions down to the bath gas temperature.[6-9] Only when the ions are given extra kinetic energy through resonance excitation do the collisions add appreciable internal energy to the ions. Therefore, during IRMPD there is a competition between energy deposition through photoabsorption and energy dissipation through collisional deactivation. In some cases the bath gas pressure is lowered to slow the collisional cooling rate and allow photodissociation, sacrificing trapping efficiency[10]. However, the addition of an optical lens to focus the laser beam to the center of the trapping volume creates a higher density flux of photons which can dissociate many ions even at normal He pressures.

2.4. Theoretical Methods

2.4.1. Structure Calculations

For optimizing ion geometries to lowest energy conformers, calculating structure energies, and calculating vibrational modes, the program Gaussian 03 was used.[11] This program can be accessed through the scientific computing facilities at UNC. The current cluster being used (Emerald) and the current protocol for running scientific computing programs and submitting jobs can be ascertained at http://www.renci.org. A good resource to begin with is http://www.renci.org/unc/computing/. A program called X-Win32 is useful to log into the research computers and display the graphic user interface (GUI) for Gaussian. Help on setting up X-Win32 can currently be found at http://help.unc.edu/4696. There are constant changes happening to the scientific computing services at UNC, and now two years

after the last job was submitted for the experiments in this dissertation, the computers utilized at that time are being phased out. Instead of describing the outdated way these services were formerly used, the current protocol for running scientific computing programs and submitting jobs can be established at the above links.

Once the user has access to scientific computing, the program GaussView should be run. GaussView is a program that allows the user to define molecule and ion geometries and the type of analysis they want run with a GUI, instead of a script-based protocol. For geometry optimizations and vibrational analysis, best results are obtained if optimization is done first using a small basis set like 3-21G (see **Chapter 1.3.3**) and then moving up to more computationally expensive methods. One must remember that vibrational analysis is only valid using the same basis set as the one that produced the optimized structure, and must be done only at stationary points on the potential energy surface.[12, 13] For this reason users are recommended to use the command "Opt+Freq" that optimizes the geometry and then calculates the vibrational frequencies.[13] The vibrational frequencies of an ion are needed for comparing two calculated IR spectra, and also calculating properties like densities and summations of states.

2.4.2. Internal Energy Distributions

There exist many mass spectrometry applications where knowing the distribution of internal energies of an ion is useful. Often this distribution is difficult to obtain, but when the ion is in thermal equilibrium with the surroundings then statistics can be of great help. The probability that an ion with internal temperature T has energy E is given in Equation 2.l.

$$p(E) = \frac{\rho(E) \cdot e^{-E/k_b T}}{\sum_j \rho(E_j) e^{-E_j/k_b T}} \qquad \text{(Equation 2.1)}$$

Here k_b is Boltzmann's constant, and $\rho(E)$ is the density of states at energy E. Density of states represents the number of ways to distribute energy such that the molecule has an energy between E and $E+dE$.[14] Thus, the units of density of states are states per energy unit e.g. states/cm^{-1}. The summation of states, a related parameter used later in this dissertation, is the integral of density of states from energy 0 to E. Programs for calculating density and summation of states are given in several publications.[14, 15]

When one can calculate the probability that an ion has any particular internal energy, the average internal energy is a simple extension, given in Equation 2.2.

$$\langle E \rangle = \frac{1}{Q}\int_0^\infty \rho(E)\cdot E\cdot e^{-E/kT}\,dE \qquad \text{(Equation 2.2)}$$

Q is the vibrational partition coefficient $\int_0^\infty \rho(E)e^{-E/kT}\,dE$. **Appendix A** shows a program written in LabView that takes a Gaussian output file and computes density of states, summation of states, internal energy distribution, and average internal energy.

2.4.3. Ion Trajectory Modeling

For simulating ion trajectories SIMION 7.0 was used.[16] SIMION allows the user to define electrodes or magnets of any shape and size and calculates the fields around these elements using Laplace's equation. SIMION files can be created such that the fields are scalable, that is, the electric fields can be multiplied by a time-dependent factor to simulate the rf fields used in mass spectrometry. Help getting started with SIMION and about setting up advanced user programs and geometries can be found at \\Asntdomain1.cas.unc.edu\users\chemistry\share\glishgroup\Group Files\Programs and Templates\Simion How-To's.

SIMION "simulation quality" was set to 3 for all simulations, and grid spacing was 0.05 mm/grid unit. Ions were placed in the starting point plus or minus a random offset, phase, and kinetic energy, within certain parameters. The subscript for randomizing initial conditions was written by Dahl and is given in the SIMION 7.0 example files. Collisions with He neutral gas were simulated using the 3D hard sphere model developed by Manura.[17] For this model, a gas mass, temperature, pressure, and ion collisional cross section must be specified. Lacking information on an ion cross section, σ, the relation in Equation 2.3 was used, where m is the ion mass.[18]

$$\sigma = 50\left(\frac{m}{100}\right)^{2/3} (in\,\mathrm{A}^2) \qquad \text{(Equation 2.3)}$$

An IMS study of the collision cross section of many hundreds of peptides of different sizes and sequences is useful for estimating cross section as well.[19] Interactions between ions could be simulated with the SIMION point charge model. In this mode, a total amount of charge is designated to be distributed amongst all the ions being simulated. For example, if 10 ions were being simulated and the total charge was 1.6×10^{-16} C, then each affects the others as if it has the charge of 100 ions, and it would be expected that the ions behave as if there were 1,000 total ions in the trap. Selected user programs from various projects can be found in **Appendix B**.

2.5. References

1. Danell, R. M.; Glish, G. L. *Advances in ion source and quadrupole ion trap performance and design*. Doctoral Dissertation, The University of North Carolina, Chapel Hill, 2001.

2. Schwartz, J. Measuring ion number and detector gain. U.S. Patent 7109474 Patent 2006.

3. March, R. E.; Todd, J. F. J. *Practical Aspects of Ion Trap Mass Spectrometry*; CRC Press: New York, 1997.

4. Cunningham, C., Jr.; Glish, G. L.; Burinsky, D. J. *High Amplitude Short Time Excitation: A Method to Form and Detect Low Mass Product Ions in a Quadrupole Ion Trap Mass Spectrometer*. J Am Soc Mass Spectrom **2006,** *17*, 81 - 84.

5. Schwartz, J. High-Q pulsed fragmentation in ion traps. U.S. Patent 7102129 Patent 2006.

6. Goeringer, D. E.; McLuckey, S. A. *Relaxation of Internally Excited High-mass Ions Simulated under Typical Quadrupole Ion Trap Storage Conditions*. Int. J. Mass Spectrom. **1998,** *177*, 163-174.

7. Asano, K. G.; Goeringer, D. E.; Butcher, D. J.; McLuckey, S. A. *Bath Gas Temperature and the Appearance of Ion Trap Tandem Mass Spectra of High-Mass Ions*. Int. J. Mass Spectrom. **1999,** *190/191*, 281-293.

8. Remes, P. M.; Glish, G. L. *Theoretical Estimation of Peptide Internal Temperature for High Amplitude Short Time Excitation Collision Induced Dissociation in a Quadrupole Ion Trap*. J Am Soc Mass Spectrom **2007,** *Submitted*.

9. Remes, P. M.; Glish, G. L. *Collisional Cooling Rates in a Quadrupole Ion Trap at Sub-Ambient Temperatures*. Int. J. Mass. Spectrom. **2007,** *265*, 176-181.

10. Colorado, A.; Shen, J. X.; Vartanian, V. H.; Brodbelt, J. *Use of Infrared Multiphoton Photodissociation with SWIFT for Electrospray Ionization and Laser Desorption Applications in a Quadrupole Ion Trap Mass Spectrometer*. Anal. Chem. **1996,** *68*, 4033-4043.

11. Frisch, M. J. *Gaussian 03, Revision C.02 Gaussian, Inc., Wallingford CT*. Gaussian 03, Revision C.02 Gaussian, Inc., Wallingford CT **2004**.

12. Ochterski, J. W. *Vibration Analysis in Gaussian*. Technical Support Information: Gaussian Inc. **1999**.

13. Foresman, J. B., Frisch Aeleen *Exploring Chemistry with Electronic Structure Methods*; Gaussian, Inc.: Pittsburgh, PA, 1993.

14. Baer, T.; Mayer, P. M. *Statistical Rice-Ramsperger-Kassel-Marcus quasi-equilibrium theory calculations in mass spectrometry*. J. Am. Soc. Mass Spectrom. **1997,** *8*, 103-115.

15. Stein, S. E.; Rabinovitch, B. S. *Accurate evaluation of internal energy level sums and densities including anharmonic oscillators and hindered rotors*. The Journal of Chemical Physics **1973,** *58*, 2438-2445.

16. Dahl, D. A. *SIMION 3D 7.0.*

17. Manura, D. *Collision Model HS1* http://www.simion.com/info/Collision_Model_HS1. Collision Model HS1 http://www.simion.com/info/Collision_Model_HS1 **2007**.

18. Quarmby, S. T.; Yost, R. A. *Fundamental Studies of Ion Injection and trapping of Electrosprayed Ions on a Quadrupole Ion Trap*. Int. J. Mass Spectrom. **1999,** *190/191*, 81-102.

19. Valentine, S. J.; Counterman, A. E.; Clemmer, D. E. *A Database of 660 Peptide Ion Cross Sections: Use of Intrinsic Size Parameters for Bona Fide Predictions of Cross Sections*. J. Am. Soc. Mass Spectrom. **1999,** *10*, 1188-1211.

Chapter 3

3. Design and Operation of a Quadrupole Ion Trap for Infrared Action Spectroscopy

3.1. Introduction

Chapter 1.1.1 introduced the idea of three dimensional structure and its importance in the proper functioning of biomolecules. A wealth of information can be derived from discerning the structure of any molecule, not just biological molecules. The structure of a molecule determines which inter- and intra-molecular reactions are possible, making conformational studies of molecules and ions an area of intense study. As described in **Chapter 1.1.2**, gas-phase, mass spectrometry-based techniques have several advantages over solution-based methodologies for structure determination, and the past ten years have seen a rapid increase in the number of studies aimed at exploiting these benefits. Although the Glish lab has traditionally focused on developing MS and MS/MS for proteomics, the study of higher order structure is not an entirely new direction. The influence of ion structure on peptide fragmentation was recognized in our lab many years ago.[2-4] In recent years, however, the availability of higher power, tunable IR lasers opened up the possibility of studying peptides and other many other ions with spectroscopic structure determinations.[5-15]. This chapter will discuss the design and operation of an instrument for doing these studies: a QITMS for IR laser spectroscopy of ions at low temperatures. This instrument is referred to as the "IR-Trap" in the Glish lab and in the rest of this dissertation.

The project started as a collaboration between the Glish, Miller, and Baer labs. The large number of possible systems for study, coupled with the Glish lab knowledge of the QITMS, the Miller lab expertise in laser spectroscopy, and the Baer lab proficiency with fundamental gas-phase ion studies prompted the building of a new instrument for IR action spectroscopy of ions. The bulk of the studies performed to that date were done using free electron lasers (FEL) as the IR light source coupled with Fourier transform-ion cyclotron resonance mass spectrometers (FT-ICR). The expense associated with building and maintaining a FEL facility and FT-ICR is beyond the means of most research labs, and it was felt that there was room for a rugged, high performance instrument based on a different platform. The QITMS is a lower cost, lower maintenance instrument with less mass resolution and accuracy than the FT-ICR, but for these types of experiments those attributes are not so important. That is, in IR action spectroscopy, the identity of the analyte is known and the parameter of interest is fragmentation efficiency, not product ion mass-to-charge value. The QITMS also offers the possibility of effectively lowering the temperature of the ions to create a more ideal spectroscopic environment. Low temperatures cool the ions that are vibrationally excited down to the ground state, simplifying the IR spectra and concentrating ion intensity into fewer IR stretches. When the QITMS electrodes are cooled, the He bath gas will equilibrate with these surfaces, and also equilibrate with any trapped ions. The FT-ICR works best at very low pressures, making the collisional cooling procedure much more inefficienct and difficult.

The Miller lab also had gained significant experience building some of the world's most high power, constant waveform (cw) periodically polled lithium niobate – optical parametric oscillators (PPLN-OPO) lasers.[16] This type of laser has very good resolution

(0.001 cm^{-1}), tunability (2500-5000 cm^{-1}), and power (3.5 W), which would offer an alternative to the FEL-based experiments, which operate in the fingerprint IR region of 40-2000 cm^{-1} with resolution of 3-120 cm^{-1} (~6% of laser wavelength) and power of 60 mJ per 5 μs pulse, repeating at 10 Hz.[11, 17] The vibrational modes that may be studied with a FEL are more complex bends and stretches, while the PPLN-OPO frequency range overlaps with more simple C-H, N-H, and O-H stretches that are easier to predict and compare to calculated structures. The combination of a high power cw PPLN-OPO and QITMS has the potential to generate data of a high quality that would compliment the FEL-FTICR work that has already been done.

3.2. Method of Low Temperature Ion Trap IR Spectroscopy

The basic method for performing action spectroscopy was described in **Chapter 1.3.1**. Several of these studies have employed electrodynamic trapping devices with cooled electrodes.[18-20] Performing spectroscopy on ions at low temperatures simplifies spectra by reducing the number of hot vibrational bands. Sensitivity at a particular laser wavelength is also increased because the ions are concentrated into a smaller number of energy states.

Previous IRMPD experiments had shown that the collisional cooling effect, discussed in **Chapters 2.3.3** and **Chapter 4**, was significant even at room temperature with a 50 W, cw CO_2 laser.[21] Although the photons from the tunable PPLN-OPO laser have more energy than a CO_2 laser, difficulties dissociating ions at low temperatures were expected because collisional cooling is expected to be magnified at lower temperatures. Therefore the proposed action spectroscopy procedure was modified to use the "two-color" excitation scheme previously implemented[22, 23] with low power tunable lasers. This technique uses the lower power tunable laser to vibrationally excite the ion at a specific resonance, and a high

power CO_2 laser to dissociate only the vibrationally-excited ions. The wavelength of the high power laser is insignificant, because an ion, once excited to the quasi-continuum of states, can absorb any wavelength of light.[11, 24, 25] Figure 3.1 shows one method of irradiating the QITMS trapping volume with two different lasers.

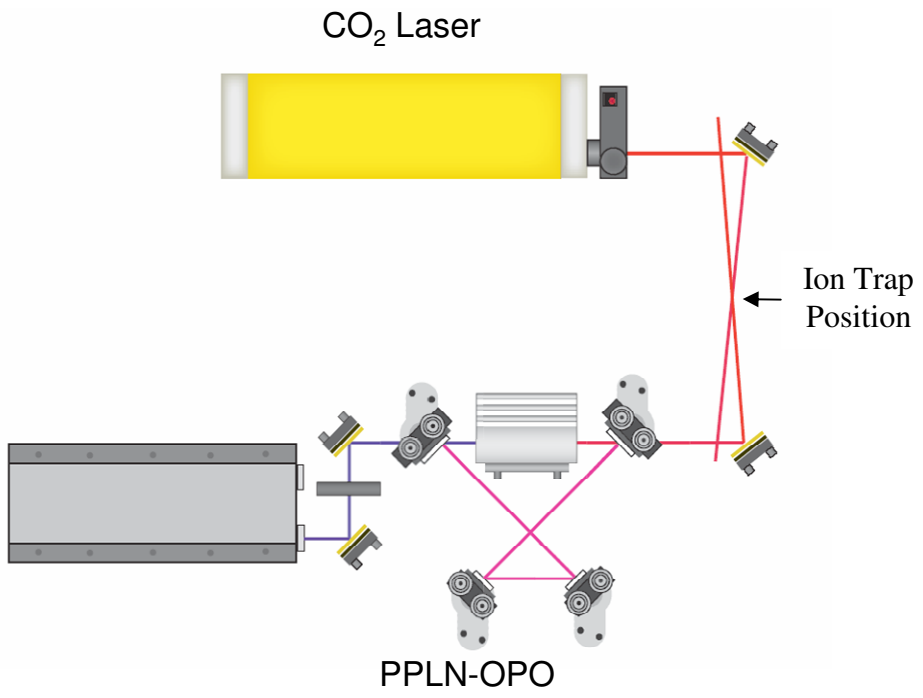

Figure 3.1. Proposed positioning of CO_2 and PPLN-OPO lasers for IRMPD spectroscopy.

3.3. Low Temperature Considerations

3.3.1. Closed Cycle Helium Refrigeration

The electrodes of the QITMS are cooled with a two stage Sumitomo RDK-408S 10K closed-cycle helium cryostat, or "cold head". Figure 3.2 depicts the cold head, with its 35 W first cooling stage and 6.3 W second stage. Using two stages instead of one decreases the heat load on any one stage, in much the same way as differential pumping decreases the gas load on any one vacuum pump. Because the blackbody radiation from a room temperature

object is appreciable, there must be a buffer between the QITMS and the vacuum housing if very low temperatures are to be reached. The 35W first cooling stage serves as this buffer, when a thermally conductive "shield" is placed in contact with it. The element to be cooled to lowest temperature, in this case the ion trap electrode, goes inside the shield in thermal contact with the 6.3 W second stage.

The cryostat cools itself by expanding and compressing He gas inside its various compartments, in what is called the Gifford-McMahon process of refrigeration. Very low temperatures can be achieved at the second stage of the cryostat through this mechanism. The minimum attainable temperature for the RDK-408S cryostat is 10 K with no heat load. When the MS components are attached to the cryostat, described below, a lowest temperature of 23 K has been reached. Lower temperatures might be possible by better polishing of the outer 1st stage shield surface to reflect blackbody radiation and act as a better buffer. The 1st stage shield could alternatively be gold plated or wrapped in mylar for the same reason.

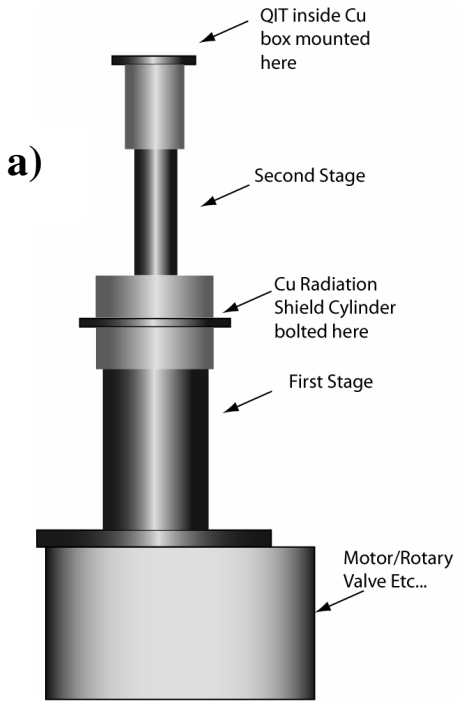

Figure 3.2. Closed-cycle helium cryostat

3.3.1.1.Temperature Controller

The cryostat has only two modes; on and off. Therefore, to reach a constant temperature at any state higher than the minimum, a heater must be attached to the cold head with a temperature sensing feedback loop. The temperature of the system is regulated with a Lakeshore 340 controller, which controls a 100 W heater attached to the cold head, and

receives feedback from a silicon diode mounted on the ion trap holder. The output impedance of the Lakeshore 340 heating loop is 25 Ohms. Three Minco, 78.4 Ohm, flexible Kapton heaters were hooked up in parallel to give 26 Ohms resistance. The power supply output impedance and heater impedance are therefore nearly matched, and near maximum heating capacity is possible. The heaters are attached with special epoxy to the side of the second stage. Care must be taken not to operate the heating circuit at 100 W output near room temperature because the heater ability to dissipate power begins to decrease as the heat sink temperature rises. The cryostat has actually been heated to 330 K, but burn spots were later found on the heaters. A better method to achieve hot temperatures for this instrument is to wrap the vacuum housing with a heating jacket.

3.3.2. Thermal Properties of Materials

The QITMS electrodes must be simultaneously in thermal contact with the cryostat and electrically insulated from it. Some material properties relevant to this problem are given for copper (Cu), stainless steel (SS), and high purity alumina (Al_2O_3) in Table 3.1.

Table 3.1. Properties of materials used in the IR-Trap.

Rough calculations of the power required to change the temperature of a given mass of material can be performed using these numbers. Equation 3.2 gives the power P necessary to change the temperature ΔT of a mass m of material with specific heat capacity C_p in time t.

$$P = \frac{m \cdot C_p \cdot \Delta T}{t} \qquad \text{(Equation 3.2)}$$

Equation 3.2 helps calculate what power refrigerator or heater is required for a given situation. The thermal conductivity, on the other hand, describes the efficiency of heat transfer through a given medium. In the case of an ion trap separated from a copper holder with alumina spacers, the alumina has a much lower thermal conductivity than copper, and is one of the limiting factors in cooling the QITMS electrodes. In practice, the temperature of the trap drops fairly quickly from room temperature down to around 100 K, after which much more time is needed to reach 23 K, on the order of several hours. Short jumps in temperature on the order of 25 K take only a few minutes, with a steady equilibrium temperature being achieved in 15-20 min. The temperature controller manual should be consulted for optimizing the temperature control algorithm.

3.4. Vacuum Housing Design

3.4.1. Trap Enclosures

A cut-away, side view of the QITMS inside a copper enclosure is shown in Figure 3.3a. The enclosure with the QITMS inside is mounted on top of the 2nd stage of the cryostat as in Figure 3b. The larger copper piece surrounding the 2nd stage enclosure is the 1st stage shield. Holes of 0.635 cm are drilled in the shield, on-axis with the entrance and exit holes of the ion trap, to allow ions to enter and leave the mass spectrometer. Ion lenses placed halfway between the first and second stage enclosures serve to focus incoming ions into the trap, and focus ejected ions into a channeltron-type electron multiplier for detection. Two more 0.635 cm holes, placed 90 degrees from those described above, allow a laser beam to traverse the instrument. The laser beam enters and leaves the trap through 3.18 mm holes in the ring electrode, passing through the center of the ion trapping volume. The He gas needed

for ion trap MS, as discussed in **Chapter 1.2.1.1**, flows through a 1/16" copper tube that winds around the outside of the 1st stage for several turns. The reduced temperature of the 1st stage shield pre-cools the gas before introducing it through the top of the 2nd stage enclosure. Mechanical drawings for these enclosures are in **Appendix E**.

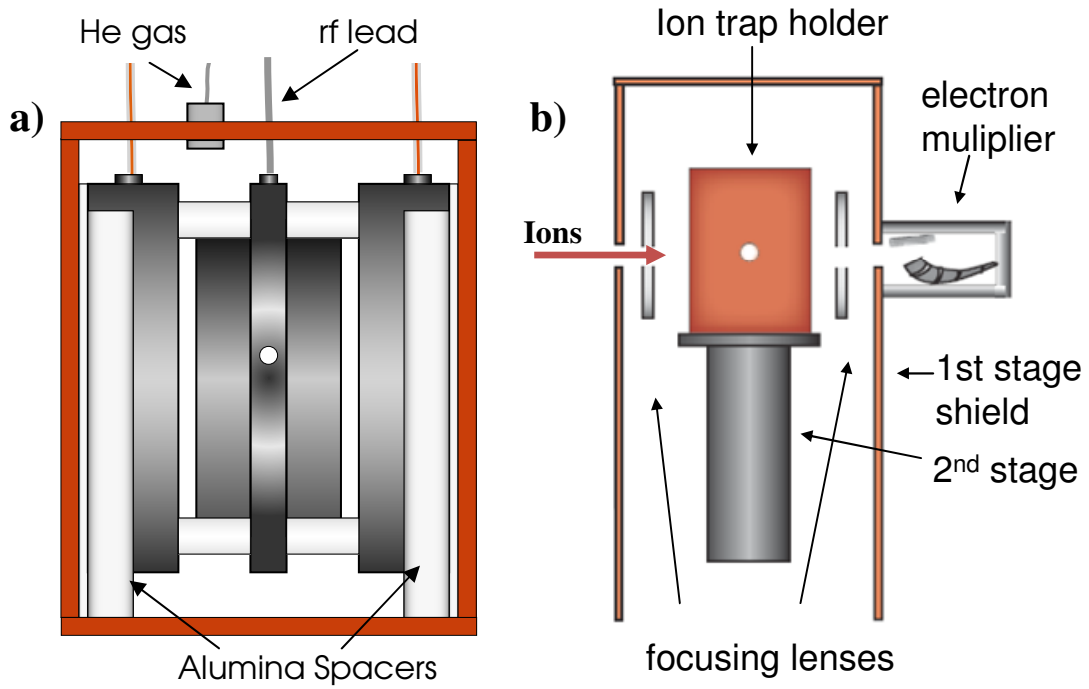

Figure 3.3. a) QITMS in gray inside copper enclosure. Endcap electrodes are separated from copper by alumina ceramics. Voltage leads and He gas enter enclosure through top piece. b) QITMS in holder from a) on top of 2nd stage of cryostat. Electron multiplier is mounted on backside of 1st stage shield.

3.4.2. Pressure Calibration

Due to the necessity of drilling holes in the enclosures for allowing ions to enter and leave, neither of the enclosures is gas-tight. However, the holes are small enough to make the flow of He into the main vacuum chamber be conductance-limited. Therefore the pressure gauge, mounted in the main vacuum chamber, does not read the same pressure as in the QITMS trapping volume. One method to estimate the pressure inside a conductance-limited QITMS is to observe a reaction of known kinetics. An attempt was made to react

H_3O^+ with isoprene and calculate isoprene pressure using the reaction rate constant[26] of $2.0x10^9$ cm^3 s^{-1} and pressure gauge sensitivity factor (gauge is calibrated for N_2) of 0.268. The gauge sensitivity factor was calculated with a program written by John Bartmass called ADO. The factor for He gas pressure (including x7 factor for gauge sensitivity of He) inside the QITMS calculated with this method was x280. Because the He flow is typically set to an indicated pressure of $3x10^{-5}$ Torr, the reaction rate method gives an actual He pressure of $8.4x10^{-3}$ Torr. The factor of x280 appeared to be much too high. Even using EI, appreciable numbers of ions begin to be trapped at ~$7x10^{-6}$ Torr indicated pressure, and up to $1x10^{-4}$ Torr has been set without arcing.

A different method of estimating the actual He pressure in the QITMS was attempted. Collisional cooling rates were measured by the method of **Chapter 4** at different indicated pressures for two conditions; the normal setup with conductance-limited He flow from QITMS to gauge, and with enclosure tops removed giving unobstructed gas flow from QITMS to gauge. The rate of collisional cooling depends strongly on He pressure, therefore when the same rate is observed for the two above conditions, a correspondence between actual and indicated pressure can be calculated. This factor (including x7 for He sensitivity) was x98, therefore an indicated pressure of $3x10^{-5}$ Torr corresponds to an actual He pressure of $3x10^{-3}$ Torr in the QITMS. Of note is that the pumping calculations described in the next section can also be used to give an estimated pressure factor, which was x140, much closer to x98 than to x280. These values seem much more reasonable. Also, the most probable error in the pumping calculation is an underestimation of the gas flow out of the enclosures, because the enclosures were assumed to be gas tight except for the 0.635 cm holes. This assumption means that x140 is probably an overestimation. The reason for the large error in

the previous ion/molecule reaction method is unclear, but because many repetitions at two different pressures of isoprene resulted in the same pressure factor, accurate measurement of isoprene pressure could be the problem.

3.4.3. Pumping Calculations

Atmospheric pressure ionization (API) sources utilize differential pumping to maximize ion transmission from outside the vacuum housing to the analyzer, and to minimize gas load on any one vacuum pump. A few equations prove to be very useful for calculating the pressure in a vacuum housing for a given gas conductance into the region, and a given pumping speed. Equation 3.3 is the system balance equation, which says that the gas throughput (mass flow rate) out of a region is equal to the gas throughput into a region.[27] P_1 and P_2 are the pressures in regions 1 and 2, where $P_1 > P_2$. Pumping speed (L/s) is S which is given by the vacuum pump manufacturer, and C is the conductance (L/s) between regions 1 and 2.

$$P_2 S = C(P_1 - P_2) \qquad \text{(Equation 3.3)}$$

Equations for C have been postulated for various pressure regimes and types of apertures[27]. One easily overlooked aspect of Equation 3.3 is that S is generally given by the manufacturer for the best case scenario, where the pump opening is not obstructed at all. When the pump is attached to the vacuum housing via an opening that constricts gas flow in any way, the actual pumping speed is affected as in Equation 3.4.

$$\frac{1}{S_{actual}} = \frac{1}{S_{pump}} + \frac{1}{C_{orifice}} \qquad \text{(Equation 3.4)}$$

3.4.4. Main Vacuum Chamber

The IR-Trap was designed to use API sources with the typical configuration of three stages of differential pumping. However, the main vacuum housing for the IR-Trap was an early model ITMS chamber, sketched in Figure 3.4. Coupling two more stages of differential pumping with a trap mounted on a cryostat required some non-traditional and perhaps non-

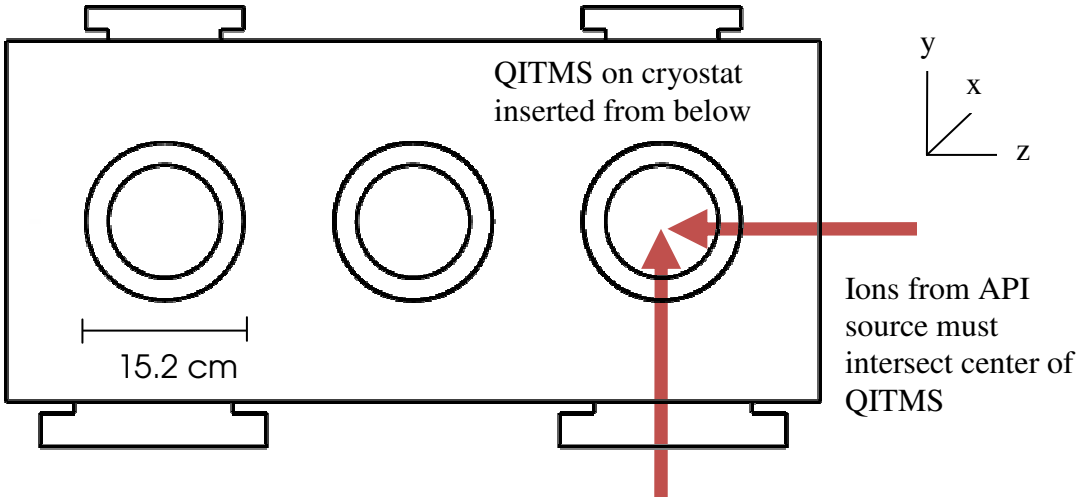

Figure 3.4. ITMS vacuum housing used as base for IR-Trap. The cold head (figure 3.1a) is inserted from the bottom into one of the two 8" flanges, and the two other differential pumping stages are attached to a 10" flange and mounted onto the side flange.

optimal design elements. Mass spectrometers are generally built in such a way so to ensure proper alignment of all apertures and ion lens. Because aperture sizes are on the order of 1 mm, alignment is a key consideration to optimum ion transmission. Optical rails are one way to ensure alignment, and the instrument described in **Chapter 8** uses this form of alignment. Another way to ensure alignment is to mount as much of the instrument as possible to the same flange, and attach the various MS components to posts mounted off of that flange. The necessity of placing the QITMS on the cryostat complicated the situation. The final design mounted the QITMS on the cryostat, which is introduced into the chamber from the bottom.

The idea was to place the QITMS in the exact center of the x and y planes in Figure 3.4. The API source (Figure 3.5, described below) is mounted on a flange at a right angle to the cryostat, therefore care had to be taken to ensure that the ion beam from this source would intersect the center of the QITMS.

3.4.5. nano-Electrospary Ionization Source

The API source was modeled after the design of the Bruker Esquire and a QITMS donated from Monsanto. Currently this source is configured for nano-ESI, although AP-MALDI or other API techniques could be performed with modifications. A schematic of the inside of the source was given in Figure 2.1. A glass capillary with a metal cap on both ends is the interface between atmospheric pressure and the first stage of differential pumping. This first region is at a pressure of about 0.3 Torr. The ions formed by nano-ESI expand into the first region and are focused to the opening of a skimmer that is 0.70 mm in diameter. A

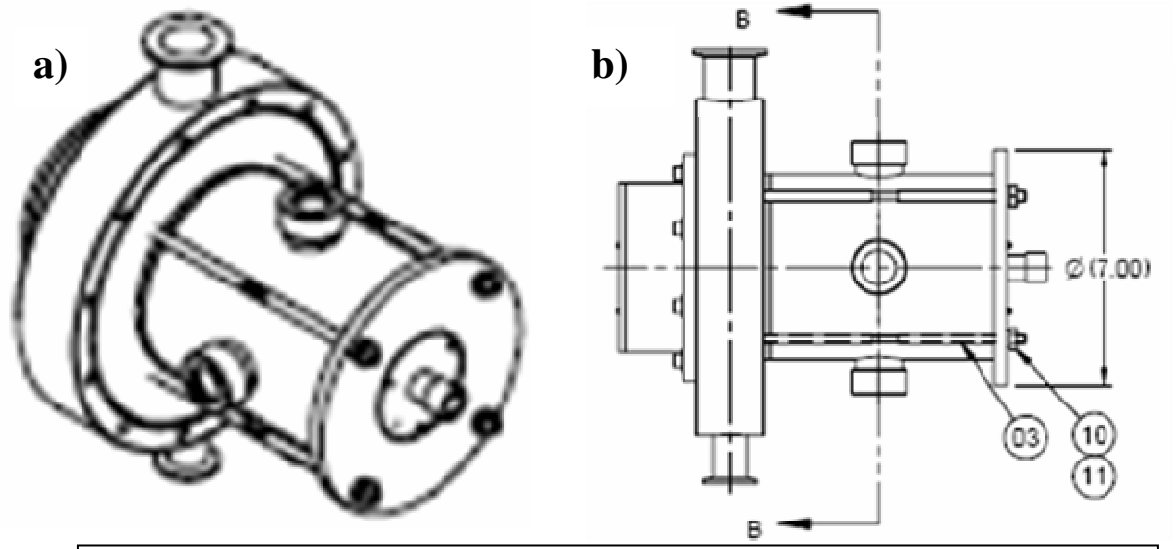

Figure 3.5. a) 3d rendering of nano-ESI source b) 2d side view of nano-ESI source. The region on the right contains the glass transfer capillary and is pumped by rough pumps to 0.3 Torr, and the region inside the 10" flange and to the left houses the octopole and is pumped by a turbo pump to 3 mTorr.

drawing showing the outside of the source is shown in Figure 3.5.a and .b. In Figure 3.5 the nano-ESI needle would be on the right side, and the ions pass to the QITMS which would be just on the left side.

3.4.6. Octopole Ion Guide

After the ions pass through the skimmer in the first pressure region, they expand into the second region of differential pumping. This region has a pressure of about 3 mTorr. Ion transmission through spaces of more than a few centimeters at these pressures is inefficient with static dc ion lenses. Multipole ion guides with rf voltages, in contrast, can transmit ions through these regions with efficiencies that approach 100%. Additionally, studies have shown that transmission increases as bath gas pressure is increased due to collisional

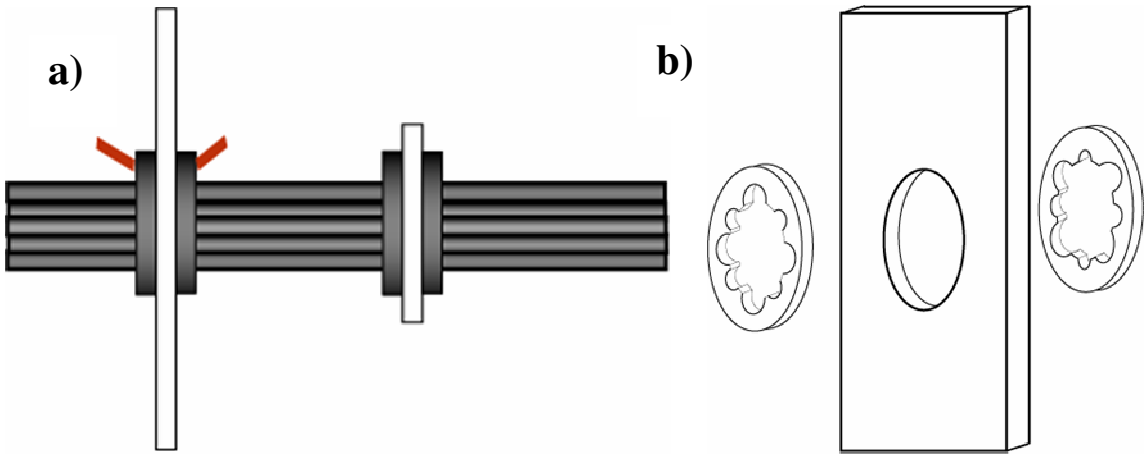

Figure 3.6. a) Side view of octopole ion guide b) detail of metal holders separated by machinable ceramic (should have used PEEK). Each metal holder is in contact with every other rod.

focusing of ions down to the center of the ion guide.[28] On the new instrument described in **Chapter 8**, the benefits of collisional focusing peak at 3-4 mTorr for peptides around 1000 Da, but proteins are transmitted better at lower pressures. Presumably this difference is because proteins have larger collisional cross sections and are more easily kinetically cooled.

The octopole ion guide design used in the IR-Trap is shown in Figure 3.6. Figure 3.6a shows a sideview of the rods, with alignment fixed at two points along the rods. Each point has a pair of metal holders shown in Figure 3.6b, each of which is affixed to opposite sets of four rods. Each metal holder has 8 holes for the rods, 4 smaller holes which contact the rods and 4 larger holes which do not contact the rods. A rf voltage is applied to the rods such that each rod has a signal 180 degrees out of phase of its neighbors. A pure octopolar field would be established in the space between all rods if they had a hyperbolic shape. Hyperbolic electrodes are difficult to machine, however, so circular rods are generally used instead. The best approximation to an octopolar field can be obtained with circular rods if the ratio of the rod radius (r) to the field radius (r_o) is 0.355.[29] No one has demonstrated, however, that this ratio gives optimum ion transmission. Two commercial octopoles in the Glish lab have ratios of 0.370 and 0.355, although some other values are in use.[30] The actual ratio used by commercial companies is usually a trade secret. Both octopoles designed for the experiments in this dissertation have $r/r_o = 0.355$, where r = 1.0 mm. The second, more robust, cheaper design is described in **Chapter 8**, and has r = 1.59 mm.

3.4.6.1. RF Oscillator

A home-built rf oscillator circuit, based on previous models[1], was designed in the UNC Electronics lab for supplying the high voltage to the octopole. The circuit is self-tuning, where the resonance frequency depends on the capacitance of the octopole, rf leads, and vacuum feedthroughs. The capacitance of these components is approximately 150 pF. With these conditions, the oscillator can output a maximum of 1200 V_{pp} at 970 kHz. Commercial instruments typically use higher frequencies (2-4 MHz) which confines the ions closer to the center axis, but higher frequency waveforms sacrifice maximum output voltage.

A tradeoff therefore exists between waveform frequency and voltage, however, enough ions can be transmitted with the current setup that further improvements are not necessary. In any case, sensitivity is not a major concern for the experiments planned for the IR-Trap. The general scheme of the oscillator circuit is shown in Figure 3.7. The fundamental operation of

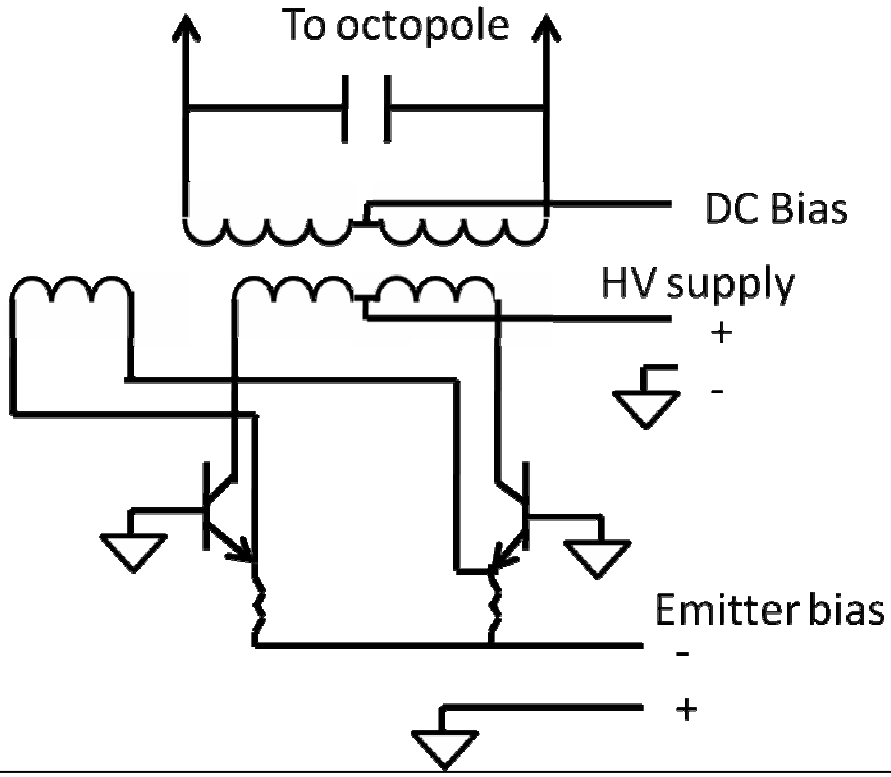

Figure 3.7. General schematic of octopole oscillator circuit.[1] Description in text.

the circuit is this: the two transistors turn on and off, effectively connecting the HV supply to ground or isolating it. The transistors operate in tandem, such that when one is open the other is closed and *vice versa*. The coil on the far left is the feedback loop that provides a signal 180 degrees out of phase with each collector so that oscillation is possible. The feedback coil alternately raises each emitter above the ground potential of the base, turning one transistor off, while lowering the other emitter below the ground potential of the base,

turning that transistor on. Where the circuit says "Emitter bias" there really is a transistor that acts as a variable resistor to change the amount of current flowing through the transistors, and thus control the output voltage amplitude. The secondary coil may be biased at a center tap to float the output voltage. The octopole dc bias is generally one of the most important voltages of an ESI instrument, because this potential referenced to the analyzer potential tends to set the kinetic energy of the ions, especially when the pressure in the octopole is high enough to collisionally cool the ions down to thermal velocities.

3.4.7. Electron Ionization Source

As described in **Chapter 2.1.3**, an EI source is invaluable for testing out the analyzer of a new instrument, and the same was true with the IR-Trap. To perform EI, the octopole ion guide in Figure 2.1 is replaced by the EI block of a TSQ 70, and the skimmer assembly is replaced by a flat piece of metal with no apertures, to seal off the EI region from atmosphere. A drawing of the EI source as it relates to the cryostat and analyzer is given in Figure 3.8. The base pressure in the EI region is 2.0×10^{-7} Torr as measured by a cold cathode gauge, and the base pressure in the main

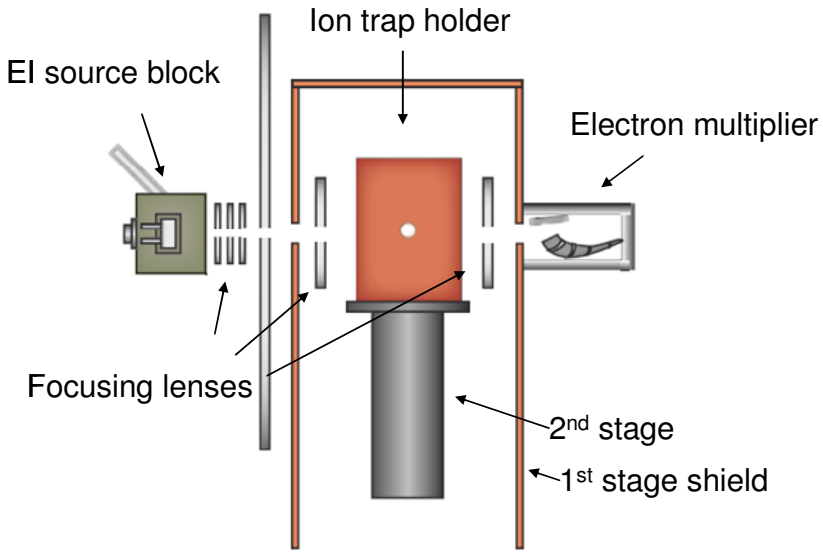

Figure 3.8 IR-Trap configured for EI. EI block from a Finnigan TSQ 70 replaces the octopole ion guide and is sealed off from atmosphere.

vacuum chamber is 8.8×10^{-8} Torr, as measured by a separate cold cathode gauge.

3.5. Operation of Instrument

3.5.1. Tuning the rf Circuit

Figure 3.9 is a diagram of the basic circuit for generating the trapping voltage for the IR-Trap. A constant-amplitude, 960 kHz sinewave is generated with a function generator. This signal is multiplied with a waveform representation of the scan function (**Chapter 2.3**) for the particular ion trap experiment. The resulting waveform is a sinewave with the scan function superimposed. This waveform is amplified from about 0.4 V to a few hundred volts and several amps by a broad-band, linear power amplifier. The gain in power is converted to

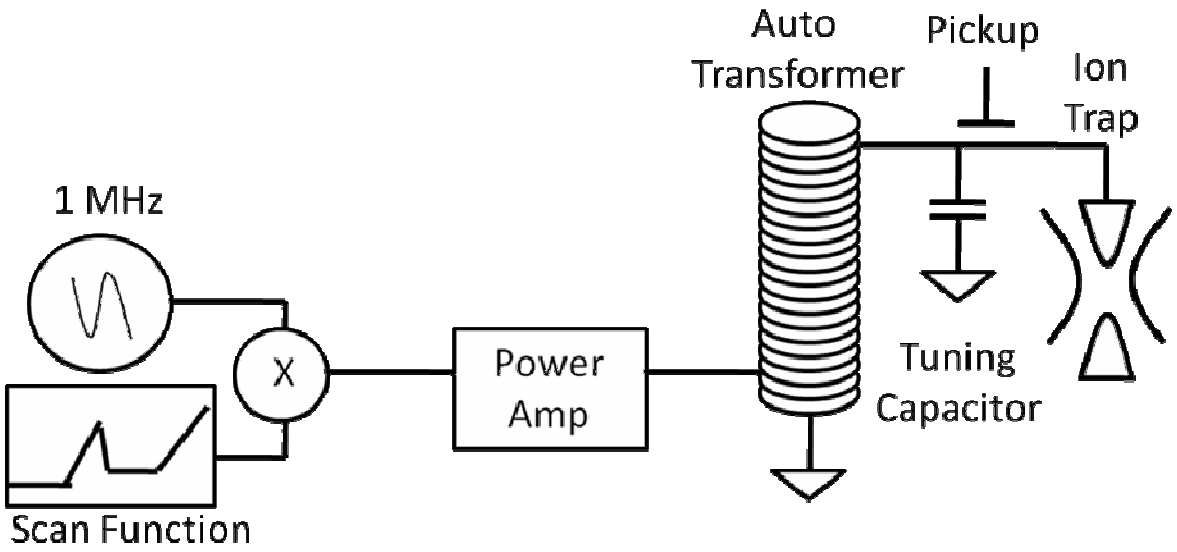

Figure 3.9. RF circuit for QITMS in open loop (no feedback) configuration.

a gain in voltage (loss in current) with a resonant LC circuit. Maximum waveform amplitudes of 7000 $V_{o\text{-}p}$ or more are obtained. The resonance frequency of the parallel LC circuit is set by the inductance (number of coil windings) and capacitance of the ion trap and tuning capacitors. Equation 1.7 for q_z value shows that for a given maximum voltage

amplitude, changing the frequency of the waveform changes the maximum ion mass-to-charge that may be analyzed. Lower drive frequencies allow a higher mass-to-charge range. Higher frequencies are only suitable for a lower mass-to-charge range but give better resolution, so there is a trade-off in choosing a drive voltage frequency.

The capacitive "pickup" in Figure 3.9 is used to monitor a representation of the output voltage amplitude. Especially at very high amplitudes, special probes are needed to monitor the voltage, therefore a calibration of actual voltage to "pickup voltage" is made at low output amplitude, so that at high voltages, the actual output can be estimated. A capacitive pickup is used in commercial systems to provide feedback for stabilizing the output amplitude as temperature fluctuations cause circuit parts to swell, altering circuit impedance. A stable output is required for high mass accuracy and mass resolution, however, the current system, which is open loop, performs reasonably well (resolving power of 700 at 1000 *m/z*) once it has warmed up.

In MS systems that use only one permanent drive frequency, the LC circuit must be tuned to the correct frequency by means of adjusting the capacitance and number of coil turns. The system in Figure 3.9 is advantageous in that the coil can be tuned to any desired frequency, and the function generator parameters can be changed as needed to give a resonance condition. Although the frequency of maximum output (as measured at low voltage with a variable frequency function generator) can be used to drive the trap, in reality higher maximum outputs can be obtained at slightly different frequencies. This is because the resonant frequency does not necessarily optimize power transfer from the power amplifier to the coil. Reflected power begins to be a problem at higher outputs when there is a mismatch in coil and power amplifier impedances. An impedance analyzer can be used to

characterize the impedance of the coil. The frequency that gives a coil impedence of 50 Ω is the best, as this is the output impedance of the power amplifier. When the coil is driven at high voltage, further frequency optimization can be done by monitoring reflected power, if the power amplifier has a suitable meter.

3.5.2. Calibrating the Mass-to-Charge Scale

Once the rf circuit parameters are set, the scan-function input to voltage output relationship should be ascertained. At any particular output, Equation 1.7 can be used to calculate the ion mass-to-charge that will be ejected. A calibration of dc control voltage versus requested ion mass-to-charge can then be made, which is referred to as the *instrument calibration* in the IR-Trap software. Often the first calibration equation, made from the capacitive pickup to actual voltage calibration, will be slightly off, and there are two methods to make adjustments in the software; a local calibration, and a global calibration.

The global-calibration program compiles a peak list of observed ion mass-to-charge values, converts to the dc control voltages used to eject those ions, and plots them versus the theoretical ion mass-to-charge. The slope m and intercept b of the best fit line to this data is the instrument calibration that gives the best average mass accuracy across a broad mass-to-charge scale. The local calibration program optimizes the instrument calibration for one particular ion mass-to-charge, which is useful for making small adjustments as the circuit heats up and stabilizes. When running CID experiments for a long period of time, the secular frequency of the parent ion needs to stay constant, otherwise there is difficulty comparing spectra taken at different times. The local calibration is done using Equation 3.9, where $m_{new,}$ m_{old}, $mass_{obs}$, and $mass_{theory}$ are the new and old instrument calibration slopes, and observed

and theoretical peak positions, respectively. A similar equation using the new and old *b* is also used, ie. instrument calibration y intercept.

$$m_{new} = m_{old} * \left(\frac{mass_{obs}}{mass_{theory}}\right) \quad \text{(Equation 3.9)}$$

The current circuit parameters and calibration give a maximum analyzed ion mass-to-charge of 600 *m/z* with ejection at q_z 0.908.

3.5.3. "Finding" Ions

Ions are produced in the manner described in **Chapter 2.1** for nano-ESI and EI. During the initial testing portion of the instrument, when the correct parameters for trapping ions were not known, simplification of the instrument tuning process was useful. A valuable technique was to disable the rf voltage on the ring electrode and find the conditions to pass ions through the trap to the electron multiplier. Although the conditions to pass ions through the trap and the conditions to optimally trap ions are not necessarily the same, the former can be a good starting point for the latter. This procedure is largely unnecessary now, but still valuable for troubleshooting.

3.6. Computer Control of Instrument

3.6.1. Summary of Control Software

The software to control the IR-Trap was written jointly with Desmond Kaplan. A thorough description of the rationale and inner workings of the instrumentation software written for ion traps in the Glish lab was documented.[31] Kaplan had written experimental design and control software for a previous instrument, and applied the lessons from that experience to the experimental design software of the IR-Trap. Wanting to understand how these instruments were controlled but not as versed in programming, the author of this dissertation was in charge of the instrument control software, which required less knowledge

of syntax. A brief, broad description of instrument control software will be presented here, that supplements Kaplan's dissertation. This description is useful for understanding the general idea of the program, or for outlining the general structure of a new instrument control program.

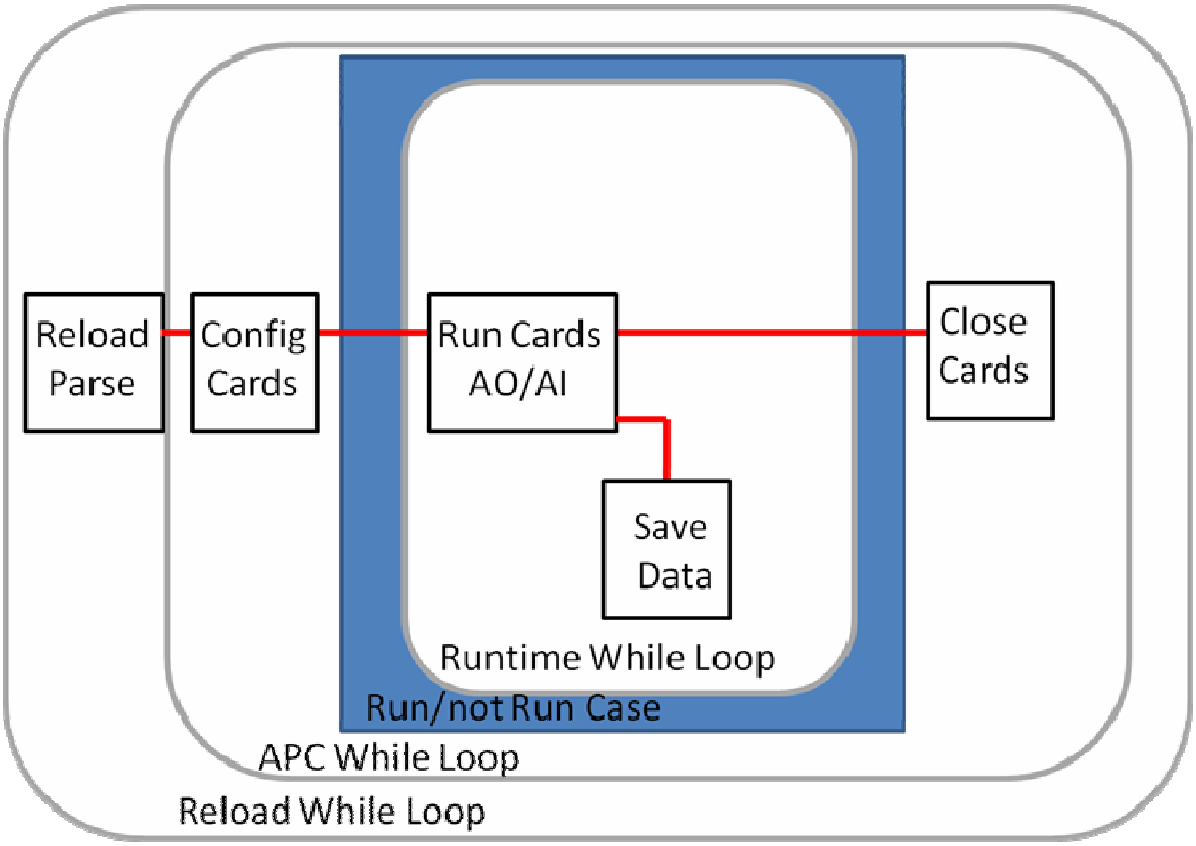

Figure 3.10. Structure of instrument control program for IR-Trap. Description in text below.

Figure 3.10 is a schematic of the instrument control program, using shapes similar to the National Instruments G programming language in which the software was written. The program is composed of three main while loops, which continue running as long as certain conditions are met. The first loop, the "Reload While Loop," is where data from global variables are used to create the scan function and parse the values into the appropriate format. The next loop is the "APC While Loop," where APC stands for automatic parameter

changing. This loop is used when the user wishes to run several experiments in a row while incrementing a certain parameter, such as excitation voltage, start mass, or the time of a process. As detailed by Kaplan, the APC function will average a certain number of spectra, increment the parameter, and continue for a given number of steps. The APC functions are in a loop only to have an extra counter for each set of spectra. At the end of each step, the APC loop is stopped, the Reload loop brings the new scan function parameters into memory, and the APC loop starts over again from zero. The addition of the APC loop to the program allows setting without ending the entire program. Finally, the "Run" button in the user interface allows the third "Runtime While Loop" to output the correct voltages and acquire spectra continuously. The hardware does not need to be reset after each scan because the card functions all run off the same timing clock.

3.6.2. Interface with PPLN-OPO

The APC function allows incrementing any experimental parameter. However, the main purpose of the IR-Trap was to run in concert with the tunable PPLN-OPO. As described in **Chapter 1.3.1** and **Chapter 3.2**, IR action spectroscopy monitors the fragmentation efficiency of an ion as a function of excitation frequency. A "handshaking" routine was programmed into the IR-Trap APC software to facilitate this experiment. The routine is: At a particular laser wavelength, the IR-Trap takes a certain number of spectra and averages them, and then sends a signal of 5V to a digital line monitored by the PPLN laser software. The PPLN software would scan to a new laser frequency and then send a 5V signal on a digital line monitored by the IR-Trap. This process repeats until the entire range of laser frequencies is scanned. There are two spare analog input lines that could be used to read a signal corresponding to the PPLN-OPO wavelength and save this value in the spectrum. An

additional data storage mode was created for action spectroscopy as well, whereby instead of saving hundreds or thousands of spectra, fragmentation efficiency at each wavelength is saved, which drastically reduces file size.

3.6.3. Data Workup

One problem with APC files, and spectra files in general, is that they can require a lot of computer memory to store. Anything a programmer can do to decrease the size of the stored files is advantageous to computer performance. One way to cut the size of files by one half is to store them as 32 bit signed integer values instead of 64 bit double precision values. When one wishes to analyze the data, the integer values are converted to double precision values with a polynomial transformation as described below. Double precision values can be written as in Equation 3.10, where *DB* is double precision value, *I* is an integer value, and *a, b, c,* and *d* are constants.

$$DB = aI^3 + bI^2 + cI + d \qquad \text{(Equation 3.10)}$$

To convert double precision numbers to integers, the roots of Equation 3.10 are computed and the first real root is stored. The scaling values *a*, *b*, *c*, and *d* are computed by the hardware driver such that this root will always be an integer.

3.6.4. IR Spectra

As described further in **Chapter 4**, the collisional cooling effect of He bath gas is significant in a QITMS, necessitating higher power lasers for dissociation than FT-ICR instruments. An attempt was made to acquire IR action spectra using the two-color method with a 30 mW, cw, commercial PPLN-OPO laser and the CO_2 laser, but no resonant dissociation was observed. We expect that the two order of magnitude increase in power afforded by the Miller lab PPLN-OPO lasers would be able to get better results. As a last

resort, ambient temperature spectra might be acquired using the 30 mW laser through the use of pulsing gas into the QITMS for injection and analysis and pumping out the gas for dissociation. This scheme was demonstrated on our system to decrease laser power requirements for dissociation by 2 fold.[32]

3.7. Summary

A QITMS for doing low temperature IR action spectroscopy has been built. The QITMS is enclosed in a copper box on top of a closed cycle helium cryostat. This system currently allows the ion trap holder and electrodes to reach a low temperature of 23 K. Mass spectra can be acquired using nano-ESI and EI over the range of possible temperatures from 23 K to 330 K. Presently the instrument is interfaced with a CO_2 laser for future implementation of the two-color resonant excitation scheme, but non-resonant IRMPD are possible at this time. Two studies utilizing IRMPD and CID on the "IR-Trap" will be described next in **Chapters 4 and 5.** Unfortunately, IR action spectra have not been acquired due to difficulties with the PPLN-OPO laser. With a working PPLN-OPO laser, high quality IR action spectra should be possible.

3.8. References

1. O'Conner, P. B. C., Catherine E.; Earle, William E. *A High Voltage RF Oscillator for Driving Multipole Ion Guides*. J Am Soc Mass Spectrom **2002**.

2. Vachet, R. W.; Asam, M. R.; Glish, G. L. *Secondary Interactions Affecting the Dissociation Patterns of Arginine-Containing Peptide Ions*. J. Am. Chem. Soc. **1996,** *118*, 6252-6256.

3. Vachet, R. W.; Winders, A. D.; Glish, G. L. *Correlation of Kinetic Energy Losses in High-Energy Collision-Induced Dissociation with Observed Peptide Product Ions*. Anal. Chem. **1996,** *68*, 522-526.

4. Vachet, R. W.; Bishop, B. M.; Erickson, B. W.; Glish, G. L. *Novel Peptide Dissociation: Gas-Phase Intramolecular Rearrangement of Internal Amino Acid Residues*. J. Am. Chem. Soc. **1997,** *119*, 5481-5488.

5. Mac Aleese, L.; Simon, A.; McMahon, T. B.; Ortega, J.-M.; Scuderi, D.; Lemaire, J.; Maitre, P. *Mid-IR spectroscopy of protonated leucine methyl ester performed with an FTICR or a Paul type ion-trap*. Int. J. Mass Spectrom. **2006,** *249/250*, 14-20.

6. Fukui, K.; Takada, Y.; Sumiyoshi, T.; Imai, T.; Takahashi, K. *Infrared Multiphoton Dissociation Spectroscopic Analysis of Peptides and Oligosaccharides by Using Fourier Transform Ion Cyclotron Resonance Mass Spectrometry with a Midinfrared Free-Electron Laser*. Journal of Physical Chemistry B **2003,** *110*, 16111-16116.

7. Chiavarino, B.; Crestoni, M. E.; Fornarini, S.; Dopfer, O.; Lemaire, J.; Maitre, P. *IR Spectroscopic Features of Gaseous C7H7O+ Ions: Benzylium versus Tropylium Ion Structures*. Journal of Physical Chemistry A **2006,** *110*, 9352-9360.

8. Polfer, N. C.; Oomens, J.; Dunbar, R. C. *IRMPD spectroscopy of metal-ion/tryptophan complexes*. Physical Chemistry Chemical Physics **2006,** *8*, 2744-2751.

9. Putter, M.; von Helden, G.; Meijer, G. *Mass selective infrared spectroscopy using a free electron laser*. Chem. Phys. Lett. **1996,** *258*, 118-122.

10. von Helden, G.; Holleman, I.; Putter, M.; Meijer, G. *IR spectroscopy on gas-phase molecules with a free electron laser*. Nucl. Instrum. Methods Phys. Res., Sect. B **1998,** *144*, 211-217.

11. Oomens, J.; Meijer, G.; Helden, G. v. *Gas Phase Infrared Spectroscopy of Cationic Indane, Acenaphthene, Fluorene, and Fluoranthene*. J. Phys. Chem. A **2001,** *105*, 8302-8309.

12. Oomens, J.; Roij, A. J. A. v.; Meijer, G.; Helden, G. v. *Gas-Phase Infrared Photodissociation Spectroscopy of Cationic Polyaromatic Hydrocarbons*. The Astrophysical Journal **2000,** *542*, 404-410.

13. Thompson, C. D.; Emmeluth, C.; Poad, B. L. J.; Weddle, G. H.; Bieske, E. J. *Rotationally resolved infrared spectrum of the Li+-D2 cation complex*. Journal of Chemical Physics **2006,** *125*, 044310/1-044310/5.

14. Loh, Z. M.; Wilson, R. L.; Wild, D. A.; Bieske, E. J.; Gordon, M. S. *Infrared Spectra and ab Initio Calculations for the Cl--(CH4)n (n = 1-10) Anion Clusters*. Journal of Physical Chemistry A **2005,** *109*, 8481-8486.

15. Wilson, R. L.; Loh, Z. M.; Wild, D. A.; Thompson, C. D.; Schuder, M. D.; Lisy, J. M.; Bieske, E. J. *Infrared spectra of the Cl--C2H4 and Br--C2H4 anion dimers*. Physical Chemistry Chemical Physics **2005,** *7*, 3419-3425.

16. van Herpen, M. M. J. W.; Li, S.; Bisson, S. E.; te Lintel Hekkert, S.; Harren, F. J. M. *Tuning and stability of a continuous-wave mid-infrared high-power single resonant optical parametric oscillator*. Applied Physics B: Lasers and Optics **2002,** *75*, 329-333.

17. Knippels, G. M. H.; van der Meer, A. F. G.; Mols, R. F. X. A. M.; Oepts, D.; van Amersfoort, P. W. *Formation of multiple subpulses in a free-electron laser operating in the limit-cycle mode*. Physical Review E: Statistical Physics, Plasmas, Fluids, and Related Interdisciplinary Topics **1996,** *53*, 2778-86.

18. Asmis, K. R.; Meijer, G.; Brummer, M.; Kaposta, C.; Santambrogio, G.; Woste, L.; Sauer, J. *Gas phase infrared spectroscopy of mono- and divanadium oxide cluster cations*. Journal of Chemical Physics **2004,** *120(14)*, 6461-6470.

19. Brummer, M.; Kaposta, C.; Santambrogio, G.; Asmis, K. R. *Formation and photodepletion of cluster ion-messenger atom complexes in a cold ion trap: Infrared spectroscopy of VO+, VO2+, and VO3+*. Journal of Chemical Physics **2003,** *119*, 12700-12703.

20. Asmis, K. R.; Pivonka, N. L.; Santambrogio, G.; Bruemmer, M.; Kaposta, C.; Neumark, D. M.; Woeste, L. *Gas-Phase Infrared Spectrum of the Protonated Water Dimer*. Science **2003,** *299*, 1375-1377.

21. Payne, A. H.; Glish, G. L. *Thermally Assisted Infrared Multiphoton Photodissociation in a Quadrupole Ion Trap*. Anal. Chem. **2001,** *73*, 3542-3548.

22. Yeh, L. I.; Okumura, M.; Myers, J. D.; Price, J. M.; Lee, Y. T. *Vibrational spectroscopy of the hydrated hydronium cluster ions H3O+.(H2O)n (n = 1, 2, 3)*. Journal of Chemical Physics **1989,** *91*, 7319-30.

23. Yeh, L. I.; Price, J. M.; Lee, Y. T. *Infrared spectroscopy of the pentacoordinated carbonium ion C2H7+*. J. Am. Chem. Soc. **1989,** *111*, 5597-604.

24. Black, J. G.; Yablonovitch, E.; Bloembergen, N. *Collisionless Multiphoton Dissociation of SF6: A statistical thermodynamic process*. Phys. Rev. Lett. **1977,** *38*.

25. Grant, E. R.; Schulz, P. A.; Sudbo, A. S.; Shen, Y. R.; Lee, Y. T. *Is Multiphoton Dissociation of Molecules a Statistical Thermal Process?* Phys. Rev. Lett. **1978,** *40*, 115-118.

26. Zhao, J.; Zhang, R. *Proton Transfer Reaction Rate Constants Between Hydronium Ion (H_3O^+) and Volatile Organic Compounds*. Atmospheric Environment **2004,** *38*, 2177-2185.

27. Moore, J. H.; Davis, C. C.; Coplan, M. A. *Building Scientific Apparatus*; Westview Press: Boulder, Co, 2003.

28. Douglas, D. J.; French, J. B. *Collisional Focusing Effects in Radio-Frequency Quadrupoles*. J. Am. Soc. Mass Spectrom. **1992,** *3*, 398-408.

29. Rao, V. V. K. R.; Bhutani, A. *Electric hexapoles and octopoles with optimized circular section rods*. Int. J. Mass Spectrom. **2000,** *202*, 31-36.

30. Wilcox, B.; Hendrickson, C. L.; Marshall, A. G. *Improved Ion Extraction from a linaer Octopole Ion Trap: SIMION analyisis and Experimental Demonstration*. J. Am. Soc. Mass Spectrom. **2002,** *13*, 1304-1312.

31. Kaplan, D. A. Improvements to the Analytical Performance of Ion Trap Mass Spectrometry. University of North Carolina, Chapel Hill, 2006.

32. Remes, P. M.; Ferzoco, A. L.; Glish, G. L. A Low Temperature Quadrupole Ion Trap for IRMPD and Laser Spectroscopy Experiments. Seattle, WA, 2006.

Chapter 4

4. Collisional Cooling in a Quadrupole Ion Trap at Sub-Ambient Temperatures

4.1. Introduction

4.1.1. The Quadrupole Ion Trap as a High Pressure Instrument

Since the development of the quadrupole ion trap as a commercial instrument, helium gas (He) has been introduced into the trapping volume at a relatively high pressure (~1 mTorr) to damp the ions' kinetic energy.[1] The high pressure of neutral gas in a quadrupole ion trap makes it unique among mass analyzers in that the ion/neutral collision frequency is quite high; it has been estimated at 20 collisions per millisecond during normal storage conditions.[2] As described in **Chapter 1.2.1.1**, the initial goals of kinetic energy damping on ion trap performance were increased mass resolving power and increased sensitivity. The addition of external ion sources to ion traps allowed for the analysis of high molecular weight ions produced by ESI[3] and MALDI.[4-6] However, to trap the injected ions, collisional damping, and thus the helium bath gas, is necessary.

While the objective of adding the bath gas is to reduce the kinetic energy of an ion, the internal energy of the ion is also affected such that during normal storage periods it may be described by a Boltzmann distribution at the temperature of the bath gas.[7-11] Whenever an ion is activated, such as during CID[12-14] or IRMPD[15-18], a simultaneous collisional de-excitation process acts to cool the ion back down to thermal internal energy. It has been proposed that the average internal temperature decrease per collision increases as the ion is

activated above the temperature of the bath gas.[19] The collisional cooling rate constant has been measured previously for the peptide leucine enkephalin at a series of trapping pressures and temperatures, at or above ambient temperature.[20] The pseudo first-order rate constant for ambient temperature and 1 mTorr He was 400 s^{-1}. This cooling process has been shown to effectively compete with activation by IRMPD; thus, many larger ions such as peptides are difficult to dissociate under normal operating conditions.[15]

4.1.2. Perceived Challenges of Low Temperature Operation for IRMPD Spectroscopy

A quadrupole ion trap instrument was recently built in our lab for the purpose of doing IRMPD spectroscopy experiments at low (<100 K) temperatures (**Chapter 3**). One of the important questions in the design of this instrument was to what extent collisional cooling would limit the ability to perform experiments at these low temperatures. The fact that trapped ions equilibrate with the He bath gas is simultaneously an advantage and a disadvantage: low ion internal temperatures can be reached, which is favorable for spectroscopy, at the price of higher collisional cooling rates and thus a need for greater laser powers to effect dissociation. The purpose of this work is to quantify the effect of collisional cooling at sub-ambient temperatures. To this end, two experiments were performed. The first experiment demonstrates the relationship between the energy required for dissociation and ion temperature. Naturally, as the temperature of the ion decreases, the amount of input energy required to reach a given internal energy will increase. It is not immediately obvious, however, if the input energy to temperature relationship should be linear, or follow some other dependence. Therefore, fragmentation efficiency curves showing the extent of dissociation versus CID voltage were obtained for various peptide ions at a series of low trap temperatures. The second experiment quantifies the collisional cooling rate constant for the

ion n-butylbenzene at a series of low trap temperatures. The two experiments are then compared and the input energy required to reach a certain internal energy can be correlated with collisional cooling rate constant.

4.2. Methods

Experiments were performed on the home-built QITMS designed for laser spectroscopy applications. The details of this instrument are discussed **Chapter 3**. The protonated molecules of the peptides GHK, YGGFL and FLLVPLG were produced by nano-ESI as in **Chapter 2.1.1.** The molecular ion of n-butylbenzene was produced by EI as in **Chapter 2.1.3**. YGGFL, GHK, and n-butylbenzene were purchased from Sigma Aldrich (St. Louis) and FLLVPLG was custom synthesized by Bayer Corp. All samples were used without any further purification.

Collisional cooling rates were measured for n-butylbenzene by the two-pulse method described by Dunbar and coworkers.[21] After equilibrating with the He bath gas, the ions are irradiated by two 3 ms pulses from the CO_2 laser, separated by a variable delay time. The delay time between laser pulses was increased sequentially from 0 ms to a time great enough for the ions to finish cooling, generally a time between 4 and 50 ms, depending on He pressure. The cooling time was varied automatically from spectrum to spectrum under computer control. The experimental timing diagram is shown in Figure 4.1a. A mass spectrum is obtained at each of a series of cooling times, and fragmentation efficiency is plotted as a function of cooling time as in Figure 4.1b. Fragmentation efficiency is defined in Equation 1.12. The collisional cooling rate can be found by fitting the fragmentation efficiency plot to an exponential decay, which will be discussed in more depth in the following theoretical section. The laser power is set such that when the variable cool time is

0, fragmentation efficiency is ~50%. Setting a constant initial fragmentation efficiency ensures that ions are relaxing from a constant maximum internal energy level. Each recorded spectra was the average of 25 scans. Each curve in the data reported here is the average of 15 separate experiments, and error bars are calculated as 95% confidence intervals.

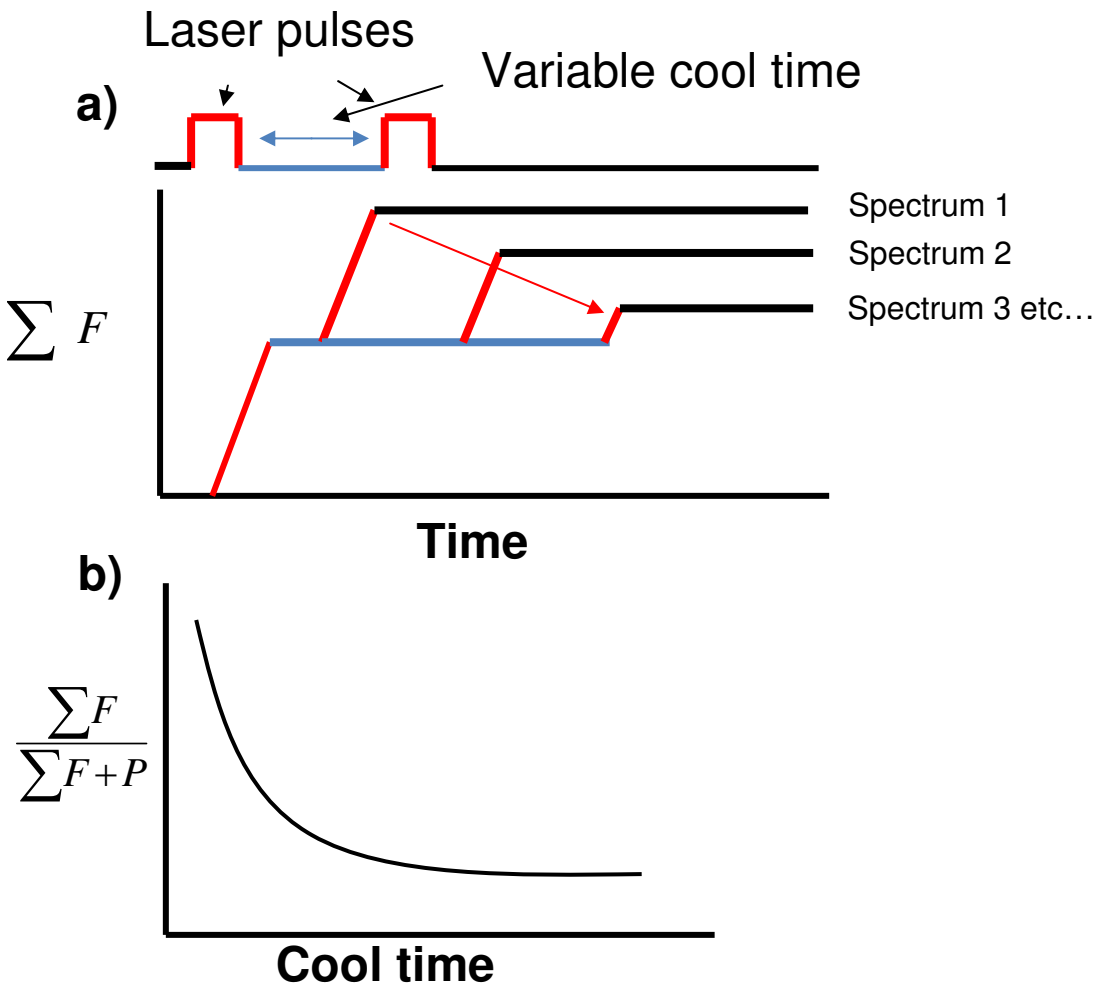

Figure 4.1. a) Experimental timing diagram for determination of collisional cooling rate constant b) theoretical cooling curve showing fragmentation efficiency decreasing as cooling time is increased.

CID is performed as described in **Chapter 1.2.1.4.2** and **2.3.1**. Plots of fragmentation efficiency versus excitation voltage were obtained at various trap temperatures, at an estimated He pressure of 3 mTorr. The excitation voltage applied to the endcap electrodes was varied under computer control such that spectra were recorded with fragmentation efficiencies from 0 to 100%. Each recorded spectrum was the average of 40 scans, and 6 separate experiments were averaged to produce each fragmentation efficiency curve.

Because the trapping volume is enclosed in a conductance limiting copper box, the He pressure in the trapping volume is higher than what is measured by the pressure gauge. A relation between the trapping volume pressure and main chamber pressure was established by comparing collisional cooling rates at two experimental conditions: the rates when the electrodes were enclosed were compared to those rates measured with the electrodes not enclosed (tops of boxes removed). The correction factor is approximately 14 times the pressure read on the pressure gauge (times an additional x7 factor for gauge sensitivity for He). This experiment was done at ambient temperature, therefore at lower temperatures the pressure inside the copper box is likely different. However, the collision frequency of ions and He is quite possibly not changed (Equation 1.1), because the increase in He density is offset by a decrease in He velocity. The decrease in He velocity is significant, because experiments with SIMION have shown that the ion kinetic energy during normal storage conditions is very close to thermal kinetic energy. As temperature is decreased, mass spectra resolution and sensitivity do not change noticeably, supporting the hypothesis that the collision frequency is constant. In any case, the pressures reported herein are those values measured at the cold cathode gauge and adjusted by x98.

4.3. Theory

4.3.1. Energy Transfer Mechanisms

The possible mechanisms of energy transfer in the IR activation experiment have been described before [19, 20] and are outlined in the following equations, where M^+ is the singly charged parent ion, M^{+*} is the activated parent ion, and He is helium bath gas.

$$M^+ + He \xrightarrow{k_{CA}} M^{+*} + He \qquad \text{(Equation 4.1)}$$

$$M^+ + h\upsilon \xrightarrow{k_{ir}} M^{+*} \qquad \text{(Equation 4.2)}$$

$$M^{+*} + He \xrightarrow{k_{ccool}} M^+ + He \qquad \text{(Equation 4.3)}$$

$$M^{+*} \xrightarrow{k_{radiative}} M^+ + h\upsilon \qquad \text{(Equation 4.4)}$$

$$M^{+*} \xrightarrow{k_{dissociation}} products \qquad \text{(Equation 4.5)}$$

The total rate of change of M^{+*} is the summation in Equation 4.6, where the rate constants, k_{CA}, k_{IR}, k_{ccool}, $k_{radiative}$, and $k_{dissociation}$ respectively refer to the rates of collisional activation, infrared activation, collisional cooling, radiative emission, and unimolecular dissociation.[20]

$$\frac{d[M^{+*}]}{dt} = k_{CA}[M^+][He] + k_{IR}[M^+][h\upsilon] - k_{ccool}[M^{+*}][He] - k_{radiative}[M^{+*}] - k_{dissociation}[M^{+*}]$$

(Equation 4.6)

Two energy transfer processes may be disregarded for the present experiments; the rate of collisional activation and the rate of radiative emission. The collisional activation rate is zero because no resonance excitation is used and the ions are allowed to reach equilibrium kinetic/internal energy levels before being photoexcited. The radiative emission rate constant for n-butylbenzene has been measured previously as being 0.97 s^{-1}. [22] This rate constant is 2-

4 orders of magnitude smaller than the collisional cooling rate constants obtained in the present study, and can thus be ignored. During the two laser excitation pulses, the change in $[M^{+*}]$ is then given in Equation 4.7.

$$\frac{d[M^{+*}]}{dt} = k_{IR}[M^{+}][h\upsilon] - k_{ccool}[M^{+*}][He] - k_{dissociation}[M^{+*}] \qquad \text{(Equation 4.7)}$$

4.3.2. Relationship Between Population of Excited Ions and Fragmentation Efficiency

The two-pulse method uses the second laser pulse to gauge the rate of cooling occurring between the laser pulses, where collisional cooling is the only significant energy transfer process taking place. With no cooling time between the two pulses, the ion will reach a certain maximum internal energy and a corresponding maximum level of dissociation. As the two pulses are separated more in time, the M^{+*} population is depleted through collisional cooling, and the number of fragments formed decreases. Monitoring fragmentation efficiency is therefore a way of following the evolution in $[M^{+*}]$. The collisional cooling rate is subsequently given by Equation 4.8, and the pseudo first-order rate constant is given by Equation 4.9.

$$\frac{d[M^{+*}]}{dt} = -k_{ccool}[M^{+*}][He] \qquad \text{(Equation 4.8)}$$

$$k'_{ccool} = k_{ccool}[He] \qquad \text{(Equation 4.9)}$$

$$\frac{[M^{+*}]}{[M_o^{+*}]} = e^{-k_{ccool}\cdot[He]\cdot t} \qquad \text{(Equation 4.10)}$$

Equation 4.8 describes an exponential decay process of the form of Equation 4.10. $[M_o^{+*}]$ is the initial population of activated ions and *t* is cooling time. Fragmentation efficiency is being taken as a measure of $[M^{+*}]$, therefore plots of $\frac{FE}{FE_o}$ were fit to an exponential decay

equation and the rate constant was obtained from the curve of best fit. FE_o is fragmentation efficiency at zero cooling time.

4.4. Results and Discussion

4.4.1. Experimental Determination of Activation Energy Required to Reach a Constant Internal Energy as Temperature Decreases by CID

Plots of fragmentation efficiency versus CID excitation voltage for protonated YGGFL are shown in Figure 4.2a. When the CID voltage required to reach 50% fragmentation efficiency (a constant internal energy) is plotted versus ion trap temperature, the exponential shaped curves shown in Figure 4.2b are obtained for the three peptides studied. The exponential decay fitting parameters for the data in Figure 4.2b are given in Table 4.1.

Table 4.1. Parameters for exponential fit to $y = y_o + A \cdot e^{-Temp\,/\,B}$

Species	y_o	A	B	R^2
GHK	0.60	1.99	71.2	0.998
YGGFL	0.95	3.2	68.8	0.996
FLLVPLG	1.12	3.92	62.6	0.998

These curves follow a trend according to the size of the peptide investigated; the smallest peptide, GHK, requires the least voltage to dissociate at all temperatures, and has the smallest slope, while the biggest peptide, FLLVPLG, requires the most voltage to dissociate, and has the largest slope. This trend makes sense in the RRKM statistical dissociation model, where a larger ion will have more modes to distribute internal energy into, and thus require more energy input to dissociate. When these curves were normalized for degrees of freedom in Figure 4.2c, the curves for the smaller peptides overlap, while the curve for

FLLVPLG is slightly lower than the other two. This result is anticipated based on the slow time frame of CID activation, which allows energy to be randomized throughout the ion. Naturally it is expected that as ion temperature is decreased the energy required for dissociation increases. However, the fact that the curves in Figure 4.2b are exponential at

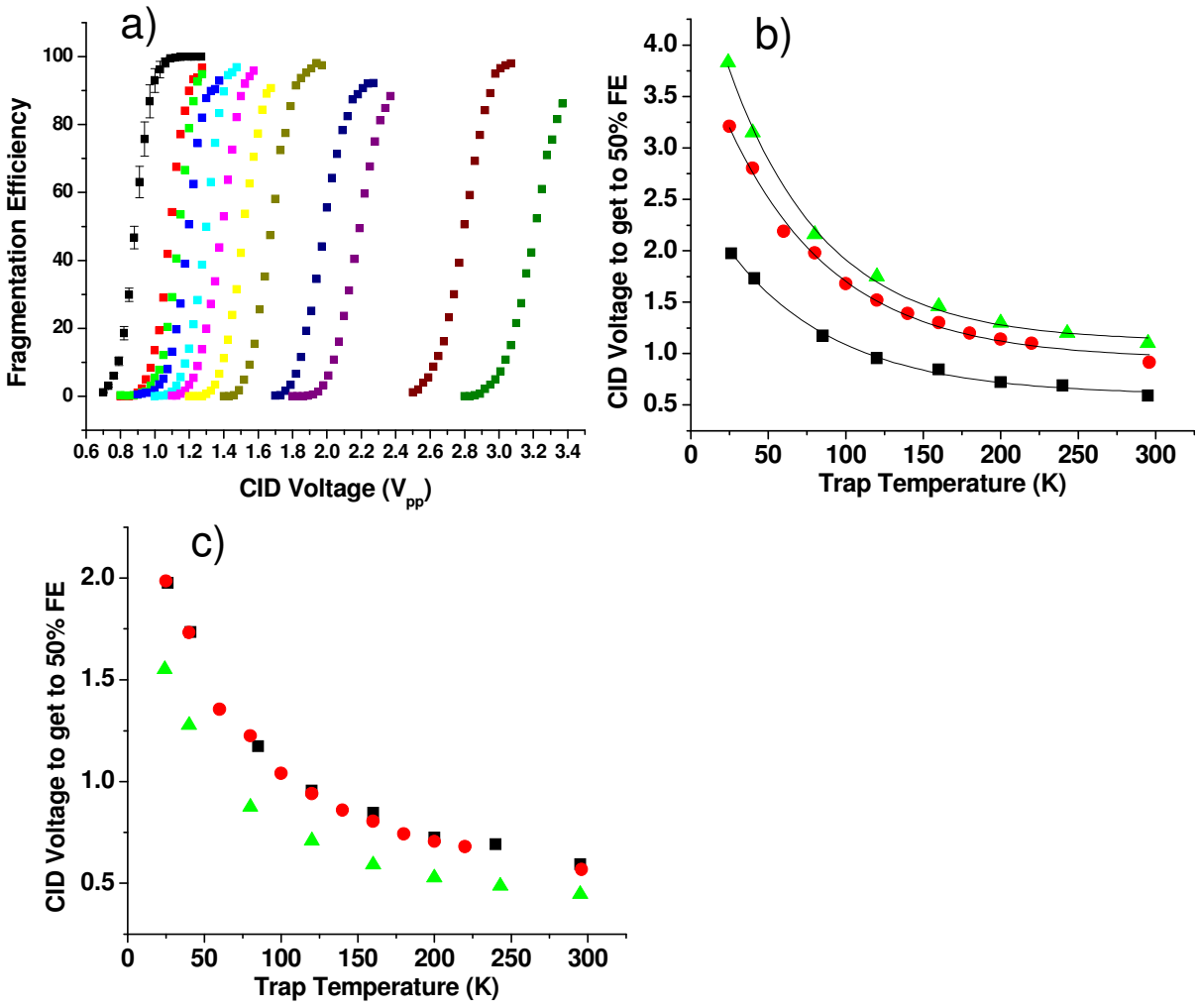

Figure 4.2. a) Fragmentation efficiency curves for $[YGGFL+H]^+$ at various trap temperatures from 295 K (left side) to 25 K (right side). Error bars are included in only the 295 K data to show typical reproducibility. b) CID voltage required to reach a constant fragmentation efficiency (a constant internal energy) at various trap temperatures. Squares are for $[GHK+H]^+$, circles for $[YGGFL+]^+$, and triangles for $[FLLVPLG+H]^+$, and the black line is an exponential decay fit to the data. c) Data in (b) normalized for degrees of freedom.

very low temperatures is not expected. Previous studies have shown a relatively linear relationship of CID voltage to internal energy gain [23].

4.4.2. Experimental Determination of Energy Required to Reach a Constant Internal Energy as Temperature Decreases by CID

Internal energy considerations actually suggest that the slope of the curves in Figure 4.2b should get less steep at very low temperatures. The latter point is demonstrated in Figure 4.3, where the average internal energy for n-butylbenzene molecular ion is plotted in the solid line as a function of ion internal temperature using Equation 2.2 for temperatures from 10 K to 900 K. Density of states were calculated by the established procedure[24] using vibrational frequencies calculated at the B3YLP/6-31G(d) level in Gaussian 03.[25] At lower internal temperatures, a small input of energy results in a larger increase in internal temperature. This is because at lower internal temperatures there are fewer states throughout which to distribute energy, and so the effective temperature of the ion changes faster. Density of states increases very quickly with ion internal temperature, so that at higher internal temperatures there are more ways to distribute energy throughout the ion. The result is a slower increase in effective temperature with energy input. The red, dashed line in Figure 4.3 shows the shape that might be expected for CID voltage versus ion trap temperature, based on the above argument. The red dashes assume 860 K as the critical dissociation *temperature* (the onset of parent ion fragmentation) and denote the internal energy that needs to be added to the ion to reach the critical dissociation *energy* of 1.9 eV.

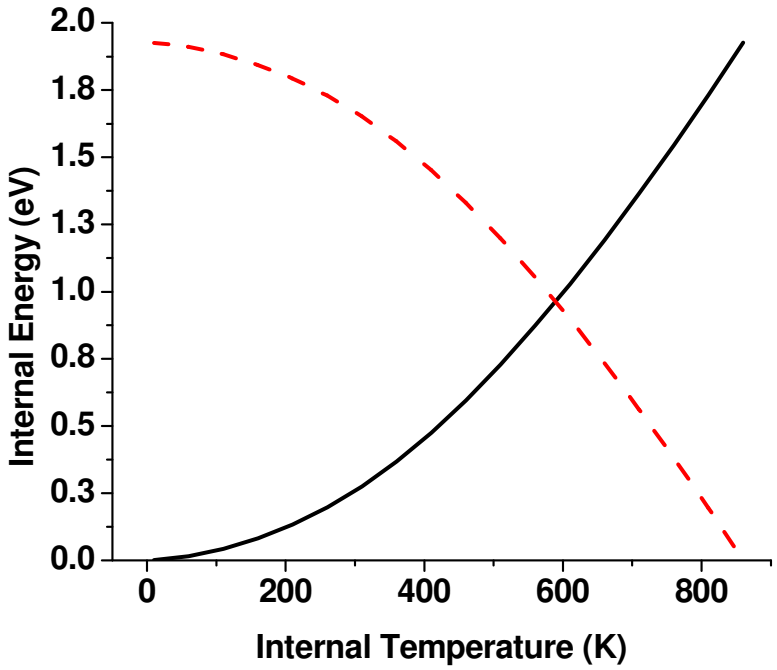

Figure 4.3. Relationship between internal energy and internal temperature for n-butylbenzene molecular ion (solid line). The dashed line is energy needed to raise the ion's temperature to 860 K.

4.4.3. Determination of Collisional Cooling Rates

The fact that the relationship between CID voltage and internal temperature in Figure 4.2b is exponential suggests that another process must be involved, and collisional cooling is an obvious candidate. Figure 4.4a shows an experimental cooling curve for n-butylbenzene, fit to an exponential decay equation. Figure 4.4b is a composite graph of pseudo first-order rate constants determined at a range of He pressures and trap temperatures. A linear relationship between collisional cooling rate constant and pressure has been demonstrated before in an ion cyclotron resonance mass spectrometer; however, these data were obtained at much lower pressures.[26] The curves in Figure 4.4b appear to increase exponentially with pressure, especially at lower trap temperatures. The same exponential increase with pressure was observed in a previous study in a QITMS. [20] At the very lowest pressures, a steady-state

ion internal energy was reached within 50 ms. This time to reach equilibrium decreases rapidly with increasing pressures, and at most normal operating pressures, equilibrium is reached in less than 10 ms.

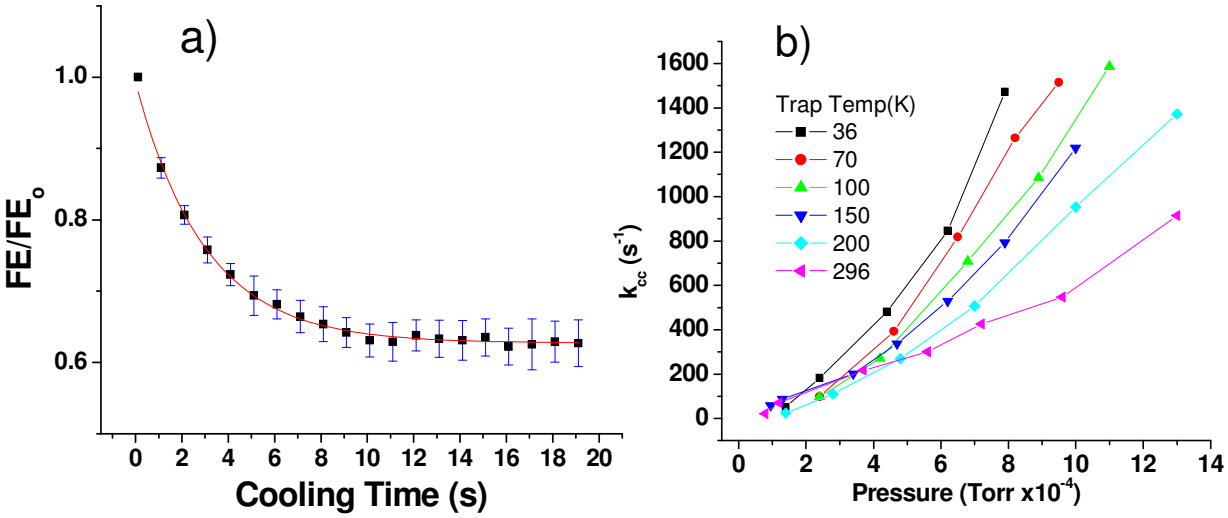

Figure 4.4. a) Experimental cooling curve for n-butylbenzene at 5.8x10^{-4} Torr He, 295 K. The pseudo first-order rate constant was 334 s^{-1} for this curve. Squares are experimental points with 95% confidence bands. The solid curve is an exponential decay fit with R^2 = 0.996. b) Pseudo first-order collisional cooling rate constants versus pressure at 36 K (squares), 70 K (circles), 100 K (up triangle), 150 K (down triangle), 200 K (diamond), and 296 K (45 degree triangle).

In Figure 4.5, the pseudo first-order rate constants for collisional cooling from Figure 4.4b at a constant pressure of 7x10^{-4} Torr are normalized and plotted on the same trap temperature axis as the normalized CID data from Figure 4.2b. It is apparent in Figure 4.5 that the voltage curves start to increase rapidly below ~100 K, the same trap temperature where the collisional cooling rate constant increases most rapidly. It is natural to conclude based on these data that the collisional cooling process is responsible for the exponentially increasing energy requirement for dissociation at low trapping temperatures. A possible interpretation of the results comes from the same density of states argument discussed in

relation to Figure 4.3. If it is assumed that each collision with a He atom takes away a given amount of energy, then at lower ion temperatures that same collision will decrease the ion's internal temperature more than at higher ion temperatures. Again, this would be because at lower ion temperatures there are fewer available energy states, so that a given input/output of energy increases/decreases the ions internal temperature to a greater extent.

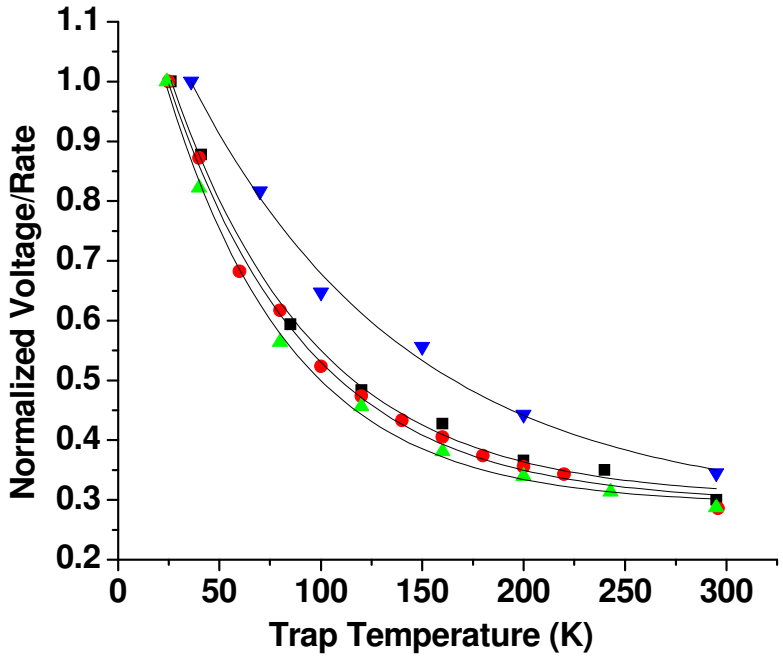

Figure 4.5. Comparison of collisional cooling rate constants vs trap temperature and CID voltage required to reach a constant internal energy vs trap temperature. The CID data are normalized to the highest voltage, and the cooling rate data is normalized separately to the highest rate constant. Squares are for $[GHK+H]^+$, circles for $[YGGFL+]^+$, up-triangles for $[FLLVPLG+H]^+$, down-triangles for collisional cooling rate constants of n-butylbenzene, and the black curves are an exponential decay fit to the data.

4.5. Conclusions

The CID voltage required to reach a constant internal energy has been determined for a series of protonated peptides at internal temperatures from 25 K to 295 K in a QITMS. A greater than linear increase in voltage is needed, especially at trapping temperatures lower

than 100 K. Collisional cooling rate constants have also been determined for a combination of pressures and trap temperatures for the molecular ion of n-butylbenzene. Collisional cooling rate constants increase exponentially as trap temperature decreases, which correlates well with the increased voltage needed for CID. Collisional cooling is an important energy transfer process in ion traps, especially at high He bath gas pressures and low trap temperatures. In low temperature IRMPD studies, such as action spectroscopy experiments where an ion must be dissociated in the presence of thermalizing bath gas pressures, it is important to have enough laser power to overcome the collisional cooling effect. We have observed in other experiments, comparing IRMPD efficiencies at different trap temperatures, that the increased laser power needed to dissociate an ion at ambient vs low trapping temperature can be 3 fold or greater. As interest shifts towards studying the structures of larger biomolecules in the gas phase, laser power could be a limiting factor, since generally speaking, larger ions have higher activation energies due to the increased number of degrees of freedom.

4.6. References

1. Stafford, G. C. J.; Kelley, P. E.; Syka, J. E. P.; Reynolds, W. E.; Todd, J. F. J. *Recent Improvements in and Analytical Applications of Advanced Ion Trap Technology*. Int. J. Mass Spectrom. Ion Processes **1984,** *60*, 85-98.

2. March, R. E. In *Encyclopedia of Analytical Chemistry*; Meyers, R. A., Ed.; John Wiley & Sons Ltd.: Chichester, 2000, pp 11848-11872.

3. VanBerkel, G. J.; Glish, G. L.; McLuckey, S. A. *Electrospray Ionization Combined with Ion Trap Mass Spectrometry*. Anal. Chem. **1990,** *62*, 1284-1295.

4. Chambers, D. M.; Goeringer, D. E.; McLuckey, S. A.; Glish, G. L. *Matrix-Assisted Laser Desorption of Biological Molecules in the Quadrupole Ion Trap Mass Spectrometer*. Anal. Chem. **1993,** *65*, 14-20.

5. Lennon, J. D. I.; Glish, G. L. *A MALDI Probe for Mass Spectrometers*. Anal. Chem. **1997,** *69*, 2525-2529.

6. Qin, J.; Steenvoorden, R. J. J. M.; Chait, B. T. *A Practical Ion Trap Mass Spectrometer for the Analysis of Peptides by Matrix-Assisted Laser Desorption/Ionization*. Anal. Chem. **1996,** *68*, 1784-1791.

7. Goeringer, D. E.; Asano, K. G.; McLuckey, S. A. *Ion internal temperature and ion trap collisional activation: protonated leucine enkephalin*. Int. J. Mass Spectrom. **1999,** *182/183*, 275-288.

8. Butcher, D. J.; Asano, K. G.; Goeringer, D. E.; McLuckey, S. A. *Thermal Dissociation of Gaseous Bradykinin Ions*. Journal of Physical Chemistry A **1999,** *103*, 8664-8671.

9. Asano, K. G.; Butcher, D. J.; Goeringer, D. E.; McLuckey, S. A. *Effective Ion Internal Temperatures Achieved Via Boundary Activation in the Quadrupole Ion Trap: Protonated Leucine Enkephalin*. J. Mass Spectrom. **1999,** *34*, 691-698.

10. Plass, W. R.; Cooks, R. G. *A Model for Energy Transfer in Inelastic Molecular Collisions Applicable at Steady State or Non-Steady State and for an Arbitrary Distribution of Collision Energies*. J Am Soc Mass Spectrom **2003,** *14*, 1348–1359.

11. Remes, P. M.; Glish, G. L. *Theoretical Estimation of Peptide Internal Temperature for High Amplitude Short Time Excitation Collision Induced Dissociation in a Quadrupole Ion Trap*. J Am Soc Mass Spectrom **2007,** *Submitted*.

12. McLuckey, S. A. *Principles of Collisional Activation in Analytical Mass Spectrometry*. J. Am. Soc. Mass Spectrom. **1992,** *3*, 599-614.

13. Louris, J. N.; Cooks, R. G.; Syka, J. E. P.; Kelley, P. E.; Stafford, G. C.; Todd, J. F. J. *Instrumentation, Applications, and Energy Deposition in Quadrupole Ion Trap Mass Spectrometry*. Anal. Chem. **1987,** *59*, 1677-1685.

14. Douglas, D. J. *Mechanism of the Collision-Induced Dissociation of Polyatomic Ions Studied by Triple Quadrupole Mass-Spectrometry*. J. Phys. Chem. **1982,** *86*, 185-191.

15. Payne, A. H.; Glish, G. L. *Thermally Assisted Infrared Multiphoton Photodissociation in a Quadrupole Ion Trap*. Anal. Chem. **2001,** *73*, 3542-3548.

16. Gabryelski, W.; Li, L. *Photoinduced Dissociation of Electrospray-Generated Ions in an Ion Trap/Time-of-Flight Mass Spectrometer Using a Pulsed CO2 Laser*. Rapid Commun. Mass Spectrom. **2002,** *16*, 1805-1811.

17. Goolsby, B. J.; Brodbelt, J. S. *Tandem Infrared Multiphoton Dissociation and Collisionally Activated Dissociation Techniques in a Quadrupole Ion Trap*. Anal. Chem. **2001,** *73*, 1270-1276.

18. Little, D. P.; Speir, J. P.; Senko, M. W.; Oconnor, P. B.; McLafferty, F. W. *Infrared Multiphoton Dissociation of Large Multiply-Charged Ions for Biomolecule Sequencing*. Analytical Chemistry **1994,** *66*, 2809-2815.

19. Goeringer, D. E.; McLuckey, S. A. *Relaxation of Internally Excited High-mass Ions Simulated under Typical Quadrupole Ion Trap Storage Conditions*. Int. J. Mass Spectrom. **1998,** *177*, 163-174.

20. Black, D. M.; Payne, A. H.; Glish, G. L. *Determination of Cooling Rates in a Quadrupole Ion Trap*. J Am Soc Mass Spectrom **2006,** *17*, 932-938.

21. Asamoto, B.; Dunbar, R. C. *Observation of the infrared radiative relaxation of iodobenzene ions using two-light-pulse photodissociation*. J. Phys. Chem. **1987,** *91*, 2804-2807.

22. Uechi, G. T.; Dunbar, R. C. *Thermometric study of CO2 laser heating and radiative cooling of n-butylbenzene ions.* Journal of Chemical Physics **1993,** *98*, 7888-7897.

23. Goeringer, D. E.; McLuckey, S. A. *Evolution of Ion Internal Energy During Collisional Excitation in the Paul Ion Trap: A Stochastic Approach*. Journal of Chemical Physics **1996,** *104*, 2214-2221.

24. Stein, S. E.; Rabinovitch, B. S. *Accurate evaluation of internal energy level sums and densities including anharmonic oscillators and hindered rotors*. The Journal of Chemical Physics **1973,** *58*, 2438-2445.

25. Frisch, M. J. *Gaussian 03, Revision C.02 Gaussian, Inc., Wallingford CT*. Gaussian 03, Revision C.02 Gaussian, Inc., Wallingford CT **2004**.

26. Dunbar, R. C. *Time-resolved photodissociation study of relaxation processes in gas-phase styrene ion.* Journal of Chemical Physics **1989,** *91*, 6080-6085.

Chapter 5

5. Mapping the Distribution of Ion Positions as a Function of Quadrupole Ion Trap Mass Spectrometer Operating Parameters to Optimize Infrared Multiphoton Dissociation

5.1. Introduction

Lasers have been used as a tool for the photo dissociation of ions in mass spectrometers for at least 35 years.[1] Trapping instruments such as the QITMS are advantageous for photo dissociation because they serve to hold the ions in the laser path, allowing multiphoton processes such as IRMPD. Lasers and trapping instruments have been employed in a variety of applications, ranging from determination of radiative and collisional cooling rates [2-4], ion tomography[5, 6], primary structure elucidation of proteins and peptides [7-12], assistance of electron capture dissociation (ECD)[13], and finally more recently, infrared action-spectroscopy [14-18].

Of fundamental importance in any laser photo dissociation experiment is that the volume defined by the ion trajectories, henceforth denoted as the ion cloud, intersects the irradiating volume of the laser. Satisfying the condition of ion/laser overlap might seem trivial, necessitating only optimization of the laser alignment optics, until the dynamic nature of the ion cloud in a QITMS is considered. As will be discussed in detail in later sections, in a QITMS the force pushing an ion towards the center of the trap (where the laser is typically focused) depends on a number of instrumental parameters. Any alteration of this force is reflected in the dimensions of the ion cloud. Thus, when the laser beam profile is near the

same size as the ion cloud radius, a change in instrumental parameters can have an effect on the efficiency of photo dissociation. This effect is more pronounced when the laser beam is focused to very small diameters relative to the ion cloud size, but is also noticeable with larger diameter laser beams, due to the Gaussian (non-homogenous) beam intensity profile. Ion cloud dimensions were measured previously in a QITMS for an ion tomography experiment.[6] The ion radial and axial distributions were mapped by scanning the position of a XeCl excimer laser and measuring fragmentation efficiency. The purpose of that study was to correlate ion cloud dimensions to space charge related mass shifts, therefore the parameter that was varied was the number of ions trapped, and the other trapping parameters were kept constant. The present work will demonstrate that various other QITMS instrumental parameters affect the efficiency of IRMPD, contrary to conventional wisdom. A combination of experimental and theoretical methods is used to map the distribution of ion positions as a function of these parameters.

5.2. Influence of q_z, Mass, and Trapping Frequency on Pseudopotential Well Depth

In Figure 5.1, the axial pseudopotential well depth has been plotted as a function of various ion trapping parameters using Equation 1.8. Figure 5.1a varies q_z values for a 445 Da ion at a trapping frequency of 838 kHz, Figure 5.1b varies rf trapping frequency for a 445 Da ion at $q_z = 0.25$, and Figure 5.1c varies ion mass-to-charge at $q_z = 0.25$ and rf trapping frequency of 838 kHz. The restoring force pushing an ion towards the center of the ion trap (the "bottom" of the pseudopotential well) increases with potential as in Equation 5.1.

$$F = m \cdot a = -e \cdot \nabla \cdot \Phi \qquad \text{(Equation 5.1)}$$

Where m is ion mass, a is acceleration, e is the fundamental unit of charge, and Φ is potential. Therefore, all other parameters being equal, a smaller ion cloud is expected for

traps operating at higher rf voltage (q_z), at higher frequency, and for ions of larger mass-to-charge ratios. The depth of the pseudopotential well approaches zero at values of the parameters that might be considered close to typical, especially for IRMPD. If a small well depth leads to a diffuse ion cloud, then trapping conditions may need to be adjusted for optimum dissociation efficiency.

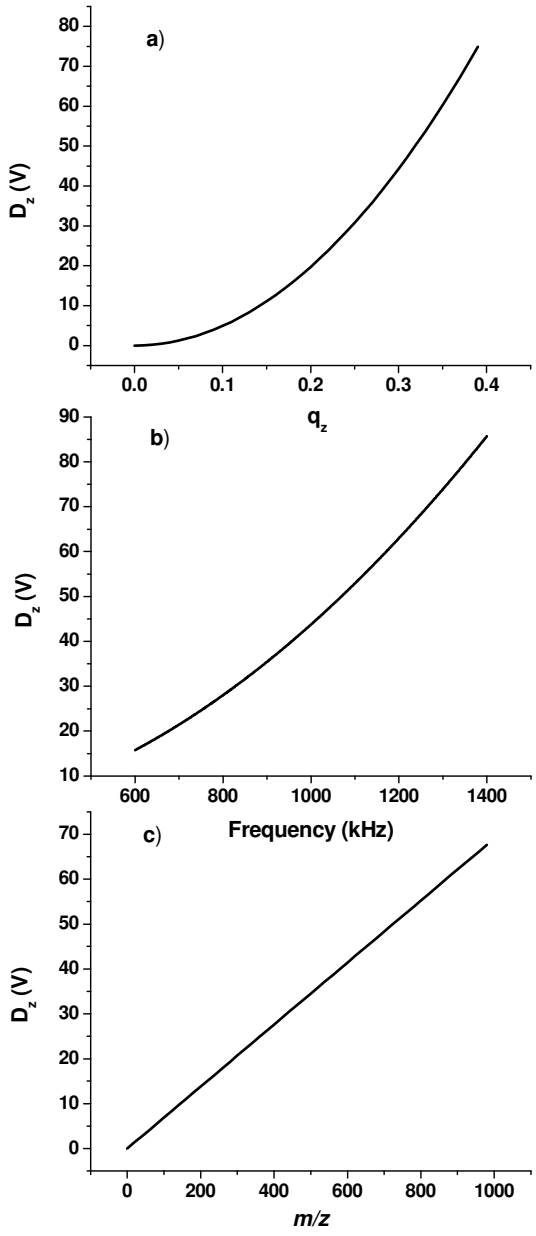

Figure 5.1. Pseudopotential trapping well depth as a function of: a) q_z value, for 445 Da, Ω = 838 kHz b) rf trapping frequency, for 445 Da, q_z = 0.25 c) ion mass-to-charge, q_z = 0.25, Ω = 838 kHz

The goal of this study is to vary q_z value, rf drive frequency, and ion mass-to-charge ratio to examine the effects of these parameters on the positional distribution of ions in the trap. Similar to previous studies,[6, 19] laser dissociation will be used as a tool to observe these changes. In the present study, however, IRMPD with a CO_2 laser is used, and the operating parameters of the QITMS are varied. There is no provision for scanning the position of the laser beam; the beam is kept centered in the middle of the trapping volume, and changes in the efficiency of

dissociation are monitored as trapping parameters are varied. The changes in dissociation efficiency are linked to changes in ion cloud size because as an ion's radius of oscillation gets smaller it will spend more time inside the laser beam absorbing photons, and will more readily dissociate. When an ion is stored in the QITMS at conventional He bath gas pressures (~1 mTorr), collisional processes effectively bring the ion's vibrational temperature into equilibrium with the room temperature He bath gas.[4, 20, 21] Ion activation via IRMPD can be significantly retarded by this collisional cooling, which is on the order of 400 s^{-1}.[4] However, with a smaller ion cloud that receives a higher flux of photons, the IRMPD process will compete better with the collisional cooling effect of the bath gas, resulting in more dissociation.

5.3. Experimental Methods

5.3.1. Instrumental

The QITMS used in this experiment is described in **Chapter 3**. Nano-ESI was performed as in **Chapter 2.1.1** for the protonated peptide molecules of tetracycline, GHK, and FLLVPLG. EI was performed on n-butylbenzene as described in **Chapter 2.1.3**. Samples were purchased from Sigma Aldrich (St. Louis) and FLLVPLG was custom synthesized by Bayer Corp. All samples were used without any further purification.

For these experiments the laser beam profile was characterized. The manufacturer specified beam width is 3.5 mm with a 4mR full angle divergence. The theoretical beam full width at half maximum at the center of the trap is therefore (half angle divergence x focal length) equal to 0.76 mm. This was verified experimentally by using a razor blade mounted on a precision translation stage to find the positions where the beam power was attenuated by 7% and 93%, and dividing this distance by $\sqrt{2}$. The average of 3 measurements obtained in

this manner was 0.78 ± 0.02 mm. Great care was taken to ensure that the laser beam passed through the center of the trapping volume.

IRMPD was performed as described in **Chapter 2.3.3**. Each spectrum was the average of 25 scans. Generally, each curve in the data reported here is the average of 5 separate experiments, and error bars are calculated as 95% confidence intervals. The rf level during irradiation by the laser was varied from one spectrum to the next with a computer-run script. The rf levels used corresponded to q_z values ranging from 0.05 to 0.60. When it was necessary to change the frequency of the main drive rf, the location of the tap on the secondary coil of the rf amplification tank circuit was changed and capacitors were added or taken away. The new resonant frequency of the system was characterized, and the frequency of the trapping rf function generator was changed to the new resonant value. A new mass scale calibration was then made at the new frequency using a capacitive pickup to monitor the rf voltage levels.

5.3.2. SIMION Simulation Parameters

Ions trajectories were simulated with SIMION 7.0 (**Chapter 2.4.3**) for 1 ms with a time resolution of ~ 5 ns. Initial kinetic energy was set to 0.15 eV ± 20% in a random direction. This value was chosen based on separate simulations characterizing the kinetic cooling of an ion for extended periods of time while subjected to ~ mTorr pressures of helium. Ions of 445 Da at various kinetic energies up to as great as 25eV were all observed to relax down to kinetic energies in the 0.02-0.20 eV range. The ions therefore have kinetic energies comparable to that of the He bath gas, which is 0.039 eV at 300 K. Most of the kinetic relaxation takes place in the first 10 ms, with equilibrium levels being reached by ~15 ms for all conditions except low pressure ($1x10^{-4}$ Torr He). 100 ions were independently

simulated at rf levels corresponding to q_z values of 0.05 to 0.90, with a step size of 0.05. The amount of time that an ion spent in various parts of the trap was recorded and averaged for each q_z value, and then used to create probability maps of ion position. Figure 5.2 illustrates how the time an ion spends in each of 30 concentric volumes was tracked. Each volume in Figure 5.2 is 0.05 mm thick, thus volume 1 is the solid cylinder from 0 mm to 0.05 mm away

Figure 5.2. Close up of center of SIMION electrode array used to simulate ion trajectories. The time an ion spends in each of 30 cylinders in the center of the trap was recorded to produce a distribution of probability as a function of radius. An ion trajectory at $q_z = 0.10$ is shown, where the ion color is changed in each of the 30 cylinders for emphasis. The left and right electrodes are the endcaps through which ions enter and exit the trap. The top and bottom electrodes are actually one cylindrical ring electrode where the trapping voltage is applied.

from the center, volume 2 is a hollow cylinder from 0.05 mm to 0.10 mm away from the center, etc. The 30 cylinders are collectively the largest ion trapping volume that a laser beam could possibly irradiate, because the hole in the ring electrode is ~3 mm.

To attempt to validate the modeling, several checks were performed. A theoretical model was fit to the experimental data by assuming that IRMPD fragmentation efficiency depends on the probability of the ion being inside the laser beam, as is described below. Two other validations of the modeling were comparing collision frequency and the axial cloud size from the literature to SIMION determined values. The number of collisions per experiment for the tetracycline simulation was determined to be 23.1 collisions/ms, during normal "storage" q_z values of 0.05-0.60. This is in good agreement with the value of 20 collisions/ms reported previously [22], although this number should vary depending on ion cross section. A previous study determined the ion cloud radius to be 0.60 mm in the axial direction for an ion of 105 Da, at a q_z of 0.30, and a pressure of 1.75×10^{-4} Torr. [6] These conditions were simulated in SIMION and only the axial position of the ions was recorded. The result showed an ion cloud full-width-half-maximum radius of 0.57 mm, in good agreement with the experiment.

5.3.3. Theoretical Fragmentation Efficiency

With experimental IRMPD spectra, the definition used for fragmentation efficiency is given in Equation 1.12. To show that the SIMION modeling was giving accurate results, a method of computing simulated fragmentation efficiency was devised. The simulations were then compared with the experimental results. The fragmentation efficiency is expected to be a function of the probability of finding the ion in the laser beam volume multiplied by a

constant which is dependant on molar absorptivity and the ion's critical energy of dissociation. Equation 5.2 gives this simulated fragmentation efficiency.

$$FE = \frac{\sum_{i=0}^{i=radius} t_i}{T} \cdot C \cdot 100\% \qquad \text{(Equation 5.2)}$$

FE is fragmentation efficiency, t_i is the time spent in ion volume *i* of the 30 volumes that were recorded, *T* is total time, and *C* is a constant. The times spent in volumes 0 up to some critical radius (the laser beam radius) are summed: beyond this critical radius the calculation assumes that the rate of collisional cooling is greater than the rate of IR activation, resulting in no dissociation. The SIMION probability maps described in the Ion Trajectory Modeling section were used with Equation 5.2 to generate a theoretical fragmentation efficiency. Generally, for a given ion and trap pressure, *C* was set constant, and the critical radius was varied for each laser power used, from 0.10 mm to 0.50 mm. This is because as laser power increases an ion absorbs more photons per unit time, thus less time is needed for dissociation to occur. Increased laser power, therefore, should cause the ions at larger radii to absorb enough photons to dissociate.

5.4. Results

5.4.1. Effect of rf Voltage on Ion Cloud Size

The result of IRMPD of tetracycline at constant laser power and increasing the rf voltage level (q_z value) is shown in Figure 5.3. Clearly as q_z value is increased, the parent ion is dissociated more efficiently. Presumably this is because at higher q_z values the ions are experiencing a stronger restoring force (see Equation 1.8) pushing them towards the center of the trap, which increases the overlap of the ion cloud with the laser beam. At high laser power, fragmentation efficiency levels off at a maximum value around q_z=0.3. At lower

laser powers, fragmentation efficiency keeps increasing past a q_z of 0.3, although at a slower rate. Lower laser power effectively allows more "resolution" in the observation of ion cloud size, since at higher laser powers an ion may absorb enough photons to dissociate even away from the center of the laser beam profile. Rf heating should not be a factor, since it has already been shown in a thermal dissociation experiment in a QITMS that rf level did not significantly affect the level of dissociation.[23]

5.4.2. Ion Trajectory Simulations

Figure 5.3 also shows a comparison of experimental fragmentation efficiency with theoretical values calculated from SIMION results. This fitting of experimental and

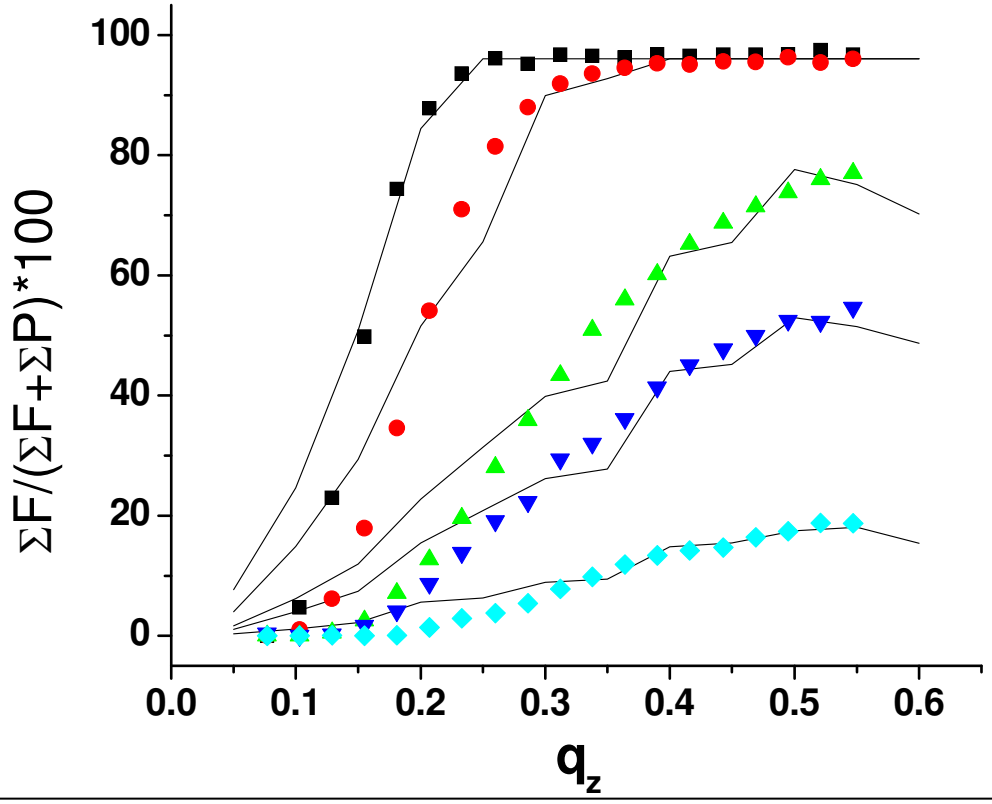

Figure 5.3: Experimental fragmentation efficiency versus q_z value for tetracycline at various laser powers. Large diamond is 12 W, down-triangle is 13.5 W, up-triangle is 15 W, circle is 17.5 W, and square is 20 W. Fits to calculated fragmentation efficiency are shown in solid, using Equation 5.2.

simulated fragmentation efficiency shows that the changes in fragmentation efficiency with q_z value can indeed be explained by changes in ion cloud size. It would be difficult to try to extract an ion cloud size directly from the experimental data, although it seems fair to conclude qualitatively that the ion cloud is getting smaller as q_z gets bigger. The assumption can be made that the ion cloud diameter is on the scale of the laser beam waist of 0.78 mm, and is fully contained within this area at higher q_z, but it would be hard to be more precise. A more quantitative ion cloud size can be determined through examination of the calculated results. The probability of finding a protonated tetracycline ion (445 Da, 1.56×10^{-18} m^2, 7.0×10^{-4} Torr) at a given radius is plotted in Figure 5.4 at various q_z values. There are several features of interest in this plot. At low q_z the ion cloud is spread out over a greater volume, and then progressively gets smaller until around $q_z = 0.4$. The ion cloud size stays fairly constant until $q_z = 0.7$ where it starts to experience higher amplitude excursions from the center of the trap. It may be significant that ion cloud size stops decreasing at $q_z = 0.4$, because this is the limit beyond which higher order ion oscillations have appreciable amplitude and the pseudopotential model is not valid. Notice also that the peak of ion probability is not at the very center of the trap, rather around a radius of 0.25 mm. This is presumably because the ion velocity is at a maximum through the center of the trap and so the ion spends less time in the center than at the "turn-around" point of the ion's trajectory, where its velocity decreases to zero and then reverses direction. The shape of the ion distribution may actually suggest that a laser beam located just slightly off center axis could give better overlap with the ion cloud than a beam aligned perfectly at the middle of the trap.

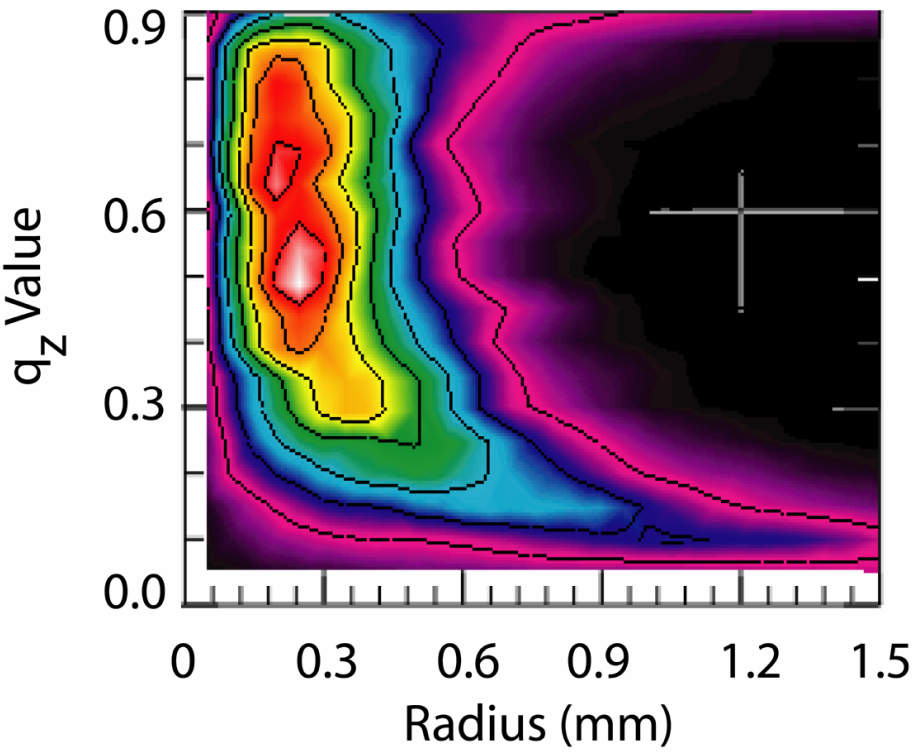

Figure 5.4. Calculated probability distribution for ion position at various q_z values for protonated tetracycline ion (445 Da, 1.56×10^{-18} m^2, 7.0×10^{-4} Torr). In the vertical dimension, each line denotes a probability of 0.02. Therefore, the area at the far right is at a probability of 0.0, while the peak at a radius of 0.3 mm and q_z value of 0.5 is a probability of 0.14-0.16.

5.4.3. Effect of Drive Frequency on Ion Cloud Size

IRMPD was performed on the n-butylbenzene ion generated by EI. Again, the q_z value was varied and the fragmentation efficiency was recorded. This was done at two different drive frequencies: 844.5 kHz and 1148 kHz. The results are shown in Figure 5.5a, where the squares represent data points taken at 1148 kHz and the triangles are 844.5 kHz data points. Curves of the same type/color represent equal laser powers. Comparing different frequency results at the same laser power, the high frequency curve is at significantly higher fragmentation efficiency than the lower frequency curve. This result makes sense because well depth varies as the square of trapping frequency (Equation 1.8), so

at higher frequencies, ions are in a smaller ion cloud. A true comparison of the effect of two different frequencies on ion cloud size can be made, because all other experimental parameters are the same. That is, at both frequencies the ion requires the same number of photons to dissociate, because the trap pressure and the calculated collision frequency were equal at both frequencies. The only difference, therefore, is the ion cloud size, which is affecting laser overlap and the photon absorption rate. Trajectory modeling (Figure 5.5b) shows that the most probable ion position at a q_z of 0.30 is at a radius of 0.35 mm at 844.5 kHz, while this position is 0.26 mm at 1148 kHz.

5.4.4. Effect of Mass on Ion Cloud Size

Unfortunately an experiment to probe the ion cloud size for ions of different masses is difficult to design. Observing the IRMPD fragmentation efficiency at different q_z values for different size ions does not allow conclusions about relative ion cloud size to be drawn, because larger ions will require more photons to be absorbed for dissociation. Thus, the positional dependence of fragmentation efficiency is convoluted with different energetic requirements for dissociation. One can hypothesize that since mass is in the numerator in Equation 1.8, that heavier ions will be at smaller radii than lighter ions when compared at the same q_z value. Naturally, however, when different size ions are stored in the QITMS at the same time, they have different q_z values. In this second case, one expects the smaller ions at higher q_z to be closer to the center of the trap. Fragmentation efficiency vs q_z curves for the peptides GHK and FLLVPLG were qualitatively similar to those obtained for tetracycline. An attempt was made to normalize the different energetic requirements of different size ions to a CID breakdown curve experiment and/or to the number of degrees of freedom of each ion, without success, as of yet. Trajectory calculations, however, can illuminate the situation,

as is shown in Figure 5.5b. The 134.2 Da n-butylbenzene ion, plotted as triangle data points, is most likely found at a radius of 0.45 mm, as opposed to the 445.5 Da tetracycline ion, shown in circles, which has a highest probability at 0.35mm.

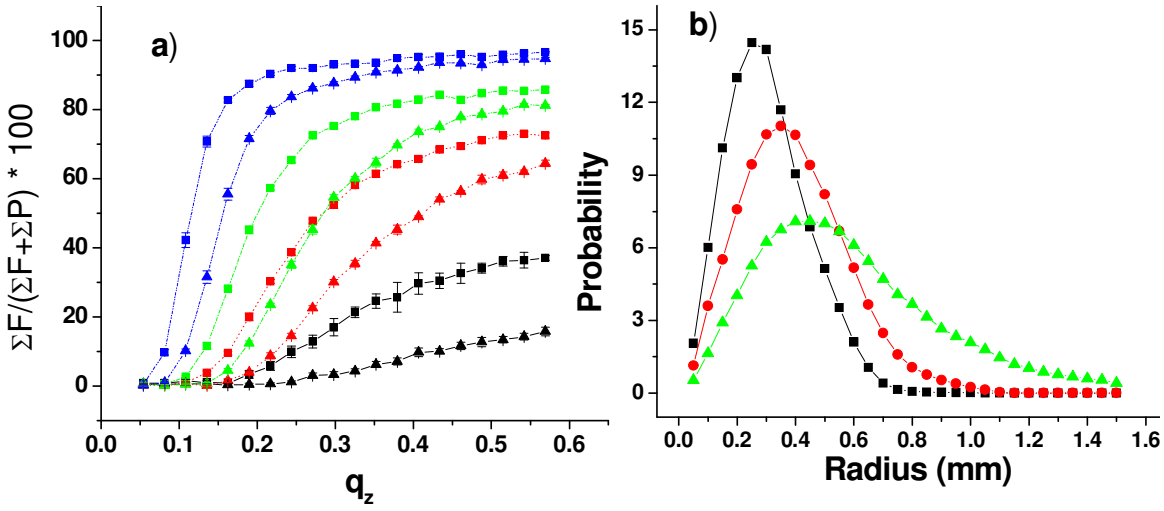

Figure 5.5. a) Fragmentation efficiency versus q_z value for n-butylbenzene molecular ion at 7.0×10^{-4} Torr, for several laser powers and trapping frequencies. Squares are 1148 kHz and triangles are 844.5 kHz. Lines of the same type/color are the same laser power. b) SIMION modeling of ion probability versus distance from center of trap at q_z=0.30. Square points are for 1148 kHz, 445.5 Da, circles are for 844.5 kHz, 445.5 Da, and triangles are for 844.5 kHz, 134.2 Da.

5.5. Conclusions

The size of the ion cloud in a QITMS has a noticeable effect on IRMPD dissociation efficiency. Maximal overlap of the ion cloud with the highest flux volume of the laser beam can be obtained by optimizing several parameters that determine the magnitude of the restoring force pushing the ion towards the center of the trap. From the equation for the depth of the pseudopotential well (Equation 1.8), the most important factors are trapping voltage, trapping frequency, and ion mass. Ion mass obviously is not a parameter that can be optimized, although it is interesting that a higher mass-to-charge ion (eg. a protein) should actually experience better laser overlap then a smaller peptide, if both ions were irradiated

while at the same q_z value. Trapping frequency is generally not a parameter that maybe adjusted easily; however, this study suggests that when one is designing an instrument for IRMPD, a higher frequency drive voltage can be advantageous, especially when laser power is seen to be a limiting factor in the experiment. Because rf trapping instruments are commonly operated a high bath gas pressures, the rate of collisional cooling competes with the rate of energy deposition through photon absorption. Therefore the q_z value may be adjusted to higher values to allow maximum activation of the ion. A high q_z value increases the low mass cut-off and lower mass product ions may not be trapped. A possible operating procedure to address this issue would be to start IRMPD at a high q_z value and decrease the rf voltage over the course of laser irradiation, so that successive generations of product ions could be formed and continue to be trapped in the instrument.

5.6. References

1. Dunbar, R. C. *Photodissociation of the CH_3Cl^+ and N_2O^+ Cations*. J. Am. Chem. Soc. **1971,** *93*, 4354-4359.

2. Uechi, G. T.; Dunbar, R. C. *Radiative relaxation rate determination by competitive photodissociation of n-butylbenzene ions.* Journal of Chemical Physics **1990,** *93*, 1626.

3. Dunbar, R. C. *Infrared radiative cooling of isolated polyatomic molecules.* Journal of Chemical Physics **1989,** *90*, 7369-7375.

4. Black, D. M.; Payne, A. H.; Glish, G. L. *Determination of Cooling Rates in a Quadrupole Ion Trap*. J Am Soc Mass Spectrom **2006,** *17*, 932-938.

5. Vining, B. A.; Li, G.-Z.; Marshall, A. G. *Laser-Induced Fluorescence for Ion Tomography in a Penning Trap*. J. Am. Soc. Mass Spectrom. **1998,** *9*, 925-930.

6. Cleven, C. D.; Cooks, R. G.; Garrett, A. W.; Nogar, N. S.; Hemberger, P. H. *Radial Distributions and Ejection Times of Molecular Ions in an Ion Trap Mass Spectrometer: A Laser Tomography Study of Effects of Ion Density and Molecular Type*. J. Phys. Chem. **1996,** *100*, 40-46.

7. Boué, S. M.; Stephenson, J. L.; Yost, R. A. Photodissociation of Electrosprayed Ions in the Quadrupole Ion Trap. Atlanta, Georgia, 1995.

8. Gabryelski, W.; Li, L. *Photo-induced Dissociation of Electrospray Generated Ions in an Ion Trap/Time-of-Flight Mass Spectrometer*. Review of Scientific Instruments **1999,** *70*, 4192-4199.

9. Little, D. P.; Speir, J. P.; Senko, M. W.; O'Connor, P. B.; McLafferty, F. W. *Infrared Multiphoton Dissociation of Large Multiply Charged Ions for Biomolecule Sequencing*. Anal. Chem. **1994,** *66*, 2809-2815.

10. Thompson, M. S.; Cui, W.; Reilly, J. P. *Fragmentation of singly-charged peptides by photodissociation at λ = 157nm*. Angewandte Chemie International Edition **2004,** *43*, 4791-4794.

11. Cui, W.; Thompson, M. S.; Reilly, J. P. *Pathways of Peptide Ion Fragmentation Induced by Vacuum Ultraviolet Light*. J. Am. Soc. Mass Spectrom. **2005,** *16*, 1384-1398.

12. Colorado, A.; Shen, J. X.; Vartanian, V. H.; Brodbelt, J. *Use of Infrared Multiphoton Photodissociation with SWIFT for Electrospray Ionization and Laser Desorption Applications in a Quadrupole Ion Trap Mass Spectrometer*. Anal. Chem. **1996,** *68*, 4033-4043.

13. Tsybin, Y. O.; Witt, M.; Baykut, G.; Kjeldsen, F.; Hakansson, P. *Combined infrared multiphoton dissociation and electron capture dissociation with a hollow electron beam in Fourier transform ion cyclotron resonance mass spectrometry*. Rapid Commun. Mass Spectrom. **2003,** *17*, 1759-1768.

14. Pivonka, N. L.; Kaposta, C.; Bruemmer, M.; von Helden, G.; Meijer, G.; Woste, L.; Neumark, D. M.; Asmis, K. R. *Probing a strong hydrogen bond with infrared spectroscopy: vibrational predissociation of BrHBr-.Ar*. Journal of Chemical Physics **2003,** *118*, 5275-5278.

15. Oomens, J.; Meijer, G.; Helden, G. v. *Gas Phase Infrared Spectroscopy of Cationic Indane, Acenaphthene, Fluorene, and Fluoranthene*. J. Phys. Chem. A **2001,** *105*, 8302-8309.

16. Oomens, J.; Moore, D. T.; Helden, G. v.; Meijer, G.; Dunbar, R. C. *The site of Cr+ attachment to gas-phase aniline from infrared spectroscopy*. J. Am. Chem. Soc. **2004,** *126*, 724-725.

17. Putter, M.; von Helden, G.; Meijer, G. *Mass selective infrared spectroscopy using a free electron laser*. Chem. Phys. Lett. **1996,** *258*, 118-122.

18. von Helden, G.; Holleman, I.; Putter, M.; Meijer, G. *IR spectroscopy on gas-phase molecules with a free electron laser*. Nucl. Instrum. Methods Phys. Res., Sect. B **1998,** *144*, 211-217.

19. Williams, J. D.; Cooks, R. G.; Syka, J. E. P.; Hemberger, P. H.; Nogar, N. S. *Determination of Positions, Velocities, and Kinetic Energies of Resonantly Excited Ions in the Quadrupole Ion Trap Mass Spectrometer by Laser Photodissociation*. J. Am. Soc. Mass Spectrom. **1993,** *4*, 792-797.

20. Goeringer, D. E.; McLuckey, S. A. *Relaxation of Internally Excited High-mass Ions Simulated under Typical Quadrupole Ion Trap Storage Conditions*. Int. J. Mass Spectrom. **1998,** *177*, 163-174.

21. Payne, A. H.; Glish, G. L. Thermally-Assisted Infrared Multiphoton Photodissociation in a Quadrupole Ion Trap. Chicago, IL, 2001.

22. March, R. E. In *Encyclopedia of Analytical Chemistry*; Meyers, R. A., Ed.; John Wiley & Sons Ltd.: Chichester, 2000, pp 11848-11872.

23. Asano, K. G.; Goeringer, D. E.; McLuckey, S. A. *Thermal Dissociation in the Quadrupole Ion Trap: Ions Derived From Leucine Enkephalin*. Int. J. Mass Spectrom. **1999,** *185/186/187*, 207-219.

Chapter 6

6. Theoretical Estimation of Peptide Internal Temperature for High Amplitude Short Time Excitation Collision Induced Dissociation in a Quadrupole Ion Trap

6.1. Introduction

As described in **Chapter 1.2.1.4.2**, CID is done by accelerating an ion into a target, generally neutral gas molecules. The kinetic energy of the ion motion is converted into internal energy, causing the ion to dissociate. The amount of energy converted from kinetic to internal energy is not a simply derived quantity. Each collision of an ion with a bath gas molecule may result in internal energy deposition ranging from no energy (elastic collision) to the full center of mass collision energy. Another possibility is for internal energy of the ion to be converted into kinetic energy of the neutral atom, that is, the ion's internal vibrational modes may be cooled by the collision. With larger ions, several collisions with the same neutral target may even occur.[3] Furthermore, in a QITMS each collision can occur with a wide range of ion kinetic energies, making the kinetic energy converted to internal energy a more widely varying quantity than it would be. Based on these considerations, the amount of internal energy gained with each collision in a CID experiment is not trivial to calculate.

Because of the complexity of the CID process, theoretical studies have been conducted that estimate the extent of ion activation by conventional CID in a QITMS as an increase in internal temperature.[2, 4] This, of course, assumes that the activation is a thermal process, where the internal energy distribution of ions can be described by Boltzmann's

equation. The assumption appears to be reasonable for CID in trapping instruments under multiple (>15) collision conditions, at least as a first order approximation. [5-7]

Chapter 2.3 describes the parameters for doing conventional and HASTE CID. As the acronym suggests, HASTE differs from conventional CID in a QITMS in terms of the voltages used, and the time scales of the CID event. HASTE involves much less activation time than conventional CID, and appears to increase the internal energy of the parent ion significantly. Increased product ion formation is observed for HASTE CID, some of which comes from dissociation pathways that cannot be accessed by conventional CID. An added benefit of using such a short activation period is that a clear temporal distinction can be made between when the ion is activated and when it is dissociated. With HASTE, parent ions can be quickly excited at optimal instrumental conditions for CID, but then product ion formation can occur under conditions which allow ions in a wide mass-to-charge range to be trapped.[8] Conventional CID suffers from the fact that optimal excitation conditions do not allow the product ions whose mass-to-charge values are less than ~1/3 that of the parent ion to be trapped.[9] The present study does not explore the temporal advantage particular to HASTE, but instead focuses on HASTE's energetic gain. Experiments showed fragmentation patterns for HASTE CID that suggested the ions were activated to higher internal energies than for conventional CID. The purpose of this study is to semi-quantitatively estimate this increase in internal energy as an effective ion temperature. Unfortunately, the method previously proposed for estimating ion temperatures under conventional CID conditions cannot be simply applied under HASTE conditions.[2] Internal temperatures of thousands of Kelvin are the result, which is unreasonable based on calculating mass spectra at these temperatures. This may suggest that the HASTE activation process is not thermal. However, the results of

this work show that the thermal approximation, at least as far as it concerns the internal energy distribution of the ions immediately before dissociation, may be reasonable.

6.2. Unimolecular Reaction Basics

The dissociation of an ion in a CID experiment can be thought of as having an activation step and a dissociation step.[10] In the activation step, shown in Equation 6.1, the internal energy of the parent ion ABC^+ is increased by collisions with the neutral bath gas N. In the dissociation step (Equation 6.2), some bond(s) of ABC^+ are broken, yielding product ions AB^+ and C [11, 12].

$$ABC^+ + N \longrightarrow ABC^{*+} \qquad \text{(Equation 6.1)}$$

$$ABC^{*+} \longrightarrow AB^+ + C \qquad \text{(Equation 6.2)}$$

The rate of the second step can be qualitatively understood by looking at the Rice-Rampsberger-Kassel (RRK) Equation 6.3,

$$k(E) = v\left(\frac{E - E_o}{E}\right)^{s-1} \qquad \text{(Equation 6.3)}$$

where $k(E)$ is the rate constant of dissociation, v is a factor related to entropy, E is the internal energy of the parent ion, E_o is the critical energy of dissociation, and s is the number of degrees of freedom. As E is increased, the term in parenthesis approaches one, and the dissociation rate approaches some maximum defined by v. The parenthetical term is the probability that the critical bond has enough energy to break, if internal energy is distributed statistically through out all the bonds in the ion. In a QITMS, product ion AB^+ (Equation 6.2) remains trapped, and will dissociate if its internal energy is great enough, as in Equation 6.4.

$$AB^+ \longrightarrow A^+ + B \qquad \text{(Equation 6.4)}$$

The internal energy of product AB^+ in Equation 6.2 can be determined quantitatively as a statistical partitioning of excess internal energy between AB^+ and C, as will be described in detail in a later section. However, in general terms, as the internal energy of the parent ion ABC^+ increases, so too will the internal energy of product ion AB^+ increase, increasing the rate of appearance of A^+.[13] The formation of more product ions by a variety of different pathways gives more information about the parent ion ABC^+, facilitating structural elucidation. Therefore, to some extent, the more ABC^+ can be activated, the more useful the CID experiment becomes.

6.3. Methods and Theory

6.3.1. Experimental Parameters

The internal energy of ions activated by HASTE and conventional CID was estimated as an internal temperature by comparing calculated MS/MS spectra at different parent ion internal temperatures with experimental spectra. The simulated spectra used parent ion effective temperatures of 300 K to 900 K. The experimental spectra were taken at ambient temperature, with resonant excitation voltages of 0.75 V_{pp} to 6.00 V_{pp}. When a simulated spectrum at a given internal temperature matched the experimental spectrum, this temperature was taken to be the experimental effective temperature of the parent ion. A match was determined by minimizing the sum of the squared differences between relative ion intensities of the two spectra. The ions investigated were $[YGGFL+H]^+$, $[YGGFL+Na]^+$, $[YGAFL+Na]^+$, and $[CH_3COONa]_6Na^+$. The experimental spectra were taken using nano-ESI on a Bruker Esquire QITMS, as described in **Chapter 2.1.1**. Spectral comparison was done with software written in LabVIEW 7.1 [14]. The CID conditions used for each ion can be found in Table 6.1. The q_z value (**Chapter 1.2.1.2**) was adjusted slightly to optimize the

experiments for MS/MS efficiency. Adjusting q_z value to more than the typical q_z = 0.25 was necessary because the higher voltages used during HASTE increase the likelihood that the parent ion is ejected before it dissociates. For conventional CID there was no noticeable difference in efficiencies in the q_z range between 0.25 and 0.30. Typical optimized MS/MS efficiencies (Equation 1.11) were 75-95% for conventional CID, 10-50% for HASTE CID. Although the slightly higher q_z value used for HASTE raises the nominal low mass cutoff value for trapping ions in the QITMS,[8, 9] it has been demonstrated that quickly ramping down the main rf voltage after HASTE will trap many ions formed below this cutoff, so that using a higher q_z value for HASTE does not have to be a disadvantage.[8]

Table 6.1: Experimental CID parameters

	$[YGAFL+Na]^+$	**$[YGGFL+Na]^+$**	**$[YGGFL+H]^+$**	**$[CH_3COONa]_6Na^+$**
Conventional CID				
V_{pp}	1.15	1.15	0.85	0.75
q_z	0.25	0.25	0.25	0.25
Time (ms)	40	40	40	40
HASTE CID				
V_{pp}	6.00	5.00	4.90	2.20
q_z	0.30	0.30	0.29	0.28
Time (ms)	2	2	2	2

6.3.2. Simulation of Mass Spectra

All calculations were done in LabVIEW 7.1, unless stated otherwise. The procedure for simulating a MS/MS spectrum has 3 basic steps, outlined here and subsequently discussed in more detail. (1) The probability *p(E)* that an ion has a certain internal energy is determined. *p(E)* is also known as the internal energy distribution. (2) Rice-Rampsberger-Kassel-Marcus (RRKM) theory is then used to determine the rate of fragmentation of the parent ion into its product ions, once certain reaction parameters are determined. Relative

intensities of parent and product ions can then be calculated. (3) The internal energy for those product ions that dissociate is calculated, and RRKM theory is again used to compute second generation parent and product ion intensities. Step (3) is repeated for each subsequent product ion generation, i.e. AB^+ dissociating to give A^+.

6.3.2.1. Internal Energy Distributions

The internal energy distribution, *p(E)*, is calculated as described in **Chapter 2.4.2.** This method requires the knowledge of the vibrational frequencies of the ion, which for this work were calculated on energy minimized structures at the B3LYP/6-31G(d) level of theory with Gaussian 03, as described in **Chapter 2.4.1.** [15] These frequencies were scaled by a factor of 0.9614 to account for anharmonicity effects which are not considered in the frequency calculations.[16]

As an approximation, it was assumed that the internal energy of the parent ion after activation in the CID event could be described by an effective temperature T_{eff}. *p(E)* was

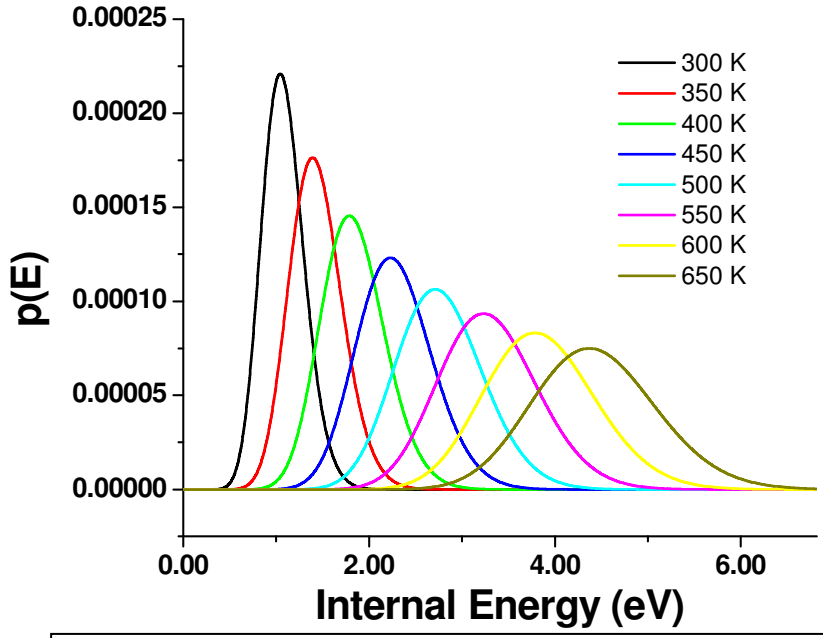

Figure 6.1. Thermal internal energy distributions at different effective temperatures for $[YGGFL+H]^+$.

calculated for a range of different T_{eff}, shown in Figure 6.1. At each T_{eff} a MS/MS spectrum was simulated. When a calculated spectrum matched well with an experimental spectrum, the T_{eff} used in the calculation was deemed to be the internal temperature achieved by the parent ion.

6.3.3. Rates of Dissociation

The RRKM equation, given by Equation 6.6, more accurately describes rates of unimolecular reaction than the RRK form.[11]

$$k(E) = \frac{N^{\neq}(E - E_o)}{h \cdot \rho(E)} \qquad \text{(Equation 6.6)}$$

$N^{\neq}(E\text{-}E_o)$ is the summation of states for the transition state, calculated again by the direct count method, and h is Plank's constant. While computational programs such as Gaussian 03 can be used to find transition state structures and their vibrational frequencies[17], such calculations are computationally expensive, especially for larger structures. However, the transition state frequencies can be estimated from the parent ion frequencies by deleting a vibration assumed to be the reaction coordinate and scaling the first few frequencies (which have the most effect on $N^{\neq}$) by a factor S.[11] Values of $S > 1$ give a transition state with entropy $\Delta S^{\neq} < 0$, while values of $S < 1$ give a transition state with $\Delta S^{\neq} > 0$. This treatment of the transition state is acceptable because RRKM theory is sensitive only to $\Delta S^{\neq}$, not to the absolute transition state frequencies.[5] If E_o and S are known for a particular dissociation(s), then the calculation of a MS/MS spectrum with a certain $p(E)$ can be performed. Figure 6.2a demonstrates this process visually. The internal energy distribution $p(E)$ of the parent ion is shown in the top part of Figure 6.2a. The rate versus internal energy relationship (RRKM curves) for two competitive dissociations of the parent ion are depicted in Figure 6.2b. The dotted, horizontal line in Figure 6.2b is the experimental time scale of the CID event. The

intersection of the RRKM curves with the experiment time scale line defines the internal energy necessary to observe these reactions, which also divides *p(E)* into three sections in this case. Section 1 (diagonal forward-slashes) in Figure 6.2a is the fraction of the parent ions that do not have enough internal energy to dissociate during the experiment; section 2 (diagonal back-slashes) refers to the fraction of ions that dissociates only by reaction pathway 1; and section 3 (horizontal lines) refers to the fraction of ions that dissociates by both reaction pathways 1 and 2. Section 3 can be distributed between reaction pathways 1 and 2 based on the relative magnitudes of the dissociation rates at a given internal energy. The resulting mass spectrum, plotted on a relative abundance axis in Figure 6.2c, is then the integral of section 1 for the parent ion intensity, integral of section 2 plus part of section 3 for product ion 1 intensity, and part of section 3 for the product ion 2 intensity. The procedure

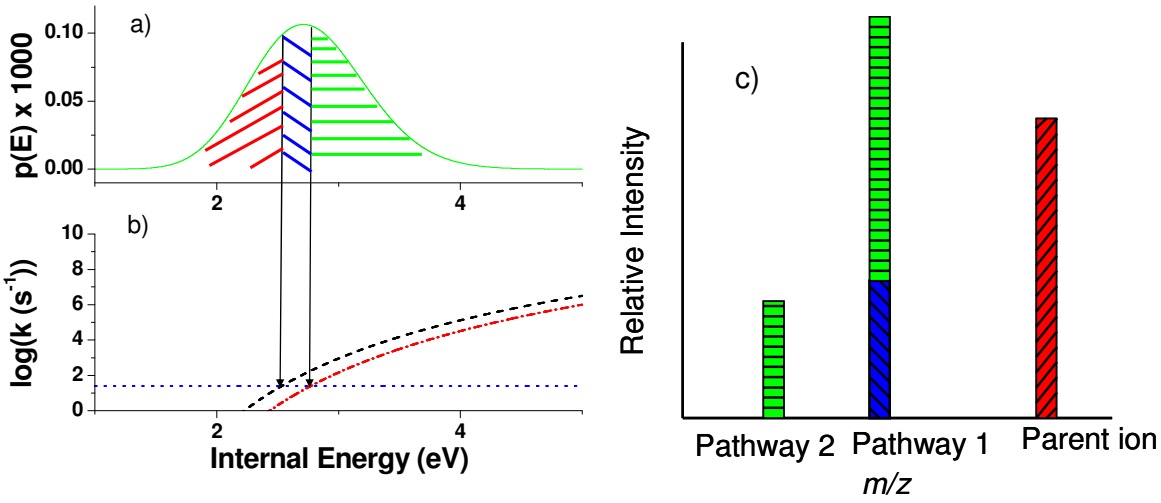

Figure 6.2. a) Internal energy distribution divided into three sections: section 1, the portion of ions not having enough internal energy to dissociate, is diagonal bars slanting low to high, section 2, the portion of ions that dissociate by pathway 1 only, is diagonal bars slanting high to low, section 3, the portion of ions that dissociate by both pathways 1 and 2, is horizontal bars. b) Dotted line is instrumental time scale. Dash-dash and dash-dot-dash lines are rate vs internal energy relationships for two competing reactions pathways 1 and 2, respectively. c) The resulting simulated mass spectrum, where the style of bar denotes the ions' energetic origin in Figure 6.2a.

outlined above, integrating at an energy interval of 50 cm^{-1}, was used to calculate MS/MS spectra.

6.3.4. RRKM Parameters

Unless E_o and the transition state frequencies are already known for a particular dissociation, they must be obtained experimentally. A procedure for doing this has been described previously for CID in a Fourier-transform ion cyclotron resonance (FT-ICR) mass spectrometer.[5, 18, 19] The same basic procedure was followed in this study. Conventional CID was performed on the parent ion and on each of the relevant product ions at various resonance excitation voltages. Breakdown curves of ion abundance versus voltage are shown in Figure 6.3. These experimental breakdown curves were constructed from spectra obtained on the Bruker Esquire. Note that the Bruker Esquire effects CID by applying the resonance excitation voltage only to one endcap electrode, while the other endcap is grounded. The

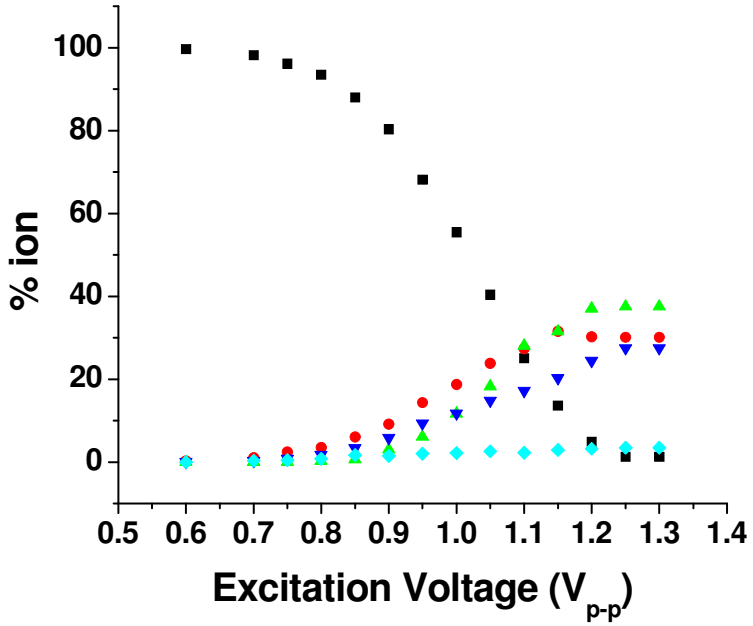

Figure 6.3. Experimental breakdown curves for the a_4^+ ion of YGGFL dissociating to its product ions in conventional CID. Squares are a_4^+, circles are $[a_4\text{-}17]^+$, up-triangles are the rearrangement ion at 323 u^1, down-triangles are b_3^+, and diamonds are GGF^+

electric field gradient is half as big as it would be if this voltage was applied to each endcap with a 180° phase difference, so the voltages needed to dissociate an ion are larger than in ion traps that use excitation on both endcaps. In previous experiments[5, 18, 19] the experimental CID voltages were transformed into collision energies, and experimental breakdown curves were fitted to calculated breakdown curves, varying E_o and S to get the best possible match. This procedure is possible in a FT-ICR instrument where the collision energies can be calculated more precisely, but not in a QITMS, where the kinetic energy of the ions are constantly changing. In our study, CID voltage was converted into average parent ion temperature, using a method described for conventional CID in a QITMS.[2] The details of this transformation are too lengthy to describe here, but are straightforward to implement in practice. It has been noted that the temperature scale is not absolute, and calibration may be necessary. [2] Temperature scale calibration has been done for various ions.[4] A comparison of these two methods [2, 4] is shown in Figure 6.4a, where resonance excitation voltage versus average parent ion temperature is plotted for an ion of *m/z* 515 at a bath gas pressure of 1mTorr in the Bruker Esquire. The two methods agree closely in the range of temperatures used in this study. Figure 6.4b shows the results of fitting an experimental breakdown curve to one calculated for the a_4^+ ion of YGGFL. The dots are experimental points, with CID voltage converted to internal temperature via the above method [2], and the lines represent peak

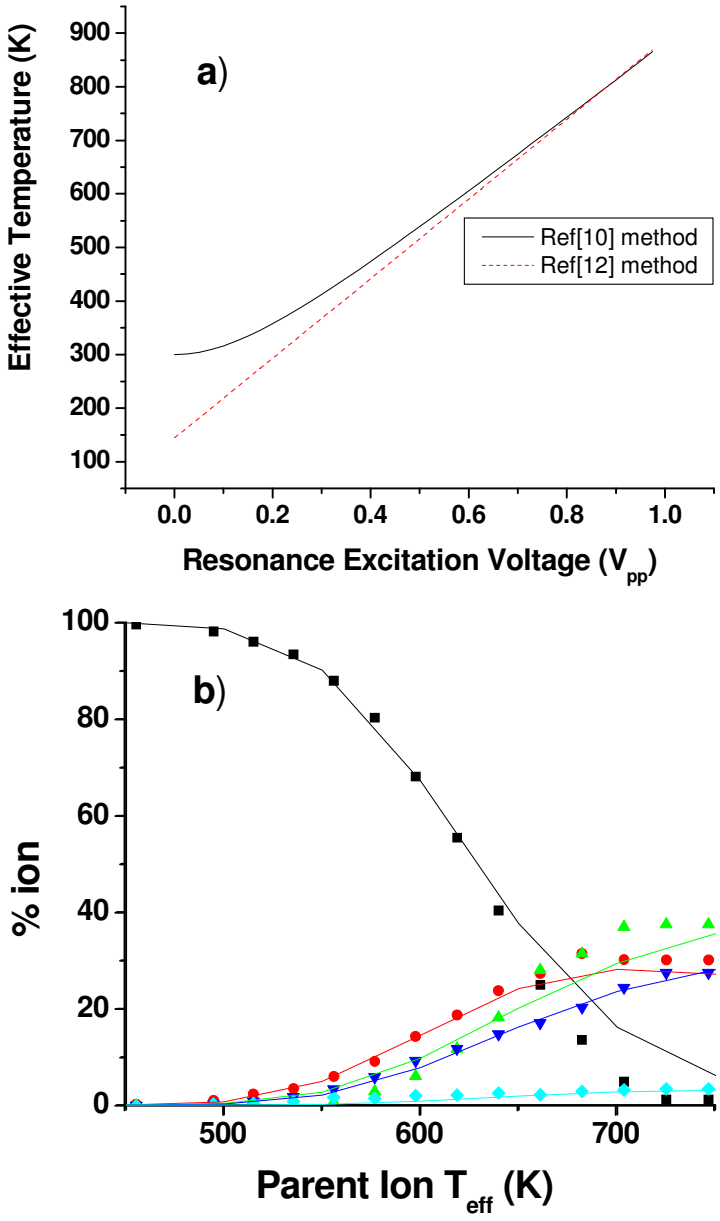

Figure 6.4. a) Comparison of two methods for calculating the internal temperature of ions during conventional CID. Solid line is method from Ref[2], dotted line is method from Ref[4] b) Fit of experimental breakdown curves to calculated breakdown curves for the a_4^+ ion of YGGFL, using Ref[2] method for voltage to T_{eff} transformation. Symbols are as in figure 6.3.

intensities calculated at 10 K intervals. The actual resonance excitation voltage used by the Bruker Esquire was measured with a Tetronix TDS 420 digital oscilloscope, triggered off a Stanford Research DG535 pulse generator, which in turn was triggered by a signal produced by the Esquire electronics during the ion gating period of the CID experiment. The on-screen requested voltage was found to match the measured voltage, as long as the "Fast Calc" button on the MS/MS screen was not selected. The dissociation pathways of the four ions in this study are given in Scheme 6.1. The dissociation pathways for $[YGGFL+H]^+$ had been elucidated previously. [1, 20, 21] The breakdown curve procedure was carried out for all the relevant ions, that is, for all the ions that have dissociation products coming from $[YGGFL+H]^+$ in Scheme 6.1.

Scheme 6.1: Dissociation pathways for a) $[YGGFL+H]^+$ b) $[YGXFL+Na]^+$ c) $[CH_3COONa]_6Na^+$ RA denotes the rearrangement ion at 323 u[1]

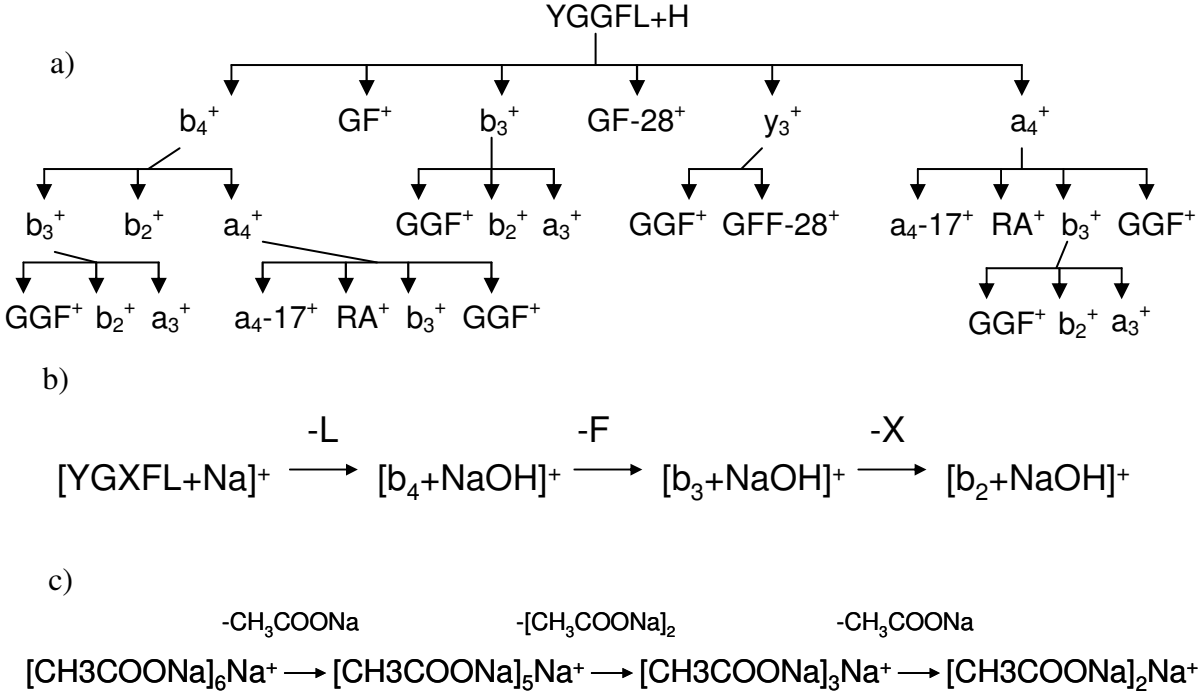

6.3.5. Product Ion Internal Energy

Once a set of E_o and S values is found for each unimolecular reaction, two more procedures must be completed before a full mass spectrum, one that includes all consecutive and competitive dissociations, can be calculated. The first procedure is the calculation of the internal energy distribution of the product ions that consecutively dissociate. This distribution is given by Equation 6.7, [13]

$$p(E,\varepsilon) = \frac{\rho_1(\varepsilon)\rho_2(E - E_o - \varepsilon)d\varepsilon}{\int_0^{E-E_o} \rho_1(\varepsilon)\rho_2(E - E_o - \varepsilon)d\varepsilon} \qquad \text{(Equation 6.7)}$$

where $p(E,\varepsilon)$ is the internal energy distribution of the product ion (given a parent ion internal energy of E), ε is the internal energy of the product ion, $\rho_1(\varepsilon)$ is the density of states of the product ion, and $\rho_2(E-E_o-\varepsilon)$ is the density of states of the product neutral. The procedure for finding the final $p(E, \varepsilon)$ is outlined in figure 6.5. Figure 6.5a shows the internal energy distribution of those parent ions that had enough internal energy to dissociate. $p(E,\varepsilon)$ was then calculated at each E represented by the dots in Figure 6.5a. The $p(E,\varepsilon)$ curves are shown plotted together in Figure 6.5b. These curves were then summed and multiplied by a normalizing factor so that the integral of the final curve in Figure 6.5c equaled one. This final $p(E)$ curve is then used to calculate the intensities of the next generation product ions.

6.3.6. Final Scaling of Calculated Intensities

Finally, a set of parent and product ion intensities can be calculated for each generation of ions. However, each generation's intensity is normalized to one, because each $p(E)$ curve has an integral equal to one. Therefore, each generation of product ions must be scaled by the intensity of its precursor. For example, in Equation 6.8, if 80% of ABC^+ goes

to AB^+, and 25% of AB^+ goes to A^+, then in the actual MS/MS spectrum, ABC^+ has relative intensity 20%, AB^+ has relative intensity 60%, and A^+ has relative intensity 20%.

$$\underset{20\%}{ABC^{*+}} \longrightarrow \underset{80\%}{AB^+ + C}$$

(Equation 6.8)

$$\underset{75\%}{\{AB^+} \longrightarrow \underset{25\%}{A^+ + B\}} \xrightarrow{\text{x } 0.80} \underset{60\%}{AB^+} \longrightarrow \underset{20\%}{A^+ + B}$$

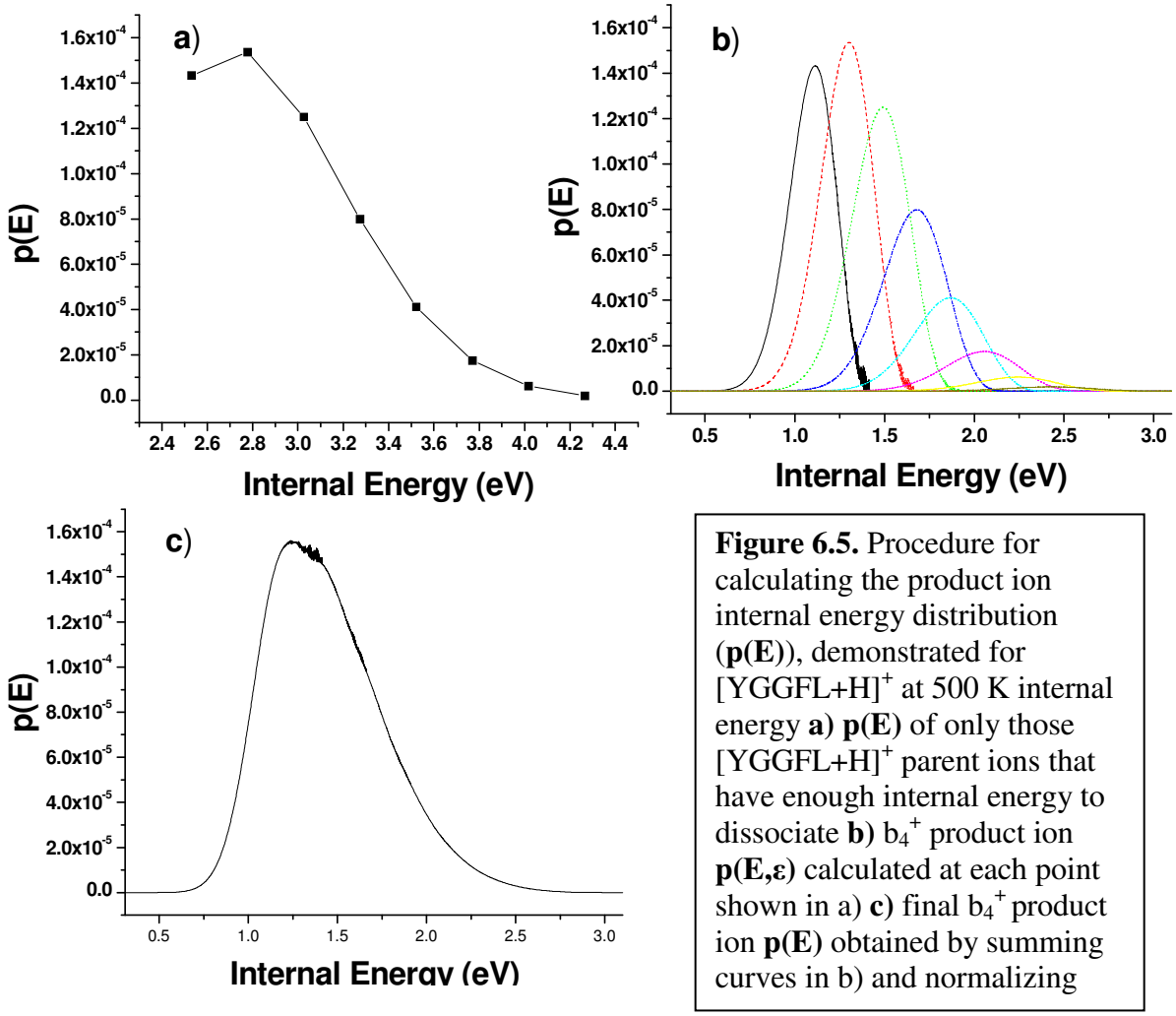

Figure 6.5. Procedure for calculating the product ion internal energy distribution (**p(E)**), demonstrated for $[YGGFL+H]^+$ at 500 K internal energy **a) p(E)** of only those $[YGGFL+H]^+$ parent ions that have enough internal energy to dissociate **b)** b_4^+ product ion **p(E,ε)** calculated at each point shown in a) **c)** final b_4^+ product ion **p(E)** obtained by summing curves in b) and normalizing

6.4. Results and Discussion

6.4.1. RRKM Parameters

The E_o and S values obtained by fitting breakdown curves are shown in Table 6.2. Critical energies for the $[YGGFL+H]^+$ to b_4^+ transition and b_4^+ to a_4^+ transition were taken from the literature [22], and S was varied to fit the breakdown curves. Initial estimates for the parameters of other reactions could be determined by comparing the supplementary voltage at the onset of dissociation of an unknown pathway to a known pathway. Other studies have shown that the values obtained in the breakdown curve method are not reliable as absolute thermodynamic values if there is more than one reaction in competition.[18] If a parent ion dissociates by a low and high energy pathway, the low energy pathway will compete with further activation of the parent ion, lessening the amount of the high energy product ion that will form. However, within the limits of the conventional CID experiment, the parameters in Table 6.2 were able to accurately describe the dissociation of the parent ions.

Table 6.2a: RRKM parameters derived from fitting of breakdown curves for $[YGGFL+H]^+$. RA denotes the rearrangement ion at 323 u [1]

Parent Ions	**Product Ions**						
		b_4^+	**a_4^+**	**b_3^+**	**y_3^+**	**GF^+**	**$GF\text{-}28^+$**
$[M+H]^+$	**E_o(eV)**	1.10	1.17	1.17	0.96	1.09	1.07
	S	0.83	0.82	0.84	1.12	0.97	1.00
b_4^+		a_4^+	b_3^+	b_2^+			
	E_o(eV)	1.32	1.37	1.41			
	S	0.42	0.45	0.49			
a_4^+		a_4^+-NH_3	RA^+	b_3^+	GGF^+		
	E_o(eV)	1.605	1.69	1.685	1.63		
	S	0.63	0.57	0.58	0.67		
b_3^+		b_2^+	a_3^+	GGF^+			
	E_o(eV)	1.22	1.19	1.18			
	S	0.85	0.93	1.07			
y_3^+		GF^+	$GF\text{-}28^+$				

	E_o(eV)	1.27	1.45				
	S	0.70	0.60				

Table 6.2b: RRKM parameters derived from fitting of breakdown curves for $[YGAFL+Na]^+$, $[YGGFL+Na]^+$, $[CH_3COONa]_6Na^+$

Parent Ions	**Product Ions**			
$[YGAFL+Na]^+$		**$[b_4+NaOH]^+$**	**$[b_3+NaOH]^+$**	**$[b_2+NaOH]^+$**
	E_o(eV)	1.30	1.22	1.40
	S	0.84	0.84	0.97
$[YGGFL+Na]^+$		**$[b_4+NaOH]^+$**	**$[b_3+NaOH]^+$**	**$[b_2+NaOH]^+$**
	E_o(eV)	1.31	1.40	1.78
	S	0.84	0.84	0.97
$[CH_3COONa]_6Na^+$		**$[CH_3COONa]_5Na^+$**	**$[CH_3COONa]_3Na^+$**	**$[CH_3COONa]_2Na^+$**
	E_o(eV)	1.05	1.13	1.04
	S	0.60	0.60	0.80

6.4.2. Comparison of Simulation and Experiment

When the first, preliminary simulations were performed, it was observed that product ions were formed with more internal energy than expected. This was clear from observing the b_4^+/a_4^+ ratio of YGGFL, which has been used as an indicator of the internal energy deposited into the parent ion.[23, 24] Typically for YGGFL, the b_4^+/a_4^+ ratio is much greater than one at low CID voltages, and makes a transition to less than one as CID voltage is raised. In the first simulations, the b_4^+/a_4^+ ratio was less than one as soon as b_4^+ was formed, indicating that b_4^+ was being formed from $[YGGFL+H]^+$ with an average internal energy much higher than the critical energy for dissociation to a_4^+ of 1.32eV. Experimentally, however, when product ions are formed they are no longer in resonance with the CID voltage (their mass and therefore secular frequency in the ion trap has changed) and collisions with the He bath gas have an overall cooling effect instead of an activating effect. Thus, product ions possibly are cooled significantly before they dissociate.[24] A collisional cooling term, k_{cc}, was therefore subtracted from the RRKM calculated rates to obtain the final dissociation

rate of the product ions, as in Equation 6.9. The collisional cooling term is not subtracted from the dissociation rates of the parent ions because they are being accelerated by the excitation field, and therefore the probability of a collision resulting in a loss of internal energy is much smaller.

$$k_{final} = k_{reaction} - k_{cc} \qquad \text{(Equation 6.9)}$$

The collisional cooling rates of peptides in a QITMS at 1 mTorr have been calculated previously.[25] When the diffuse scattering method is applied to YGGFL[25], the resulting k_{cc} is 1800 s^{-1} when activated to 830 K, and 1100 s^{-1} when activated to 545 K. A recent experimental study in our lab found this rate to be 400 s^{-1} for YGGFL at 1 mTorr when activated for 5 ms with a 50 W CO_2 laser (an activation of 90 K or 0.9 eV).[26, 27] This result agrees with the master equation modeling[25], where extrapolation of the master equation data for an ion with the number of degrees of freedom of YGGFL yields k_{cc}=600 s^{-1} for a 300 K activation. The best results were found when k_{cc}=500-2000 s^{-1}. 2000 s^{-1} was used in the results shown. This number, which was obtained empirically, is reasonable when compared to the above theoretical and experimental values. Figure 6.6 shows the results of comparing simulated to experimental MS/MS spectra for conventional and HASTE CID. The sum of the squared differences in relative peak intensities between experiment and calculation was used to find the temperature that gave the best fit. Differences in internal temperature between HASTE and conventional CID, as opposed to absolute temperature values, are more informative for analyzing the results across all the ions studied, because disparities in ion structure and vibrational modes have an influence on the calculated *p(E)* at a given temperature. For the sodiated peptide ions, the internal temperature of the HASTE activated parent ions was 80-90 K higher than the conventional CID activated ions, while the sodiated

cluster ion had a difference of 115 K. The protonated peptide ion, YGGFL, was activated 285 K higher with HASTE than conventional CID. Table 6.3 summarizes this temperature data. The above temperature differences translate to an average parent ion internal energy about 1.0 eV higher for the sodiated ions, and about 3.5 eV higher for protonated YGGFL. The resulting increase in product ion intensities for HASTE compared to conventional CID is apparent in Figure 6.6a-h. The result that the protonated ion $[YGGFL+H]^+$ was activated to much higher internal temperature than the sodiated ions stands out. This higher calculated temperature might be explained by the complexity of the $[YGGFL+H]^+$ dissociation pathways. The many competitive dissociations present may compound the error in determining dissociation parameters, and a Boltzmann distribution might be a worse approximation for $[YGGFL+H]^+$ internal energies after HASTE activation than for conventional CID. It should be noted that if only a_4^+, b_4^+, and $[M+H]^+$ are considered for $[YGGFL+H]^+$, then an activated temperature of 650 K results, which is in better agreement with the sodiated ion data.

Table 6.3: Effective Temperatures Achieved During Conventional CID and HASTE CID

	$[YGAFL+Na]^+$	**$[YGGFL+Na]^+$**	**$[YGGFL+H]^+$**	**$[CH_3COONa]_6Na^+$**
Conventional T_{eff}(K)	610	675	545	500
HASTE T_{eff}(K)	690	765	830	615
ΔT_{eff}(K)	80	90	285	115

The calculated intensities of the $[b_2+NaOH]^+$ ions and $[CH_3COONa]_2Na^+$ ion did not match the experiment very well, as is seen in Figure 6.6, even though the breakdown curves from their respective parent ions had a very good fit.(not shown) It is possible that the later generation ions are formed through multiple pathways, which could be determined through

double resonance experiments. Overall, there is a good visual fit between experimental and simulated CID spectra. This lends some credence to the original approximation that a thermal distribution of ion internal energies could be assumed for CID activated parent ions.

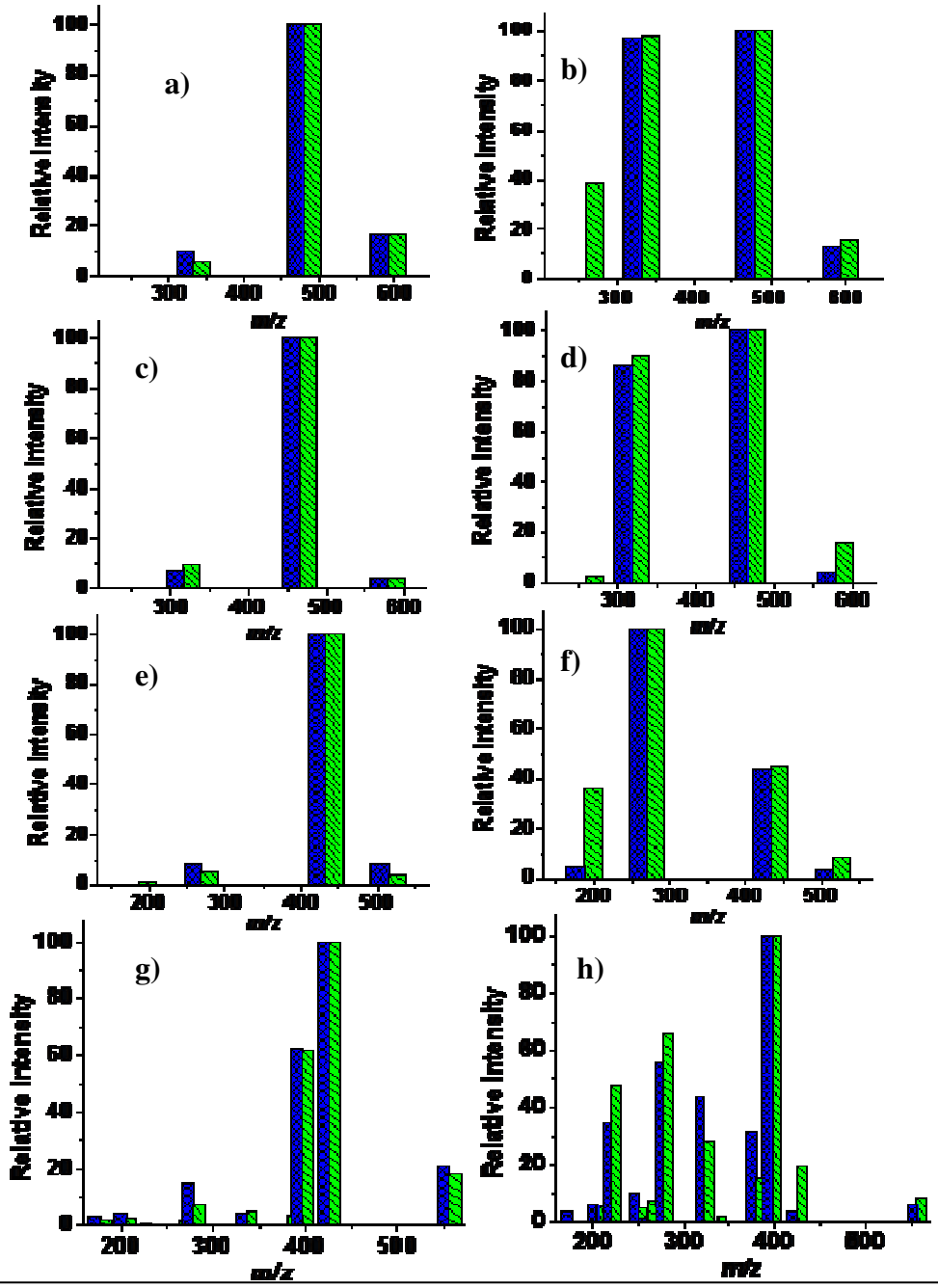

Figure 6.6. Blue, x-striped boxes are calculated ion abundances, green, diagonally-striped boxes are experimental ion abundances. Calculations were done at 1 mTorr with $k_{cc} = 2000$ s^{-1}. (a)(b) Conventional and HASTE CID for $[YGAFL+Na]^+$, where theoretical effective temperatures were 610 K and 690 K, respectively. (c)(d) Conventional and HASTE CID for $[YGGFL+Na]^+$, where theoretical effective temperatures were 675 K and 765 K, respectively. (e)(f) Conventional and HASTE CID for $[CH_3COONa]_6Na^+$, where theoretical effective temperatures were 500 K and 615 K, respectively. (g)(h) Conventional and HASTE CID for $[YGGFL+H]^+$, where theoretical effective temperatures were 545 K and 830 K, respectively.

6.5. Conclusions

The temperature of ions activated by conventional CID and HASTE CID has been estimated via a comparison of theoretical MS/MS spectra calculated at different parent ion effective temperatures with experimental MS/MS spectra. The effect of collisional cooling had to be included in the calculations to adequately fit the experimental to calculated spectra. Reaction parameters for each dissociation pathway were determined by fitting experimental and theoretical breakdown curves. The results indicate that the sodiated ions were activated to an average internal temperature of 95 K higher, and the protonated ion was activated 285 K higher using HASTE CID over conventional CID. This translates into an average internal energy of 1.0 eV higher for the sodiated ions and 3.5 eV higher for the protonated ion. As mentioned in the results section, the protonated ion result is somewhat suspect, and the difference in internal temperatures for the protonated ion may in fact be closer to 105 K, 1.0 eV higher internal energy. This study does not claim to provide exact values of the extent of ion activation for the investigated ions, rather, an estimation has been made of the advantage of HASTE CID over conventional CID in terms of internal temperature increase. Relatively simple algorithms were used describe the dissociation kinetics of the ions fairly accurately, as is apparent from Figure 6.6. The likelihood that a thermal internal energy distribution would approximate the activation of ions by HASTE CID was questionable in the onset of the study, because the HASTE CID process probably involves a smaller number of much higher energy collisions than conventional CID. Activation by HASTE may therefore be comparable to higher collision energy CID, such as those obtained on a triple quadrupole instrument.

6.6. References

1. Vachet, R. W.; Bishop, B. M.; Erickson, B. W.; Glish, G. L. *Novel Peptide Dissociation: Gas-Phase Intramolecular Rearrangement of Internal Amino Acid Residues*. J. Am. Chem. Soc. **1997,** *119*, 5481-5488.

2. Goeringer, D. E.; McLuckey, S. A. *Evolution of Ion Internal Energy During Collisional Excitation in the Paul Ion Trap: A Stochastic Approach*. Journal of Chemical Physics **1996,** *104*, 2214-2221.

3. Marzluff, E. M.; Beauchamp, J. L. In *Large Ions: Their Vaporization, Detection and Structural Analysis*; Baer, T. N., Cheuk-Yiu; Powis, Ivan, Ed.; John Wiley and Sons Ltd: Chichester, 1996, pp 115-143.

4. Gabelica, V.; Karas, M.; De Pauw, E. *Calibration of Ion Effective Temperatures Achieved by Resonant Activation in a Quadrupole Ion Trap*. Anal. Chem. **2003,** *75*, 5152-5159.

5. Laskin, J.; Byrd, M.; Futrell, J. *Internal energy distributions resulting from sustained off-resonance excitation in FTMS. I. Fragmentation of the bromobenzene radical cation*. Int. J. Mass Spectrom. **2000,** *195/196*, 285-302.

6. Plass, W. R.; Cooks, R. G. *A Model for Energy Transfer in Inelastic Molecular Collisions Applicable at Steady State or Non-Steady State and for an Arbitrary Distribution of Collision Energies*. J Am Soc Mass Spectrom **2003,** *14*, 1348–1359.

7. Asano, K. G.; Goeringer, D. E.; McLuckey, S. A. *Thermal Dissociation in the Quadrupole Ion Trap: Ions Derived From Leucine Enkephalin*. Int. J. Mass Spectrom. **1999,** *185/186/187*, 207-219.

8. Cunningham, C., Jr.; Glish, G. L.; Burinsky, D. J. *High Amplitude Short Time Excitation: A Method to Form and Detect Low Mass Product Ions in a Quadrupole Ion Trap Mass Spectrometer*. J Am Soc Mass Spectrom **2006,** *17*, 81 - 84.

9. Louris, J. N.; Cooks, R. G.; Syka, J. E. P.; Kelley, P. E.; Stafford, G. C.; Todd, J. F. J. *Instrumentation, Applications, and Energy Deposition in Quadrupole Ion Trap Mass Spectrometry*. Anal. Chem. **1987,** *59*, 1677-1685.

10. Douglas, D. J. *Mechanism of the Collision-Induced Dissociation of Polyatomic Ions Studied by Triple Quadrupole Mass-Spectrometry*. J. Phys. Chem. **1982,** *86*, 185-191.

11. Baer, T.; Mayer, P. M. *Statistical Rice-Ramsperger-Kassel-Marcus quasi-equilibrium theory calculations in mass spectrometry*. J. Am. Soc. Mass Spectrom. **1997,** *8*, 103-115.

12. Baer, T.; Hase, W. L. *Unimolecular Reaction Dynamics*; Oxford University Press: New York, 1996.

13. Vestal, M. L. *Theoretical studies on the unimolecular reactions of poly-atomic molecule ions*. Journal of Chemical Physics **1965,** *43*, 1356-69.

14. *LabVIEW [software] 7.1 National Instruments Corporation.*

15. Frisch, M. J. *Gaussian 03, Revision C.02 Gaussian, Inc., Wallingford CT*. Gaussian 03, Revision C.02 Gaussian, Inc., Wallingford CT **2004**.

16. Scott, A. P.; Radom, L. *Harmonic Vibrational Frequencies: An Evaluation of Hartree-Fock, Moeller-Plesset, Quadratic Configuration Interaction, Density Functional Theory, and Semiempirical Scale Factors*. J. Phys. Chem. **1996,** *100*, 16502-16513.

17. Foresman, J. B., Frisch Aeleen *Exploring Chemistry with Electronic Structure Methods*; Gaussian, Inc.: Pittsburgh, PA, 1993.

18. Laskin, J.; Denisov, E.; Futrell, J. H. *Fragmentation energetics of small peptides from multiple-collision activation and surface-induced dissociation in FT-ICR MS*. Int. J. Mass Spectrom. **2002,** *219*, 189-201.

19. Laskin, J.; Denisov, E.; Futrell, J. *A comparative study of collision-induced and surface-induced dissociation. 1. Fragmentation of protonated dialanine*. J. Am. Chem. Soc. **2000,** *122*, 9703-9714.

20. Vachet, R. W.; Ray, K. L.; Glish, G. L. *Origin of Product Ions in the MS/MS Spectra of Peptides in a Quadrupole Ion Trap*. J. Am. Soc. Mass Spectrom. **1998,** *9*, 341-344.

21. Jue, A.; Racine, A. H.; Glish, G. L. Comparison of Dissociation Pathways at Ambient and Elevated Temperatures in a Quadrupole Ion Trap. Nashville, TN, 2004.

22. Schnier, P. D.; Price, W. D.; Strittmatter, E. F.; Williams, E. R. *Dissociation Energetics and Mechanisms of Leucine enkephalin (M+H)+ and (2M+X)+ Ions (X=H, Li, Na, K, and*

Rb) Measured by Blackbody Infrared Radiative Dissociation. J. Am. Soc. Mass Spectrom. **1997,** *8*, 771-780.

23. Vachet, R. W.; Glish, G. L. *Effects of Heavy Gases on the Tandem Mass Spectra of Peptide Ions in the Quadrupole Ion Trap*. J. Am. Soc. Mass Spectrom. **1996,** *7*, 1194-1202.

24. Asano, K. G.; Goeringer, D. E.; Butcher, D. J.; McLuckey, S. A. *Bath Gas Temperature and the Appearance of Ion Trap Tandem Mass Spectra of High-Mass Ions*. Int. J. Mass Spectrom. **1999,** *190/191*, 281-293.

25. Goeringer, D. E.; McLuckey, S. A. *Relaxation of Internally Excited High-mass Ions Simulated under Typical Quadrupole Ion Trap Storage Conditions*. Int. J. Mass Spectrom. **1998,** *177*, 163-174.

26. Black, D. M.; Payne, A. H.; Glish, G. L. *Determination of Cooling Rates in a Quadrupole Ion Trap*. J Am Soc Mass Spectrom **2006,** *17*, 932-938.

27. Goeringer, D. E.; Asano, K. G.; McLuckey, S. A. *Ion internal temperature and ion trap collisional activation: protonated leucine enkephalin*. Int. J. Mass Spectrom. **1999,** *182/183*, 275-288.

Chapter 7

7. On the Time Scale of Internal Energy Relaxation of AP-MALDI and Nano-ESI Ions in a Quadrupole Ion Trap

7.1. Introduction

An understanding of ion internal energy is of primary interest to researchers studying the structures of gas phase ions. As mentioned in **Chapter 1.1.1**, how fast an ion will dissociate, which mechanisms will be involved, and how many products will be observed all have a large dependence on the amount of internal energy in the ion and the experimental time window for dissociation.[1-4] If background information on the dissociation pathways is available, then RRKM theory can determine the dissociation kinetics of the various dissociation pathways as a function of internal energy, and mass spectra or tandem mass spectra (MS/MS) can be predicted. [5-7] Internal energy also dictates the possible three dimensional (3D) structure adopted by the ion, and 3D conformation has been shown to influence dissociation pathways in MS/MS.[8, 9]

Because MS/MS spectra have a dependence on conformation and internal energy, the various factors that determine ion internal energy and how its magnitude might change over the course of an experiment are important to understand. A typical experiment using a QITMS lasts several hundred milliseconds, during which time a large number of variables can effect an ion population's distribution of internal energy. The theoretical calculation of ion internal energy in a QITMS is a complex quantum chemical calculation, in which many factors must be considered, such as the kinetic energy of the ion, the vibrational energy states

of the ion, and the probability of energy transfer from one state to another.[10] These considerations are complicated by the necessary presence of helium (He) bath gas at ~1.3×10^{-3} mbar in the QITMS to improve sensitivity and mass resolution.[11] Other types of mass spectrometers typically operate at pressures low enough to ensure that the flight path of the ion is shorter than the mean free path between collisions with background neutral gas. Conversely, in a QITMS, with several tens of collisions per millisecond, an ion may experience many thousands of collisions over its lifetime in the experiment.[12] Each of these collisions has the potential for changing the internal energy of the ion, ultimately having an effect on the mass spectrum that will be produced.

Indeed, the collision of an ion with a neutral gas molecule is one of the most important means for energy transfer in mass spectrometry, with the most common application of this process being CID. When an ion collides with a neutral molecule such as He, kinetic and internal energy may be inter-converted. Because energy is conserved, Equation 7.1 can be written, where KE_0, KE_F, IE_0 and IE_F are respectively, initial kinetic energy, final kinetic energy, initial internal energy, and final internal energy of the ion and colliding He atom. He, being monoatomic, has no internal energy unless electronically excited in the collision.

$$KE_0^{ION} + IE_0^{ION} + KE_0^{HE} = KE_F^{ION} + IE_F^{ION} + KE_F^{HE} \qquad \text{(Equation 7.1)}$$

The change in internal energy of the ion is the quantity of interest, and so Equation 7.1 may be rearranged to Equation 7.2, where Δ denotes the final value minus the initial value. Consideration of Equation 7.2 shows that an ion may be excited in a collision through a conversion (reduction) of either the ion's or He's kinetic energy, and conversely an ion may

be cooled by transferring its internal energy into an increase in kinetic energy of the ion or He.

$$\Delta IE^{ION} = -\Delta KE^{ION} + -\Delta KE^{HE} \qquad \text{(Equation 7.2)}$$

Whether an ion gains or loses internal energy in a collision depends on the probability of energy transfer between states, and is a problem that has been considered theoretically for a QITMS. [10, 13] In particular, the evolution of peptide internal energy with time due to collisional cooling in a QITMS has been investigated.[13] Plots of calculated internal energy versus time revealed that a series of homologous peptide ions $(AG)_n$, where n=8-32, excited to 450 K would all relax to room temperature in less than 10 ms. Experiments designed to test this theoretical treatment have been published recently[14, 15], where two laser pulses are used to probe ion internal energy as a function of time (see **Chapter 4**). Ions were irradiated with one laser pulse and allowed to cool for a set amount of time before being irradiated again. During the time between pulses, the ions lose internal energy to collisions with He, causing the second laser pulse to dissociate a smaller percentage of parent ions. Using the efficiency of fragmentation as a measure of internal energy, relaxation times for excited ions at typical operating pressures of $9.3\text{-}1.5 \times 10^{-3}$ mbar were observed to be on the order of 5 to 20 milliseconds.

7.1.1. Reexamination of Reported Results

Recently, a study has been reported that concludes internal energy relaxation of peptide ions through He collisions to be a relatively inefficient process requiring several hundred milliseconds when the experiment is conducted in a QITMS.[16] Supporting the results was a cited observation that the process of internal vibrational relaxation through collisions is ~100 times slower than collisional kinetic energy relaxation. If true, the

conclusion could be drawn that if kinetic relaxation takes place in 1-10 ms, then internal energy relaxation must take place in 100-1000 ms. The referenced study described the vibrational relaxation of $N_2^{+\cdot}$ through collisions with a variety of noble gases, in which the cooling process with He was least efficient.[17] It would be an over-simplification, however, to assume that the collision induced vibrational relaxation behavior of $N_2^{+\cdot}$, which has 1 vibrational degree of freedom and a density of states of 1 per cm^{-1} at room temperature, could be used as an accurate predictor of the collision induced vibrational relaxation behavior of a medium sized peptide such as leucine enkephalin (YGGFL), which has 228 degrees of freedom and a density of states of $3.4x10^{36}$ per cm^{-1} at room temperature. As our group has an interest in the mechanisms and kinetics of internal energy transfer processes in mass spectrometry experiments, the study described here undertakes a reexamination of the cited work.

7.1.2. Possible Factors Leading to Discrepancies

An important experimental parameter that could be responsible for the very long predicted relaxation times described in the previous study could be the use of long ion accumulation, or gate, periods (400 ms), and it is on this point that our investigation will focus. The long gate time was justified by Konn et. al. as a desire to accumulate equal numbers of ions over equal lengths of time in a comparison of the internal energies of ions produced by atmospheric pressure matrix assisted laser desorption ionization (AP-MALDI) and nano-electrospray ionization (nano-ESI). Because a lower flux of ions was produced by AP-MALDI, and the QITMS has a finite trapping capacity, it was reasoned that the trapping volume could be "overfilled" in the high ion flux, nano-ESI case such that after 400 ms, equal numbers of ions would be accumulated using both ionization methods. Undeniably, a

plot of ion abundance versus gate time will show abundance leveling off after a time, so the authors' supposition of equal ion populations for both ionization techniques is probably accurate. However, operation of a QITMS under high space charge conditions introduces a new set of variables with respect to ion motion, namely an added dc potential.

The stability equations for a QITMS (Equations 1.4-1.7) help demonstrate the probable effect of this new dc potential. Using Equations 1.4-1.7, one observes that a positive U will decrease an ion's secular frequency. Traditionally, U would be induced instrumentally, but a dc potential can also be induced by a collection of charged particles. A potential induced by a cloud of charged particles is, however, expected to vary as the density of the cloud changes. The ion isolation event immediately preceding CID provides a likely opportunity for a change in ion cloud density. During isolation, the ion cloud is likely to experience several different trapping environments, most notably a gain in kinetic energy as the q_z value approaches a resonant ejection point, and a decrease in the depth of the pseudopotential trapping well as q_z is reduced to the value used for CID. The depth of the pseudopotential well is given in Equation 1.8.[18, 19] The purpose of the present investigation is to demonstrate experimentally and theoretically that these varying trapping environments lead to changes in ion secular frequency when a large population of ions is present. When CID is performed using a single excitation frequency on a population of ions whose secular frequency changes, internal energy measurements based on fragmentation efficiency taken at different times are inevitably inaccurate.

7.2. Methods

Experiments were carried out on two instruments: a Bruker (Billerica, MA) Esquire ion trap for AP-MALDI and nano-ESI experiments, and also a modified Finnigan (San Jose,

CA) ITMS that has been described previously[20], used for supplementary experiments with nano-ESI. The Bruker Esquire has a modified Analytica (Branford, CT) electrospray ionization source which has been fitted with a flared glass capillary [21]. The flared capillary coupled with a Lexan sample holder and Plexiglass mounting assembly create a simple aerodynamic AP-MALDI source as described in **Chapter 2.1.2**.[22, 23] AP-MALDI and nano-ESI were carried out as described in **Chapter 2.1.1** and **2.1.2**. The relative stability of AP-MALDI and nano-ESI generated ions was compared by dissociating the ions *via* CID (with an incremented excitation waveform amplitude) and recording fragmentation efficiency as shown in Equation 1.12.

Figure 7.1 illustrates the scan function (rf trapping voltage applied to the ring electrode changes versus time) for the ITMS experiments. The rf trapping voltage is proportional to the lowest m/z trapped, or "start mass" at any particular time. This condition

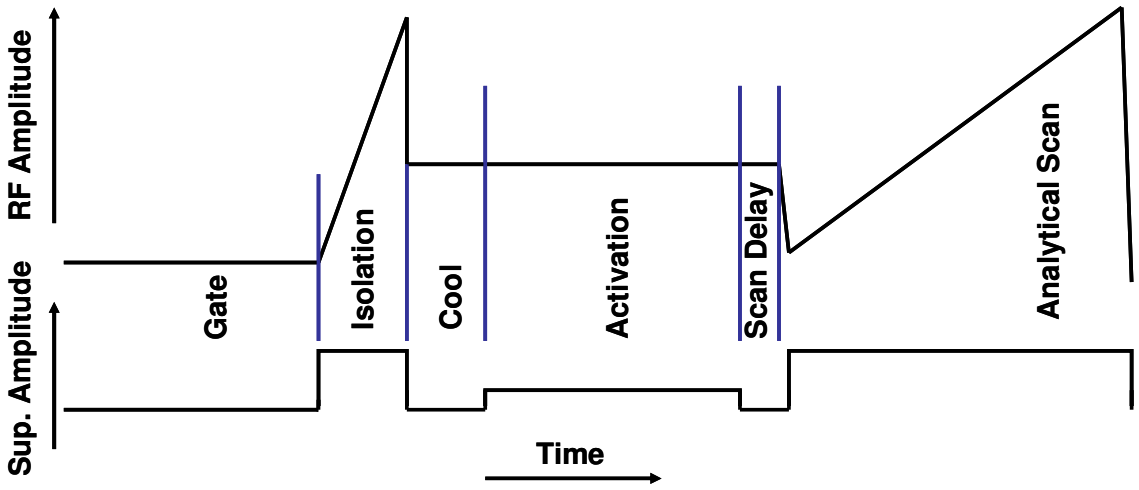

Figure 7.1. Scan function for Finnigan ITMS showing rf trapping voltage as a function of time, and the timing of supplementary waveforms for ion ejection and excitation. Typical times are as follows: Gate = 30 ms, Isolation = 10 ms, Cool time = 30 ms, Activation = 40 ms, Scan Delay = 5 ms. All segments are drawn to scale except the analytical scan segment, which is 5555 Da/sec.

allows “start mass” or “low mass cut-off” to be used interchangeably as the y-axis label. Details about the Bruker scan function were obtained using a digital oscilloscope to monitor the rf voltage on the dynode with the endcaps grounded. The Bruker scan function takes about 90 ms to isolate the ions, with the remainder of the scan function being very similar to that of the ITMS. CID was performed either with the basic scan function depicted in Figure 7.1, or alternatively, with no ion isolation, and FE could be plotted where ΣF in Equation 1.15 is replaced by the intensity of just one selected product ion. To gauge the effect of cooling time on ion dissociation, the time before CID in the scan function was incremented manually for each acquired spectrum. Spectra were acquired as the average of 20 scans, and error bars were calculated as 95% confidence intervals on 5-8 experiment repetitions the same day.

A direct reading of the pressure inside the ion trapping volume is not possible for the Bruker Esquire, because transport of the He bath gas to the ionization pressure gauge is attenuated by conductance limiting electrode spacers. However, previous experiments [22] have demonstrated calibration of the pressure gauge with the ion/molecule reaction of cytochrome c and dimethylamine. These experiments showed a factor of ~100x between ionization gauge pressure and ion trapping volume pressure for the Bruker Esquire. The present experiments were performed at a pressure reading of 3.0×10^{-5} mbar, with the pressure in the trap estimated to be about 3×10^{-3} mbar. The peptides desArg^{1}bradykinin (PPGFSPFR), desbrg^{9}Bradykinin (RPPGFSPF), Sar-Angiotensin II (Sar-RVYIHPF), and angiotensin III antipeptide (GVYVHPV) were purchased from Sigma Aldrich (St. Louis, MO) and used without further purification as in **Chapter 2.1**.

7.2.1. Equalizing Number of Ions for Both Ionization Techniques

To minimize the effects of space charge, while standardizing conditions as much as possible between AP-MALDI and nano-ESI, the same ion accumulation time of 30 ms was used in both cases. An accumulation time of 30 ms is only enough time for 1 laser pulse for AP-MALDI, and many fewer ions are produced by AP-MALDI than by nano-ESI over a given time period for the current experiments. Therefore, to equalize the ion populations between the two experiments, the rf voltage amplitude of the transfer hexapole was decreased for nano-ESI. In most cases, the maximum 700 V_{pp} hexapole voltage was used for AP-MALDI, and ~100 V_{pp} was used for nano-ESI. A 30 ms gate time only allows time for one laser pulse for AP-MALDI, but this was enough to accumulate a sufficiently large ion population for these experiments. The ion abundance in arbitrary units of the parent ion for the Bruker experiments was ~3-5x10^3, while the maximum ion abundance allowed by the DAC was approximately 1x10^8.

7.2.2. Higher Time Resolution Cooling Study

The Finnigan ITMS was used to examine the effect of cool time on CID for nano-ESI ions. The ITMS software controls all scan function parameters with microsecond resolution. Cooling time and CID excitation frequency were varied automatically under software control. Isolation was achieved by increasing the rf amplitude for 10 ms to eject ions having mass-to-charge ratios (m/z) less than the parent ion, while no attempt was made to isolate higher m/z ions. Spectra were acquired as the average of 25 scans, and error bars were calculated as 95% confidence intervals on 5 experiment repetitions the same day. The electrodes do not have conductance limits to gas transport, so the measured ionization gauge pressure is the ion trapping volume pressure, after correction for the ionization potential of

He (i.e., multiplying by 7 to correct for the lower gauge sensitivity). A pressure of 9.3×10^{-4} mbar of He was used for the experiments.

7.2.3. Ion Trajectory Calculations

SIMION 7.0 was used to simulate the ion isolation event. Simulation parameters were as in **Chapter 2.4.3**. Ion position was monitored at regular time intervals and Fourier transforms of the time domain data performed to gauge ion secular frequency under different space charge conditions. The user program for doing this work is in **Appendix B**.

7.3. Theory

7.3.1. Calculation of Space Charge Effects

Some of the effects of ion interactions can be estimated using calculations having various degrees of sophistication. Most pertinent to the present experiments is an estimation of the dc voltage magnitude induced by a group of ions, which can result in a shift in ion secular frequency. The voltage induced at a particular distance (radius) r away from a point charge q is given by the first term in Equation 7.3, where ε_o is the permittivity of vacuum. The voltage induced by a number of point charges can be expressed as a sum as in Equation 7.3.

$$V = \frac{q_1}{4\pi\varepsilon_o r_1} + \frac{q_2}{4\pi\varepsilon_o r_2} + \cdots \qquad \text{(Equation 7.3)}$$

7.3.2. Sphere of Constant Charge Density

The simplest case calculation assumes that the ions are distributed uniformly in a sphere of a given radius. In a general sense, the voltage induced by a volume charge is given in Equation 7.4,

$$V = \frac{1}{4\pi\varepsilon_0} \int \frac{\rho}{r} d\tau \qquad \text{(Equation 7.4)}$$

where ρ is charge density, r is distance to a particular point, and $d\tau$ is the volume element[24]. The integral can be numerically approximated as shown in Equation 7.5, where N is number of ions, r_s is the radius of the sphere and r_i is the radius of each particular volume element.

$$V = \frac{1}{4\pi\varepsilon_0}\sum_i \frac{Nq}{r_s^3}\frac{1}{r_i}\cdot[r_i^3 - r_{i-1}^3] \qquad \text{(Equation 7.5)}$$

7.3.3. Gaussian Distribution

A more realistically shaped ion cloud can be described using a Gaussian distribution.[25, 26] In this case, higher dc voltages would be expected in the center of a Gaussian distribution of charges than in the center of a sphere of constant charge density of similar size, because in the former case most of the ions are located at the center of the distribution. With a distribution of a given size and a certain number of ions, the magnitude of induced voltage at the center can be estimated using Equation 7.6, where p is the width of each slice of the distribution, and σ is the standard deviation of the distribution.

$$V = \frac{2}{4\pi\varepsilon_0}\cdot\sum_{n=0}^{\infty}\sum_{r=np}^{r=(n+1)p}\frac{1}{\sigma\sqrt{2\pi}}\exp\left[-\frac{r^2}{2\sigma^2}\right]\cdot\frac{Nq}{\left(\frac{np+(n+1)p}{2}\right)} \qquad \text{(Equation 7.6)}$$

7.4. Results and Discussion

7.4.1. Comparison of AP-MALDI vs. nano-ESI

Figure 7.2 shows results of experiments done using the Bruker Esquire. Plots of fragmentation efficiency versus CID excitation voltage show that for the peptides studied, the onset of dissociation and 50% fragmentation efficiency point for AP-MALDI comes at an equal or greater energy than for nano-ESI. One conclusion based on these data is that the AP-MALDI ions have either slightly lower internal energies or slightly higher critical energies of dissociation. A previous study of the dissociation onset energies of liquid

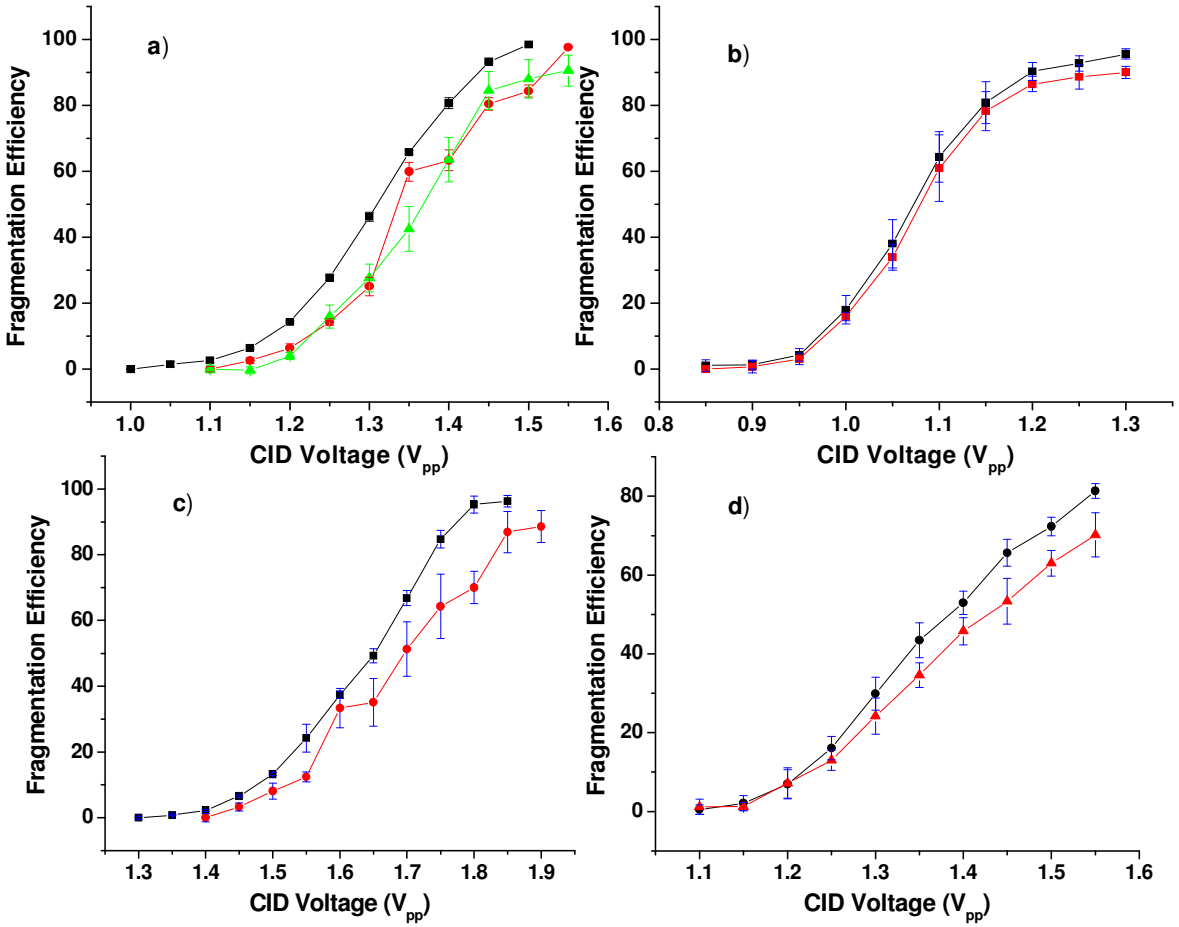

Figure 7.2. Fragmentation efficiency versus CID excitation voltage. Squares denote nano-ESI, circles are AP-MALDI using DHB matrix, and triangles are AP-MALDI using CHCA matrix. a) desArg^{9}bradykinin b) angiotensin III antipeptide c) Sar-angiotensin II d) desArg^{1}bradykinin

secondary ion mass spectrometry (LSIMS) ions versus nano-ESI ions found that the nano-ESI ions dissociated with lower excitation energies than the LSIMS ions, suggesting that the LSIMS ions had either lower internal energies, or higher critical energies of dissociation.[27] However, in the LSIMS case, as well as the present AP-MALDI case, the hypothesis that nano-ESI ions have different internal energies is doubtful, based on studies of internal energy cooling in a QITMS (*vide supra*). The cited works show with theory and experiment that the time-frame for excited ions to relax to equilibrium internal energy via collisional cooling at 1.33×10^{-3} mbar is on the order of 10 ms. Ongoing research in our laboratory on cooling rates

of excited peptide ions indicates that at $9.3x10^{-4}$ mbar equilibrium internal energy is reached in about 20 milliseconds. Therefore, if the ion internal energies imparted by AP-MALDI and nano-ESI are the same, then any difference in dissociation behavior must be due to different critical energies of dissociation, which may be attributable to different ion conformations. The plots in Figure 7.3 show fragmentation efficiency versus cool time before CID, demonstrating little or no change in dissociation as a function of time. This result suggests that any excess or difference in internal energy between ionization methods has already been dissipated through collisions with the bath gas. Figure 7.3c shows fragmentation efficiency versus cool time with shorter gate times, no parent ion isolation, and 10 ms CID, to minimize the amount of collisional cooling possible before dissociation. In this case, a slight decrease in dissociation is observed in the first 10 ms, after which fragmentation efficiency stabilizes. Thus, even at the limit of minimum collisional cooling before dissociation, there are no significant changes in fragmentation efficiency over time.

The present results also contradict recent conclusions made by Konn et al. on the effects of ionization mechanism on internal energy and cool time prior to CID.[16] Differences in "50% fragmentation efficiency" points between nano-ESI and AP-MALDI ions were explained based on differences in gas-phase basicities between the analyte and the MALDI matrix, which has shown some correlation to ion internal energy in a study of dissociation rate of a dinucleotide with several different matricies.[28] However, that work was carried out in an FT-ICR spectrometer at an approximate pressure of $1.3x10^{-8}$ mbar, which did not permit ions to thermalize before CID. Therefore, any differences in internal energy deposition resulting from ionization could be preserved. The conditions of AP-MALDI and ~$1.3x10^{-3}$ mbar storage in a QITMS are markedly different than conventional MALDI under

high vacuum conditions in an FT-ICR spectrometer. The study of Konn and coworkers reported dramatic changes in fragmentation efficiency versus cool time over several hundred milliseconds. An initial increase in dissociation was observed in the first 100 ms, followed by a gradual decrease in dissociation extending out to 250 and even 1000 ms in one example. In the next series of experiments, we will show that ion secular frequency can change substantially under high space charge conditions, which is both interesting in itself and also may offer an explanation for the results of Konn and coworkers that is consistent with measured collisional cooling rates.

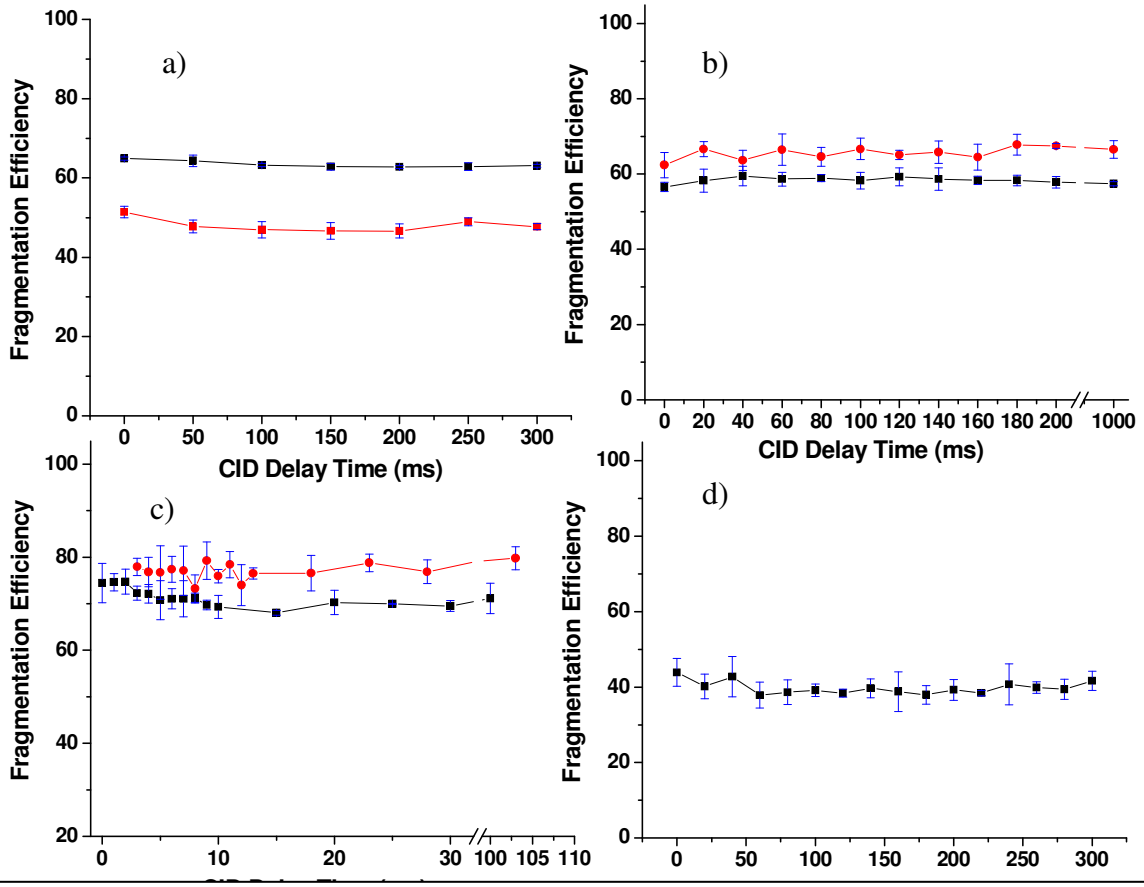

Figure 7.3. The effect of cooling time before CID on fragmentation efficiency. Squares denote nano-ESI, circles are AP-MALDI using DHB matrix, and triangles are AP-MALDI using CHCA matrix. a) desArg^{9}bradykinin b) angiotensin III antipeptide c) angiotensin III antipeptide, 1 ms gate nano-ESI, 4 ms gate AP-MALDI, no precursor ion isolation d) desArg^{1}bradykinin.

7.4.2. *Effect of Ion Population on Cooling Curves*

Figure 7.4a shows fragmentation efficiency of desArg^{1}bradykinin versus cooling time for gate times of 20 and 200 ms. The trace for 200 ms gate time shows a dramatic decrease in the first few milliseconds after ion isolation and then levels off. In Figure 7.4b, the same initial drop in fragmentation efficiency is observed for the angiotensin III antipeptide. The second data point indicates a higher efficiency than the first, followed by a rapid decrease to a base level by ~2 ms. The shape of the plot in Figure 7.4b resembles the results reported by Konn et. al. except that the time scales differ by 2 orders of magnitude. Their interpretation was that an initial increase in dissociation after isolation could be caused by the kinetic dampening of the ion cloud after parent ion isolation at higher q_z value. While that explanation could be part of the answer, the disparity between the results for large and small ion populations in Figure 7.4a raises the possibility that space charge effects could be playing

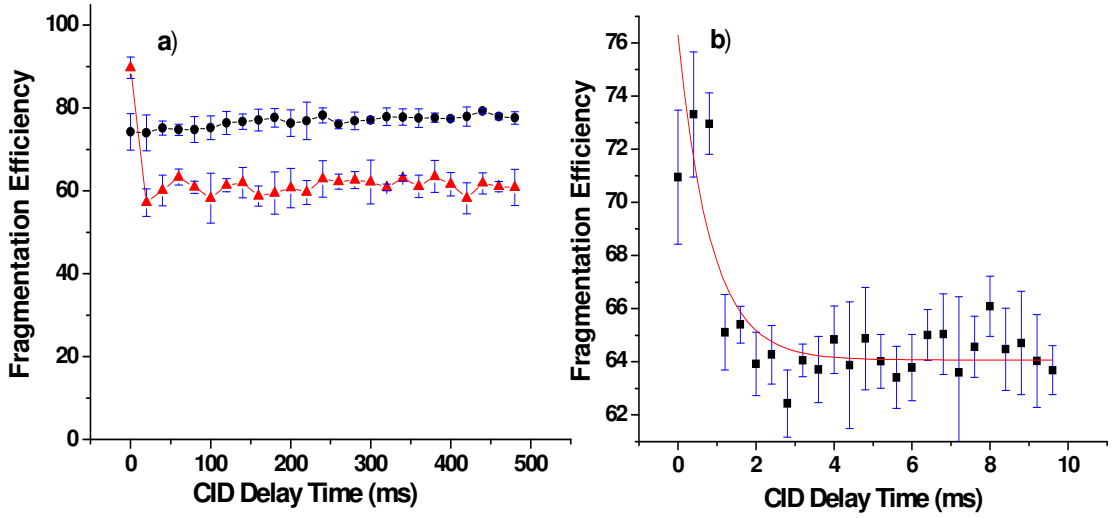

Figure 7.4. Effect of cooling time before CID on fragmentation efficiency. a) desArg^{1}bradykinin, squares and circles correspond to 20 ms, 590 mV_{pp} excitation and 200 ms, 400 mV_{pp} ion accumulation time, respectively. b) angiotensin III antipeptide, short time scale experiment. Solid red curve is exponential decay fit to data with decay constant of 1197 s^{-1}.

a significant role. Space charge has been used as a tool for effecting dissociation, *via* a technique called multipole storage assisted dissociation (MSAD).[29] MSAD is a method of doing CID primarily in hexapole or octopole ion storage devices, wherein space charge causes the ion cloud to expand, resulting in acceleration of the ions at larger radii where the electric field is larger. Subsequent higher energy collisions with background neutral gas then cause fragmentation.[30] Hexapole and octopole ion traps, due to the inherent non-linear relationship between radial position and electric field, might be expected to exhibit MSAD more effectively than a quadrupole, where the relationship is linear between electric field and radial position. Nevertheless, MSAD has been observed in a linear quadrupole.[31] For this reason, experiments were performed with both the Bruker Esquire and ITMS to try to form ions by MSAD. The results showed no dissociation when large ion populations were trapped and allowed time to fragment without any supplementary excitation waveform. Consequently, our attention shifted from MSAD to the prospect that ion secular frequencies could be changing over time as the ion cloud expands and condenses, resulting in varying overlap between ion secular frequency and excitation frequency.

7.4.3. Experimentally Measured Shifts in Secular Frequency

The effect of varying the frequency of the CID excitation voltage is exemplified in Figures 7.5a and 7.5b and summarized in Table 7.1. Both plots display two curves, one representing no cooling time (squares), and a second showing 100 ms between isolation and CID (circles). Figure 7.5a uses a 50 ms gate time, while Figure 7.5b uses 200 ms gate time. In Figure 7.5a, a shift in the center of the peak to -100 Hz is apparent at the longer CID delay time. In Figure 7.5b a more pronounced shift of -400 Hz at the higher gate time is observed. The trend is an increasingly larger shift to lower frequencies as ion population increases.

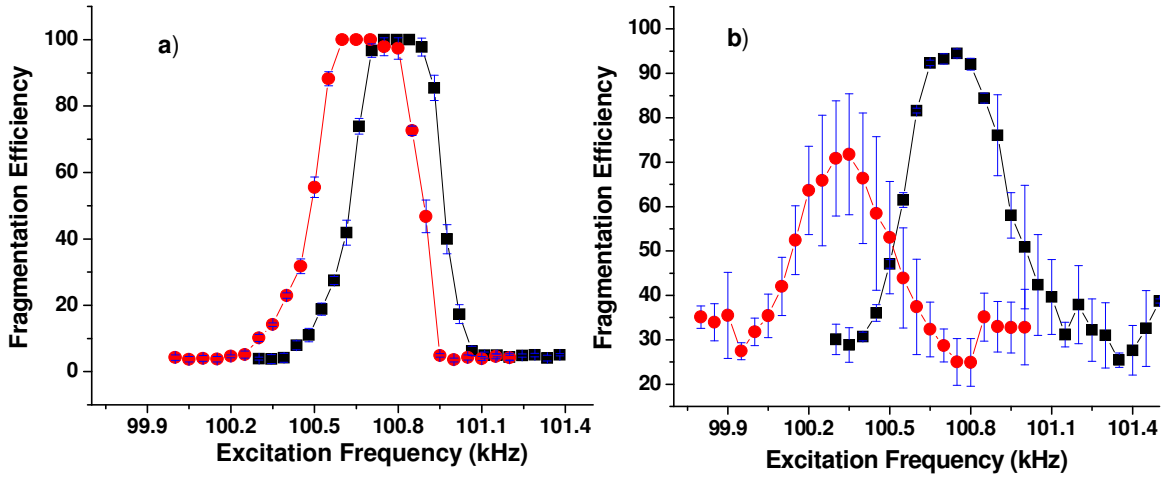

Figure 7.5. Fragmentation efficiency versus CID excitation frequency, squares are no delay between isolation and CID, circles are 100 ms delay between isolation and CID a) 50 ms gate time, 400 mV_{pp} squares, 800 mV_{pp} circles b) 200 ms gate time, 400 mV_{pp} squares, 1600 mV_{pp} circles

These data could be explained if one considered that during the parent ion isolation event, the parent ions would be axially excited, due to off-resonant power absorption of the supplementary voltage used to eject the unwanted ions from the trap. This axial expansion would separate the parent ions in space, minimizing their interactions. When the supplementary voltage is removed and the rf voltage is lowered (see Figure 7.1), the ion cloud would eventually condense down to a smaller volume, where the interactions between the ions are maximized. As the ion cloud goes from a large volume to small volume, an increase in dc trapping potential and decrease in secular frequency would be expected.

Table 7.1: Ion Secular Frequency in kHz at Times After Parent Ion Isolation

	Gate Time (ms)			
Cool Time (ms)	**50**	**100**	**150**	**200**
0	100.80	100.80	100.78	100.73
100	100.70	100.59	100.44	100.33
ΔHz	-100	-210	-340	-400

7.4.4. Ion Trajectory Simulations

A portion of the scan function from Figure 7.1 was simulated in SIMION 7.0, using the parameters described in the Methods section. An ion with m/z 905 (to simulate

desArg[1]bradykinin or desArg[9]bradykinin) was trapped for 3 ms at q_z = 0.598 while a supplementary ac voltage corresponding to q_z = 0.605 (256,989 Hz) and 6.0 V_{pp} was applied in a dipolar fashion to the endcap electrodes. After 3 ms, the supplementary voltage was turned off and the rf voltage was dropped to a q_z = 0.253 for 37 ms. The results for the simulation of a single ion are displayed in Figure 7.6. Figure 7.6a shows the evolution of ion kinetic energy, Figure 7.6b shows axial position, and Figure 7.6c shows radial position. The ion kinetic energy is highest during the first 3

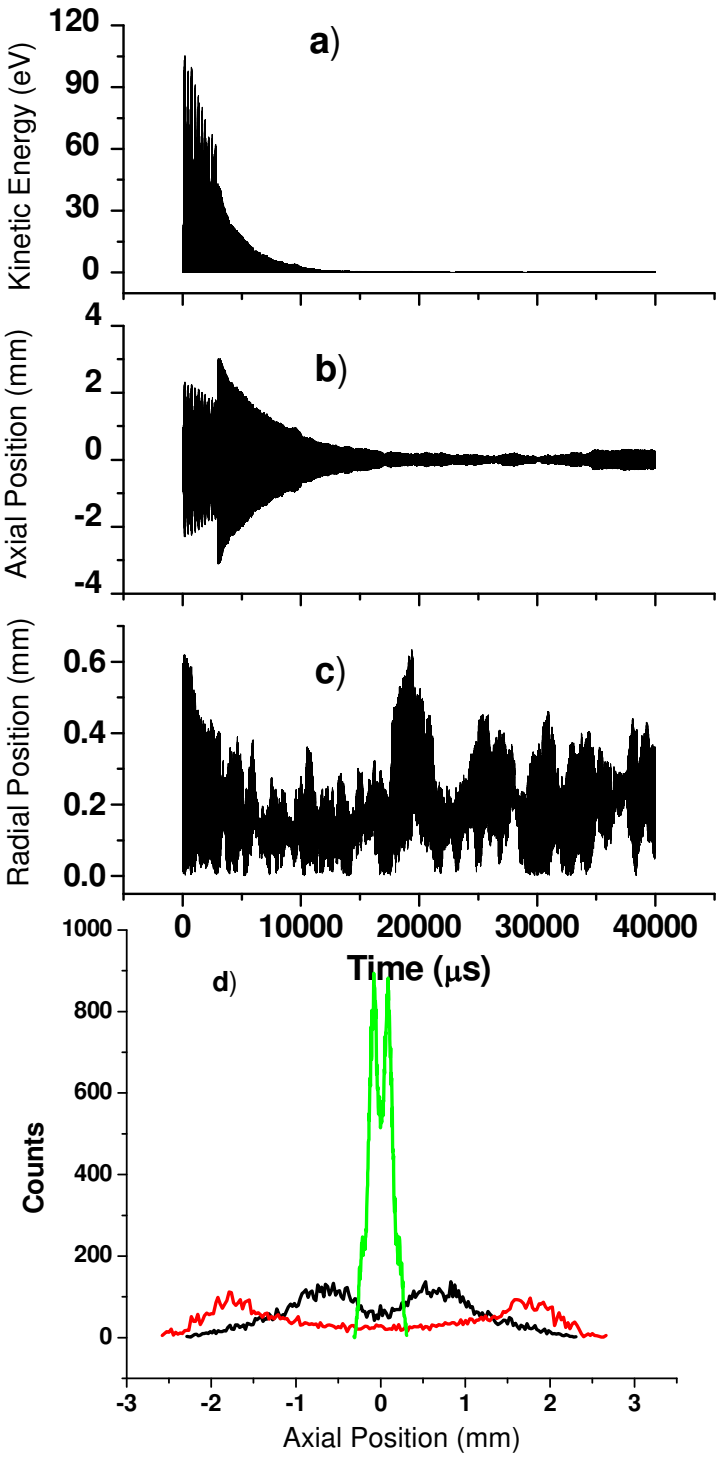

Figure 7.6. Simulation of precursor isolation. Ion parameters given with respect to time. a) kinetic energy b) axial position c) radial position d) histogram of ion axial positions during isolation (black curve), immediately after isolation (red curve), and at equilibrium (green curve).

ms, when off-resonance excitation from the supplementary ac voltage is absorbed and causes acceleration of the ion in a beat-like pattern. When the supplementary voltage is turned off and the rf voltage dropped to q_z = .253, the ion kinetic energy begins to subside, while the ion axial excursions very quickly jump up to higher values before decreasing. The ion radial position is not substantially altered over the course of the entire experiment, which is not surprising given that the excitation from the supplementary voltage was in the axial direction, and ion motion in the axial and radial dimensions is uncoupled in a pure quadrupolar field. The initial expansion of ion motion in the axial direction after dropping the rf voltage is due to the accompanying drop in the depth of the pseudopotential trapping well, given in Equation 1.8. Figure 7.6d is a histogram of ion axial positions during various parts of the parent ion isolation experiment. The black line distribution is during isolation, the red distribution is immediately after isolation, and the green distribution is after equilibrium has been reached. Although not apparent in Figure 7.6, when many ions with varied initial positions and velocities are simulated at the same time, the dished shape of each excitation and equilibrium distribution blends together into a more Gaussian-shaped curve, and the distribution immediately after isolation extends out to 7 mm. Many ions were not simulated at once because of computational expense. Regardless of how many ions are simulated, the salient point from these simulations is that the changing trapping environment used to isolate a parent ion for CID has a noticeable effect on the size of the ion cloud. Immediately after isolation, the high kinetic energy retained from off-resonance excitation coupled with the drop in pseudopotential well depth results in an axially diffuse distribution of ions. Subsequently through collisions with bath gas helium neutrals, the ions collapse down to the center of the trap, becoming much more concentrated.

7.4.5. Theoretical Shift in Secular Frequency

The effect of space charge on ion motion was investigated with ion trajectory simulations by using the coloumbic repulsion model described in the **Chapter 2.4.3**. Ten ions were simulated at once in a QITMS for 2 ms at $q_z = 0.253$. The amount of interaction charge on each ion was varied from 1.6×10^{-19} C to 1.6×10^{-15} C. Therefore the simulation assumes that the total number of ions in the QITMS was varied from 10 to 100,000 ions. Fourier analysis was performed on the time trace of each ion's axial position, and the average of each frequency domain spectrum was plotted, as shown in Figure 7.7a. The solid trace is 10 ions, dashes are 10,000 ions, dots are 25,000 ions, dash-dot is 50,000 ions, and dash-dot-dot is 100,000 ions. A broadening of the peak and shift towards lower frequencies is observed as the "number" of ions in the trap is increased. The average frequency values for each condition are plotted in Figure 7.7b (95% confidence intervals). There is no significant change in frequency until 10,000 ions, after which the average frequency drops linearly as ion number is increased. The greatest experimentally observed shift in ion secular frequency was 400 Hz, as seen in Table 7.1. Because the exact number of ions in the experiment is not known, one must conclude that either the SIMION simulation is overestimating the effect of space charge, or under space charge conditions the QITMS only holds on the order of 5000-10,000 ions. Estimations of the expected frequency shift versus number of ions are shown in Figure 7.7c and 7.7d, using Equations 7.5 and 7.6, respectively. Figure 7.7c assumes a spherical distribution of constant charge density, and Figure 7.7d uses a Gaussian-shaped axial distribution of a given width (3σ). The largest frequency shift in Figure 7.7c is 120 Hz for 100,000 ions in a sphere of radius 0.40 mm. The voltage induced by larger spheres decreases to the point where almost no frequency shift is calculated for a 6mm sphere with

100,000 ions. The frequency shifts in Figure 7.7d are much more pronounced than in Figure 7.7c, because the ions are concentrated at the center of the Gaussian distributions. A realistically sized distribution[25] with outer radius of 1 mm gives a shift of 400 Hz at 100,000 ions. An experiment to estimate the actual number of ions contained in the QITMS under

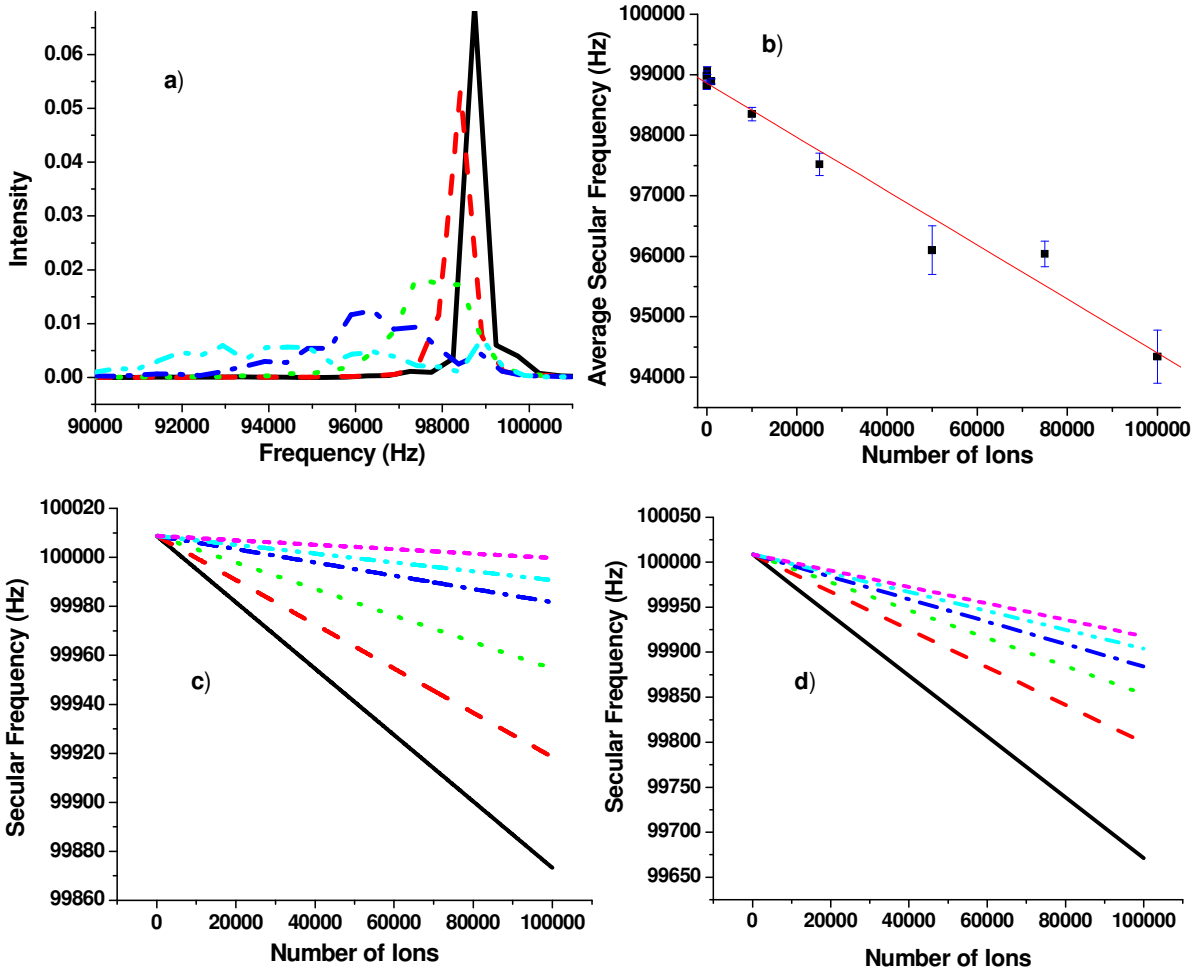

Figure 7.7. a) Fourier transform of simulated ion axial positions over a 2 ms time period. The solid trace is 10 ions, dashes are 10,000 ions, dots are 25,000 ions, dash-dot is 50,000 ions, and dash-dot-dot is 100,000 ions. b) Average frequency for 10 simulated ion trajectories versus number of ions in trap. c) Calculation of secular frequency versus number of ions for sphere of constant charge density. Solid trace is 0.4 mm radius, dash is 0.6 mm, dot is 1.0 mm, dash-dash-dot is 2.0 mm, dash-dot-dot is 3.0 mm, and small dash is 6.0 mm. d) Calculation of secular frequency versus number of ions for Gaussian distribution of ions. Solid trace is 1.0 mm outer radius, large dash is 2.0 mm, dot is 3.0 mm, dash-dot is 4.0 mm, dash-dot-dot is 5.0 mm, and small dash is 6.0 mm.

various conditions would be helpful in judging the relative merits of the various theoretical methods employed. However, all the methods concur on the point that a decrease in secular frequency is to be expected as the density of ions increases.

7.5. Conclusions

Many factors contribute to the internal energy of ions in a QITMS. Chief among these factors is the energy transfer process between the ion and the neutral helium bath gas molecules. Evidence has been presented that upon introduction of ions into the QITMS, equilibrium ion internal energy is reached fairly rapidly, on the order of ~10 ms. Peptide ions produced by nano-ESI and AP-MALDI dissociate with nearly the same CID onset voltage and 50% fragmentation efficiency point, although in some cases the AP-MALDI ions require more excitation voltage to dissociate. If collisional cooling of internally excited ions occurs in a few milliseconds, as experimental and theoretical studies suggest, then the differences in dissociation of ions produced by nano-ESI and AP-MALDI must be due to different ion conformations.

Typical QITMS operations such as parent ion isolation for CID may increase the kinetic energy of the ions, possibly increasing the ion internal energy as well. However, because the rate of internal energy dissipation appears to be fast, only slight variations in dissociation efficiency are observed when a cool time is inserted between isolation and CID. Injecting large numbers of ions into a QITMS increases the space charge in the trap, which can add an effective dc offset to the trapping voltage, altering the secular frequencies of ion oscillation. Because a voltage induced by a cloud of ions depends on the ion density, parameters which affect the size of the ion cloud will change the induced dc offset. When ion populations were very large, decreases in secular frequency of several hundred Hertz

were observed, measuring from immediately after ion isolation relative to 100 ms after ion isolation. This change in secular frequency could make estimations of relative ion internal energy problematic, particularly if the method used depends on a resonance condition being achieved between the frequency of excitation voltage and ion secular frequency. If a cool time of approximately 20 ms is inserted between parent isolation and CID, then equilibrium kinetic energy and ion positions can be assured, and any shift in secular frequency induced by space charge will be of lesser consequence.

7.6. References

1. McLafferty, F. W.; Wachs, T.; Lifshitz, C.; Innorta, G.; Irving, P. *Substituent Effects in Unimolecular Ion Decompositions. XV. Mechanistic Interpretations and the Quasi-Equilibrium Theory*. J. Am Chem. Soc. **1970,** *92*, 6867-6880.

2. Baer, T.; Mayer, P. M. *Statistical Rice-Ramsperger-Kassel-Marcus quasi-equilibrium theory calculations in mass spectrometry*. J. Am. Soc. Mass Spectrom. **1997,** *8*, 103-115.

3. Baer, T.; Hase, W. L. *Unimolecular Reaction Dynamics*; Oxford University Press: New York, 1996.

4. Marcus, R. A.; Rice, O. K. *Session on Free Radicals: The Kinetics of the Recombination of Methyl Radical and Iodine Atoms*. Journal of Physical and Colloid Chemistry **1951,** *55*, 894-908.

5. Laskin, J.; Futrell, J. *Internal Energy Distributions Resulting from Sustained Off-Resonance Excitation in Fourier Transform Ion Cyclotron Resonance Mass Spectrometry. II. Fragmentation of the 1-Bromonaphthalene Radical Cation*. Journal of Physical Chemistry A **2000,** *104*, 5484-5494.

6. Laskin, J.; Byrd, M.; Futrell, J. *Internal energy distributions resulting from sustained off-resonance excitation in FTMS. I. Fragmentation of the bromobenzene radical cation*. Int. J. Mass Spectrom. **2000,** *195/196*, 285-302.

7. Vestal, M. L. *Theoretical studies on the unimolecular reactions of poly-atomic molecule ions*. Journal of Chemical Physics **1965,** *43*, 1356-69.

8. Vachet, R. W.; Bishop, B. M.; Erickson, B. W.; Glish, G. L. *Novel Peptide Dissociation: Gas-Phase Intramolecular Rearrangement of Internal Amino Acid Residues*. J. Am. Chem. Soc. **1997,** *119*, 5481-5488.

9. Vachet, R. W.; Winders, A. D.; Glish, G. L. *Correlation of Kinetic Energy Losses in High-Energy Collision-Induced Dissociation with Observed Peptide Product Ions*. Anal. Chem. **1996,** *68*, 522-526.

10. Plass, W. R.; Cooks, R. G. *A Model for Energy Transfer in Inelastic Molecular Collisions Applicable at Steady State or Non-Steady State and for an Arbitrary Distribution of Collision Energies*. J Am Soc Mass Spectrom **2003,** *14*, 1348–1359.

11. Stafford, G. C. J.; Kelley, P. E.; Syka, J. E. P.; Reynolds, W. E.; Todd, J. F. J. *Recent Improvements in and Analytical Applications of Advanced Ion Trap Technology*. Int. J. Mass Spectrom. Ion Processes **1984,** *60*, 85-98.

12. March, R. E. *An Introduction to Quadrupole Ion Trap Mass Spectrometry*. J. Mass Spectrom. **1997,** *32*, 351-369.

13. Goeringer, D. E.; McLuckey, S. A. *Relaxation of Internally Excited High-mass Ions Simulated under Typical Quadrupole Ion Trap Storage Conditions*. Int. J. Mass Spectrom. **1998,** *177*, 163-174.

14. Black, D. M.; Payne, A. H.; Glish, G. L. *Determination of Cooling Rates in a Quadrupole Ion Trap*. J Am Soc Mass Spectrom **2006,** *17*, 932-938.

15. Remes, P. M.; Glish, G. L. *Collisional Cooling Rates in a Quadrupole Ion Trap at Sub-Ambient Temperatures*. Int. J. Mass. Spectrom. **2007,** *265*, 176-181.

16. Konn, D. O.; Murrell, J.; Despeyroux, D.; Gaskell, S. J. *Comparison of the Effects of Ionization Mechanism, Analyte Concentration, and Ion "Cool-Times" on the Internal Energies of Peptide Ions Produced by Electrospray and Atmospheric Pressure Matrix-Assisted Laser Desorption Ionization*. J Am Soc Mass Spectrom **2005,** *16*, 743-751.

17. Kato, S.; Bierbaum, V. M.; Leone, S. R. *Laser fluorescence and mass spectrometric measurements of vibrational relaxation of N:(v) with He, Ne, Ar, Kr, and Xe**. Int. J. Mass Spectrom. Ion Proc. **1995,** *149/150*, 469-486.

18. March, R. E.; Todd, J. F. J. *Practical Aspects of Ion Trap Mass Spectrometry*; CRC Press: New York, 1997.

19. Major, F. G.; Dehmelt, H. G. *Exchange-Collision Technique for the rf Spectroscopy of Stored Ions*. Physical Review **1968,** *170*, 91-107.

20. VanBerkel, G. J.; Glish, G. L.; McLuckey, S. A. *Electrospray Ionization Combined with Ion Trap Mass Spectrometry*. Anal. Chem. **1990,** *62*, 1284-1295.

21. Glish, G. L.; Danell, R. M. *Electrospray Ionization Device*. Patent 2004.

22. Danell, R. M.; Glish, G. L. *Advances in ion source and quadrupole ion trap performance and design*. Doctoral Dissertation, The University of North Carolina, Chapel Hill, 2001.

23. Danell, R. M. *An Atmospheric Pressure MALDI Probe for Use with ESI Source Interfaces*. The 48th ASMS Conference on Mass Spectrometry and Allied Topics. Long Beach, CA, 2000.

24. Griffiths, D. J. *Introduction to Electrodynamics*; Prentice-Hall Inc.: Upper Saddle River, 1999.

25. Cleven, C. D.; Cooks, R. G.; Garrett, A. W.; Nogar, N. S.; Hemberger, P. H. *Radial Distributions and Ejection Times of Molecular Ions in an Ion Trap Mass Spectrometer: A Laser Tomography Study of Effects of Ion Density and Molecular Type*. J. Phys. Chem. **1996,** *100*, 40-46.

26. Li, G.-Z.; Guan, S.; Marshall, A. G. *Comparison of Equilibrium Ion Density Distribution and Trapping Force in Penning, Paul, and Combined Ion Traps*. J. Am. Soc. Mass Spec. **1998,** *9*, 473-481.

27. Danell, A. S.; Glish, G. L. *Evidence for Ionization-Related Conformational Differences of Peptide Ions in a Quadrupole Ion Trap*. J. Am. Soc. Mass Spectrom. **2001,** *12*, 1331-1338.

28. Stevenson, E.; Breuker, K.; Zenobi, R. *Internal energies of analyte ions generated from different matrix-assisted laser desorption /ionization matrices*. Journal of Mass Spectrometry **2000,** *35*, 1035-1041.

29. Sannes-Lowery, K.; Griffey, R. H.; Kruppa, G. H.; Speir, J. P.; Hofstadler, S. A. *Multipole Storage Assisted Dissociation, A Novel In-Source Dissociation Technique for Electrospray Ionization Generated Ions*. Rapid Commun. Mass Spectrom. **1998,** *12*, 1957-1961.

30. Håkansson, K.; Axelsson, J.; Palmblad, M.; Håkansson, P. *Mechanistic Studies of Multipole Storage Assisted Dissociation*. J. Am. Soc. Mass Spectrom. **2000,** *11*, 210-217.

31. Black, D. *Novel Methods for Characterization of Intact Proteins by Mass Spectrometry*. Ph.D., University of North Carolina, Chapel Hill, 2005.

Chapter 8

8. Design and Construction of a FAIMS-QEB for Higher Order Structure Determinations

8.1. Introduction

MS is used routinely to identify proteins that are digested into peptides and then fragmented by tandem MS, the so-called "bottom-up" proteomics methodology.[1, 2] A number of automated sequencing programs have been developed to analyze the experimental MS/MS spectra produced in this way.[3] Most of these programs incorporate some chemical information about the fragmentation process, the most common "rule" being that peptides typically fragment into b_n and y_n type ions.[4] Type b_n and y ions are the most commonly observed collision induced fragments, but other unimolecular reactions yielding high relative abundance product ions are possible. These unexpected fragment ions can occur *via* rearrangement reactions, significantly complicating spectral interpretation.[3, 5, 6] Although even b and y ions are thought to form through rearrangements[7, 8], the more complex, unexpected rearrangements are mediated by intramolecular interactions that are more difficult to predict. Improvements to automated peptide sequencing programs could be made by increasing the understanding of peptide fragmentation mechanisms.

The MS/MS methods mentioned above are also applicable to the characterization of protein ions, not just peptide ions. Protein identification by the "top-down" approach, where proteins are analyzed and dissociated intact instead of initial enzymatic digestion, has several advantages over the bottom up method, including less sample preparation and the ability to

better characterize post-translational modifications.[9, 10] The larger number of atoms in proteins increases the complexity and number of intramolecular interactions, and thus increases the likelihood of complicated rearrangement reactions. Protein ions of different conformation might be expected to have dissociation spectra that are more different than for peptides of different conformation.

The unexpected fragmentation peaks are indicators of the ability of MS/MS to probe higher order structure. The problem is that the MS/MS information is not very readily interpretable. A new instrument has been proposed by the Glish lab for deciphering the relationship between MS/MS data and higher order structure information. This instrument has a high field asymmetric waveform ion mobility spectrometer (FAIMS) coupled to a quadrupole mass filter (Q), multipole rf-only ion guide (q), an electric sector (E) and magnetic sector (B). The intention of the instrument is to select ions by conformation and characterize their fragmentation products and pathways by a host of MS/MS techniques, including low and high energy CID, IR and/or UV photodissociation, electron capture dissociation (ECD)[11], electron transfer dissocitation (ETD)[12], and ion/molecule reactions. By first selecting an ion by conformation and then dissociating it, a systematic study of higher order structural influences on MS/MS data can be undertaken.

Details of some of the experiments possible with an EB instrument are explained elsewhere[13, 14], but briefly, an EB is capable of high energy CID and kinetic energy loss measurements that are useful for studying ion intramolecular interactions. These methods were applied to peptide ions without prior conformational selection in the past; the FAIMS-Qq-EB will be able to apply kinetic energy loss methods to the study of shape selected

peptide and protein ions. The remainder of this chapter will describe the design and initial results of the FAIMS-Qq portion of the instrument.

8.2. Instrumental Layout and Rationale

Figure 8.1 is a drawing of the entire FAIMS-Qq-EB instrument. Ions are generated by nano-ESI and passed into the FAIMS device. Conformational selection of ions based on differential mobilities as described in **Chapter 1.4.2** is carried out. The ions enter a high pressure region (1 Torr) pumped by a Leybold D 65 B rough pump with a pumping speed of 25 L/s. A prototype Bruker ion funnel focuses ions into the next pressure region with rings that start at 25.4 mm diameter and go down to an aperture size of 2.0 mm. The middle pressure region is operated at about 1-4 mTorr, adjustable with a leak valve open to atmosphere. An octapole ion guide transfers ions through a 2.5 mm aperture into the low

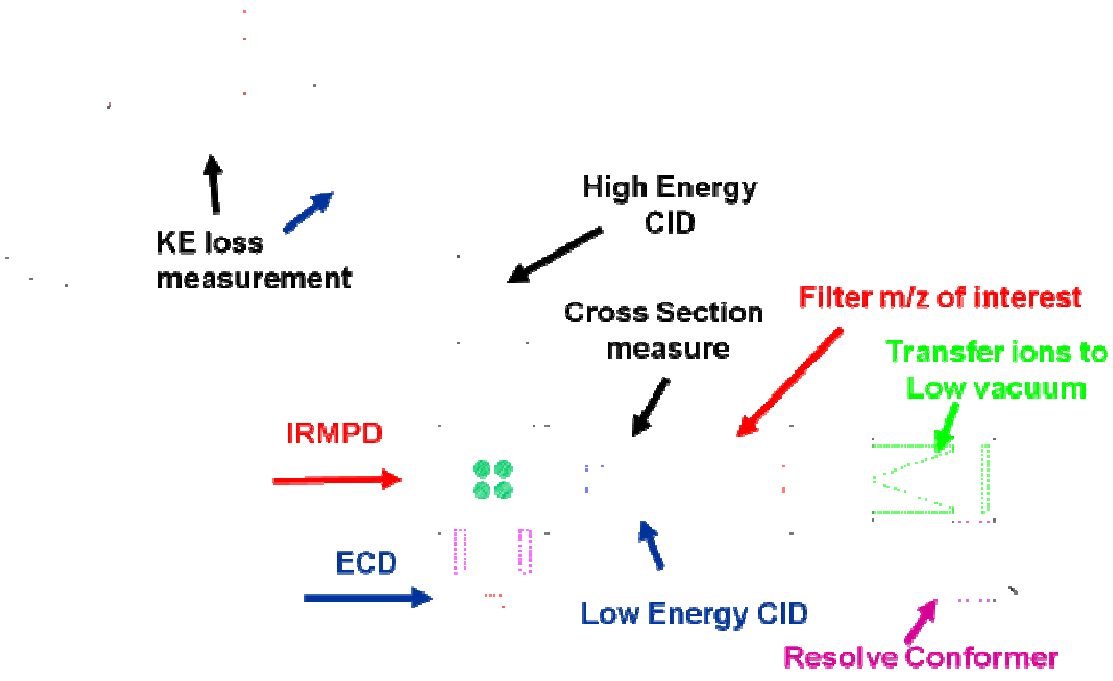

Figure 8.1. Diagram of FAIMS-Qq-EB instrument. The interface between the Qq and EB does not exist yet, but as depicted, a quadrupole bender and linear ion trap capable of ECD have been planned for.

pressure region. Both the middle and low pressure regions have their own 330 L/s Pfeiffer TPH 330 turbomolecular pumps. The low pressure region has a pressure of about $2x10^{-6}$ Torr. Ions are filtered according to mass-to-charge ratio with an Extrel 8.5mm quadrupole with pre- and post-filters. Following the mass analyzing quadrupole is a Finnigan TSQ 700 quadrupole in a gas-tight housing. The ability to introduce gases here makes a number of experiments possible. Low energy CID, IRMPD, ion/molecule reactions, or collision cross section measurements could take place in the rf-only quadrupole. This is as much of the instrument as will be discussed in this chapter, although there are plans for many other components in the interface between Qq and EB, including a linear ion trap (LIT) from Hitachi capable of ECD, shown in Figure 8.1.

8.3. Pumping Calculations

Equations 3.3 and 3.4 were used to determine the optimum aperture sizes and vacuum pumping speeds to reach the desired working pressures in each region of the instrument. The results of these calculations concluded that a base pressure of $5.0x10^{-6}$ Torr could be obtained in the analyzer region with pumps in our laboratory, using a 2.5 mm diameter aperture between octapole and analyzer regions, and a 2.0 mm diameter aperture between source and octapole regions. These calculations were done assuming a lower capacity rough pump for the source, around 12 L/s, but a 25 L/s pump was acquired, helping the situation immensely. The source pressure is now 0.6 Torr , the octapole region pressure is $1.3x10^{-3}$ Torr, and the main chamber pressure is $2.0x10^{-6}$ Torr.

The pressure in the source is adjustable from 0.6 Torr to 1.3 Torr by choking off the roughing pump with a variable conductance valve. Optimum ion transmittance was found to take place from 0.6 to 1.0 Torr, with a clear decrease in signal at higher pressures. The

pressure in the octapole region is adjustable using a leak valve open to atmosphere that terminates in this region. A pressure of about $4x10^{-3}$ optimizes transmittance of peptides, presumably *via* collisional cooling down to the center axis of the octapole.[15] Within the operable pressure range, the optimum pressure for transmitting proteins appears to be at the lowest pressure of $1.3x10^{-3}$ Torr. Proteins have larger collision cross sections than peptides and therefore undergo more collisions. Perhaps for this reason a lower pressure in the octapole optimizes protein transmittance.

8.4. FAIMS Considerations

As described in **Chapter 1.4.2**, conventional IMS has a well-developed theory relating experimental signal to collision cross section, but it is a pulsed technique. Ions must be accumulated in a region before a drift tube and periodically pulsed to the detector. Unless multiplexing is used, the utilization of a constant ESI beam is about 1%, due to the low duty cycle and high ion losses at the IMS-MS interface.[16] FAIMS is attractive for coupling ESI to a constant ion beam device like the EB because 100% of the transmitted ion beam can be utilized, reducing signal averaging requirements. Although collision cross section data cannot be directly inferred from FAIMS spectra, supplementary energy loss experiments in the quadrupole collision cell can characterize collision cross sections using Equation 1.26. The energy loss method gives the average collision cross section of all ion species passed through the collision cell to the detector, therefore for best accuracy, only one conformation should be analyzed at a time. This requirement ultimately dictated the type of FAIMS that could be used, as described in the next section.

8.4.1. Planar versus Cylindrical Geometry

The choice of FAIMS analyzer geometry depends strongly on the intended purpose. The original FAIMS device consisted of two parallel plates.[17] As will be shown, this type of geometry has high resolving power (Equation 1.25) but poor ion transmission. Ion diffusion is not constrained in the direction orthogonal to the electric field, resulting in a ribbon-type ion beam and inefficient coupling to a circular aperture. A cylindrical geometry[18] allowed for much higher ion transmittance, with an associated decrease in resolving power. The cylindrical geometry has been useful for improving signal-to-noise of high background samples and for decreasing liquid chromatography method development times by adding a second dimension of separation. The latter application includes increasing selectivity between two ions of very similar mass-to-charge in MS-based quantitation studies. In quantitation experiments often FAIMS resolution is not of critical importance, because transmittance of an internal standard at the same instrumental parameters is desirable. These applications are not as feasible with the planar geometry on a commercial instrument because of the marked decrease in ion transmittance inherent to the planar design.

Recently, however, a planar FAIMS device was constructed with a novel interface that improved ion transmission to the mass spectrometer somewhat.[19] A horizontal "slit" consisting of eleven 0.13 mm holes spaced on a 4mm line was found to increase ion signal by 250% over a single equal conductance circular aperture.[19] The resolving power with the planar device was 2 to 4 times the resolving power of the cylindrical device. The limitations of measuring cross section by the energy loss experiment (described in the first paragraph of section **8.4** of this chapter) dictate that the FAIMS separation have the highest resolving power possible, therefore the planar FAIMS geometry was the logical choice. The loss in

sensitivity can hopefully be partially compensated by using higher analyte concentrations, signal averaging, and temperature gradients, the last of which will be described in the next section.

8.4.1.1.Field Shape

The differences between planar and cylindrical FAIMS arise because of the shape of the electric field between the electrodes. The electric field between two cylinders is described by Equation 8.1.

$$E = \frac{V}{r \ln\left(\frac{R_{out}}{R_{in}}\right)} \qquad \text{(Equation 8.1)}$$

V is the voltage on the inner cylinder, R_{out} and R_{in} are the radii of the outer and inner cylinders, respectively, and r is the radial position between the two cylinders, where $R_{in} \leq r \leq R_{out}$. The black line in Figure 8.2 graphs the electric field between two cylinders using Equation 8.1 for R_{in} = 0.7 cm and R_{out} = 0.9 cm for a voltage gradient of 3300 V. The electric field varies from almost 19 kV/cm near the inner electrode to 14.5 kV/cm near the outer electrode. The effect of the inhomogeneous electric field is to focus ions to a particular radius, R_{eq}, when a suitable compensation voltage (CV) is set.[20] If the ion is at $r < R_{eq}$, then the compensation field is not great enough to keep the ion from drifting away from the inner electrode. If $r > R_{eq}$, then the force from the CV field overcomes the dispersion voltage (DV) field, and the ion moves toward the inner electrode. Thus, the ion is focused at R_{eq}, where the drift from the CV is balanced by the drift from the DV.

The electric field between two planar electrodes is graphed in red in Figure 8.2. Equation 8.1 is used and R_{in} = 10000.7 cm and R_{out} = 10000.9 cm. The electric field for a planar device is constant at all positions between the electrodes, such that there is no focusing effect with this geometry. The planar FAIMS ions are not all focused to a R_{eq}, rather, a stable ion will leave the device at basically the same radius it entered.

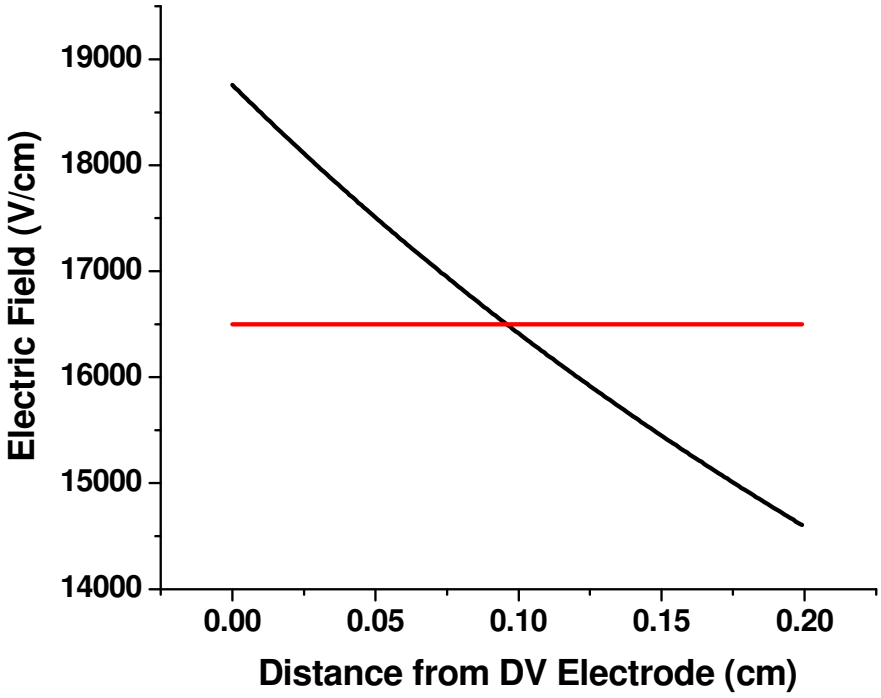

Figure 8.2. Electric field gradient at 3300 V in a 2 mm space with cylindrical electrodes (black) having R_{in}=0.7 cm and R_{out}=0.9 cm and planar electrodes (red). The dispersion voltage (DV) electrode is at 0.00 cm.

8.4.1.2.Simulations

Simulations of ion motion help to better understand the FAIMS separations. The basic requirement for a stable ion trajectory is that the net ion position over one waveform cycle does not change, or Equation 8.2[21].

$$\int_0^{\frac{1}{f}} K(t)E(t)dt = 0 \qquad \text{(Equation 8.2)}$$

Rearranging Equation 1.19 gives the integrand of Equation 8.2, i.e. the distance an ion travels over a given time interval. *K(t)* is given in Equation 1.22, *E(t)* in Equations 1.24 and 8.1, and f is the waveform frequency in Hz. Ion position for $[Cl]^-$, calculated at 1 ns intervals, is plotted in Figure 8.3 for a 300 kHz waveform to illustrate how ions are separated in FAIMS. The y axis is ion position *r*, relative to electrodes at 0.7 and 0.9 cm. The black line is an ion with an incorrect CV applied; after one waveform cycle this ion has already drifted a net +0.005 cm. To reach the outer electrode at 0.9 cm will take 180 more waveform cycles, or 600 µs. Conversely the red trace is for an ion with the correct CV applied; after 180 waveform cycles, this ion will still be found in the center of the analytical gap at 0.80 cm.

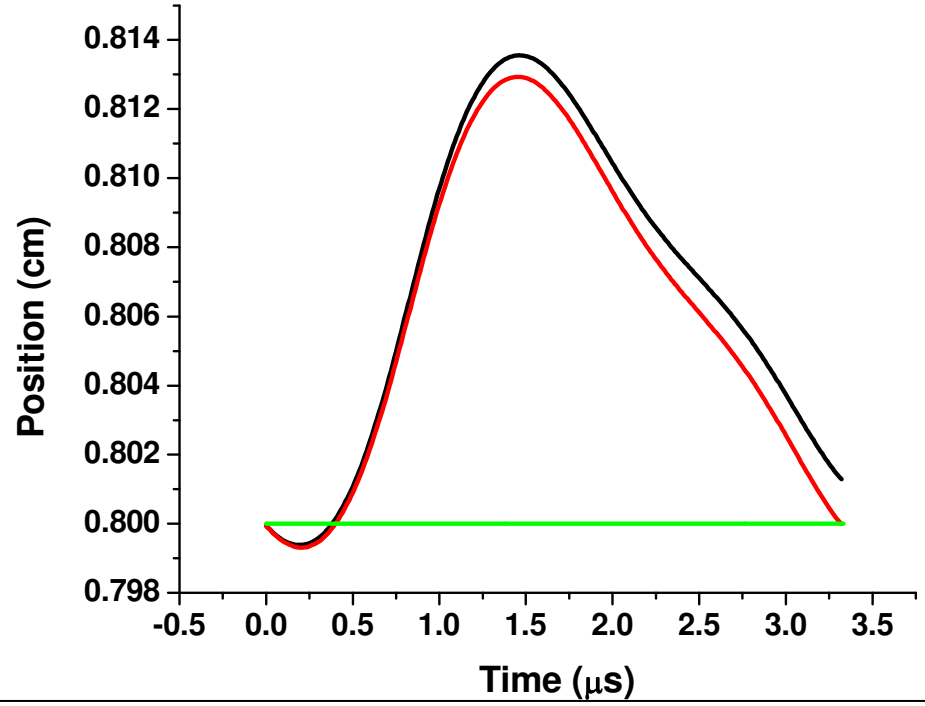

Figure 8.3. Simulation of $[Cl]^-$ for DV=-3300 V, f = 300 kV over one waveform cycle in FAIMS. The black line is with an incorrect CV applied, the red line is for the optimum CV applied. The green line marks the starting position.

Extending the ion simulation for longer time periods (typical residence time is 100-200 ms) illustrates the focusing effect described in the previous section. Figure 8.4a shows

simulations of $[Cl]^-$ for cylindrical FAIMS. Each line color represents an ion started at a different radius. Regardless of initial position, the ions quickly reach the same equilibrium radius. The annotated numbers represent the CV used for that simulation. For cylindrical FAIMS, a large range of CV can be used to pass the ion through the device at a range of different R_{eq}. In Figure 8.4b are plotted $[Cl]^-$ trajectories in a planar FAIMS. A much

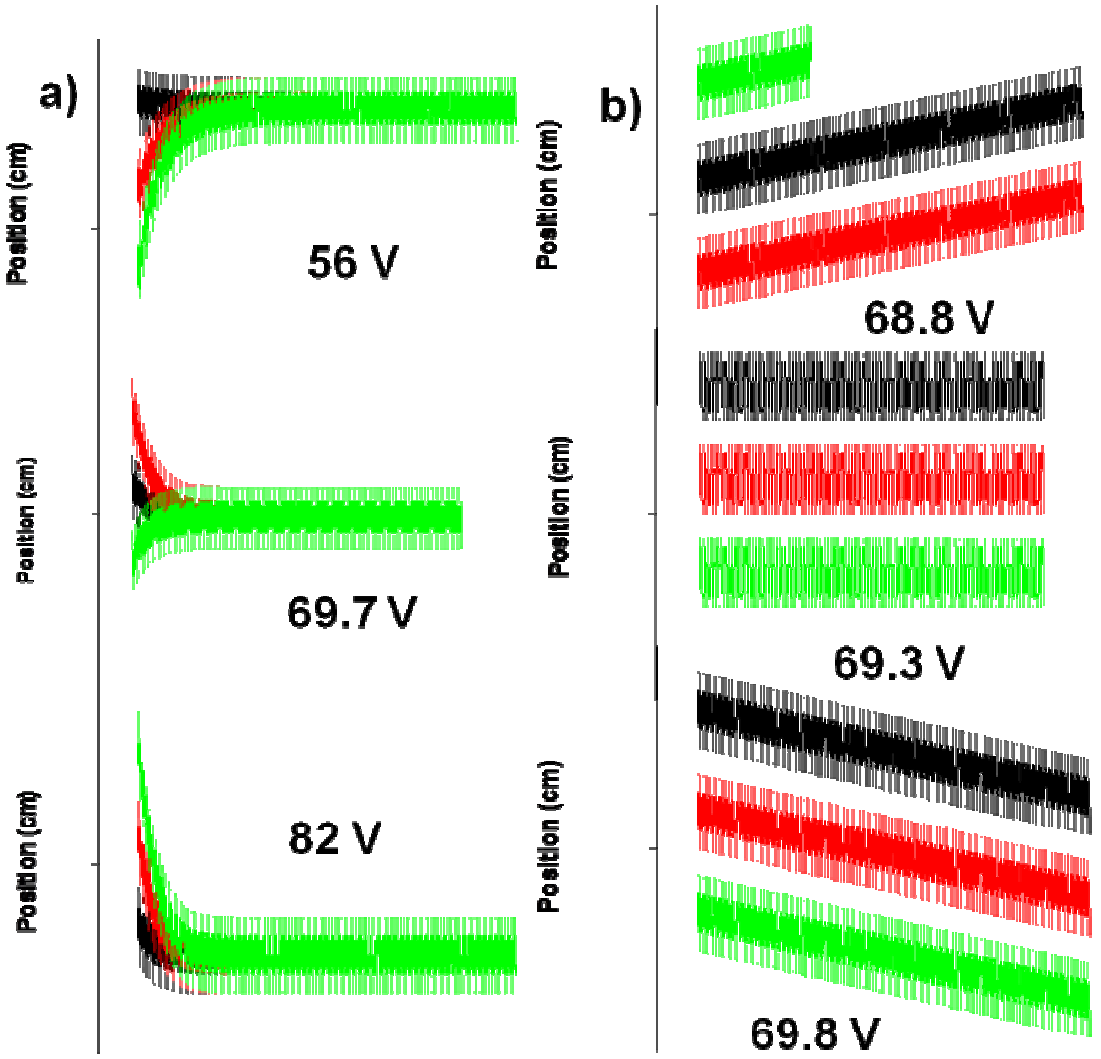

Figure 8.4. Simulations of $[Cl]^-$ in cylindrical FAIMS a) and planarl FAIMS for f = 300 kHz, DV = -3300 V. b). Ion colors correspond to different initial positions, and annotated numbers correspond to the CV of the waveform.

smaller range of CV will pass the ion through the device in this case. At any CV other than the optimum, a constant drift towards one of the electrodes is apparent. An ion can still pass through the planar FAIMS at CV other than the optimum if the ion reaches the exit before hitting an electrode. Therefore, the ion residence time in the planar FAIMS is one parameter that can be used to control the resolution of separation[19].

These simulations can be done in the manner described previously[20] to calculate spectral peak shapes for different device geometries and conditions. Figure 8.5 shows calculated peak shapes for [Leucine-H]$^-$ in a planar FAIMS for various gas flow rates. The gas flow can be used to change the ion residence time and introduce a measure of control into the sensitivity and resolution of analysis. **Appendix A** shows the FAIMS simulation

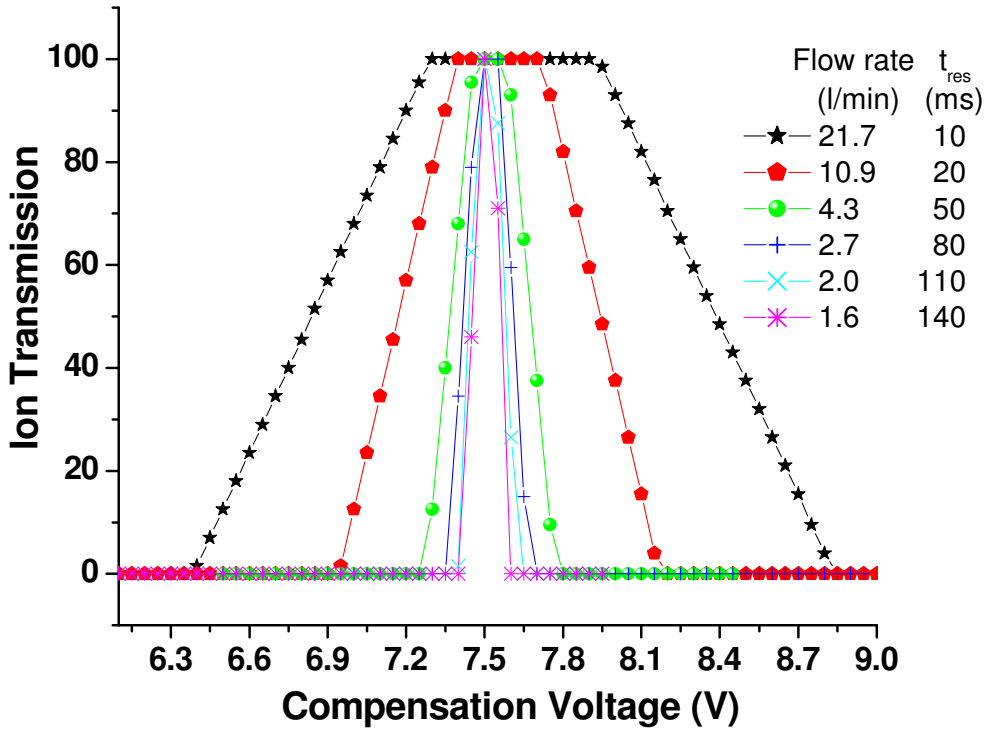

Figure 8.5. Calculated spectra for [Leucine-H]$^-$ in a planar FAIMS for f = 300 kHz, DV= -3300 V and various ion residence times. Diffusion and space charge were not taken into account.

program. As of now, the program has the ability to calculate the effects of diffusion and space charge, but the manner in which these effects are implemented in LabVIEW is rather slow, so Figure 8.5 doesn't include them. A better way would be to write the program in C++ and run simulations using the UNC Scientific Computing resources. Efforts to learn C++ are underway, and the author plans to write this program, even if it is not done before leaving UNC.

8.4.2. Buffer Gas

Some effort has gone into understanding the effect of buffer gas composition on FAIMS separations.[22, 23] The separation of ions in homomolecular gases (as opposed to mixtures like N_2/He) such as N_2, O_2, CO_2, N_2O, and SF_6 by FAIMS can be described fairly accurately by Equation 1.22 when the constants *a* and *b* have been determined.[23] Although N_2 is the most commonly used gas, use of O_2 sometimes requires larger magnitude CVs, which improves sensitivity in cylindrical FAIMS devices due to increased focusing and also expands the separation space.[22] Mixtures of gases are also common. The mobility of an ion in a mixture of gases can be described by Blanc's law in Equation 8.3, which defines mobility in a mixture as the weighted sum of mobilities in individual gases. In Equation 8.3, x_i is the abundance of gas *i*, and K_i is its mobility.

$$\frac{1}{K_{mix}} = \sum_i \frac{x_i}{K_i} \qquad \text{(Equation 8.3)}$$

Equation 8.3 holds when the mixed gases are of similar sizes, e.g. N_2/O_2, but at high fields, mixtures of gases with significant size differences exhibit behavior that deviates significantly from this theory.[23] For example, He/N_2 at 50/50 v/v has been used for the analysis of tryptic peptides in a FAIMS-MS system, resulting in an increase in peptide sequence coverage and 4 fold increase in sensitivity over N_2.[24] The effect of He is thought to be due to a decrease in

the long range attractive forces which initiate clustering of buffer gas on ions at lower fields. Evaporating of the buffer gas clusters at high fields causes an increase in mobility, and A type ion behavior (see **Chapter 1.4.2**).[23] In He, however, most ions are of the C type, where mobility decreases at higher fields. Impressive performance has been demonstrated by the gas mixture He/SF_6 50/50 v/v, where a resolving power of 100 was reported for the Cs^+ ion.[23] Apparently this behavior does not hold for all analyte ions, and He/SF_6 is not a widely used FAIMS gas medium. Mixtures of He/N_2 give the best results over a wide range of analytes, and this mixture at up to 50/50 v/v is the current buffer gas offered on commercial FAIMS systems. Although sensitivity increases as He content is raised, higher He content is not feasible due to lower voltage breakdown thresholds and decreased vacuum pumping performance.[23] Gas flow regulation and mixing is done on our system with two MKS 1179A mass flow devices (Wilmington, MA).

8.4.3. Temperature

Temperature control of the FAIMS electrodes is possible on the commercial FAIMS system from ThermoFisher, and was recently reported.[25] The temperature of a FAIMS system is expected to influence separation because gas number density *N* is a function of temperature, and ion mobility depends on *E/N*, as in Equation 1.22. This observation yields two main reasons for temperature control. The first reason is that if the electrodes are actively maintained at a set temperature, external influences such as heated ion sources and building air temperature will not influence results.[25] A more complicated second reason for regulating electrode temperature is to tune resolving power through the use of temperature gradients. Changing the temperature of one electrode changes gas number density and field (*E/N*) near the electrode surface. For example, in Figure 8.2 the field in a cylindrical FAIMS

is plotted for both electrodes having the same temperature. If the inner electrode (0.0 cm) was heated relative to the outer electrode (0.2 cm), the *E/N* near 0.0 cm would be increased. The ion focusing effect would likewise be accentuated, and a broader, higher intensity peak would result. Lowering the temperature of the inner electrode relative to the outer electrode would decrease E/N near 0.0 cm, attenuating the focusing effect. A higher resolution, lower intensity peak would be produced. Interestingly, for planar FAIMS, differential heating of the electrodes should produce an *E/N* gradient where none existed before, introducing a focusing effect in this device. Temperature control could provide a means for a middle ground between planar FAIMS resolution and cylindrical FAIMS sensitivity. Simple calculation of field (V/cm) using Equation 2.1 divided by number density show that the E/N differential in cylindrical FAIMS in Figure 8.2 is 75.9 Td – 59.3 Td = 16.6 Td. By heating one electrode of the planar FAIMS in Figure 8.2 to 396 K while actively maintaining the other electrode at 296 K, the E/N differential would be 89.0 Td – 66.6 Td = 22.4 Td. This gradient should be able to provide a focusing effect with planar FAIMS comparable to that in ambient temperature cylindrical FAIMS. Our planar FAIMS has been fitted with Peltier devices manufactured by Melcor (Trenton, NJ) to achieve electrode heating or cooling.

A low temperature FAIMS has also been proposed for a purpose other than resolution control. A protein study with a FAIMS-IMS-MS instrument reported some unfolding caused by the FAIMS device.[26] Protein cross sections were measured by IMS with and without prior FAIMS separation. When ions were passed through the FAIMS there was a general broadening of IMS peaks towards larger cross sections. The unfolding was rationalized as most likely happening via collisional heating upon initial injection of ESI ions into the FAIMS, because protein unfolding during the actual FAIMS separation would likely result in

the loss of these ions against one of the electrodes. With lower temperature electrodes (low temperature buffer gas), ions would need to gain more energy before they were able to unfold. Analysis of IMS data of protein ions heated to different temperatures led to the conclusion that cooling the FAIMS electrodes to ~250 K should mitigate any unfolding process initiated as the ion enters the FAIMS.

8.5. FAIMS-Qq Design

8.5.1. Use of TSQ 700

A Finnigan TSQ 700 triple quadrupole mass spectrometer was chosen as the foundation for the FAIMS-Qq part of the new instrument. The availability of a surplus TSQ 700 in the Glish lab was fortuitous for several reasons. The height of the TSQ vacuum chamber was the exact same as the height of the ion source of the Finnigan MAT 900 EB mass spectrometer, so coupling the two vacuum chambers should be simplified. Although the TSQ 700 had never produced any results in our lab because of computer problems, a number of power supplies and instrument hardware pieces were in good condition. A set of National Instruments PCI cards were used to tap into the TSQ 700 boards and control various power supplies from a program written in LabVIEW 7.1 that will be described later. The boards controlled in the LabVIEW program include a high voltage rf generator, 16 different ±200 V DC power supplies, 4 different gas solenoids, a ±20 kV dynode, a -3.5 kV supply for an electron multiplier, and 3 different thermocouple pressure gauges. The hardware items acquired from the original TSQ 700 consisted of the vacuum chamber itself and turbo pumps, an optical rail for alignment of the ion focusing elements, the two quadrupole mass filters, dynode and electron multiplier assembly, and various ion lenses. A schematic of the entire instrument is shown in Figure 8.6

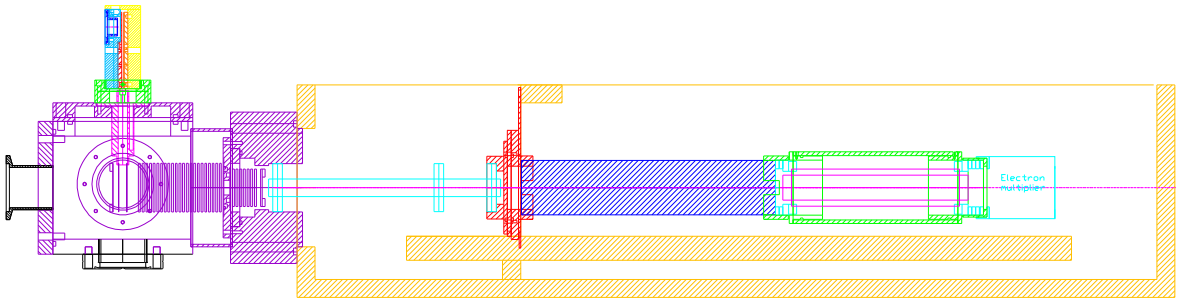

Figure 8.6. Schematic of FAIMS-Qq. Ions are produced via nano-ESI at 1, and pass through the FAIMS into the source (purple). A deflector bends the ions 90 degrees into an ion funnel, while neutrals and large solvent clusters should be unaffected. An octapole (light blue) guides the ions to the Extrel quadrupole mass filter (dark blue) and then through a gas collision cell (green) containing a Finnigan TSQ 700 quadrupole (pink) operated in rf only mode. An orthogonal dynode/electron multiplier setup (light blue) allows for detection of ions after the collision cell or for passing ions into the next part of the instrument, which will be a quadrupole bender and EB sector mass spectrometer.

8.5.2. FAIMS

The planar FAIMS constructed for our experiments is shown in Figure 8.7. This is almost an exact replica of the planar FAIMS used by Richard Smith's group at Pacific Northwest National Laboratories (PNNL).[19] The ions traverse a length of 5 mm along the electrodes, which are spaced by 2.0 mm. The surfaces of the electrodes were hand-polished to high smoothness to minimize the risk of arcing. Key features given by Keqi Tang of PNNL should be repeated. (1) The CV should be applied to the electrode that the ions pass through during injection, so they don't have to overcome the full strength of the DV to enter the analyzer. (2) The CV and DV voltages need to be floated at 10-30 volts above the potential of the vacuum chamber interface, shown in black in Figure 8.7. In our case, the interface is held at about 300 V, so a small isolation transformer was acquired to isolate the power supplies for the CV and DV and float them at 330 V. This raises issues with communicating to the CV supplies with a computer referenced to 0V versus the CV supply.

One way to solve this problem is to use optically coupled devices. An optically coupled transistor uses a light-emitting diode to control the base current of a transistor. A ground referenced computer can in this way transmit a signal to a device with a different common reference. The optically coupled CV circuit diagram is shown in **Appendix C**. (3) The FAIMS electrodes should be kept as clean as possible. Initially the electrodes should be sonicated and cleaned thoroughly with methanol. The FAIMS should then be hooked up to the carrier gas and a constant flow of N_2 should pass over the electrodes to keep particles from adsorbing to the surface. Cleanliness of the electrodes is of critical importance to the operation of the instrument.

The most difficult practical aspect of FAIMS is not the building of the device itself, but construction of a rf generator for outputting the required asymmetric waveform (see

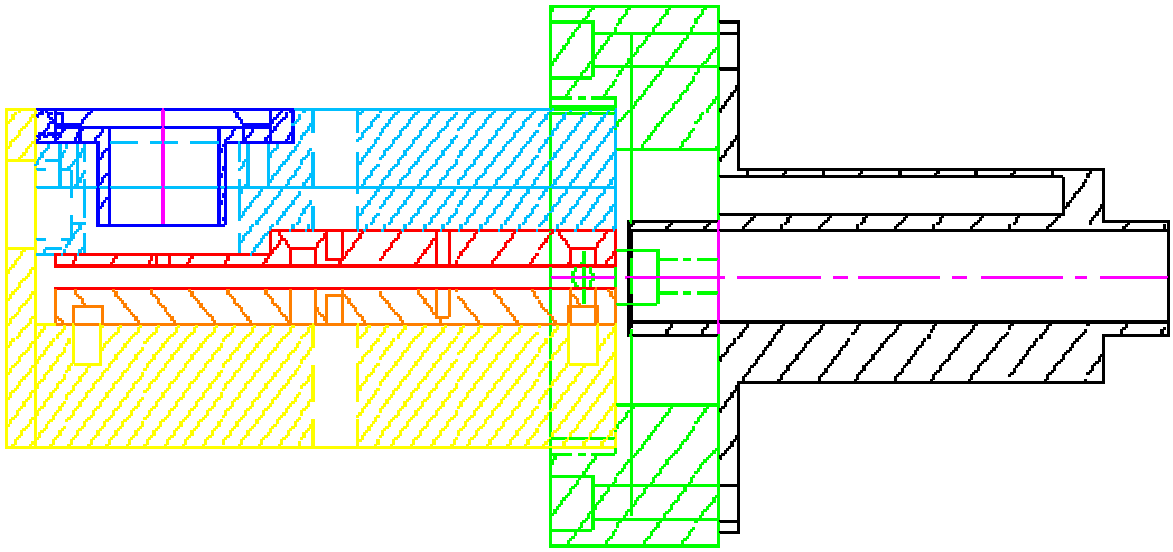

Figure 8.7. Drawing of FAIMS instrument. ESI curtain plate is in blue, upper electrode (CV voltage) in red, lower electrode (DV) in orange, all surrounded by PEEK insulator (light blue and yellow). PEEK holder in green attaches to vacuum interface in black. A horizontal slit consisting of 11x 0.13 mm holes disposed evenly over 4 mm admits gas from atmosphere and ions at a calculated flow rate of 1.75 L/s.

Figure 1.7). The UNC electronics shop has been working on a circuit based off the design from the company Ionalytics that was acquired by ThermoFisher (Aug, 2005). A circuit diagram is given in **Appendix C.**

8.5.3. Source

A new high pressure ion source was designed for using a Bruker prototype ion funnel, depicted in Figure 8.8. Ion funnels are a relatively new technology for improving the transfer of ions at high pressures.[27-30] A rf voltage is applied to each of a series of rings such that each ring voltage is 180 degrees out of phase with the neighboring rings. The ring diameter is generally about 25.4 mm for some distance before it linearly decreases to the conductance limiting aperture diameter, around 2.0 mm. Each ring is connected to the next ring with 10 MΩ resistors such that a voltage applied to the first ring creates a linearly decreasing dc gradient. The dc gradient pushes the ions towards the funnel aperture and also towards the rings themselves. The rf field pushes the ions away from the rings, such that a potential well is established at the balance position between rf and dc fields.[29] Ions of larger mass-to-charge reside closer to the rings, and ions of smaller mass-to-charge reside further away from the rings. The mass-to-charge range of ions passed by the funnel can be controlled primarily by rf voltage frequency and dc voltage gradient.[29] Interestingly, the low mass cut-off does not depend at all on rf voltage amplitude.

The ion prototype ion funnel acquired from Bruker operates by the same principles as other ion funnels except each ring is divided into four quadrants. Instead of making a series of solid metal rings, the Bruker rings are made from printed circuit boards, a much more economical option. The rings in this case are 1.6 mm thick and spaced by the same amount. There are 23 rings on one side of the conductance limiting plate, and 7 rings on the lower pressure side of the instrument. This dual-funnel arrangement improves ion transfer by confining ions as they expand into the lower pressure region. The high pressure region source built to house the ion funnel can be seen in Figure 8.8. Ions are introduced into the source orthogonally to the main instrument axis and deflected into the ion funnel. In this way the gas load and neutral species abundance is decreased. Currently the Bruker ion funnel is being driven with an rf voltage of 200-400 V_{pp}, at 2.1 MHz. The deflector is set to 350 V, the first ring to 160 V, last ring to 0 V. A list of all the optimum voltages needed to operate the whole instrument is in **Appendix D**.

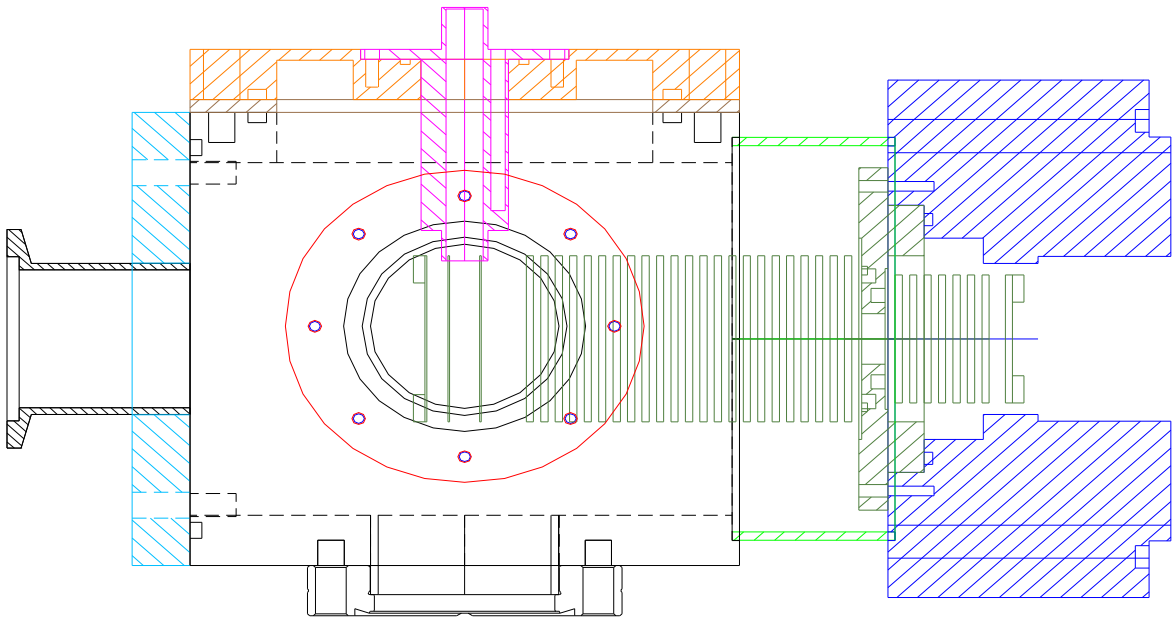

Figure 8.8. Electrospray source with interface (pink) and dual stage ion funnel (green).

8.5.4. Octapole

Ions are guided from the high pressure ion funnel to the low pressure analyzer by an octapole ion guide. The operation of the octapole is the same as in **Chapter 3.4.6**, only a new design was constructed for the FAIMS-Qq. The reason for the new design was that the octapole needed to be 20 cm long instead of 12 cm. The UNC instrument shop raised the concern of warping the rods when they are welded to the metal holder plates of the previous design. The new octapole was built such that the rods are held in place without welding. The scheme is shown in Figure 8.9. This design requires larger diameter rods to accommodate the use of screws as fasteners. The increased rod radius and thus field radius implies an increased rf voltage requirement to pass ions. The octapole of **Chapter 3.4.6** had a field radius r_o = 2.81 mm, while the new octapole has r_o = 4.47 mm. The voltage requirement is expected to increase as the square of r_o,[31] therefore the new octapole needs 2.5 times the rf voltage amplitude of the old octapole's 400 V_{pp}. The rf oscillator described in **Chapter 3.4.7** is capable of 1200 V_{pp}, and experiments show that optimum transmission is achieved at around 1000 V_{pp}, in agreement with theory. Ions can be trapped in the octapole by using the entrance and exit lenses to stop ions or pulse them out. Trapping in the octapole could be useful

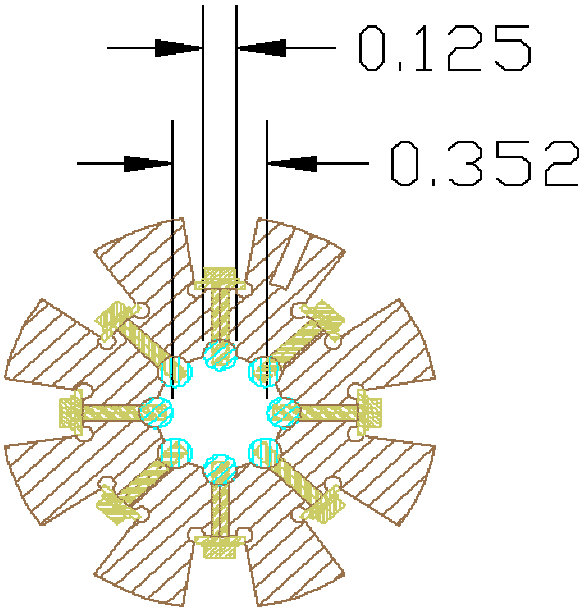

Figure 8.9. Octapole ion guide rods (blue) are held into position on PEEK holder by 00-80 screws. Rod and field radii are given.

for increasing the duty cycle of experiments in the rf-only quadrupole.

8.5.5. Quadrupole Mass Filter

An Extrel quadrupole with 8.5mm diameter rods and 850 kHz drive frequency was purchased for the Q portion of the instrument. There was an attempt to use the TSQ rf boards to do mass analysis, but there were problems with the dc rod driver supplies. Because mass analysis is a key part of the experiment, a full Extrel quadrupole system was acquired. The TSQ rf generator was modified to accommodate the Extrel rf leads and enabled connection to the TSQ rf feedthroughs. The custom software system described below provides control voltages to operate the quadrupole.

8.5.6. Reaction Region

One of the TSQ 700 quadrupoles was used for the reaction region. A gas tight cell was designed to hold the quadrupole and apply the rf voltage for passing or trapping ions. Two tubes connect to the cell, one for introduction of gas to the cell, and one for measuring the pressure in the cell. So far attempts to measure gas pressure in the cell have not agreed with pumping calculations. Collision cross section measurements described below seem to agree better with calculated pressures than with measured pressures. Further optimization of the measurement scheme is needed. Ions can be trapped by applying suitable voltages (~40 V) to entrance and exit lenses and raising the gas pressure in the cell.

8.6. Isolation Transformers

Typically, EB instruments accelerate ions to 5-10 kV for analysis. The resolution of mass analysis and amplification of the kinetic energy release during high energy CID increases with higher accelerating voltage. The potential of the FAIMS-Qq and all its related power supplies must be 5-10 kV above the potential of the EB to give the ions the optimum

kinetic energy. A 1:1 isolation transformer was custom built by Lenco Electronics (McHenry, Ill.) capable of isolating 10 kV between primary and secondary windings. The 10 kV dc voltage is applied to one lead of the secondary and to the instrument 3rd pin grounding prong. The output from the secondary is plugged into the TSQ 700 for distribution to all the FAIMS-Qq power supplies. As with the CV circuit mentioned above, the 10 kV floating supplies raise the issue of how to provide control from a grounded computer. In this case optical coupling was used again. A grounded computer connected to the internet is used to remote desktop into a floating computer (with all instrument control cards) that is connected to the internet via a fiber optic converter. The converter is LGC120A from Blackbox (Lawrence, Pa).

8.7. Control Software

An instrument control program was made using LabVIEW 7.1. National Instruments data acquisition and analog out boards were used to receive and transmit all necessary voltages. The data acquisition board is a PCI-MIO-16E-1 with 2 analog out (AO) and 32 analog in (AI) lines. There are two PCI-6713 boards with 8 AO and 8 digital output (DO) lines each. Finally a PCI-6703 was purchased that has 16 AO lines. This last board has 16 bit resolution, which is necessary for controlling the Extrel quadrupole rf level. The other 15 AO lines will be useful for controlling the EB later on, or for adjusting a few voltages on the FAIMS-Qq which are currently under manual control. There is no card bus connecting all the various cards together, so software timing is used instead of the more efficient hardware timing used to control the IR-Trap (**Chapter 3**). The control software program is given in more detail in **Appendix A**.

8.8. Results

8.8.1. EI

The instrument was first set up and tested without the FAIMS analyzer. The optimum conditions for nano-ESI had not been found yet, and there was difficulty determining if problems with mass analysis were due to the kinetic energy of the ions or the improper tuning of the Extrel mass analyzer. Nano-ESI ions would hit the detector in rf-only non-mass analyzing mode, but there was no signal when the Extrel would be set to scan through mass-to-charge values. In retrospect, these observations are not surprising, because theoretical studies have shown that operating a quadrupole in mass resolving mode versus non-resolving mode places limitations on ion radial position and kinetic energy.[32] Because EI sources produce better characterized ion beams, a TSQ 700 EI source was found in lab that could be attached in place of the high pressure ESI source. Perfluorotributylamine (PFTBA) was analyzed by the EI method described in **Chapter 2.1.3.** PFTBA is an ideal compound for testing mass spectrometry systems because it is a volatile liquid that produces relatively high mass-to-charge ions. When PFTBA could be mass analyzed by the Extrel quadrupole, stopping curves were obtained to characterize the optimal ion kinetic energy. Knowledge of the optimal ion kinetic energy (4-10 eV) helped to guide nano-ESI lens settings.

8.8.2. Nano-ESI

After successfully analyzing ions produced by EI, nano-ESI was attempted again, still without the FAIMS analyzer. The large number of degrees of freedom in lens settings made the process difficult, but eventually a set of lens voltage values was found that produces the correct ion kinetic energies and focuses ions to allow mass analysis of ions from 100 to 4000

m/z. Ions of mass 100 Da to 69 kDa have been successfully analyzed. While some lens voltages appear to have little effect on ion transmission, others must be controlled to within tenths of a volt for desired operation. The most important lens voltages are the apertures between the high pressure source and octopole region, the octapole dc bias, and octapole entrance and exit lenses. A full list of all lens voltages is given in **Appendix D.** A heating circuit was attached to the vacuum interface to help in desolvating nano-ESI ions, and this seems to help signal. When the FAIMS is attached to the instrument, a counter-current flow of N_2 performs desolvation, making heating unnecessary. Figure 8.10 is a montage of all the protein ions that have been mass analyzed thus far.

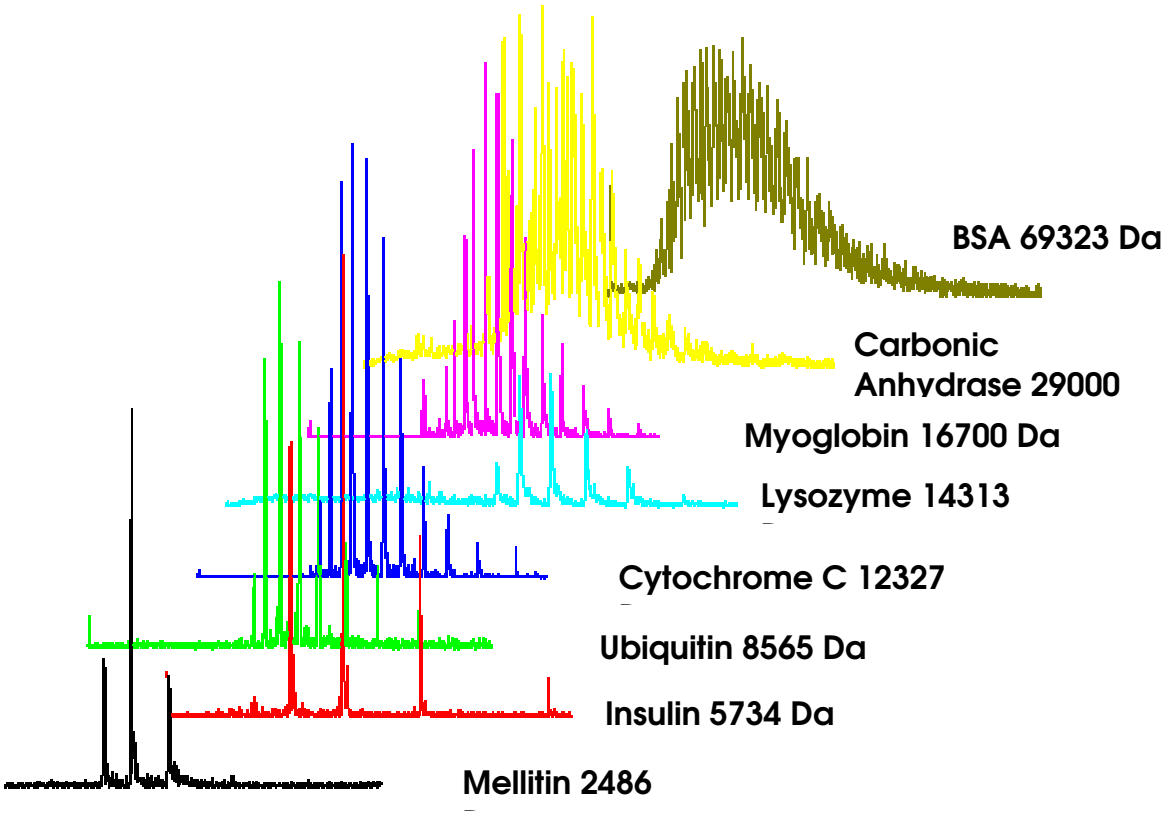

Figure 8.10. Overlay of all the proteins analyzed by nano-ESI on the Qq instrument to date.

8.8.3. Trapping

Trapping of ions in the rf-only quadrupole will be necessary for ion/molecule reactions or photodissociation experiments. Trapping in the octapole could be useful for ion/molecule reactions as well, or for increasing the duty cycle of trapping experiments in the rf-only quadrupole. While a reaction is happening in the rf-only quadrupole, ions can be simultaneously accumulated in the octapole and then pulsed into the rf-only quadrupole when the reaction is finished. Utilization of the ESI beam can be greatly increased with this method.

Figure 8.11 shows the timing diagram and ion signal overlaid from a trapping event in the octapole. The octapole exit lens is set to >30 V during an ion loading period, after which the entrance lens is set to >30 V to keep any more ions from entering. Depending on the experiment, raising the entrance lens may not be necessary. The high pressure of gas in the octapole dampens ion kinetic energy such that 5 V on the entrance lens will let ions in, but is enough to keep them from coming out in that direction. In a third step, the octapole exit lens is set to a lower voltage than the octapole dc bias and the ions are pulsed through the two quadrupoles into the electron multiplier. An analogous procedure is used for trapping ions in the rf-only quadrupole, and a combination of the steps is used to trap ions in the octapole and pass them to the rf-only quadrupole. The loading and trapping times can be varied depending on the particular experiment being carried out.

The tail of ions in Figure 8.11 comes from a distribution of ion times hitting the detector. Ions presumably reside along the entire 20 cm length of the octapole, and a significant portion of ions take many axial oscillations before they are ejected. The ejection profile can be modified, however, by changing the trapping time octapole. Longer trapping

times lead to a narrower range of ejection times and ions that have a lower average kinetic energy. The longer time to collisionally cool creates a condition where the ions are concentrated along the center axis of the octapole, decreasing the number of oscillations the

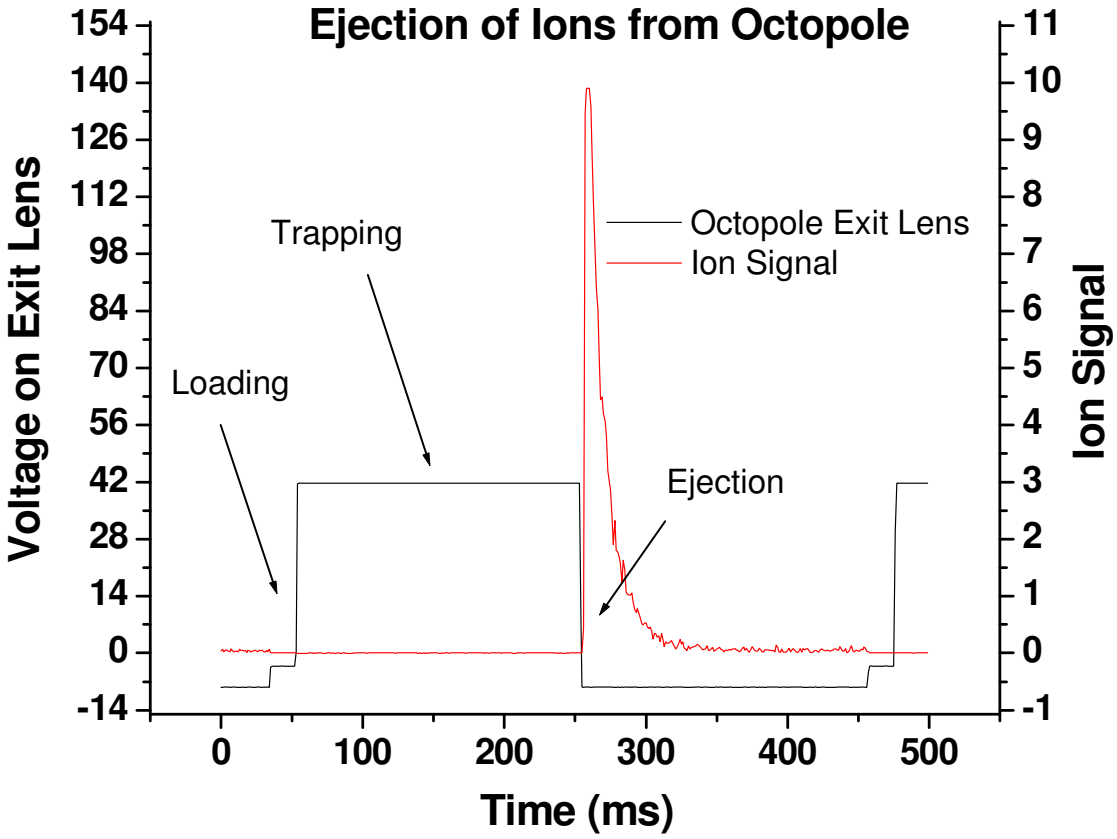

Figure 8.11. Timing diagram for trapping ions in octapole with ion signal on electron multiplier overlaid. Event timing amplitude does not necessarily correspond to actual voltage experience by ions. Further explanation of diagram is in text.

ion must make before being ejected.

8.8.4. Collision Cross Section Measurements

Collision cross sections were measured by the method in **Chapter 1.4.2** where kinetic energy lost as ions travel through a gas filled collision cell was measured. Three measurements are needed, the actual pressure of N_2 in the collision cell, the kinetic energy of the ions with no N_2 gas present, and the kinetic energy of the ions after passing through the

N_2. The kinetic energy of ions after they passed through the rf-only quadrupole was measured by increasing the voltage on the exit lens in small increments. The rf-only quadrupole dc bias was 0 V, and the lens after the exit lens was set to 0 V. The first and second derivatives of ion signal with respect to exit lens voltage were used to provide a peak profile of ions at each kinetic energy and a value for most probable kinetic energy, respectively. Previous studies have used the point of 10% decrease in ion signal as the average ion kinetic energy, but this method seemed to have been chosen because it gave good cross section results, and have no physical basis.[33] Similar results were obtained with both methods in our case, but the first and second derivative method seems less subjective and gives the kinetic energy as the voltage where most ions are stopped.

Figure 8.12 shows stopping curves taken for the 10^+ charge state of ubiquitin. The reproducibility of the stopping curves is good, judging from the error bars on the ion abundance points. The energy loss method of cross section measurement has been shown to be accurate on a relative scale, but is generally higher than measurements taken by other methods. Therefore these data are generally scaled to a known value to "anchor" the cross section scale.[33] The data in Figure 8.12 were anchored to the measurement of the 13^+ charge state of ubiquitin. With this procedure a calculated cross section of 2080 A^2 was obtained for the 10^+ charge state, which is close to the literature value of 2035 A^2 (average of both conformers observed for 10^+).[33]

At the moment, the pressure of N_2 in the rf-only quadrupole is regulated with a metering valve and measured by a cold cathode gauge that is connected to the cell via a plastic tube. The base pressure read by the cold cathode gauge is 1.4×10^{-4} Torr, even though the base pressure in the main vacuum chamber is 3×10^{-7} Torr. This gauge could have a leak

or the connection to the vacuum housing might need to be modified. Conductance calculations of the type in **Chapter 3.4.3** estimate the conductance of the collision cell to be 0.482 L/s, so that the factor between gas pressure read in the main chamber and collision cell pressure is 500x. Calculated cell pressures give more realistic cross section estimations of 100's of square angstroms for peptides, and 1000's of square angstroms for proteins. Measured pressures are generally too high, and result in wildly different collision cross section estimations at each cell pressure. When calculated pressures are used, a very similar calculated cross section results at each pressure.

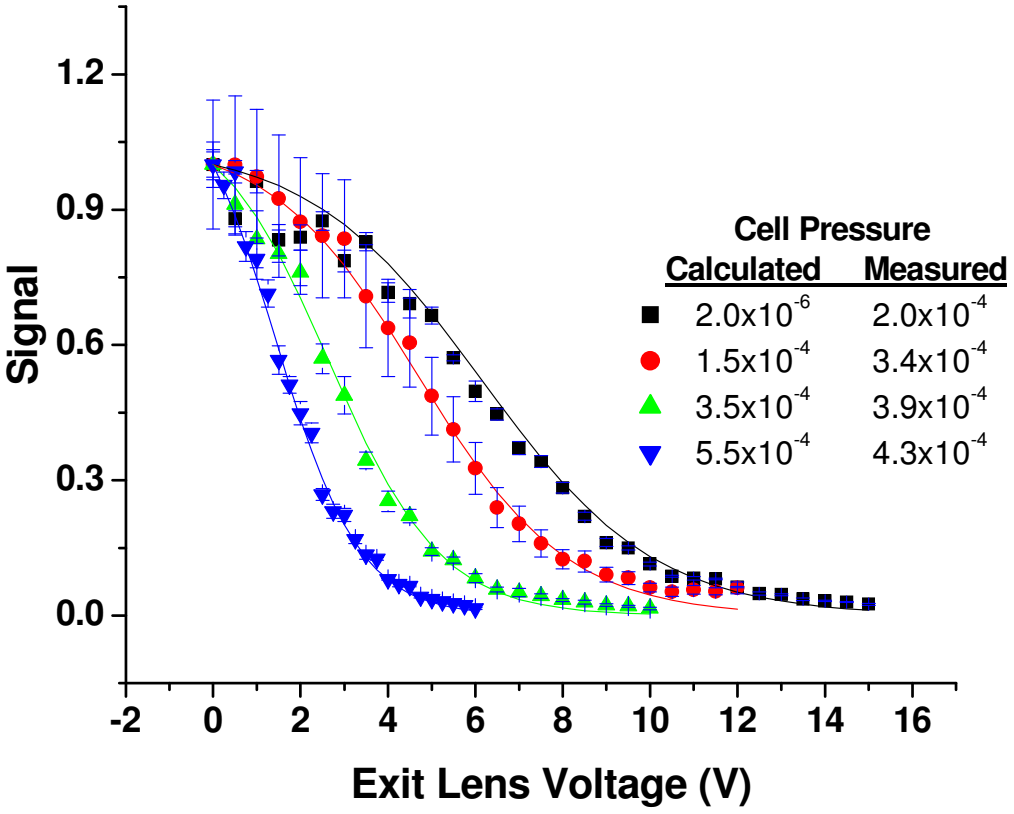

Figure 8.12. Stopping curves taken of the 10^{+} charge state of bovine ubquitin at different indicated cell pressures. There are still problems with the physical pressure measurement of cell pressure.

8.8.5. FAIMS

As mentioned previously, the difficulties in making a FAIMS device lie in producing the asymmetric waveform. Two LC circuits, one resonating at frequency = f and another at frequency = f*2, must be coupled together with a variable DC offset. The main complication is that several different circuit component impedances change as the output is varied. The power supplies driving the coils have variable output impedance, and the coils themselves change resonance frequency slightly with output amplitude, perhaps due to thermal expansion of the coil forms. The phase of the waveforms must also be 90 degrees to get the optimum waveform shape. The simulations from this chapter (vide supra) have been useful for evaluating the quality of actual waveforms produced by the circuit, before actual experiments take place. Figure 8.13a shows one prototype waveform in black, along with several other waveform shapes. All the waveforms have a low harmonic frequency of 664 kHz and various ratios and phases of low frequency harmonic versus high frequency harmonic. Simulation results using each of the waveforms in a planar device are in Figure 8.13b. The simulation CV is set to zero and the ions are allowed to drift based on their high to low field mobilities. The trajectories with steepest slope are the most useful, because they allow for the most resolving power. The results demonstrate that several different waveform shapes can give good performance, with waveform amplitude being the most important variable. The lowest acceptable performance is given by the thin black line, corresponding to DV = 4kV, phase = 90, ratio = 2. The prototype waveform would have a separation space of a few volts, and not be capable of high resolution spectra. The UNC Electronics shop is improving the circuit by adding variable vacuum capacitors, which should allow for better performance.

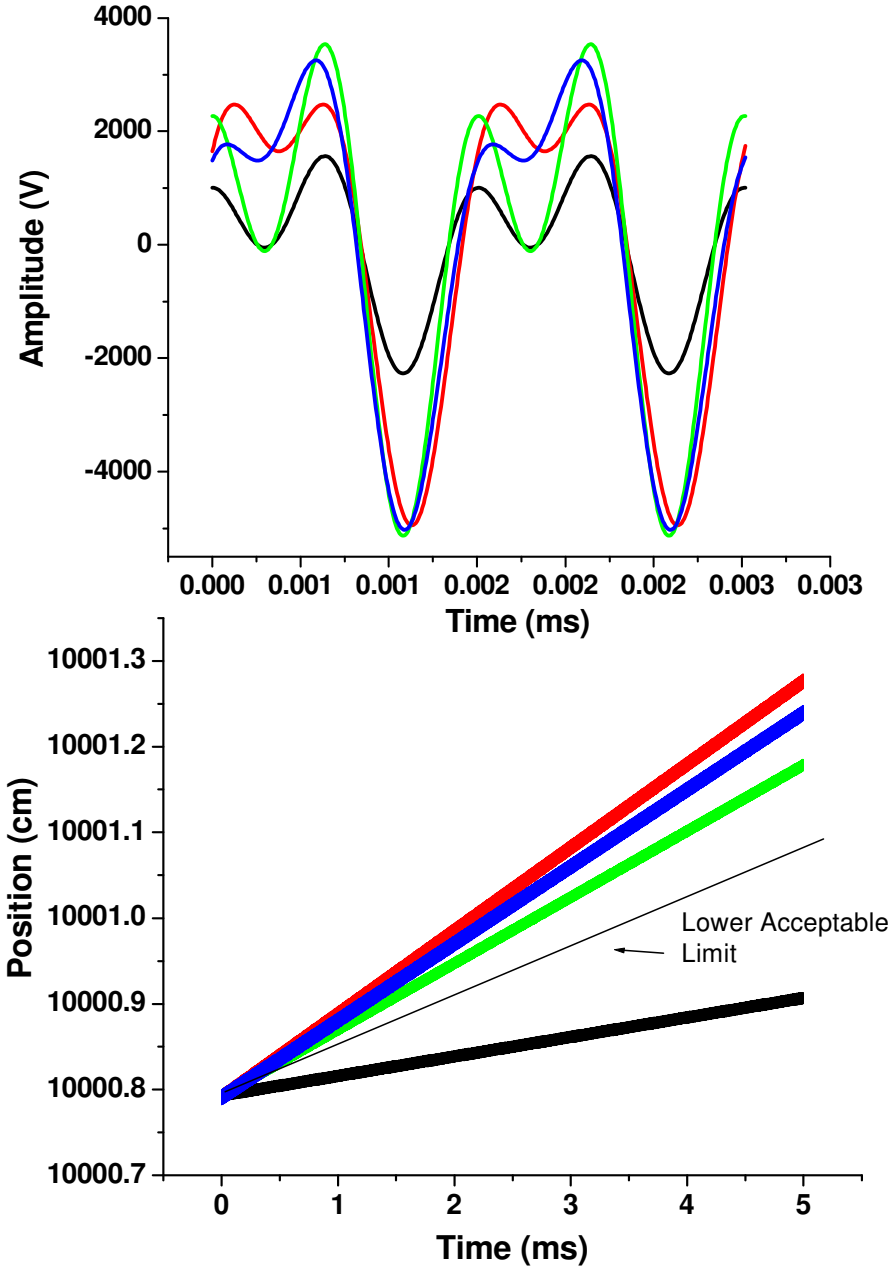

Figure 8.13. a) Dispersion voltage waveforms. Prototype waveform (black): DV = -2.2 kV, phase = -119, ratio = 1. Red waveform: DV = -5.0 kV, phase = -90, ratio = 2. Blue waveform: DV = -5.0 kV, phase = -119, ratio = 2. Green waveform: DV = -5.0 kV, phase = -119, ratio = 1.
b) Simulation results for $[Leucine\text{-}H]^-$ in a planar-FAIMS with above waveforms. Thin black line labeled "Lower Acceptable Limit" is for DV = -4.0 kV, phase = -90, ratio = 2.

8.9. Summary

The front end of the FAIMS-Qq-EB instrument has been built and used for some preliminary studies. A TSQ 700 triple quadrupole mass spectrometer system was converted by the addition of a new electrospray source, octapole ion guide, resolving quadrupole, and collision quadrupole cell. The tuned system is now capable of analyzing peptides and proteins of a wide range of molecular weights. A planar FAIMS device was built that interfaces with the electrospray source. Simulations predict that high resolution separations of peptide and protein conformers will be possible with this FAIMS when a suitable waveform generator is procured. The planar FAIMS will have the advantage over cylindrical FAIMS of high resolution, with resolution and sensitivity control provided by varying the ion residence time. Further control of resolution and sensitivity are predicted to arise from active, differential temperature control of the electrodes which introduces a focusing E/N gradient.

The flexibility of the hardware and software has been tested with initial experiments to trap and eject ions in the octapole and collision cell, and to show that collision cross section determination is possible through the use of energy loss measurements. Although the FAIMS-Qq still has to be coupled to the EB and several other components, the established project timeline is being followed, and the good performance of the current instrument bodes well for the future.

8.10. References

1. Yates, J. R., III *Mass Spectrometry and the Age of the Proteome*. *J. Mass Spectrom.* **1998,** *33*, 1-19.

2. Yates, J. R.; McCormack, A. L.; Eng, J. *Mining Genomes with MS*. *Anal. Chem.* **1996,** *68*, 534A-540A.

3. Sadygov, R. G.; Cociorva, D.; Yates, J. R. *Large-scate database searching using tandem mass spectra: Looking up the answer in the back of the book*. *Nature Methods* **2004,** *1*, 195-202.

4. Roepstorff, P. *Proposal for a Common Nomenclature for Sequence Ions in Mass Spectra of Peptides*. *Biomed. Mass Spectrom.* **1984,** *11*, 601.

5. Vachet, R. W.; Bishop, B. M.; Erickson, B. W.; Glish, G. L. *Novel Peptide Dissociation: Gas-Phase Intramolecular Rearrangement of Internal Amino Acid Residues*. *J. Am. Chem. Soc.* **1997,** *119*, 5481-5488.

6. Yague, J.; Paradela, A.; Ramos, M.; Ogueta, S.; Marina, A.; Barahona, F.; de Castro, J. A. L.; Vazquez, J. *Peptide rearrangement during quadrupole ion trap fragmentation: Added complexity to MS/MS spectra*. *Anal. Chem.* **2003,** *75*, 1524-1535.

7. Paizs, B.; Suhai, S. *Fragmentation pathways of protonated peptides*. *Mass Spectrom. Rev.* **2005,** *24*, 508-548.

8. Paiz, B.; Suhai, S. *Towards understanding the tandem mass spectra of protonated oligopeptides. 1: mechanism of amide bond cleavage*. *J. Am. Soc. Mass Spectrom.* **2004,** *15*, 103-113.

9. Kelleher, N. L.; Lin, H. Y.; Valaskovic, G. A.; Aaserud, D. J.; Fridriksson, E. K.; McLafferty, F. W. *Top Down versus Bottom Up Protein Characterization by Tandem High-Resolution Mass Spectrometry*. *J. Am. Chem. Soc.* **1999,** *121*, 806-812.

10. Bogdanov, B.; Smith, R. D. *Proteomics by FTICR Mass Spectrometry: Top Down and Bottom Up*. *Mass Spectrom. Rev.* **2005,** *24*, 168-200.

11. Zubarev, R. A.; Kelleher, N. L.; McLafferty, F. W. *Electron Capture Dissociation of Multiply Charged Protein Cations. A Nonergodic Process*. J. Am. Chem. Soc. **1998,** *120*, 3265-3266.

12. Syka, J. E. P.; Coon, J. J.; Schroeder, M. J.; Shabanowitz, J.; Hunt, D. F. *Peptide and protein sequence analysis by electron transfer dissociation mass spectrometry*. PNAS **2004,** *101*, 9528-9533.

13. Vachet, R. W.; Asam, M. R.; Glish, G. L. *Secondary Interactions Affecting the Dissociation Patterns of Arginine-Containing Peptide Ions*. J. Am. Chem. Soc. **1996,** *118*, 6252-6256.

14. Vachet, R. W.; Winders, A. D.; Glish, G. L. *Correlation of Kinetic Energy Losses in High-Energy Collision-Induced Dissociation with Observed Peptide Product Ions*. Anal. Chem. **1996,** *68*, 522-526.

15. Douglas, D. J.; French, J. B. *Collisional Focusing Effects in Radio-Frequency Quadrupoles*. J. Am. Soc. Mass Spectrom. **1992,** *3*, 398-408.

16. Belov, M. E.; Buschbach, M. e.; Prior, D. C.; Tang, K.; Smith, R. D. *Multiplexed Ion Mobility Spectrometry-Orthognal Time-of-Flight Mass Spectrometry*. Anal. Chem. **2007,** *79*, 2451 - 2462.

17. Buryakov, I.; Krylov, E.; Nazarov, E.; Rasulev, U. *A new method of separation of multi-atomic ions by mobility at atmospheric pressure using a high-frequency amplitude-asymmetric strong electric field*. International Journal of Mass Spectrometry and Ion Processes **1993,** *128*, 143.

18. Purves, R. W.; Guevremont, R.; Day, S.; Pipich, C. W.; Matyjaszczyk, M. S. *Mass Spectrometric Characterization of a High-Field Asymmetric Waveform Ion Mobility Spectrometer*. Review of Scientific Instruments **1998,** *69*, 4094-4105.

19. Shvartsburg, A. A.; Li, F. M.; Tang, K. Q.; Smith, R. D. *High-resolution field asymmetric waveform ion mobility spectrometry using new planar geometry analyzers*. Anal. Chem. **2006,** *78*, 3706-3714.

20. Shvartsburg, A. A.; Tang, K. Q.; Smith, R. D. *Modeling the resolution and sensitivity of FAIMS analyses*. J. Am. Soc. Mass Spectrom. **2004,** *15*, 1487-1498.

21. Guevremont, R.; Barnett, D. A.; Purves, R. W.; Viehland, L. A. *Calculation of ion mobilities from electrospray ionization high-field asymmetric waveform ion mobility spectrometry mass spectrometry*. Journal of Chemical Physics **2001,** *114*, 10270-10277.

22. Barnett, D. A.; Ells, B.; Guevremont, R.; Purves, R. W.; Viehland, L. A. *Evaluation of Carrier Gases for Use in High-Field Asymmetric Waveform Ion Mobilty Spectrometry*. J. Am. Soc. Mass Spectrom. **2000**, 1125-1133.

23. Shvartsburg, A. A.; Tang, K. Q.; Smith, R. D. *Understanding and designing field asymmetric waveform ion mobility spectrometry separations in gas mixtures*. Anal. Chem. **2004,** *76*, 7366-7374.

24. Barnett, D. A.; Ells, B.; Guevremont, R.; Purves, R. W. *Application of ESI-FAIMS-MS to the analysis of tryptic peptides*. J. Am. Soc. Mass Spectrom. **2002,** *13*, 1282-1291.

25. Barnett, D. A.; Belford, M.; Dunyach, J. J.; Purves, R. W. *Characterization of a Temperature-Controlled FAIMS System*. J Am Soc Mass Spectrom **2007,** *18*, 1653-1663.

26. Shvartsburg, A. A.; Li, F. M.; Tang, K. Q.; Smith, R. D. *Distortion of ion structures by field asymmetric waveform ion mobility spectrometry*. Anal. Chem. **2007,** *79*, 1523-1528.

27. Shaffer, S. A.; Tang, K.; Anderson, G. A.; Prior, D. C.; Udseth, H. R.; Smith, R. D. *A Novel Ion Funnel for Focusing Ions at Elevated Pressure Using Electrospray Ionization Mass Spectrometry*. Rapid Commun. Mass Spectrom. **1997,** *11*, 1813-1817.

28. Shaffer, S. A.; Tolmachev, A.; Prior, D. C.; Anderson, G. A.; Udseth, H. R.; Smith, R. D. *Characterization of an improved electrodynamic ion funnel interface for electrospray ionization mass spectrometry*. Anal. Chem. **1999,** *71*, 2957-2964.

29. Page, J. S.; Tolmachev, A. V.; Tang, K.; Smith, R. D. *Theoretical and Experimental Evaluation of the Low m/z Transmission of an Electrodynamic Ion Funnel*. J Am Soc Mass Spectrom **2006,** *17*, 586 - 592.

30. Ibrahim, Y.; Tang, K.; Tolmachev, A. V.; Shvartsburg, A. A.; Smith, R. D. *Improving Mass Spectrometer Sensitivity Using a High-Pressure Electrodynamic Ion Funnel Interface*. Journal Amer. Soc. Mass Spectrom. **2006,** *17*, 1299-1305.

31. Hägg, C.; Szabo, I. *New Ion-Optical Devices Utilizing Oscillatory Electric Fields. III. Stability of Ion Motion in a Two-Dimensional Octopole Field*. Int. J. Mass Spectrom. Ion Processes **1986,** *73*, 277-294.

32. Baranov, V. I. *Analytical Approach for Description of Ion Motion in Quadrupole Mass Spectrometer*. J Am Soc Mass Spectrom **2003,** *14*, 818--824.

33. Purves, R. W.; Barnett, D. A.; Ells, B.; Guevremont, R. *Investigation of bovine ubiquitin conformers separated by high-field asymmetric waveform ion mobility spectrometry: Cross section measurements using energy-loss experiments with a triple quadrupole mass spectrometer*. J. Am. Soc. Mass Spectrom. **2000,** *11*, 738-745.

Chapter 9

9. Conclusions and Future Directions

9.1. Summary

The previous chapters have described the design and construction of two mass spectrometers for developing three dimensional mass spectrometry methods, and specific experiments carried out on these platforms. An investigation of the optimum conditions for low temperature IR action spectroscopy is detailed. The way in which different instrument parameters affect ion internal energy in a QITMS is explored, and a theoretical analysis of ion internal energy after excitation by different MS/MS procedures is shown. This chapter will summarize the results from each chapter and suggest directions for future research.

9.2. Three Dimensional Mass Spectrometry

9.2.1. Action Spectroscopy-Chapter 3

A fully functional, temperature controlled QITMS was constructed for IRMPD spectroscopy studies, fulfilling the Glish lab commitment in the ion structure determination collaboration. Trap temperatures from 23 K to 330 K were demonstrated, and the studies in **Chapters 4 and 5** made used of this "IR-Trap" platform. The most obvious future study needed for this instrument is to couple a tunable IR laser source to it and begin analyzing various ion structure problems. One experiment that was initially proposed was the study of the so-called "b-ion" formed during tandem mass spectrometry. Previous studies in the Glish

lab demonstrated that some b ions have structures different[1] from the one that is now widely accepted[2], and an IR structure determination would be an impressive piece of evidence.

Another experiment that has just started on the IR-Trap is the study of protein unfolding. Previous studies reported that protein ions can unfold by simply being stored in a QITMS for ~100 ms.[3] If different protein conformations yield different product ions in MS/MS, as we suspect, then a study of protein folding at various trap temperatures could be able to reveal the kinetics of the unfolding process.

Finally, a new set of experiments has been proposed for the ion trap, whereby FAIMS separation power would be added to the source. This would allow us the ability to select ion conformations before photo-dissociation, which would be very interesting. IR spectra would not be complicated by the presence of multiple conformers, assuming the conformation can be kept from changing inside the trap (as opposed to the proposed study in the previous paragraph). Work on this project has already started, and a modification of the API source has been designed and submitted to the UNC instrument shop. Drawings are included in **Appendix D.** The ion source from **Chapter 8** has been designed such that it could be fitted onto the IR-Trap for FAIMS experiments, and a recent collaboration with Bruker is seeking to adapt new FAIMS technology to the current IR-Trap source.

9.2.2. Ion Mobility-Chapter 8

The first part of a FAIMS-Qq-EB instrument for probing the conformation of biomolecules has been constructed. With the FAIMS device not attached to the ion source, nano-ESI spectra have been obtained for a variety of peptide and protein ions. Instrument control software was written to control the instrument and automatically scan certain parameters to obtain energy loss measurements or FAIMS spectra. Collision cross sections

were measured by the energy loss method in the collision cell. Although the pressure measurement scheme in the collision cell must be optimized, initial results using calculated pressures match with literature data.

In the next few weeks the UNC Electronics Shop should finish the dispersion voltage circuit which is necessary for FAIMS. When this is finished there are several fundamental FAIMS experiments to be done that do not require the interface and EB portion of the instrument to be attached. Theory says that the sensitivity and resolution of planar FAIMS separation can be controlled by changing the ion residence time, but this has not been shown experimentally. Changing the gas flow rate is the best way to change the ion residence time, but the current commercial instruments are not able to do this because of design limitations. Another method of controlling sensitivity and resolution is differential temperature control of the electrodes. This method has been demonstrated for cylindrical FAIMS electrodes, but the leap to using planar electrodes in this manner has not been made, which could possibly make planar FAIMS sensitivity comparable to cylindrical FAIMS. The combination of controlled ion residence time with gas flow and controlled resolution with electrode temperature could be very beneficial for increasing the compatibility of FAIMS with the LC separation time frame. A current limitation of using FAIMS with LC is that the ion residence time in FAIMS is fixed to about 200 ms, such that a scan of the entire CV range takes tens of seconds at best. This is much too long for LC peaks eluting in the same time frame.

As mentioned in **Chapter 8**, the current understanding of the mechanism of FAIMS separation is very limited. Collision cross sections cannot be obtained directly from CV spectra in the way that IMS gives collision cross sections directly from drift time data. Understanding the FAIMS mechanism is therefore a prime area for research. One way to

approach this problem would be to undergo a FAIMS study of a variety of proteins using cross sections that are either known or measured with the kinetic energy loss method. These cross sections would have to be correlated with experimentally derived *a, b,* and *c* terms describing the ion mobility as electric field changes (Equation 1.22). A combined theoretical approach using calculated ion structures might yield another intrinsic property that can be predicted based on CV data alone. The information provided by the FAIMS-MS combination could in theory be much greater than IMS-MS, because of the fact that CV value is generally not correlated to ion mass-to-charge, while there is a strong correlation between IMS drift time and ion mass-to-charge.

9.3. Collisional Cooling Measurements-Chapter 4

The desire to do IR action spectroscopy studies at low temperatures raises issues with the laser power requirements to dissociate ions. CID was used as a probe of internal energy at a series of temperatures to characterize the relationship between temperature and excitation energy required to reach a given ion internal energy[4]. The required excitation energy increased dramatically at temperatures below 100 K, suggesting that collisional cooling interactions with the He bath gas were very significant at these temperatures. A previously described method for obtaining collision cooling rate constants was applied to the cold QITMS.[5] The measured rate constants had the same temperature dependence as the excitation energy required for dissociation. The conclusion was that significantly higher excitation energies (3 fold or more) are needed for dissociation at temperatures less than 100 K, and laser power is an important factor in the design of low temperature IRMPD spectroscopy instruments.

This research has already branched out into the study of collisional cooling rate constants and ion mass.[6] The difficulty of this project lies in the fact that comparisons of experimental data are complicated by different energetic requirements for dissociation. That is, when collisional cooling behavior is being compared for the same ion at different conditions, at least the critical energy of dissociation of the ion is constant. When comparing results for ions with different critical energies and reaction surfaces, the meaning of collisional cooling comparisons is hard to assess. Our initial studies have used a theoretical calculation of internal temperature versus CID voltage to estimate the internal temperature of ions at various fragmentation efficiencies.[7] In this way the rate of internal energy loss could be compared across different size ions. Initial results are interesting because they suggest that larger ions collisionally cool faster than smaller ions, which contradicts theoretical studies. However, a few complicating factors make it difficult to fully endorse this conclusion and additional work is needed to improve our understanding of the results.

9.4. Ion Cloud Size-Chapter 5

This chapter began as a study of the optimum QITMS parameters for IRMPD. In the course of this systematic "tweaking up" of parameters, a strong dependence of fragmentation efficiency on rf voltage amplitude was observed. Other studies have shown that rf amplitude at normal ion storage levels does not noticeably change ion internal energy[8], so the results were rationalized based on dynamic ion cloud overlap with the exciting laser that depended on the depth of the pseudopotential trapping well. Fragmentation efficiency was studied as a function of trapping voltage amplitude and frequency, with the conclusion that parameters which increase pseudopotential well depth must decrease ion cloud size. That is, increased trapping frequency and amplitude increase overlap with the laser and increase fragmentation

efficiency. Ion trajectory simulations corroborated the experimental results, providing a mapping of ion cloud size as a function of voltage amplitude and frequency. The simulations also explored the effect of ion mass on cloud size, which is a difficult problem to approach experimentally. This study suggested that although IRMPD efficiency is often considered to be independent of rf voltage amplitude, in reality a number of parameters are influential. When the limiting factor for ion dissociation is laser power, trapping frequency and voltage amplitude should be considered as parameters for improving fragmentation efficiency.

One application of the study of ion cloud size is the idea that because ions in a QITMS are more likely to be found at the point where they turn around and reverse direction, the optimum laser position might be found slightly off center of the trapping volume, especially if laser spot size was decreased even further. One member of the Glish lab went as far as to focus the laser on a spot outside the ion cloud entirely and resonantly excite ions into the lasing volume with a supplementary voltage.

Finally, the fact that the laser beam was focused to a 0.8 mm spot for this study (for **Chapter 4 too**) revealed the interesting result that higher bath gas pressures can be used during dissociation than was previously possible for an unfocused beam. The higher density of photons competes more favorably with collisional cooling, allowing peptides to be dissociated at optimum bath gas pressures. Normally the bath gas pressure is reduced for IRMPD to maximize fragmentation efficiency[9, 10], which has detrimental effects on ion trapping efficiency. Researchers would be more apt to consider IRMPD as a companion or competitor to CID in ion traps if there was no need to sacrifice sensitivity.

9.5. Estimation of the Internal Temperature of Ions-Chapter 6

When new mass spectrometry techniques are introduced, comparisons to established methods are constructive for assessing the usefulness of the new methods. How the internal energy of ions will be affected is one of the key questions, because internal energy is such an important factor in mass spectrometry. When the new technique is an MS/MS method, the details of the internal energy activation are especially interesting.

This chapter used a semi-quantitative experimental and theoretical approach to compare conventional CID to a new CID procedure called HASTE. RRKM modeling was employed to calculate mass spectra at different ion internal energy distributions.[10] RRKM parameters were obtained by adapting previous methods to a QITMS.[11-13] Internal energy distributions were estimated as internal temperatures, and experimental CID spectra were matched to a theoretical spectrum of a given temperature. The results indicated that HASTE CID activated ions by about 100 K higher than conventional CID, which explained the increased number of low mass-to-charge, and 2^{nd} and 3^{rd} generation product ions formed with HASTE CID.

The methodology of this chapter could be applied to any set of activation methods that are expected to raise ion internal energy slow enough that a temperature can accurately describe the energy distribution. Therefore the method might not be very pertinent to non-ergodic methods such as ECD, ETD, or high energy CID. An interesting application of the technique, however, could be for putting quantitative numbers on ion dissociation caused by a new mass spectrometry component, such as an ion funnel or FAIMS device.

9.6. On the Time Scale of Internal Energy Relaxation of Ions-Chapter 7

Chapter 7 looks at internal energies of ions formed by two ionization methods, nano-ESI and AP-MALDI. A recent comparison of these techniques reported that ion internal energy in a QITMS evolved over several hundred milliseconds before relaxing, and that parameters such as matrix basicity could play a significant role in the ultimate ion internal energy.[14] These conclusions contradicted results from our laboratory[4, 15, 16], so the experiment was repeated to try to understand the discrepancy. One area of concern was the fact that the previous studies had operated their QITMS under severe space-charge conditions. Experimental and theoretical data are presented that show how ion-ion interactions change the secular frequency of ions in the ion trap. Because ion secular frequency is actually dependent on ion cloud size when enough ions are present, internal energy estimations made with a frequency dependent method such as CID are prone to misinterpretation. A method for obtaining equal ion numbers for both ionization techniques was implemented, after which ion internal energy was probed with CID. The results concluded that less energy was required to dissociate ions formed by AP-MALDI than nano-ESI. Because ions cool down vibrationally within a few milliseconds in a QITMS, we concluded that ions formed by the different methods must have the same internal energy but different critical energies of dissociation, and thus different conformations.

An interesting and logical extension to this study would be to use the instruments built for this dissertation to further corroborate or refute the claims made in **Chapter 7.** If the IR-Trap or the FAIMS-Qq-EB could be fitted with an AP-MALDI source, the structures of AP-MALDI and nano-ESI ions could be compared. An initial idea for an AP-MALDI source for attaching to FAIMS was sketched already. The main problem is that heating of

the ion/matrix clusters is important to dissolvation, and this heating would probably have to be provided prior to FAIMS separation. A drawing of this device is included in **Appendix D.**

9.7. Conclusions

The observation has been made that although the instruments built for this work are designed to investigate three dimensional ion structures, there are no three dimensional structure determinations to be found in this thesis. While unfortunate, hopefully the instruments constructed and the experiments in this dissertation will be of use to the next generation of Glish lab experimentalists interested in ion three dimension structure. This work has shown that a QITMS can be mounted on a cold temperature cryostat and coupled with EI and nano-ESI. A better understanding of how QITMS parameters affect photodissociation results has emerged. Tools for characterizing and comparing ion internal energy, which plays an important role in ion structure, have been developed. Finally, the first part of a FAIMS-Qq-EB has been constructed, initial experiments have been performed, and FAIMS spectra should be forth coming pending a waveform generator.

9.8. References

1. Allen, J. M.; Black, D. M.; Glish, G. L. Do b3 Ions Have The Same Structure As Other b Ions? Nashville, TN, 2004.

2. Paiz, B.; Suhai, S. *Towards understanding the tandem mass spectra of protonated oligopeptides. 1: mechanism of amide bond cleavage*. J. Am. Soc. Mass Spectrom. **2004,** *15*, 103-113.

3. Myung, S.; Badman, E.; Lee, Y.; Clemmer, D. *Structural transitions of electrosprayed ubiquitin ions stored in an ion trap over similar to 10 ms to 30 s*. Journal of Physical Chemistry A **2002,** *106*, 9976-9982.

4. Remes, P. M.; Glish, G. L. *Collisional Cooling Rates in a Quadrupole Ion Trap at Sub-Ambient Temperatures*. Int. J. Mass. Spectrom. **2007,** *265*, 176-181.

5. Asamoto, B.; Dunbar, R. C. *Observation of the infrared radiative relaxation of iodobenzene ions using two-light-pulse photodissociation*. J. Phys. Chem. **1987,** *91*, 2804-2807.

6. Demireva, M. P.; Remes, P. M.; Glish, G. L. Internal Energy Relaxation of Different Mass Peptide Ions in Quadrupole Ion Trap Mass Spectrometry. Indianapolis, IN, 2007.

7. Goeringer, D. E.; McLuckey, S. A. *Evolution of Ion Internal Energy During Collisional Excitation in the Paul Ion Trap: A Stochastic Approach*. Journal of Chemical Physics **1996,** *104*, 2214-2221.

8. Asano, K. G.; Goeringer, D. E.; McLuckey, S. A. *Thermal Dissociation in the Quadrupole Ion Trap: Ions Derived From Leucine Enkephalin*. Int. J. Mass Spectrom. **1999,** *185/186/187*, 207-219.

9. Payne, A. H.; Glish, G. L. *Thermally Assisted Infrared Multiphoton Photodissociation in a Quadrupole Ion Trap*. Anal. Chem. **2001,** *73*, 3542-3548.

10. Baer, T.; Mayer, P. M. *Statistical Rice-Ramsperger-Kassel-Marcus quasi-equilibrium theory calculations in mass spectrometry*. J. Am. Soc. Mass Spectrom. **1997,** *8*, 103-115.

11. Laskin, J.; Futrell, J. *Internal Energy Distributions Resulting from Sustained Off-Resonance Excitation in Fourier Transform Ion Cyclotron Resonance Mass Spectrometry. II.*

Fragmentation of the 1-Bromonaphthalene Radical Cation. Journal of Physical Chemistry A **2000,** *104*, 5484-5494.

12. Laskin, J.; Byrd, M.; Futrell, J. *Internal energy distributions resulting from sustained off-resonance excitation in FTMS. I. Fragmentation of the bromobenzene radical cation*. Int. J. Mass Spectrom. **2000,** *195/196*, 285-302.

13. Laskin, J.; Denisov, E.; Futrell, J. H. *Fragmentation energetics of small peptides from multiple-collision activation and surface-induced dissociation in FT-ICR MS*. Int. J. Mass Spectrom. **2002,** *219*, 189-201.

14. Konn, D. O.; Murrell, J.; Despeyroux, D.; Gaskell, S. J. *Comparison of the Effects of Ionization Mechanism, Analyte Concentration, and Ion "Cool-Times" on the Internal Energies of Peptide Ions Produced by Electrospray and Atmospheric Pressure Matrix-Assisted Laser Desorption Ionization*. J Am Soc Mass Spectrom **2005,** *16*, 743-751.

15. Black, D. M.; Payne, A. H.; Glish, G. L. *Determination of Cooling Rates in a Quadrupole Ion Trap*. J Am Soc Mass Spectrom **2006,** *17*, 932-938.

16. Danell, A. S.; Glish, G. L. *Evidence for Ionization-Related Conformational Differences of Peptide Ions in a Quadrupole Ion Trap*. J. Am. Soc. Mass Spectrom. **2001,** *12*, 1331-1338.

Appendices

APPENDIX A: LABVIEW PROGRAMS

The front panel GUI of some of the most often used programs used in this dissertation are shown here with a description of what the program does. Most programs are annotated extensively, so this appendix will not waste space with too many explanations. An exception is the FAIMS-Qq program which is explained a little more. All programs should be found in the Phil folder in the Glish group space under LabVIEW.

Internal Energy/Diffuse Scattering Cooling/Vibrations

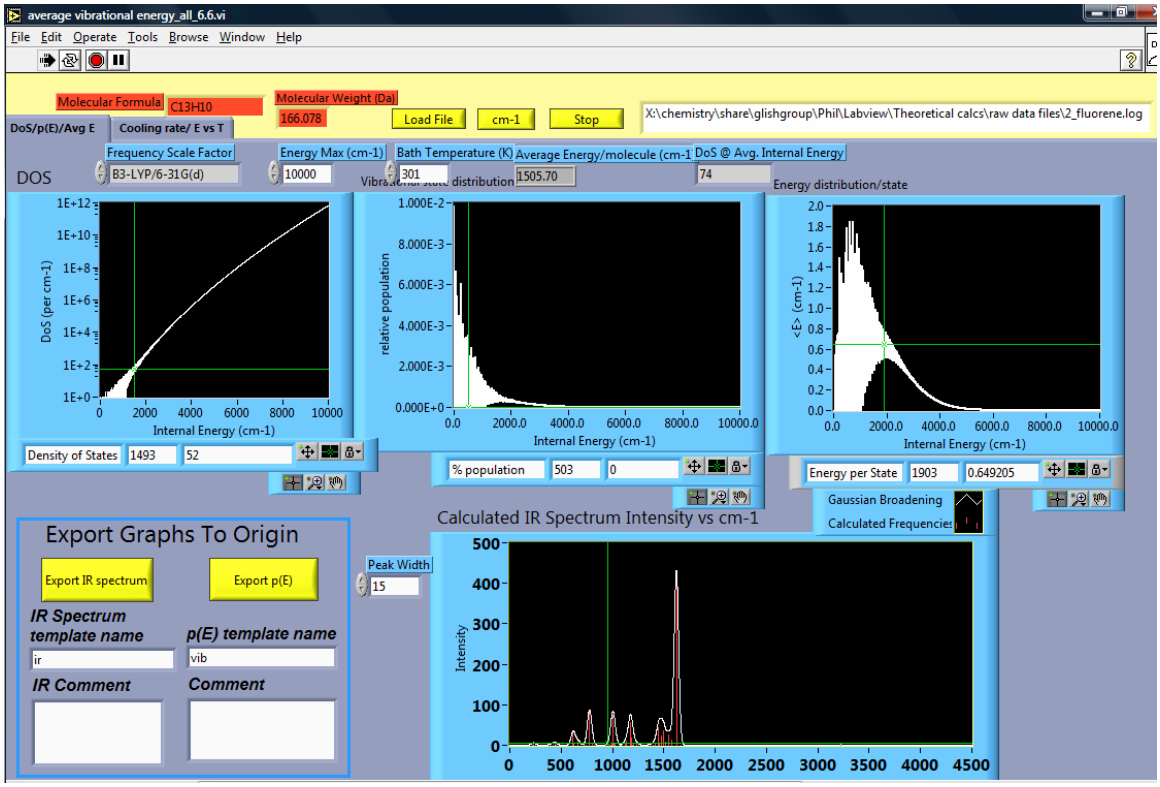

Vibrations and Cooling.llb

The **Vibrations and Cooling** program takes Gaussian output files and reads in the vibrational frequencies to calculate internal energy distributions and display calculated IR spectra. A second part of the program calculates internal energy loss by diffuse scattering.

RRKM Calculations

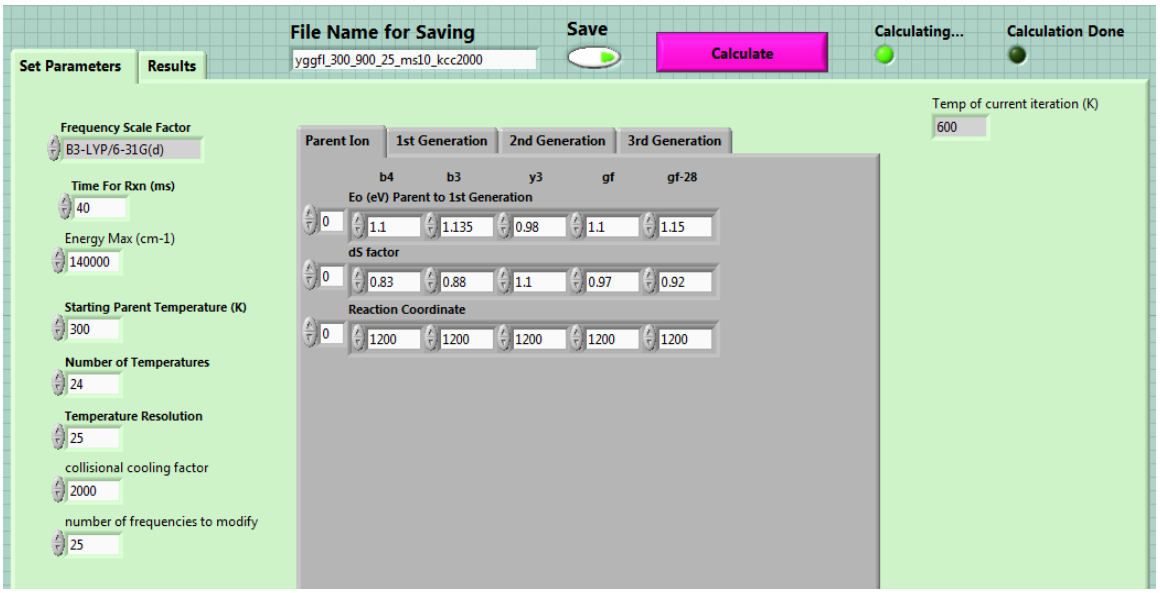

YGGFL_H_RRKM_6.0.vi

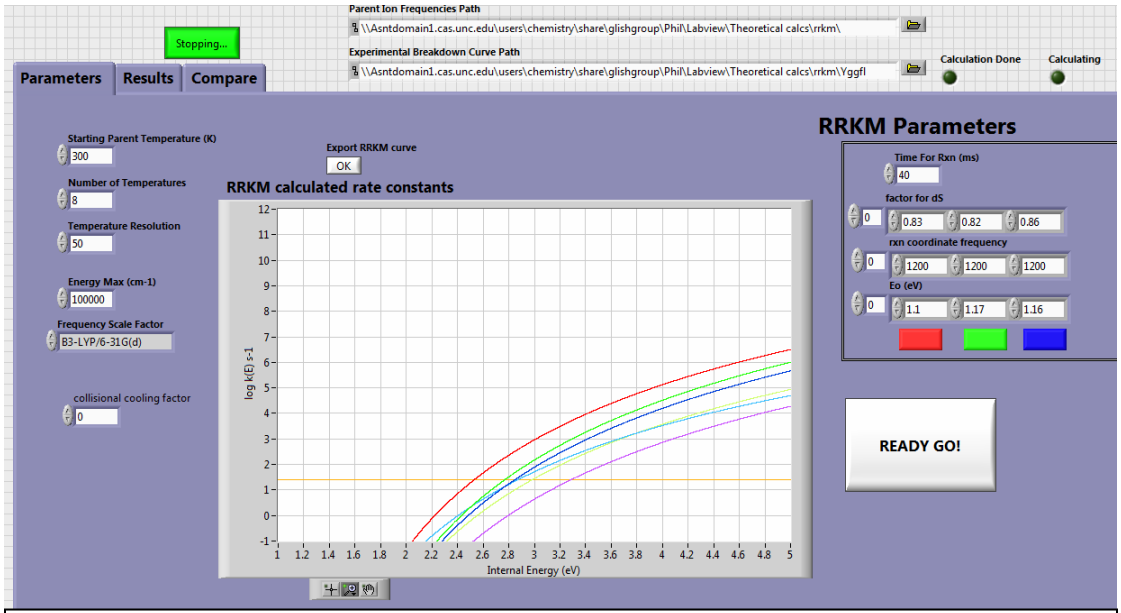

Fragmentation efficiency comparer 2.3.vi

The **YGGFL_H_RRKM_6.0** program was written to calculate mass spectra at a range of different ion internal temperatures, given dissociation parameters. Due to the

complexity of the problem, a new program has to be made for every ion that is investigated, for example $[YGGFL+H]^+$ and $[GHK+H]^+$. If fortuitously two different parent ions have the same number of product ions then the same program could be used, for example $[YGGFL+Na]^+$ and $[YGAFL+Na]^+$. The Eo and dS values must be determined experimentally as described in **Chapter 6.** The program for deriving those values, **Fragmentation efficiency comparer 2.3,** is shown above as well.

Data Workup

A number of programs have been written to expedite the workup of data. Most SIMION user programs have their own LabVIEW workup program that I can't find the data

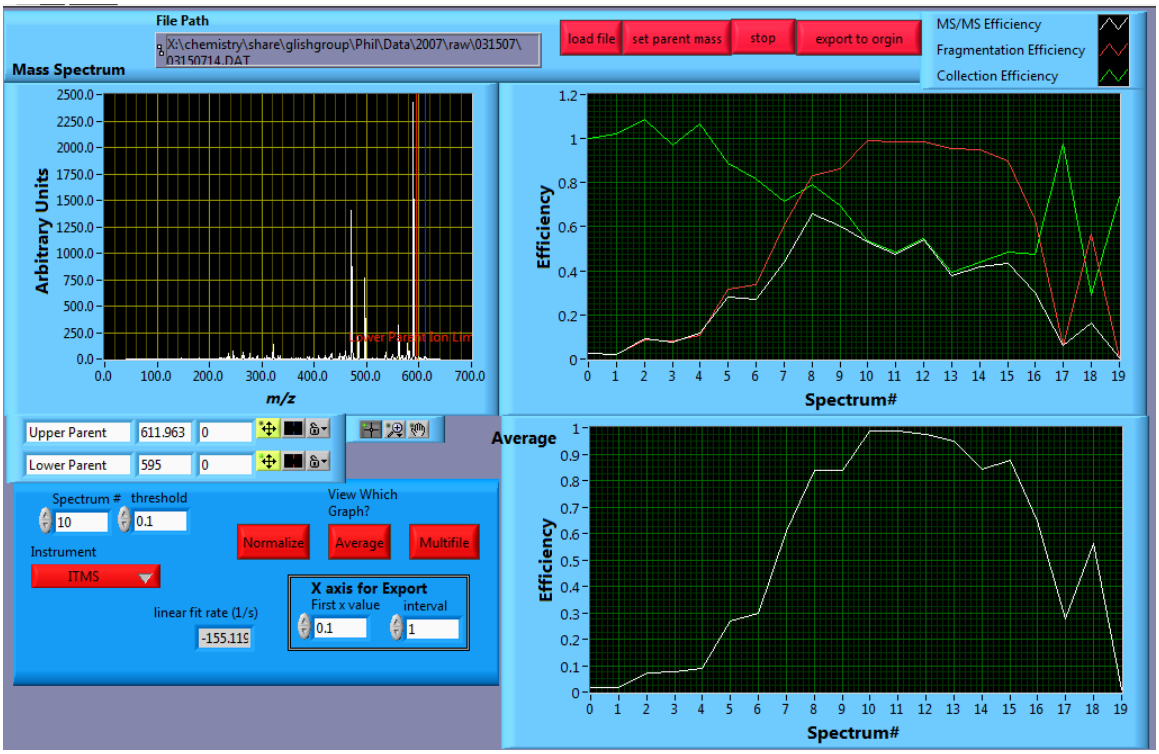

Cooling Curves Workup.llb

files to anymore, so some of them aren't in here. The first program shown, **Cooling Curves Workup,** is for quickly analyzing "key sequences" from the ITMS or APC sequences from

the IR trap. These are single files made up of numerous mass spectra where a parameter is incremented for each mass spectrum.

The next program, **Haas DA_APC2,** is important for APC scans on the IR-Trap. It takes all the microscans taken at the same condition and averages them together to save space. The Cooling Curves Workup program loads these worked up files and not raw IR-Trap APC files.

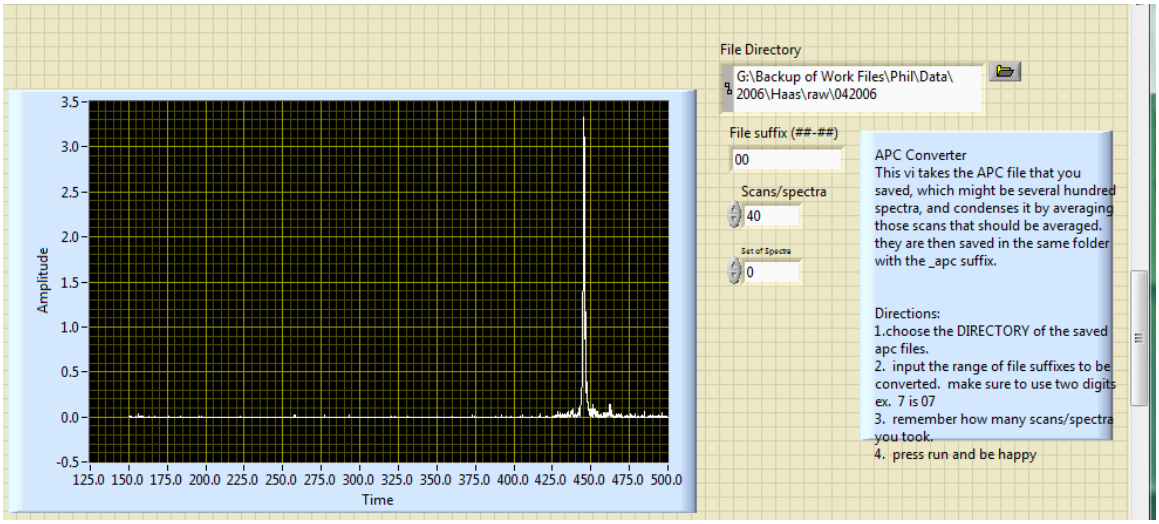

Haas DA_APC2.vi

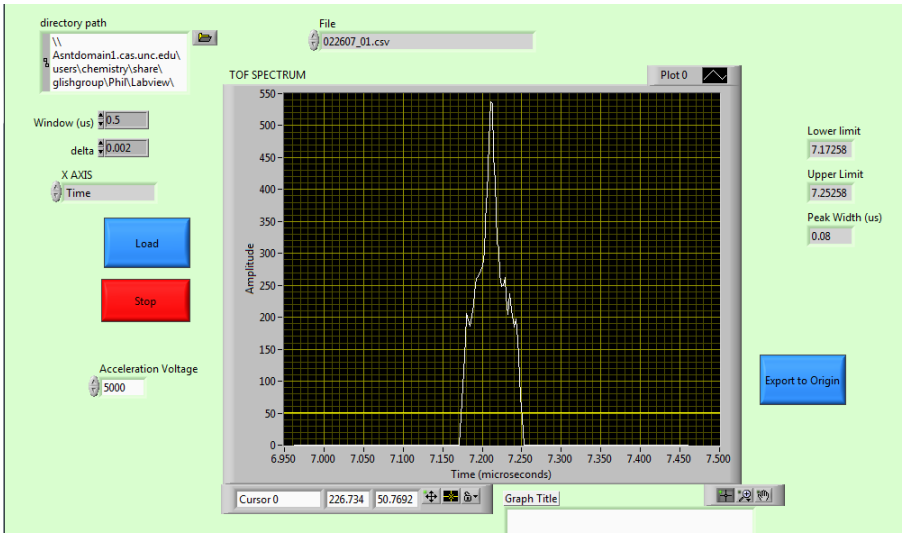

KER_TOF_SIMION.vi

The **KER_TOF_SIMION** program takes SIMION data from a kinetic energy release study, plots peaks, and gives peak widths.

To work up data from the FAIMS-Qq, **FAIMS-QEB_DA** will load multiple output files and output them to Origin. APC files can be loaded and actually worked up

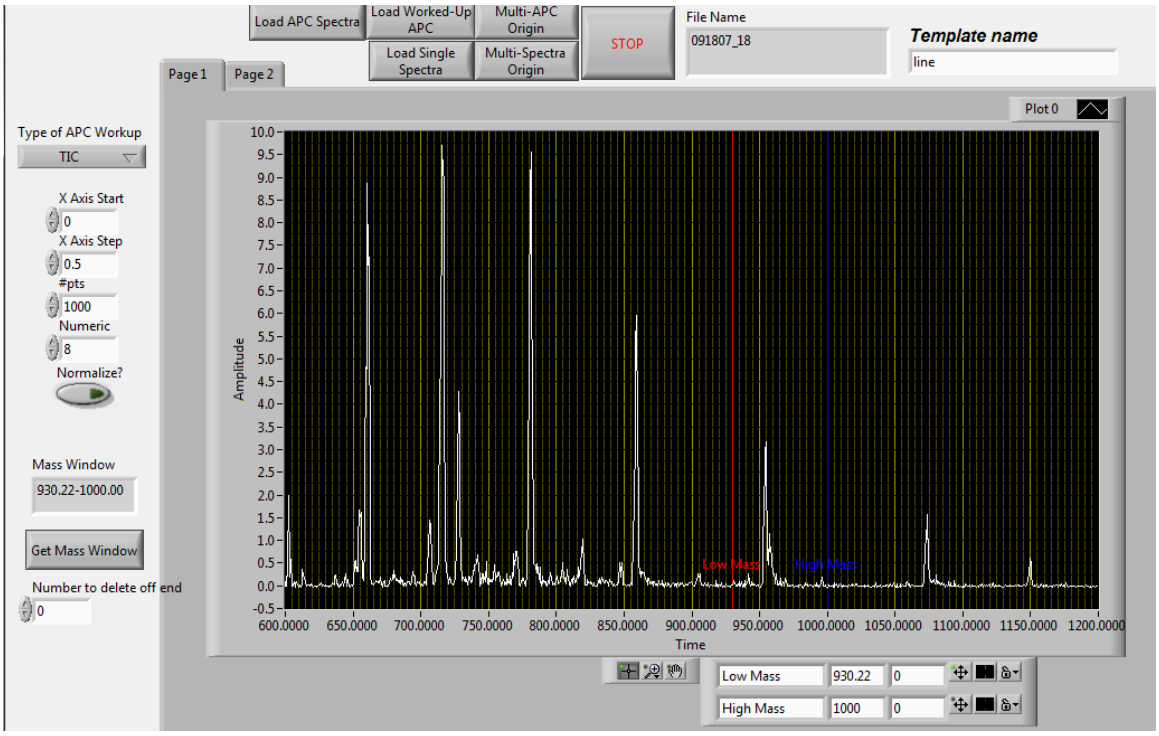

FAIMS-QEB_DA.llb

automatically. At the moment, total ion current (TIC) or TIC of a selected ion can be plotted.

FAIMS Simulation

The FAIMS simulation program was based off of Alex Shvartsburg's papers, the main one being the 2004 paper. With 16 ns timesteps, simulation of a swarm of ions for a typical residence time of 200 ms can take quite a long time. This program is not that complex when you get to the bottom of it, and C++ would probably be a better platform for writing this up.

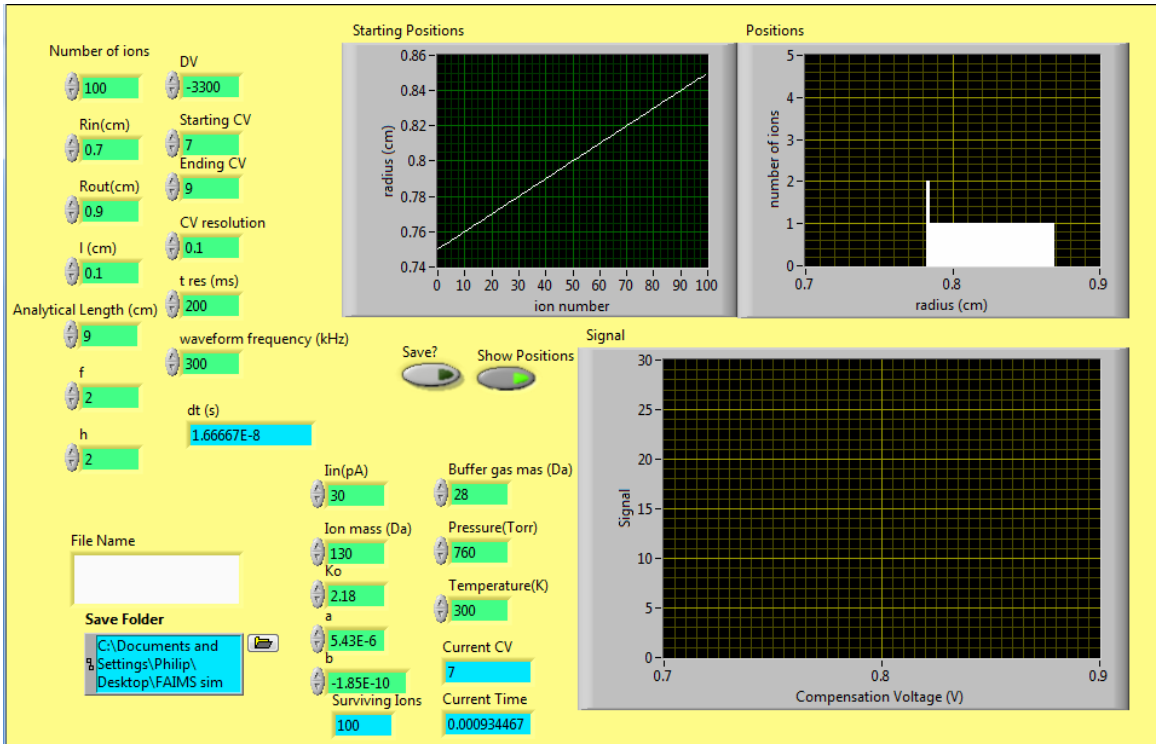

NoDiffusionScan3.0.vi

FAIMS-Qq-EB Control Program

This program controls the FAIMS-Qq right now. The functions of the buttons in the next figure are as follows: At the top left, the first 3 buttons are for "Tune" files, little configuration files that will allows one save or load all the lens voltages and parameters so

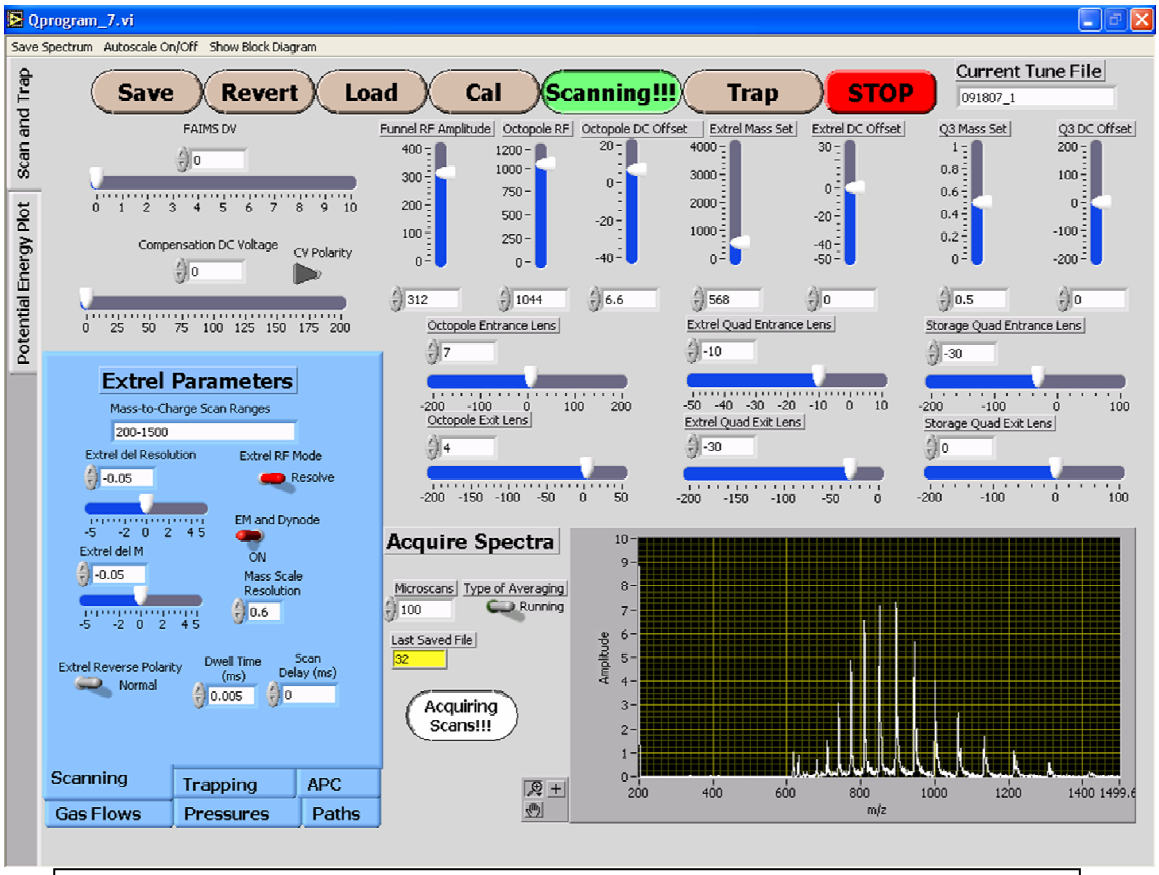

Qprogram_7.vi

that one doesn't have to write them down all the time. The "Cal" button lets one change the calibration of the any of the AO lines, such that, for example, when one wants a octopole rf amplitude of 600 V_{pp}, 5 V dc will be put out.

The "Scanning" button is for going through a range of mass-to-charge values to be run through on the Extrel quadrupole. When "Scanning" is not pushed, a static control voltage is sent to the Extrel. Therefore when "Trapping" is pushed, only one mass-to-charge ion is passed. Trapping will run through three sets of voltages: the voltages on the front

panel are during ion loading, then trapping and ejection voltages are listed in the Trapping tab at the bottom left.

The APC tab is set up to run through lists of voltages and save a spectrum at each one. There are two settings at the moment; you can step through the Storage Quad Exit Lens for measuring stopping curves in scanning or trapping mode. The second setting is for stepping through CV values for acquiring FAIMS spectra. When running the APC, make sure that averaging is set to "block" and not "running".

Hopefully most buttons in the program are self explanatory, the last thing to mention might be that the "Gas Flows" tab is for turning on and off the gas solenoid valves and setting FAIMS buffer gas flows.

APPENDIX B: SIMION PROGRAM AND GEOMETRY FILES

In this section I will just list a couple snippets of SIMION code that are useful for certain things. This first program is for operating a QITMS, adapted from the Dahl program in the SIMION 7.0 example programs. This program does a rudimentary scan function: one qz value, resonance excitation voltage and frequency are applied for a period of time, and then another set of parameters are set. I used this for the **Chapter 7** study.

```
seg Fast_Adjust                         ; generates trap rf with fast adjust
                                        ; has first pass initialization
   rcl first                            ; recall first pass flag
   x=0 gsb init                         ; if this is first reference  --> init

   rcl scaled_rf
   rcl _AMU_Mass_per_Charge *            ; multiply by mass per unit charge
   rcl _Qz_tune *                        ; rf tuning point
   sto rfvolts                           ; save rf voltage

 rcl _Tickle_Frequency                  ; get tickle frequency
   6.28318E-6 *                         ; to radians / microsecond
   rcl Ion_Time_of_Flight *             ; current tof in micro seconds
   sin
   rcl _Tickle_Voltage *

   sto Adj_Elect02
   chs
   sto Adj_Elect03

rcl ion_time_of_flight
rcl ramp_down_time
x<y gsb after_ramp

   rcl Ion_Time_of_Flight       ; current tof in micro seconds
   rcl omega *                          ; omega * tof
   rcl theta +                          ; add phasing angle
   sin                                  ; sin(theta + (omgga * tof))
   rcl rfvolts *                        ; times rf voltage
   rcl dcvolts +                        ; add dc voltage

   sto Adj_Elect01                      ; electrode 2 voltage

exit

lbl after_ramp                  ;this subroutine will just operate the trap at a different qz
  rcl scaled_rf
   rcl _AMU_Mass_per_Charge *    ; multiply by mass per unit charge
   rcl _Qz_tune_after *                 ; rf tuning point
   sto rfvolts                          ; save rf voltage

   rcl _Tickle_Frequency_after      ; get tickle frequency
   6.28318E-6 *                         ; to radians / microsecond
   rcl Ion_Time_of_Flight *     ; current tof in micro seconds
   sin
   rcl _Tickle_Voltage_after *
   sto Adj_Elect02
   chs
```

```
   sto Adj_Elect03
rtn

lbl init                                    ; parameter initialization subroutine

   1 sto first                ;              turn off first pass flag

   RCL Effective_Radius_in_cm     ; recall effective radius in cm
   entr *                  ; (r * r)
   sto r
   rcl Effective_z_in_cm
   entr *
   2 *
   rcl r +
   rcl Freqency_Hz entr * *        ; multiply by frequency squared
   5.11456E-12 *                                ;5.11456E-12 * Qz * MASS * FREQ * FREQ * (r**2+2*z**2)
   sto scaled_rf
   rcl _AMU_Mass_per_Charge *     ; multiply by mass per unit charge
   rcl _Qz_tune *                  ; rf tuning point
   sto rfvolts                     ; save rf voltage

   rcl Phaze_Angle_Deg
   >rad                            ; degrees to radians
   sto theta                       ; phasc angle

   rcl Freqency_Hz                 ; rf frequancy in hz
   6.28318E-6 *                    ; to radians / microsecond
   sto omega                       ; save frequency in radians / usec

  rtn                              ; return from subroutine
```

KE_r_z_moniterII_043007.prg

The next program snippet is again from the fast adjust part of a trapping program, where a double waveform (sum of two sine waves) is applied to the endcaps.

```
rcl _Tickle_Frequency              ; get tickle frequency
   6.28318E-6 *                    ; to radians / microsecond
   rcl Ion_Time_of_Flight *        ; current tof in micro seconds
   sin                             ; sin(theta + (omgga * tof))
   sto A
rcl _Tickle_Frequency2             ; get tickle frequency
   6.28318E-6 *                    ; to radians / microsecond
   rcl Ion_Time_of_Flight *        ; current tof in micro seconds
   rcl TF2_phase_rad +
   sin                             ; sin(theta + (omgga * tof))
   rcl A +
   rcl _Tickle_Voltage *
   sto waveform

rcl _truncate
   0
   x<y gsb cut

   rcl waveform
   sto Adj_Elect02
   sto waveform                    ; left end cap

rcl waveform
   chs
   sto Adj_Elect03                 ; set right endcap voltage

exit                               ; exit program segment
```

final study of doublewaveform and FT detection 012907.prg

This next program snippet is what was used for the **Chapter 5** study with tracking the time spent in 30 different volumes. Again it is a trapping program, so the snippet is just showing the idea behind how to track the different volumes.

```
lbl skip1
  rcl ion_Px_gu                                    ;see pg 35 notebook #7 for these numbers
  542 -
  entr *
  sto x
  rcl ion_Py_gu
  entr *
  rcl x +
  sto position
  1 x>y goto inside1
  rcl position
  4 x>y goto inside2
  rcl position
  9 x>y goto inside3
```

Etc…then

```
lbl inside1
      1 sto ion_color
      rcl in_time1
      1 +
      sto in_time1
rtn
lbl inside2
      2 sto ion_color
      rcl in_time2
      1 +
      sto in_time2
rtn
lbl inside3
            10 sto ion_color
      rcl in_time3
      1 +
      sto in_time3
rtn
```

Etc…and finally to output the data

```
rcl max_flight_time
rcl ion_time_of_flight
x>y gsb kill
rtn

lbl kill
            1 sto ion_splat

            rcl ion_time_of_flight
      rcl total_time
            rcl _qz_tune
            rcl collision

            mess ; # , # , #, #

            rcl in_time1
            rcl in_time2
            rcl in_time3
            rcl in_time4
            rcl in_time5
            rcl in_time6
```

```
rcl in_time7
rcl in_time8
rcl in_time9
rcl in_time10

mess ; # , # , # , # , # , # , # , # , # , #
```

3mm tracking 30 areas 031006.prg

The last program section I'll include is from the kinetic energy release program written for the new grant application. The equations from Metastable ions by Cooks et al. were used to model kinetic energy release in a random direction and adjust ion trajectories. Ion time of flight to reach detector was output and worked up with the LabVIEW program mentioned above.

```
SEG other_actions

rcl Next_PE_Update              ; recall time for next pe surface update
   rcl ion_time_of_flight       ; recall ion's time of flight
   x<y exit                     ; exit if tof less than next pe update
   rcl PE_Update_each_usec      ; recall pe update increment
   + sto next_pe_update         ; add to tof and store as next pe update
   1 sto Update_PE_Surface      ; request a pe surface update


rcl ion_px_mm
32                                          ; position at which CID is supposed to occur
x<=y gsb Color exit

        lbl Color
           3 sto ion_color                  ; just a visual to show at what point i'm changing the
           rcl ion_flag                     ; kinetic energies
           x=0 gsb KER exit

                lbl KER
                  1 sto ion_flag            ; turn the ion flag off so that next time we don't do
                  rcl m3 1.6605e-27 *       ; this calculation again
                  rcl T_eV * 2 * 1.602e-19 *
                  rcl m1 /                  ; calculate u2, the velocity gained by kinetic energy
                  rcl m2 /                  ; release
                  1.6605e-27 /
              1.6605e-27 /
                  sqrt
                  .001 *
                  sto u2

                  rand 3.14159 *            ; calculate random angles for the direction the KER
                  sto phi                           ; phi is 0 to 180 degrees, theta 0 to 360 degrees
                  sin                               ; x=sin(phi)cos(theta)
                  sto sin_phi                       ; y=sin(phi)sin(theta)
                  rcl phi                           ; z=cos(phi)
                  cos
                  rcl u2 *
                  sto u2_z

                  rand 3.14159 * 2 *
                  sto theta
                  sin
```

```
sto sin_theta
rcl theta
cos
sto cos_theta

rcl sin_phi
rcl cos_theta *
rcl u2 *
sto u2_x

rcl sin_phi
rcl sin_theta *
rcl u2 *
sto u2_y

rcl ion_vx_mm                   ; multiply the direction vector times u2 and add to
rcl u2_x +                      ; current velocity
sto ion_vx_mm
rcl ion_vy_mm
rcl u2_y +
sto ion_vy_mm
rcl ion_vz_mm
rcl u2_z +
sto ion_vz_mm
```

Linear_short.prg

SIMION Geometry Files

```
================================================================================
pa_define(76,76,788,p,xy)       ; 28x, 28y, 299z 3D Planar xy mirrored

; scaled for 0.3 mm/grid unit
; r0 = 282  rrod = 100  based on r = .35 r0
;ion funnel
e(1)                                            ; electrode number 1
        {                                               ; fill ion funnel plate
        fill{within{box3d(0,0,0,76,76,4)}
                notin{circle(0,0,8.35)}}        ; except for center hole
        }
e(2)                                            ; electrode number 1
        {                                               ; fill ion funnel plate
        fill{within{box3d(0,0,10,76,76,14)}
                notin{circle(0,0,13.35)}}       ; except for center hole
        }
e(3)                                            ; electrode number 1
        {                                               ; fill ion funnel plate
        fill{within{box3d(0,0,20,76,76,24)}
                notin{circle(0,0,18.35)}}       ; except for center hole
        }
e(4)                                            ; electrode number 1
        {                                               ; fill ion funnel plate
        fill{within{box3d(0,0,30,76,76,34)}
                notin{circle(0,0,23.35)}}       ; except for center hole
        }
e(5)                                            ; electrode number 1
        {                                               ; fill ion funnel plate
        fill{within{box3d(0,0,40,76,76,44)}
                notin{circle(0,0,28.35)}}       ; except for center hole
        }
e(6)                                            ; electrode number 1
        {                                               ; fill ion funnel plate
        fill{within{box3d(0,0,50,76,76,54)}
                notin{circle(0,0,33.35)}}       ; except for center hole
        }
e(7)                                            ; electrode number 1
        {                                               ; fill ion funnel plate
```

```
        fill{within{box3d(0,0,60,76,76,64)}
                notin{circle(0,0,38.35)}}       ; except for center hole
        }
e(8)                                                    ; electrode number 1
        {                                               ; fill entrance lens
        fill{within{box3d(0,0,77,76,76,81)}
                notin{circle(0,0,10)}}          ; except for center hole
        }
;octapole ion guide

e(9)                                                    ; electrode number 2
        {                                               ; fill top rod
        fill{within{circle(0,20,5) box3d(0,0,101,76,76,769)}}
        }

e(9)                                                    ; electrode number 2
        {                                               ; fill right rod
        fill{within{circle(20,0,5) box3d(0,0,101,76,76,769)}}
        }

e(10)                                                   ; electrode number 1
        {                                               ; fill right rod
        fill{within{circle(14,14,5) box3d(0,0,101,76,76,769)}}
        }

;exit lens
e(11)                                                   ; electrode number 4
        {                                               ; fill ion entry plate
        fill{within{box3d(0,0,778,76,76,788)}
                notin{circle(0,0,4.2)}}         ; except for center hole
        }
```

Octopole.gem: for ion funnel into octopole in FAIMS-Qq

```
pa_define(76,76,650,p,xy)       ; 28x, 28y, 299z 3D Planar xy mirrored

; scaled for 0.3 mm/grid unit
; r0 = 4.14  rrod = 4.75  based on r = 1.1468 r0
;entrance
e(1)                                                    ; electrode number 1
        {                                               ; fill ion funnel plate
        fill{within{box3d(0,0,0,76,76,6)}
                notin{circle(0,0,12.5)}}        ; except for center hole
        }
;prefilter
e(2)                                                    ; electrode number 2
        {                                               ; fill top rod
        fill{within{circle(0,29.6,15.8) box3d(0,0,12,76,76,98)}}
        }

e(3)                                                    ; electrode number 2
        {                                               ; fill right rod
        fill{within{circle(29.6,0,15.8) box3d(0,0,12,76,76,98)}}
        }
;mass filter
e(4)                                                    ; electrode number 2
        {                                               ; fill top rod
        fill{within{circle(0,29.6,15.8) box3d(0,0,100,76,76,550)}}
        }

e(5)                                                    ; electrode number 2
        {                                               ; fill right rod
        fill{within{circle(29.6,0,15.8) box3d(0,0,100,76,76,550)}}
        }
;postfilter
e(6)                                                    ; electrode number 2
        {                                               ; fill top rod
        fill{within{circle(0,29.6,15.8) box3d(0,0,552,76,76,638)}}
```

```
        }

e(7)                                                    ; electrode number 2
        {                                                       ; fill right rod
        fill{within{circle(29.6,0,15.8) box3d(0,0,552,76,76,638)}}
        }
;exit lens
e(8)                                                    ; electrode number 1
        {                                                       ; fill ion funnel plate
        fill{within{box3d(0,0,644,76,76,650)}
                notin{circle(0,0,12.5)}}        ; except for center hole
        }
```

Quad.gem: Quadrupole mass filter with lenses and pre/post filters

```
=============================================================================================
pa_define(399,173,1,cylindrical,y_mirror)
        ; 399x, 173y, 1z 2D cylindrical electrostatic array

locate(271)                                             ; shift working center to trap center
  {
  e(1)                                                  ;electrode 1 - trap ring electrode
    {                                                   ;draw y hyperbola (ring electrode)
    fill{within{hyperbola(0,0,70.7,100)}}
    }

locate(-7.6)
  {
  e(2)                                                  ;electrode 2 - left end cap
    {                                                   ;draw left end cap x hyperbola
    fill
      {                                                 ; twist hyperbola 90 degrees
      within{locate(,,,,,90){hyperbola(0,0,100,70.7)}}
                                                        ; exclude right half of hyperbola
      notin{box(0,0,400,400)}

      locate(-271)                                      ; shift back to left edge
        {                                               ; create interior of left end cap

        }
      }
    }
 }

locate(7.6)
  {
  e(3)                                                  ;electrode 3 - right end cap
    {                                                   ;draw right end cap x hyperbola
    fill
      {                                                 ; twist hyperbola 90 degrees
      within{locate(,,,,,90){hyperbola(0,0,100,70.7)}}
                                                        ; exclude left half of hyperbola
      notin{box(-400,0,0,400)}

      locate(-271)                                      ; shift back to left edge
        {                                               ; remove interior of right endcap

        }
      }
    fill
       {
       locate(-271)                                     ; shift back to left edge
         {
         within{box2d(397,0,399,14)}
         }
      }
    }
  }
  }
```

Stretch2.gem: Geometry file used for all QITMS programs

```
================================================================================
pa_define(152,40,1,c,y,e)       ; Create a 152x, 40y, 1z  2D
                          ; cylindrical electrostatic array

e(1)                       ; fast adjust electrode (1) of one volt
   {                       ; left edge blocking electrode
   locate(0)                  ; locate electrode at x = 0
      {
      fill{within{box(0,0,1,200)}}
      }
   }

e(2)                       ; fast adjust electrode (2) of two volts
   {                       ; left grid electrode
   locate(19)                 ; locate grid at x = 19
      {
      fill{within{box(0,0,0,200)}}
      }
   }

e(3)                       ; fast adjust electrode (3) of three volts
   {                       ; right grid electrode
   locate(51)                 ; locate grid at x = 51
      {
      fill{within{box(0,0,0,200)}}
      }
                          ; right edge detector electrode
   locate(150)                ; locate electrode at x = 0
      {
      fill{within{box(0,0,1,200)}}
      }
   }
```

Linear.gem: One geometry for TOF kinetic energy release studies

```
================================================================================
```

APPENDIX C: DIAGRAMS OF ELECTRONIC CIRCUITRY

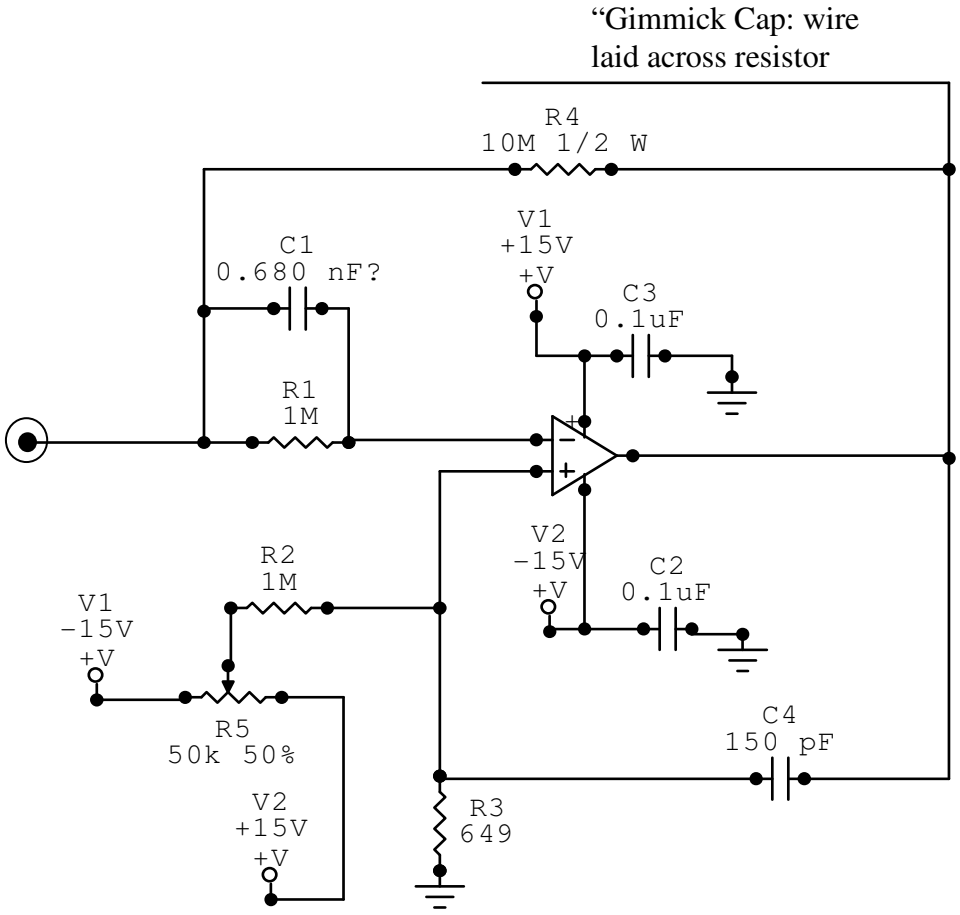

Preamplifier Circuit: Page 123, notebook #10: LM442

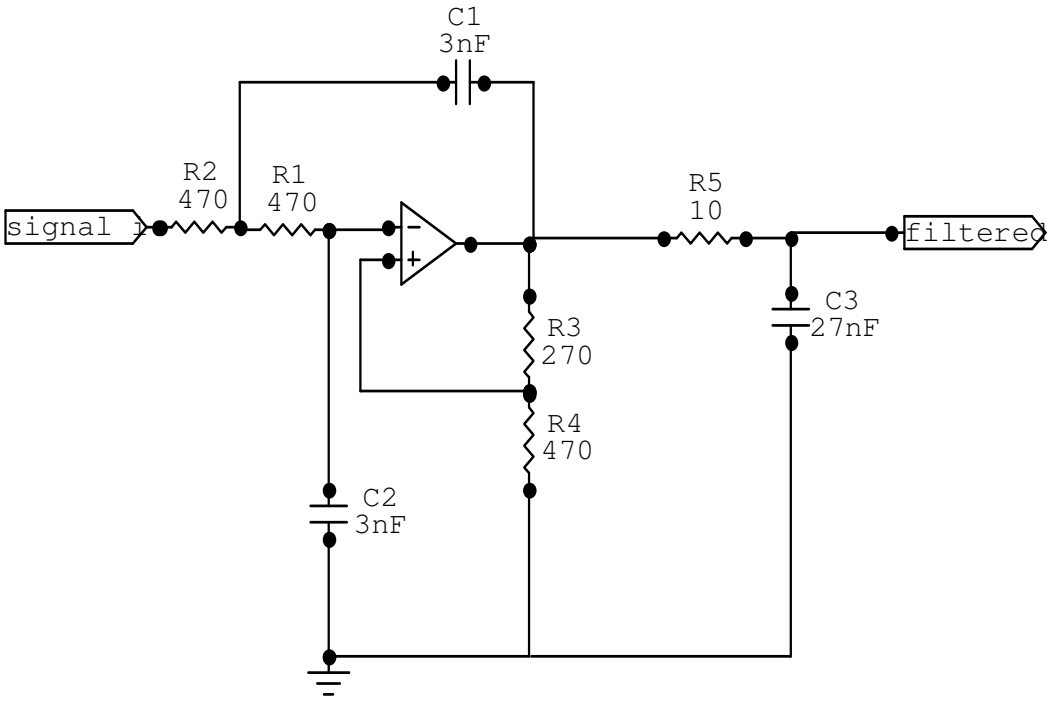

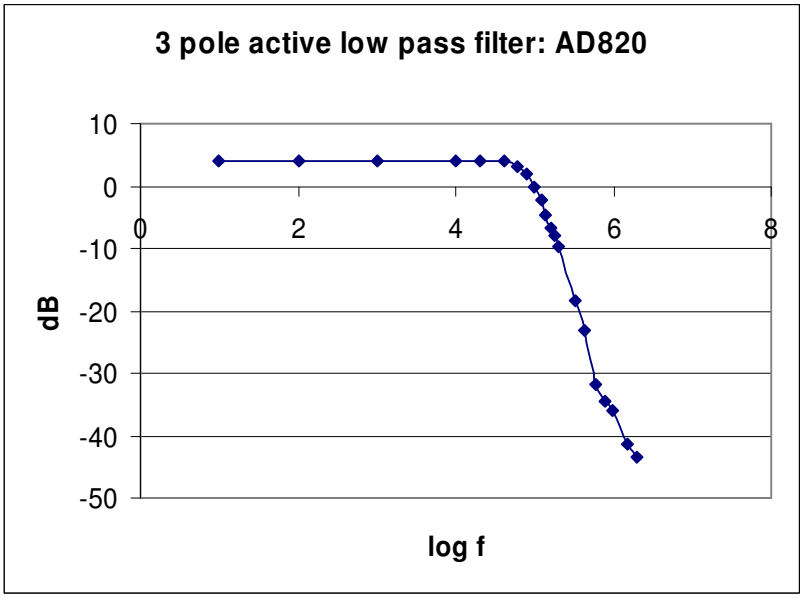

3 Pole Low Pass Filter: Using pg 274 from the Art of Electronics

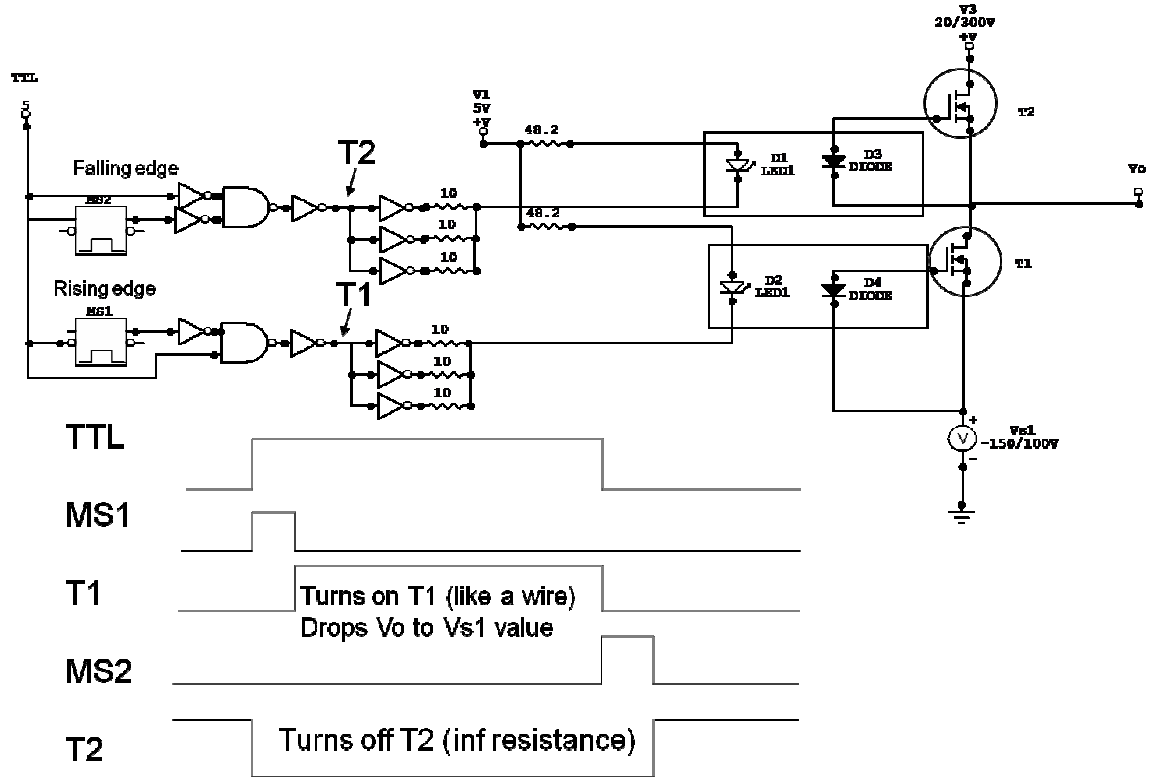

High Voltage Gate: SN74L2123N, SN74AC04, SN7400, IRFU1N60A, PVI1050

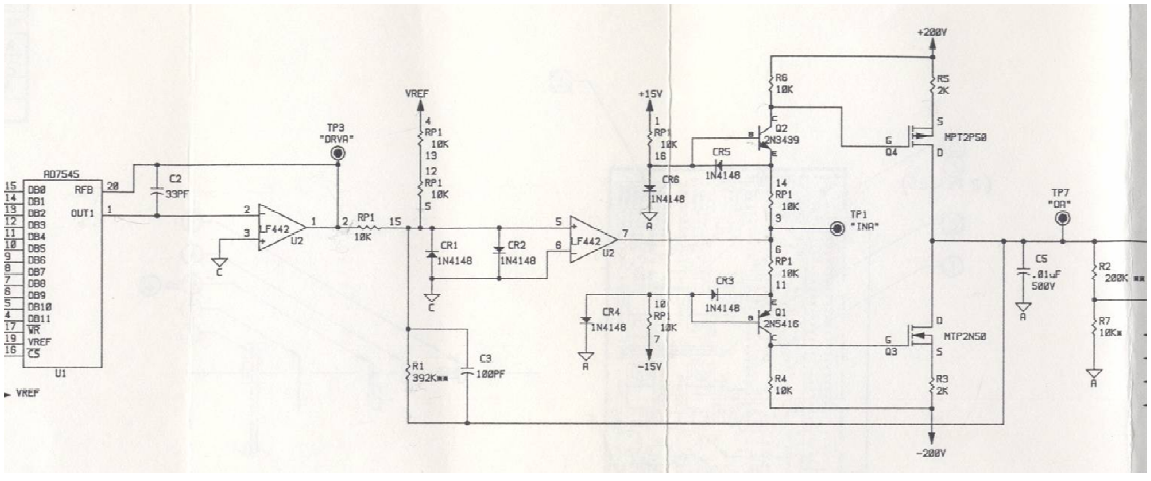

±200 V Supply: From TSQ70 Schematics

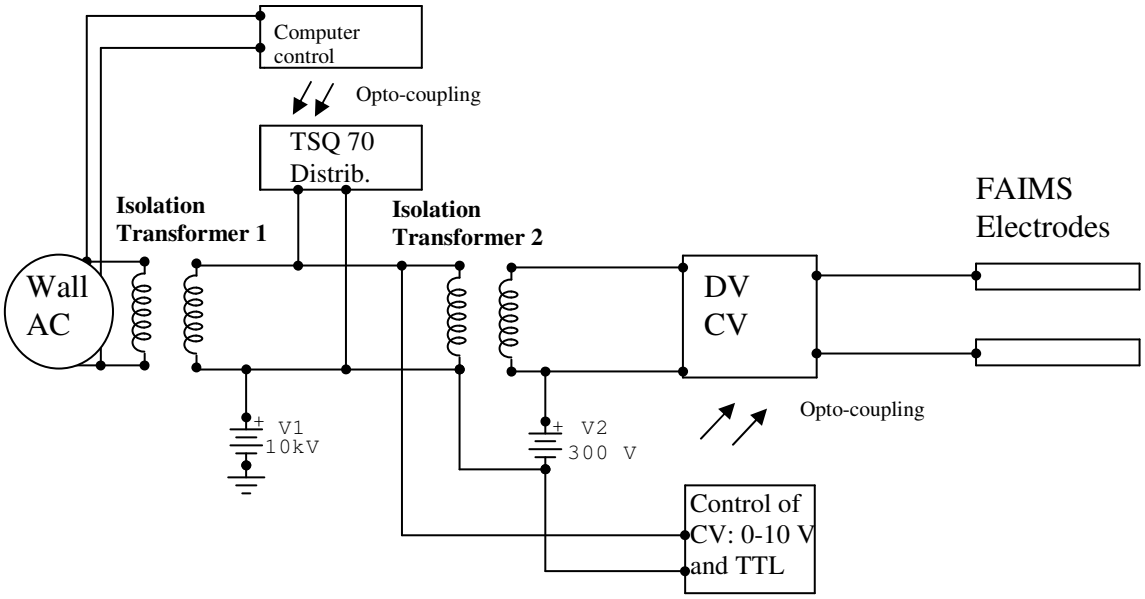

Overall Electrical Schematic for FAIMS-Qq

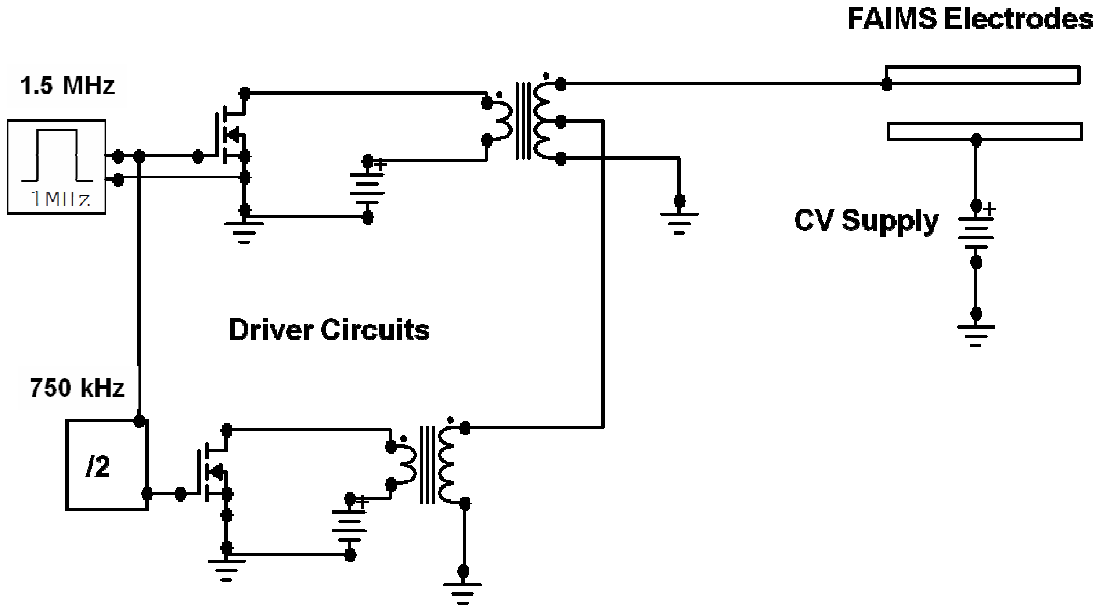

General Circuit Drawing for Dispersion Voltage Generator.

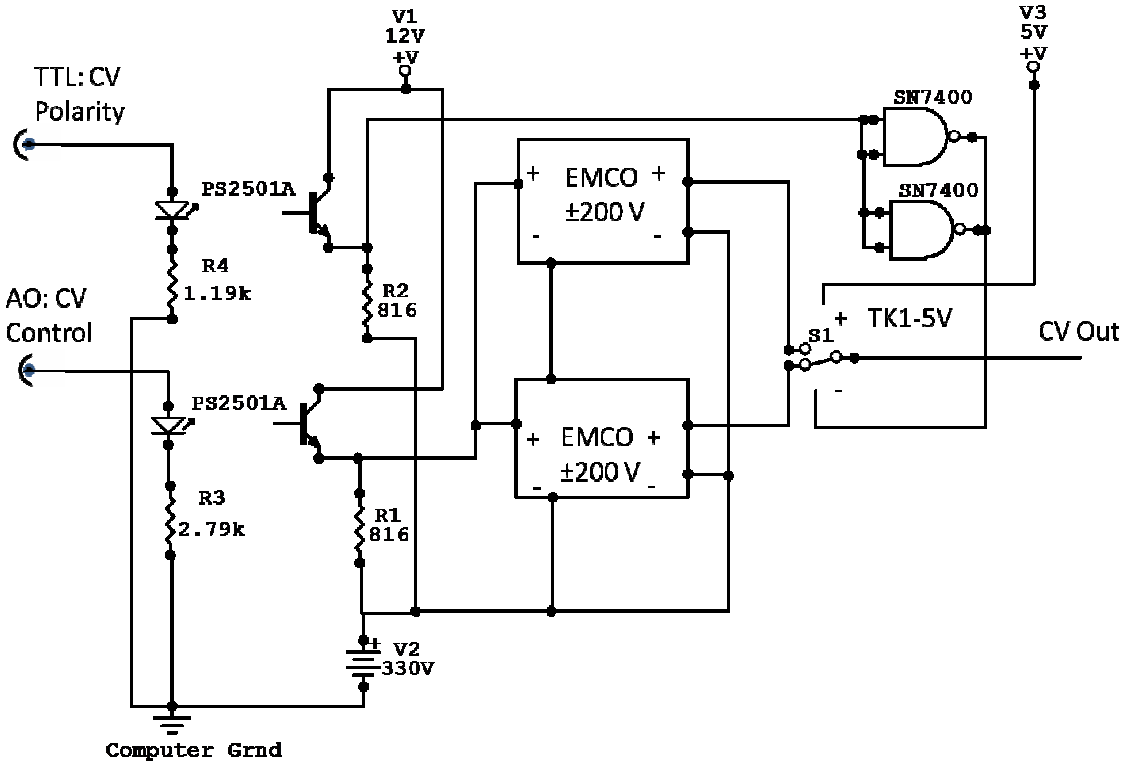

CV circuit with optical isolation: PS2501A-1-A-ND

APPENDIX D TIPS ON OPERATION OF IR-TRAP AND TSQ 700

Electron Ionization

Source V	10
Filament Off.	-60
Filament V	5
Filament A	5
Einzel Lens	
1st	-20
2nd	-200
3rd	-20

IR-Trap ESI

Front Cap	-1010
Exit Cap	200
Tube Lens	400
Skimmer	30
Octopole Offset	20
Exit Lens	-20
1st Einzel	-120
2nd Einzel	-300
Start Mass	60-150

Qq ESI

ESI	1640
Entrance	283
Deflector	354
IF+	167
IF-	grounded
SK1	18.8
SK2	18.3
IF2	0.43
OctoEntrance	6.8
OctoDC	6.9
OctoExit	3.4
OctoRF	1050 Vpp
ExtrelEntrance	-10
ExtrelDC	0
ExtrelExit	-30

Pre/Post DC	-30 to -100
StoreEntrance	-30
StoreDC	0
StoreExit	-80
StoreRF	600 Vpp
Exit2	-120
Exit3	-80
Dynode	-6000
Multiplier	-2000

APPENDIX E MECHANICAL DRAWINGS

A note about the Mechanical drawings that follow: These are mostly to get an idea about how pieces fit together and general sizes. For the files actually sent to the machine shops, the reader should find the Phil folder in the Glish space.

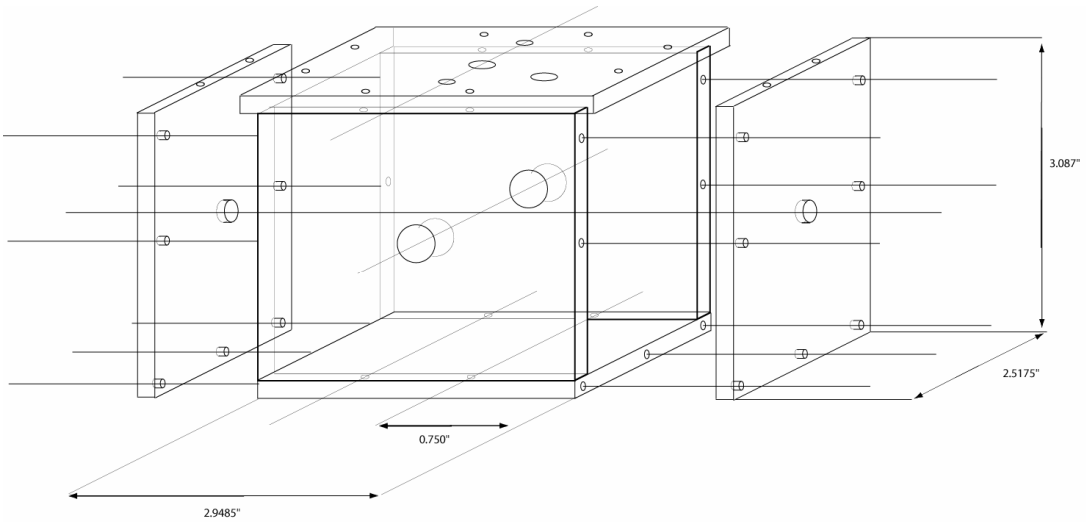

IR-Trap 2nd Stage Holder

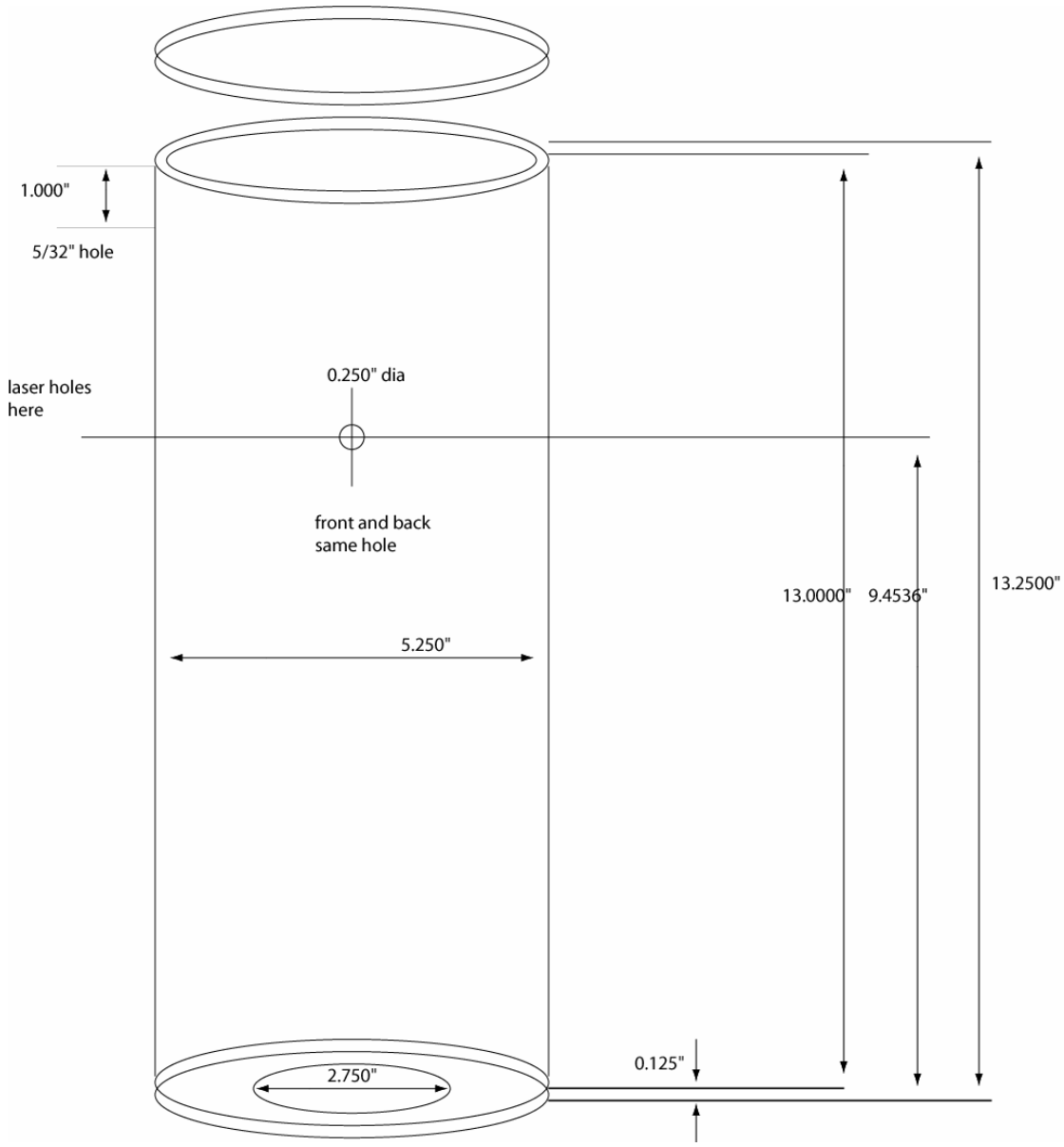

First Stage Shield for IR-Trap

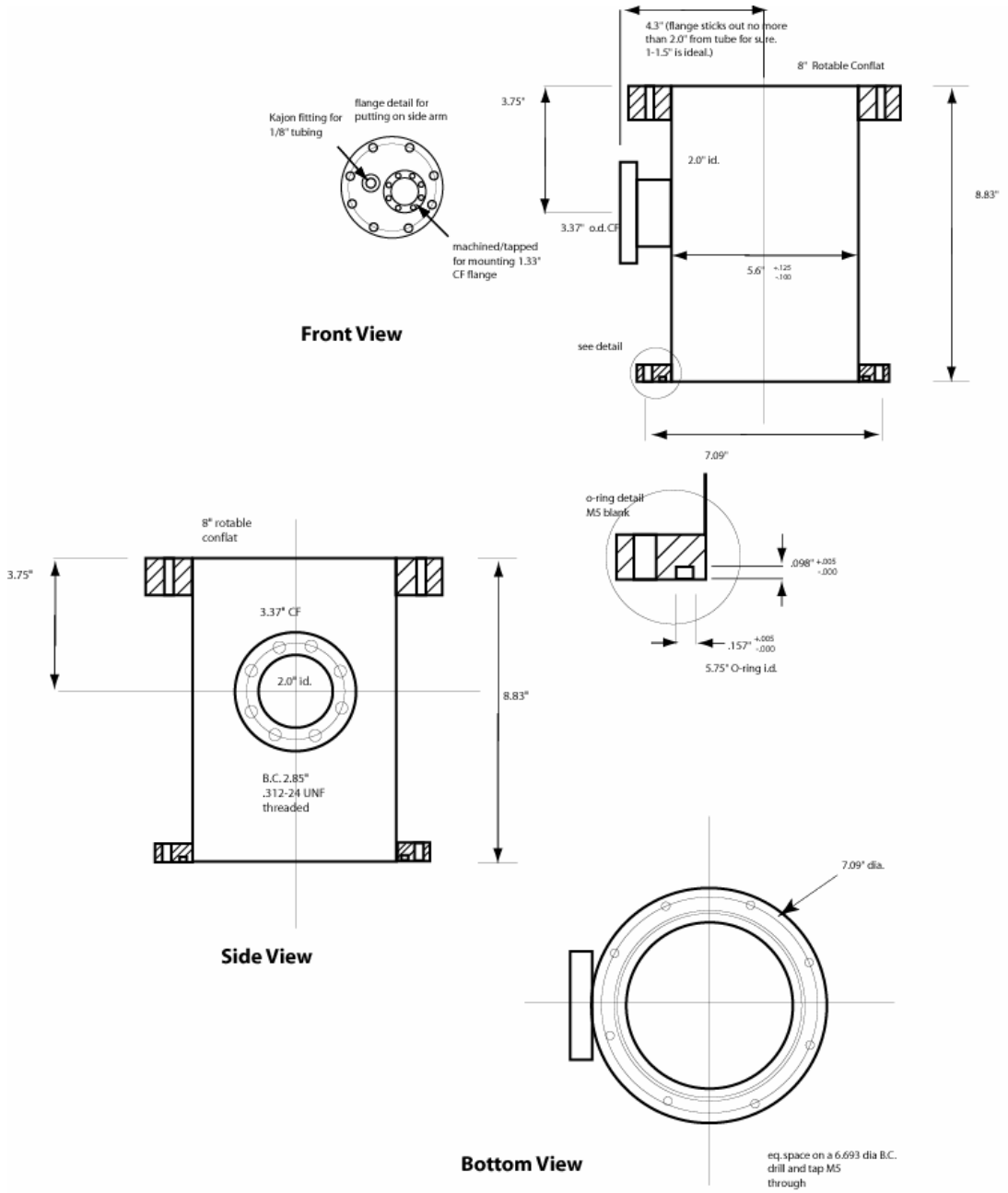

Cryostat Flange Extension for IR-Trap

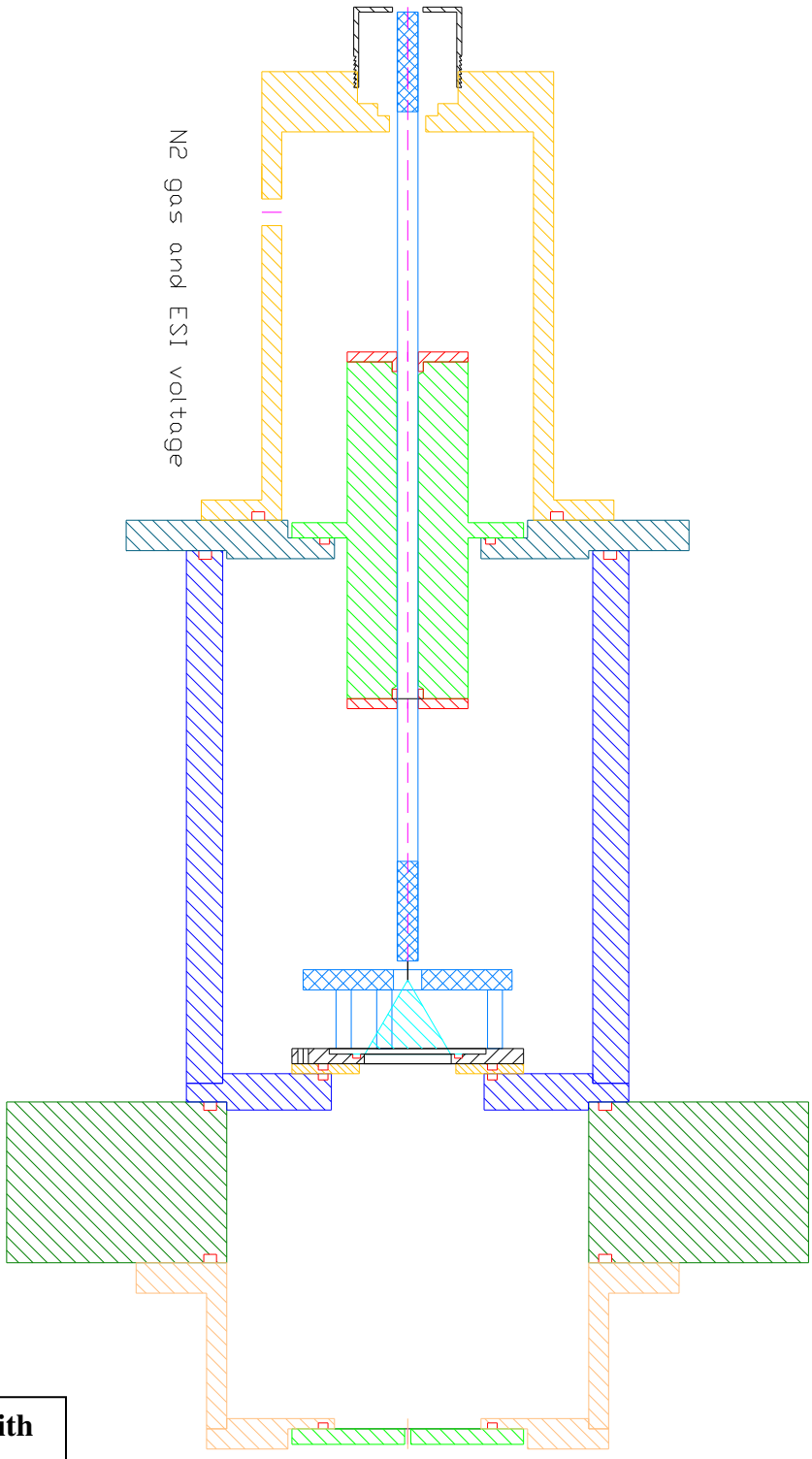

IR-Trap Source with Modifications for Bruker Capillaries:

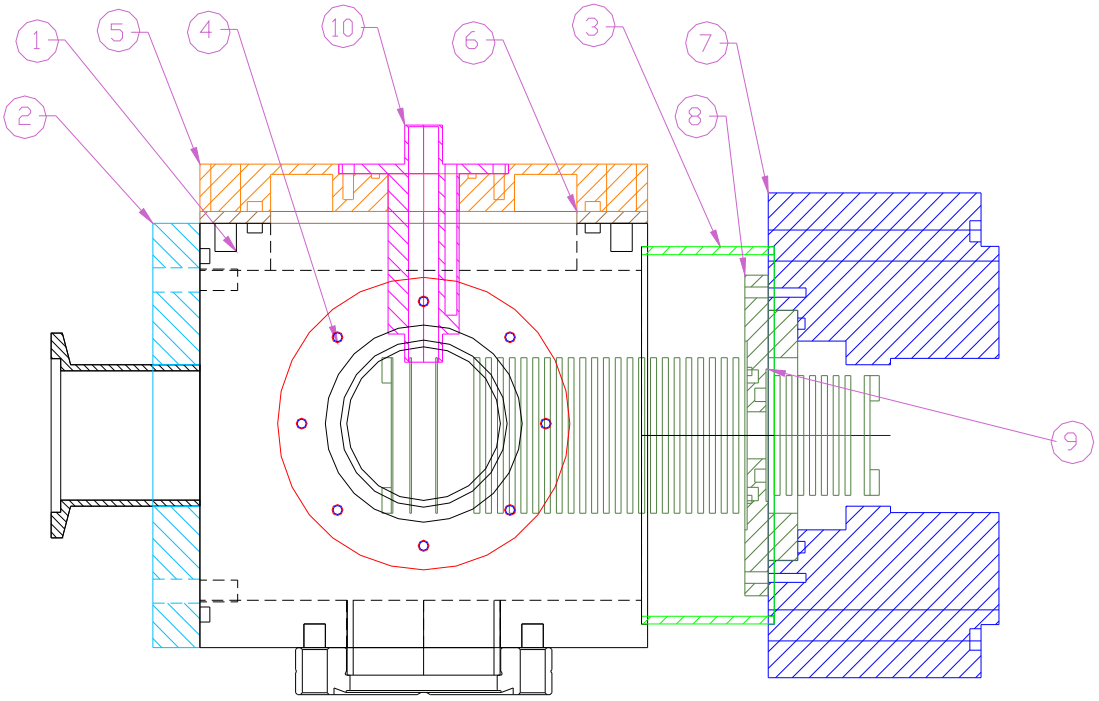

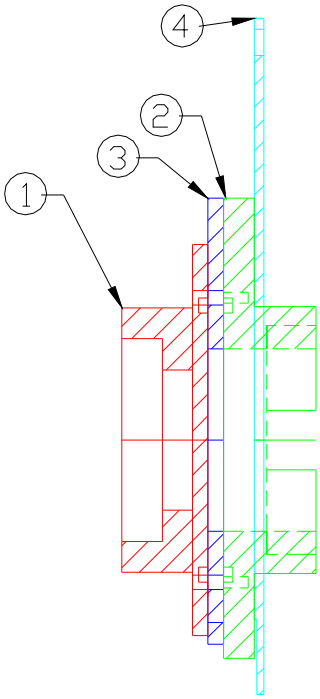

Ion Source of FAIMS-Qq instrument (above) and interface between octopole and main pressure region (right)…most of the instrument has been displayed in Chapter 8, but these are close-ups that were not included. On the right figure, 1 is octopole exit lens, 3 is PEEK spacer, 2 is Extrel quad holder, and 4 is interface between octopole and low pressure regions. 2 is welded onto 4.

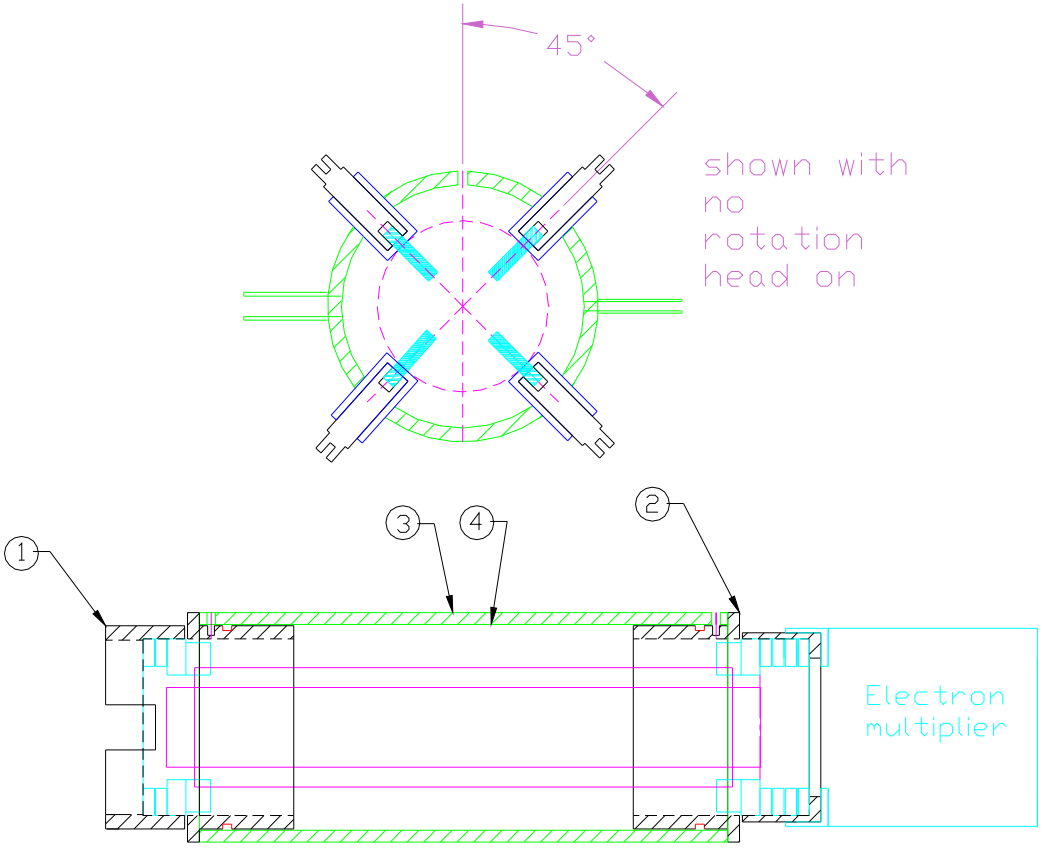

Gas tight Quadrupole Collision Cell for FAIMS-Qq. There are spaces for two lenses after Extrel quadrupole on left, and 3 lenses after collision cell on right side

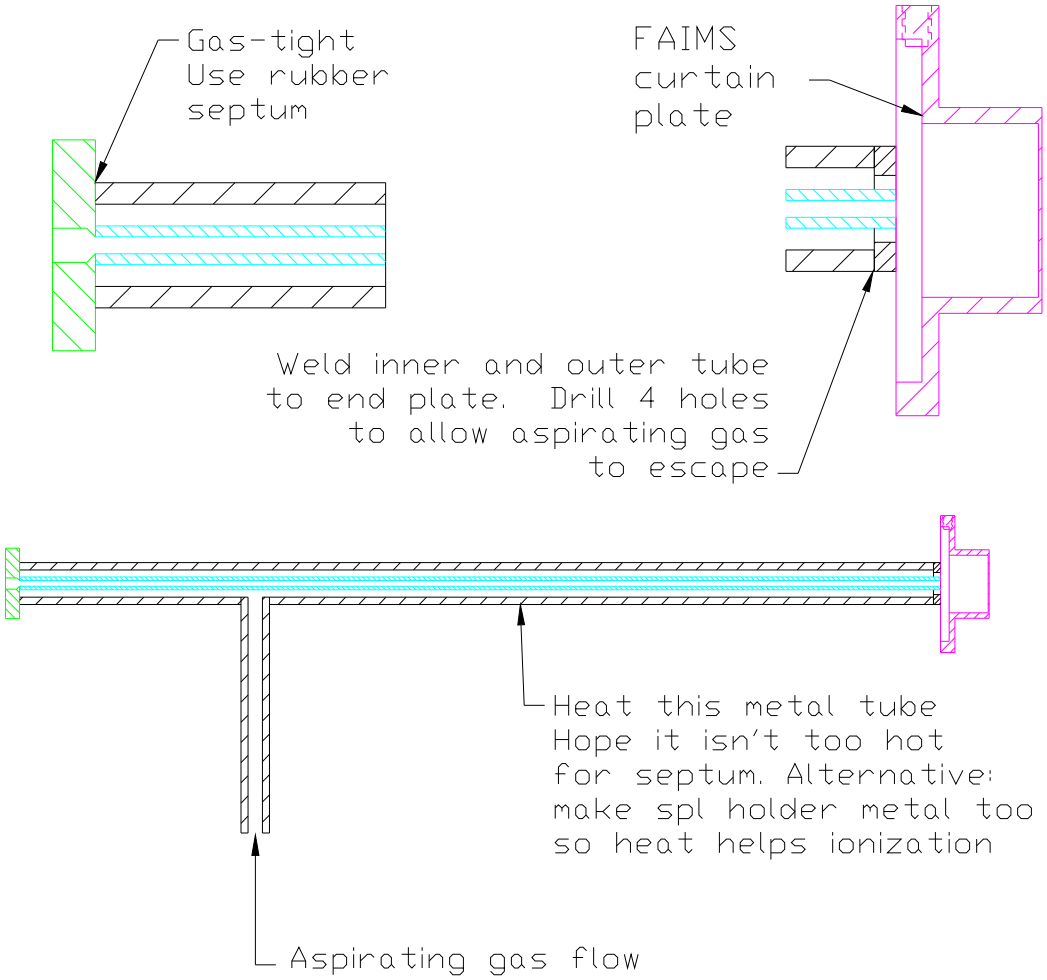

Idea to make an AP-MALDI adaptor for FAIMS